Highly deformable confined rubberised concrete elements for seismic applications

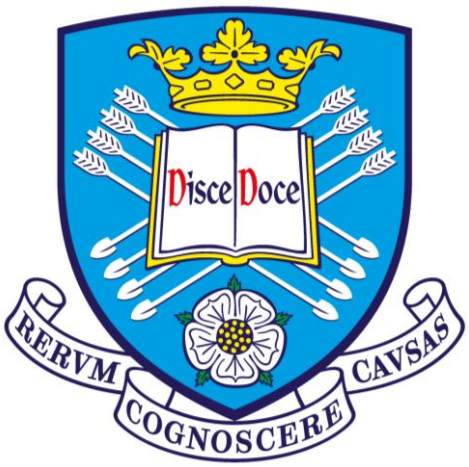

A thesis presented for the degree of

Doctor of Philosophy in Civil and Structural Engineering

at The University of Sheffield

By

Imad El Khouri

Sheffield, UK

August 2021

To *Loo Yeo*, and *Yvonne Wong*;

My friends and my role models;

You were there for me in my moment of need;

You generously believed in me, and at times rightfully doubted me;

This work would not have been without you;

Thank you!

Abstract

Short columns in reinforced concrete (RC) structures are particularly vulnerable to seismic actions. Even though steel reinforcement can be designed to impart adequate ductility, the deformability of these structural members is limited by the relatively low strain capacity of conventional concrete (CC). Recent research on rubberized concrete (RuC) and confined RuC has shown that this novel material can develop significant axial and lateral strain and it holds great potential for the development of innovative structural solutions for applications where large deformations are required.

This study aims to investigate the use of confined rubberised concrete (CRuC) in elements with high shear deformation demand, as well as provide a proof-of-concept for a cost-effective base-isolation system made of confined rubberised concrete columns.

The first part of this study examines the behaviour of short columns in a one-bay one-storey building made of conventional RC. The building collapsed with the brittle failure of the short column at a small drift ratio of 0.37% for the unrestrained column. The experimental results are used to validate a numerical model in Abaqus, which in turn is used to develop a strut and tie model (STM) to predict the behavior of RC short columns. The validated numerical and analytical models are utilized to investigate the use of highly deformable CRuC short columns. The results show that CRuC enables the development of high ductility/deformability in the columns and promotes stress redistribution within the frame, thus offering a viable solution for enhanced global capacity and deformability.

The seismic behaviour of two buildings with short columns is examined in the second phase of this study through a series of shake-table tests. While the conventional RC building exhibited short column failure, the building with CRuC short columns (CRuC-EQ) was able to withstand 25% more peak ground acceleration (PGA) than the CC building (2.0g), without showing any sign of severe damage. The CRuC short columns were able to achieve up to 7.7% drift ratio, compared to 2% for the CC short columns. The analytical STM developed was modified to fit each building and the models were subjected to the same seismic load protocol as per the experiment. The experimental and numerical results show a good agreement, which validates the model for seismic modelling.

The last part of this study investigates both experimentally and analytically the concept of a CRuC base-isolation system. The low stiffness bilinear behaviour of CRuC can be exploited to provide high damping through hysteresis, as well as lengthen the natural period of the structure to lessen the acceleration response. The CRuC-EQ building was mounted on four CRuC isolators and then tested on a shake-table with the same seismic load protocol. The isolators exhibited large drift ratios (up to 17%), and they successfully reduced the response of the superstructure at high PGA values. The concept of a CRuC base-isolation system was further examined through a series of numerical analyses and it was found that the implementation of such an innovative solution can successfully reduce inter-storey drift (up to 67%), base-shear (up to 32%), and base-moment (up to 62%).

Acknowledgements

First and foremost, I want to express my deepest gratitude to my supervisor Dr. Maurizio Guadagnini. From the first day you welcomed me in Mappin building till our last meeting, you were there for me with guidance, patience, and friendship. You made me a better researcher and person!

I want to thank Prof. Kypros Pilakoutas for the opportunity to pursue this research work. I also want to thank Dr. Iman Hajirasouliha for his supervision and our shared teaching experiences, I learned a lot from them. To Reyes and David, thank you for the technical support you provided, it was essential to build this work. Many thanks to the civil engineering team and laboratory technicians at the Technical University Gheorghe Asachi in Iasi, Romania.

For all the good times and fun we shared, I want to thank Sir Panos, Szymon, Edo, Marco, Soheil, Ilya, Michelle, Laura, Ben, and Mat, we worked hard and played JaJa style harder!

To all the researchers and friends of the Concrete and Earthquake Engineering group, namely, Samar, Niki, Andrea, Francesca and Con, thank you for all the emotional support and the good talks we had.

Harris, your wise words were very calming in some very turbulent times, thank you for that!

To Georges, Michel, and Giselle, my Sheffield family. Thank you for all the home cooked meals, the tea nights, the jokes, the political debates, the rides and the trips, and all the love we shared.

To my family; Mom, your faith and belief in me kept me going in dark times, you are my beacon; to my Dad, I am here because of you and I am proud of where I am, thank you for your support and patience; to Mazen and Hanadi, you are my strength and you stood by me throughout, I love you; to Elias, thank you for all the support and wisdom you shared with me.

List of Contents

List of Figures

Chapter 1. Introduction

Chapter 2. Literature Review

Chapter 3. Simulating the behaviour of short columns and how to enhance their capacity and ductility

Chapter 4. Shake-table tests on frames with short columns made with conventional concrete and FRP-confined rubberised concrete

List of Tables

Chapter 2. Literature Review

Chapter 3. Simulating the behaviour of short columns and how to enhance their capacity and ductility

Chapter 4. Shake-table tests on frames with short columns made with conventional concrete and FRP-confined rubberised concrete

Chapter 5. Experimental and numerical investigation of the performance of confined rubberised concrete base-isolators

List of Acronyms

AFRP	Aramid fibre reinforced polymer
CC	Conventional concrete
CC-EQ	Conventional concrete building tested on a shake-table
CC-STC	Conventional concrete building tested under monotonic loading
CDP	Concrete damage plasticity
CFRP	Carbon fibre reinforced polymer
CRuC	Confined rubberised concrete
CRuC-EQ	Building with confined rubberised concrete short columns tested on a shake-table
CRuC-ISO	Building mounted on base-isolators made of confined rubberised concrete and tested on a shake-table
DCM	Ductility class medium
FE	Finite element
FEA	Finite element analysis
FFT	Fast Fourier Transform
FO	VISION2000 fully operational drift limit
FRP	Fibre reinforced polymer
GDI	Global damage index
GFRP	Glass fibre reinforced polymer
IDR	Inter-storey drift ratio
LRB	Lead rubber bearing
LS	VISION2000 life safety drift limit
LVDT	Linear variable differential transformers
MPC	Multiple point constraint

NC	VISION2000 near collapse drift limit
O	VISION2000 Operational drift limit
PGA	Peak ground acceleration
PVC	Polyvinyl chloride
RC	Reinforced concrete
RuC	Rubberised concrete
SCME	Short column macro element
STM	Strut and tie model

List of Symbols

E_c	Elastic modulus of conventional concrete
E_{rc}	Elastic modulus of rubberised concrete
E_f	Stiffness of FRP sheet
G_C	Crushing energy (in compression)
G_F	Fracture energy (in tension)
K_c	Shape factor of the yield surface of the CDP model
K_w	Factor for the prevailing failure mode of a structural system
M_{Rb}	Sum of design moment resistances of the beams at any joint
M_{Rc}	Sum of design moment resistances of the columns at any joint
T_{NCR}	Reference return period
T_R	Return period
T_f	Natural period considered after a certain excitation, or the final state
T_i	Initial undamaged natural period
$a_{g,R}$	Reference peak ground acceleration
d_a	Maximum aggregate diameter (used for fracture energy calculation)
d_r	Storey drift according to Eurocode 2
f_{cc}^e	Effective compressive strength of confined concrete
f_{cm}^e	Effective compressive strength of concrete
f_{cm}	Mean compressive strength of concrete
f_{cr}	Critical stress of confined rubberised concrete
f_{crc}	Compressive strength of confined rubberised concrete
f_{crc}^e	Effective compressive strength of confined rubberised concrete
f_{ct}	Tensile strength of conventional concrete

f_{ky}	Characteristic yield strength of steel
f_{lu}	Ultimate strength of the reinforcing steel
f_{ly}	Yield strength of the reinforcing steel
f_{sy}	Yield strength of the shear stirrups
f_{rc}	Uniaxial compressive strength of rubberised concrete
$f_{rc,t}$	Peak tensile strength of rubberised concrete
f_u	Ultimate rupture strength of FRP sheet
g_k	Unfactored permanent area load
q_0	Basic value of the behaviour factor
q_k	Unfactored imposed area load
r_c	Shape factor of the post peak branch of concrete uniaxial behaviour
t	Thickness of FRP sheet
$w_{h,A}$	Width of the back face at node A in the SCME
$w_{h,B}$	Width of the back face at node B in the SCME
$w_{h,D}$	Width of the back face at node D in the SCME
w/c	Water-cement ratio by weight
$w_{s,A}$	Width of the strut at node A in the SCME
$w_{s,B}$	Width of the strut at node B in the SCME
$w_{s,C}$	Width of the strut at node C in the SCME
$w_{v,B}$	Width of the bearing face at node B in the SCME
$w_{v,D}$	Width of the bearing face at node D in the SCME
α_i	Factor for type of non-structural elements and their arrangements in the structure
α_s	Shear ratio
α_u/α_1	Overstrength factor

δ_s	Shear component of the displacement
ε_c	Peak compressive strain of concrete
ε_{cr}	Critical strain of confined rubberised concrete
ε_{crc}	Ultimate axial strain of confined rubberised concrete
ε_{crc}^{e}	Effective ultimate axial strain of confined rubberised concrete
ε_{fu}	Rupture Strain of FRP sheet
ε_{rc}	Strain at peak compressive strength of rubberised concrete
λ_L	Geometry scale factor
λ_a	Acceleration scale factor
λ_t	Time scale factor
σ_{b0}	Initial equi-biaxial compressive yield stress
σ_{c0}	Initial uniaxial compressive yield stress
h	Storey height
Ψ	Dilation angle of the CDP model
K	Lateral stiffness
M	Moment
Sa	Spectral acceleration
T	Natural period
V	Shear
l	Width of the column
q	Behaviour factor from Eurocode 8
v	Reduction factor for drift calculation (Eurocode 2)
α	Angle of inclination of the strut
φ	Confined strength ratio in Mander et al.'s concrete confinement model

ϵ	Eccentricity of the yield surface of the CDP model
λ	Factor accounting for the type of rubber used in Bompa et al.'s rubberised concrete constitutive model
ρ_{vr}	Percentage of rubber replacement by volume

Chapter 1

Introduction

1.1 RESEARCH MOTIVATION

The relatively high material stiffness of unreinforced conventional concrete (CC), along with its inherent limited ductility, can be undesirable during earthquakes, as the action that structural elements attract is proportional to their stiffness. For the same displacement, a stiffer structure will attract higher lateral loads, while more flexible and ductile structures can resist the seismic movements and generate lower lateral forces (base shear).

Current seismic codes (e.g. ACI 318-14 (ACI Committee 318, 2014), and Eurocode 8 (EN 1998-1, 2004)) aim to design reinforced concrete (RC) structures that can meet desired performance levels in terms of ductility and energy dissipation capacity. However, these two structural properties are limited by the deformation (strain) capacity of RC structural elements and connections. Although a target ductility can be achieved by confining concrete with proper detailing of the steel reinforcement, large amounts of lateral reinforcement (links/stirrups) are often required to increase the inherently low strain capacity of concrete to acceptable values. This complicates the construction process, and hence increases overall costs. Systems like base isolation, viscous fluid dampers, friction dampers, and many other passive and active control devices have also been developed to enhance energy dissipation and reduce the base shear demand on the structure as well as the inter-storey drift. Some of these devices utilize laminated rubber to achieve large deformation and energy dissipation. However, these devices are expensive and complicated to install and require regular maintenance and monitoring, which makes them not ideal to be used in developing countries. Enhancing the deformation capacity of concrete, at the material level, could pose as a passive and inherent solution that can lead to more ductile RC elements. Such a solution would allow for engineers to utilise the enhanced concrete properties in high ductility demand regions of the building, by simply designing specific structural elements with the enhanced stress-strain properties.

1.2 RUBBERISED CONCRETE AND POTENTIAL APPLICATIONS

A possible candidate material for the development of highly deformable elements is Rubberised Concrete (RuC), where crumb rubber particles derived from waste tyre shredding replace part of the aggregates in the concrete mix. While the inclusion of rubber aggregates can reduce the compressive strength and the Young's modulus of concrete, RuC can develop higher axial strains than CC for the same level of applied stress (Raffoul et al., 2017).

In the UK alone, it is reported that 30 M scrap tyres are disposed of annually, and globally this figure reaches 1 Billion (Rahman et al., 2012). In 2010, Post-Consumer Tyre arisings for EU countries were found by ETRA to be 3.4 M tonnes per year (ETRA, 2010). Around 48% of these arisings gets dumped in landfills or incinerated for energy recovery. However, the EU Waste Framework Directive discourages incineration as a disposal method, thus it is desired that as many tyres and/or their constituents are re-used in preferably high value applications because of their excellent intrinsic physical properties. Legislative authorities alongside researchers have realised the need to push forward the concept of circular economy and reusing by-products of one industry in another. The Anagennisi project, which was funded under the 7th Framework Programme of the European Commission in 2014-2017, examined the feasibility of reusing all tyre components in concrete with the aim to develop innovative structural solutions and applications (Pilakoutas, 2017). One of the main hypotheses of Anagennisi was that rubber crumb can partially replace aggregate to lead to a more deformable/ductile concrete, owing to the relative low elastic modulus of the rubber.

While RuC on its own may not be viable for structural applications, however, confined RuC (CRuC), via Fibre Reinforced Polymer (FRP) jacketing, retains the high lateral and axial deformability of RuC, while increasing the axial capacity of the confined section. Although a considerable amount of work has already been done to characterise the mechanical properties

of RuC and CRuC, and examine experimentally the behaviour of structural elements incorporating the two materials, there is a need to explore the effect of using CRuC elements on the overall performance of more complex structural systems.

Depending on the type of structural application and construction limitations, the use of RuC and CRuC could aid the development of innovative structural systems, such as:

1) Coupling beam systems: where beams (acting as shear links) are used to connect two independent systems, such as shear walls, or as link beams between a moment resisting frame to a shear wall (Figure 1.1). Coupling beams are designed to resist large shear forces and dissipate energy through shear deformation.

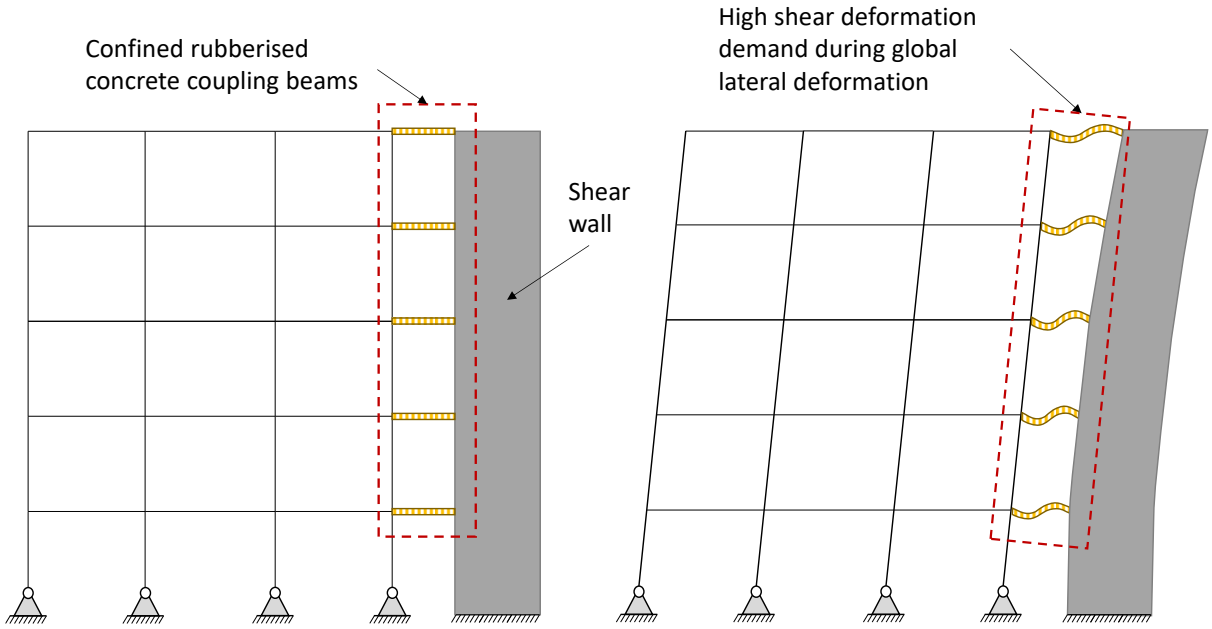

Figure 1.1: Undeformed and deformed shape of a moment resisting frame connected to a shear wall with confined rubberised concrete shear links

2) Plastic hinge zones in RC structures: CRuC can undergo large inelastic deformations, which in turn will enable greater energy dissipation and enhance the ductility of the structure. (example: column ends, or dog-bone concrete connections).

3) Integral bridges: CRuC could be used in portions of the piers and abutments to increase the deformability of the connections, whereas RuC could be used in the transition slab to accommodate the displacement of the bridge deck.

4) Base-isolation systems (Figure 1.2): where the deformation, and hence damage, is localised in the base-isolating foundation, thus protecting the superstructure in the event of a severe earthquake. The low Young's Modulus of RuC (Raffoul et al., 2016) and its energy dissipation properties (Xu et al., 2018) could be exploited to increase the flexibility of the structure and shift its natural period, which would reduce the response acceleration during an earthquake.

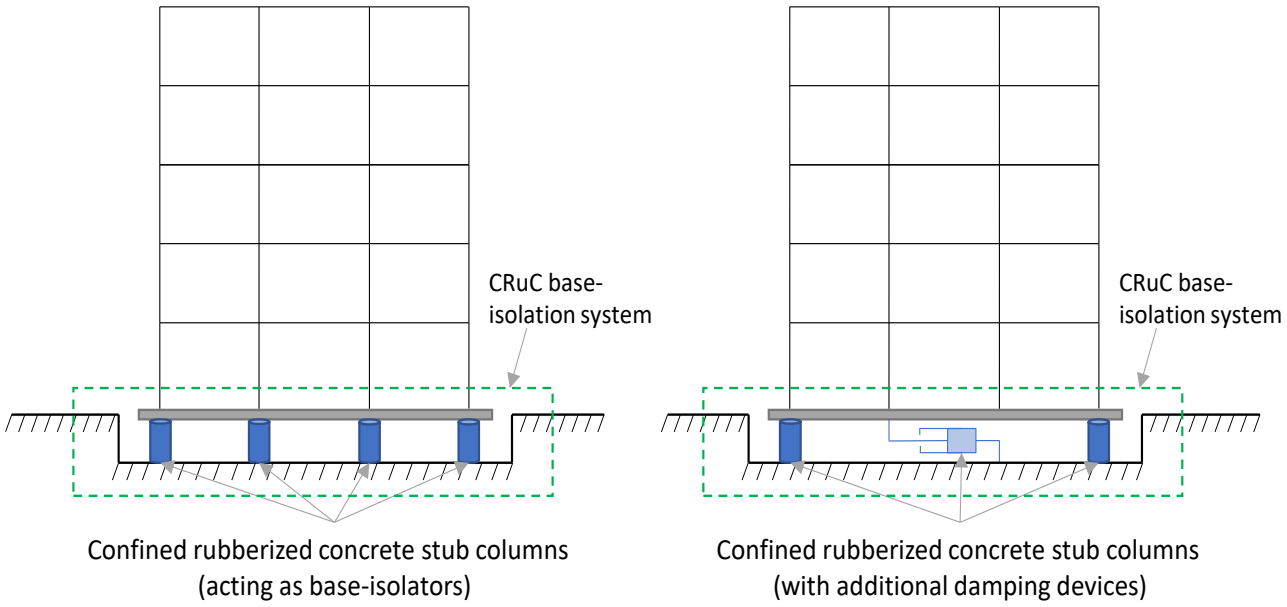

Figure 1.2: Base-isolation using rubberised concrete stub columns with and without additional damping devices

5) Structural elements with high shear and deformability demand: typical examples include short columns (Figure 1.3), and short elements in eccentrically braced RC frames (Figure 1.4). Such elements are prone to fail in a brittle manner in the event of a severe earthquake.

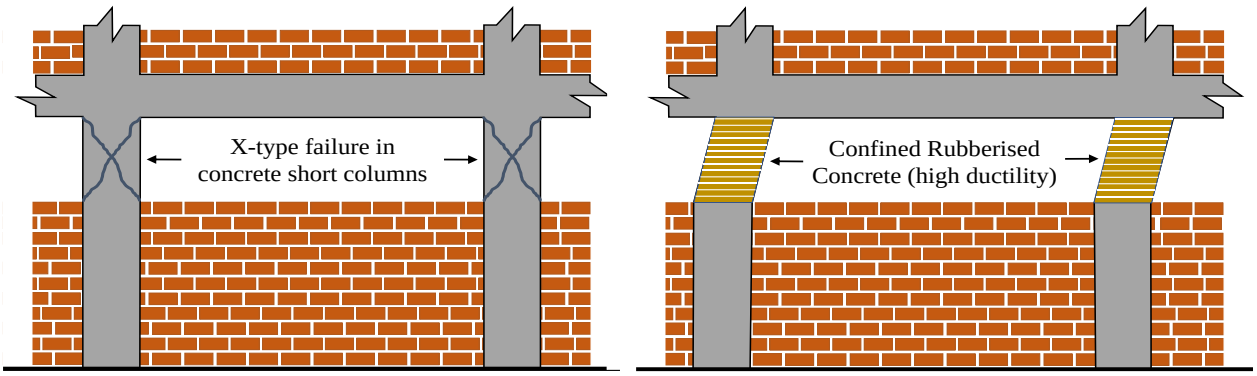

Figure 1.3: Behaviour of short columns made of CC (left) and CRuC (right) under lateral loading

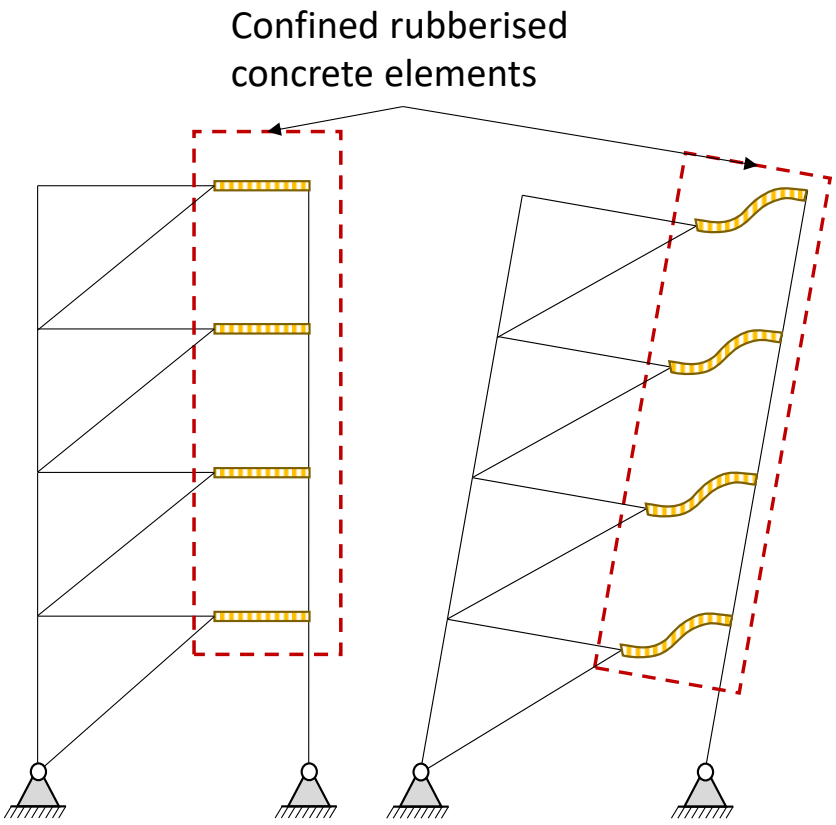

Figure 1.4: Shear links made of CRuC in eccentrically braced RC frames

1.3 AIMS AND OBJECTIVES

The aim of this research is to leverage the unique mechanical properties of CRuC and develop innovative, cost-effective structural solutions for seismic applications.

To achieve this aim, a series of large-scale experimental tests were carried out and complemented by analytical and numerical analyses. The main objectives of this research are summarised as follows:

1) Examine the behaviour of an RC building with CC short columns subjected to monotonic cyclic lateral loading, in order to investigate the main resisting mechanism and associated failure mode.

2) Develop a reliable Finite Element (FE) modelling technique for the building tested in 1) and gain additional insights into the behaviour of short columns.

3) Based on the outcome of objectives 1) and 2), develop an analytical model that can accurately capture the behaviour of reinforced CC short columns and that can be easily implemented in current software frameworks for simulating the seismic response of structural systems.

4) Examine and compare, both experimentally and analytically, the seismic performance of RC buildings with CC short columns and the novel CRuC short columns.

5) Extend the analytical model developed in 3) to account for the CRuC material in the short columns, and validate the model against the results of the shake-table tests performed in 4).

6) Investigate experimentally and analytically, the concept of using CRuC elements as a base-isolation system.

1.4 THESIS LAYOUT

This thesis comprises six chapters and three appendices. Chapters 1, 2, 5 and 6 are written in the conventional thesis format, while Chapters 3 and 4 are presented in a format suitable for publication and are to be submitted to ACI structural Journal, and Bulletin of Earthquake Engineering, respectively. A description of these chapters and how they address the aim and objectives is given below.

Chapter Two presents the background information that is related to the various aspects of this thesis; namely, the mechanical behaviour of RuC and CRuC at the material and structural element level, the behaviour of short columns, and the concept of base-isolation.

Chapter Three investigates the behaviour of short columns by testing a one-bay one-storey building with CC short columns under lateral loading (Objective 1). The results are then used to validate an FE model of the building (Objective 2). An analytical model is proposed and implemented in OpenSees (Mazzoni et al., 2009) to predict the behaviour of a frame with short columns, and the output is compared to the experimental results (Objective 3). The FE model and the analytical model are then extended to include CRuC short columns. The results of the numerical investigations are used to compare the performance of the two structural solutions and examine the contribution of the newly developed high deformability elements.

Chapter Four extends the work presented in Chapter 3 and examines both experimentally and analytically the seismic behaviour of two otherwise identical RC buildings with conventional CC short columns and CRuC short columns (Objective 4). The experimental response of the two buildings is compared in terms of observed damage, period elongation, drift in the short columns, roof acceleration, and strain in the reinforcement. The analytical model developed in Chapter 3 is modified and adapted to simulate the tested buildings, and a series of dynamic analyses are performed implementing the same seismic load protocol as in the experiments. The results are compared in terms of displacement time-history (Objective 5).

Chapter Five explores both experimentally and numerically the concept of a base-isolation system made of CRuC columns (Objective 6). The building with CRuC short columns tested as part of the experimental programme described in Chapter 4 was retrofitted, mounted on top of four circular CRuC columns, and subjected to the same seismic record and load protocol. The performance of the CRuC base-isolators is examined in depth, and the response of the superstructure, with and without base-isolation, is compared. The second part of the chapter extends the experimental work and provides a comparative evaluation of the performance of a fixed-base building and a CRuC base-isolated building subjected to dynamic loading through a series of non-linear numerical analyses (Objective 7). The response is compared in terms of natural period of the two structures, inter-storey drift, roof displacement and acceleration, and base-shear and base-moment.

Chapter Six summarises the research work done, highlights the general conclusions from Chapters 3-5, and gives recommendations for future work.

1.5 REFERENCES

ACI Committee 318. (2014). Building Code Requirements for Structural Concrete (ACI 318-14) and Commentary.

EN 1998-1. (2004). Eurocode 8: Design of structures for earthquake resistance - Part 1: General rules, seismic actions and rules for buildings. In Comité Européen de Normalisation (CEN).

ETRA. (2010). The European Tyre Recycling Association. http://www.etra-eu.org

Mazzoni, S., McKenne, F., Scott, M. H., & Fenves, G. L. (2009). Open System for Earthquake Engineering Simulation User Manual, Version 2.0. Pacific Earthquake Engineering Center, University of California. http://opensees.berkeley.edu

Pilakoutas, K. (2017). Innovative Reuse of All Tyre Components in Concrete. https://cordis.europa.eu/project/id/603722

Raffoul, S., Garcia, R., Escolano-Margarit, D., Guadagnini, M., Hajirasouliha, I., & Pilakoutas, K. (2017). Behaviour of unconfined and FRP-confined rubberised concrete in axial compression. Construction and Building Materials, 147, 388–397. https://doi.org/10.1016/j.conbuildmat.2017.04.175

Raffoul, S., Garcia, R., Pilakoutas, K., Guadagnini, M., & Medina, N. F. (2016). Optimisation of rubberised concrete with high rubber content: An experimental investigation. Construction and Building Materials, 124, 391–404. https://doi.org/10.1016/j.conbuildmat.2016.07.054

Rahman, M. M., Usman, M., & Al-Ghalib, A. A. (2012). Fundamental properties of rubber modified self-compacting concrete (RMSCC). Construction and Building Materials, 36, 630–637. https://doi.org/10.1016/j.conbuildmat.2012.04.116

Xu, B., Bompa, D. V., Elghazouli, A. Y., Ruiz-Teran, A. M., & Stafford, P. J. (2018). Behaviour of rubberised concrete members in asymmetric shear tests. Construction and Building Materials, 159, 361–375. https://doi.org/10.1016/j.conbuildmat.2017.10.091

Chapter 2

Literature review

This chapter provides a literature review on the material properties of unconfined and confined rubberised concrete. In addition, the effect of using RuC and CRuC in structural elements such as beams, columns, and joints is compiled from previous research. Finally, some of the possible structural applications of confined rubberised concrete are conceptualised to utilise its unique high ductility.

2.1 PROPERTIES OF RUBBERISED CONCRETE

Compared to conventional concrete, RuC has been reported to have a lower compressive and tensile strength, lower elastic modulus, and lower flexural strength (Siddique & Naik, 2004; Najim & Hall, 2010; Pacheco-Torgal et al., 2012; Raffoul et al., 2016; Rashad, 2016; Mohammed et al., 2017; Strukar et al., 2019; D. Li et al., 2020; Habib et al., 2020; Wang et al., 2020; Yi et al., 2020, 2021; Youssf et al., 2020; Roychand et al., 2020). The compressive strength of RuC with 100% rubber content can be up to 90% lower than that of conventional concrete (Toutanji, 1996; Khatib & Bayomy, 1999; Sukontasukkul & Chaikaew, 2006; Batayneh et al., 2008) and the decrease in strength and stiffness is proportional to the percent replacement of rubber in the mix. Figure 2.1 shows the stress versus axial and lateral strain of RuC cylinders with various fine rubber content tested in uniaxial compression. The identification 10F corresponds to 10% fine rubber replacement by volume of aggregates.

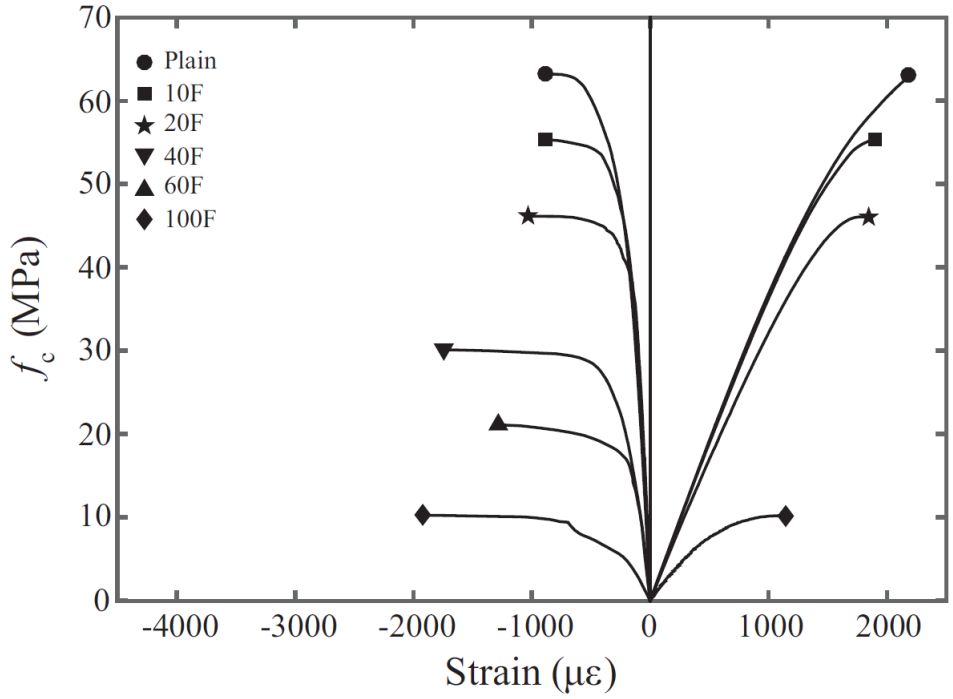

Figure 2.1: Uniaxial compressive stress-strain behaviour of RuC with fine rubber replacement (Raffoul et al., 2017)

Table 2.1 shows the mechanical properties of unconfined RuC with different percentages of rubber replacement and particle size, taken from the research by Raffoul et al., 2017.

Table 2. 1: Mechanical properties of unconfined RuC with different rubber contents and particle size

ID	% of Fine rubber	% of Coarse rubber	Total aggregate replaced (%)	f_c (MPa)	E_c (GPa)	ε_{cp} ($\mu\varepsilon$)	ε_{clp} ($\mu\varepsilon$)	ε_{cLOP} ($\mu\varepsilon$)
Plain	0	0	0	61.7±4.1	39.4	2180	885	550
10F	10	0	4.5	53.4±2.1	38.8	1900	890	560
20F	20	0	9	43.2±4.3	35.6	1840	1000	415
40F	40	0	18	32±0.9	-	-	1745	-
60F	60	0	27	20.6±1	-	-	1280	-
100F	100	0	45	9.6±0.7	19.9	1140	1925	150
10C	0	10	5.5	45.9±3.1	38.7	1830	695	390
20C	0	20	11	35.5±6.4	37.0	1590	700	310
40C	0	40	22	25.3±4	26.9	1670		290
60C	0	60	33	15.8±4.3	20.5	1430	3040	230
100C	0	100	55	8.7±1.4	14.0	1080	1440	150
40F&C	40	40	40	10.5	18.3	1320	3005	125
60F&C	60	60	60	7.1±1.2	11.4	1420	3565	135

The fine rubber particle size is 0-5 mm, whereas the coarse rubber was of two size gradation, 5-10 mm, and 10-20 mm. fc is the compressive strength in MPa, Ec is the modulus of elasticity, ε_{cp} and ε_{clp} are the axial strain and lateral strain at fc, respectively. ε_{cLOP} is the axial strain at the limit of proportionality (LOP), which is an indicator of the start of microcracking.

As can be seen from Table 2.1, with the increase in total percentage of aggregate replacement, there is a decrease in the compressive strength of RuC, as well as its young's modulus and peak axial strain. However, the lateral strain at peak strength increases with increase in rubber content. This lateral expansion may be utilised to increase the efficiency of lateral confinement. The lower strength can be mainly attributed to the a) low stiffness and high Poisson ratio of rubber, resulting in stress concentrations within the mix, b) rubber's hydrophobic nature that causes weak rubber-cement matrix bonding, c) increased porosity and air content, and d) higher mix non-homogeneity due to difference in aggregate densities (G. Li et al., 2004; Bignozzi & Sandrolini, 2006; Ganjian et al., 2009). Using pre-treatment methods, such as soaking the rubber aggregates in water or chemicals like sodium hydroxide or sulphuric acid, and using various additives in the concrete mix, like fly ash or silica fumes, can address some of the issues indicated above and has been shown to improve the performance of rubberised concrete (Siddika et al., 2019, 2020). For example, pre-treating the rubber particles with Acetone or Methanol breaks down the zinc stearate coating off the surface of rubber, which increases the roughness and hence the bonding with the cement paste (Sugapriya & Ramkrishnan, 2018). Pre-treatment with Acetone showed the best improvement with an increase in compressive strength of 28% compared to the untreated RuC samples, while Methanol treatment increased the strength by 22% (Rivas-Vázquez et al., 2015). Sodium Hydroxide pre-treatment has shown to improve the compressive strength of rubberised mortar by up to 36% (Muñoz-Sánchez et al., 2017) (rubberised mortar was made with rubber particles of size <4 mm).

Despite the apparent reduction in the static mechanical strength properties for RuC when compared to CC, recent research studies have reported that RuC has higher ductile performance, as well as larger vibration damping coefficient and energy absorption (Zheng et al., 2008; Najim & Hall, 2012; Liu et al., 2013; Xue & Shinozuka, 2013; Moustafa et al., 2017; Pham et al., 2018; Eltayeb, Ma, Zhuge, Youssf, Mills, et al., 2020). RuC also has a much softer post-

peak behaviour, specifically under shear stress, which enhances ductility and energy absorption (Xu et al., 2018). More importantly, RuC has the ability to expand laterally under uniaxial compression up to 300% more than CC. The large lateral expansion of RuC can in turn be exploited to activate and exploit the possible confinement provided by a lateral reinforcement, thus increasing the axial capacity. For example, by confining RuC with FRP, the high lateral expansion enables a higher exploitation of the confining FRP and can result in confined strengths up to 10 times the unconfined one (Raffoul et al., 2017).

2.2 PROPERTIES OF CONFINED RUBBERISED CONCRETE

2.2.1 Mechanical properties of CRuC

To recover the strength and exploit the potential deformation capacity that RuC can offer, recent research has examined the use of FRP confinement to produce FRP confined rubberised concrete. Li et al. (2011) tested CRuC cylinders cast in prefabricated Glass FRP (GFRP) pipes (Li et al., 2011). Relatively low aggregate replacement volumes were used for fine (15% and 30% of fine rubber) and coarse (15% of coarse rubber) aggregates. Whilst GFRP CRuC was up to 5.25 times stronger than unconfined RuC specimens, relatively low compressive strengths of 16.3 to 22.9 MPa were achieved. Moreover, the ultimate axial strain at failure of the CRuC cylinders was only 1.2%, which is similar to the ultimate strain of normal FRP-confined concrete. Youssf et al. (2014) tested CRuC cylinders cast in preformed Carbon FRP (CFRP) tubes (Youssf et al. 2014). Low fine aggregate replacement volumes of 0%, 5%, 10% and 20% of crumb tyre rubber were used in the mixes. The compressive strength of CFRP CRuC cylinders ranged from 61.7 MPa (for 1 CFRP layer) to 112.5 MPa (for 3 CFRP layers), thus being suitable for structural applications. However, the stress-strain behaviour of the CFRP CRuC cylinders and CFRP-confined conventional concrete cylinders was similar, and therefore the deformability potential of rubber was not realised. More recently, Duarte et al. (2016) tested “short” RuC columns confined with cold formed steel tubes (Duarte et al. 2016).

In this case, only the coarse aggregate was replaced with rubber (5% or 15% volume replacement). Whilst the columns' ductility was increased by up to 50%, the use of steel tubes promoted local buckling and limited the capacity of the specimens. Based on these results, it is evident that the use of small volumes of rubber aggregate replacement (below 20-30%) is insufficient to achieve a highly deformable CRuC that can be used in structural applications. However, whilst large volumes of aggregate replacement are expected to promote a better use of the properties of rubber, several technological challenges needed to be solved to mitigate the negative effect of rubber on the fresh and hardened properties of CRuC. Raffoul et al. (2017) tested CRuC cylinders with 60% rubber replacement by volume of both fine and coarse aggregates, confined with two and three layers of Aramid FRP (AFRP) (Raffoul et al., 2017). The three-layer CRuC cylinder reached an ultimate strength of 75 MPa, at which the AFRP ruptured, and an axial strain of around 5% was recorded, which is 14 times more than the CC counterpart (Figure 2.2).

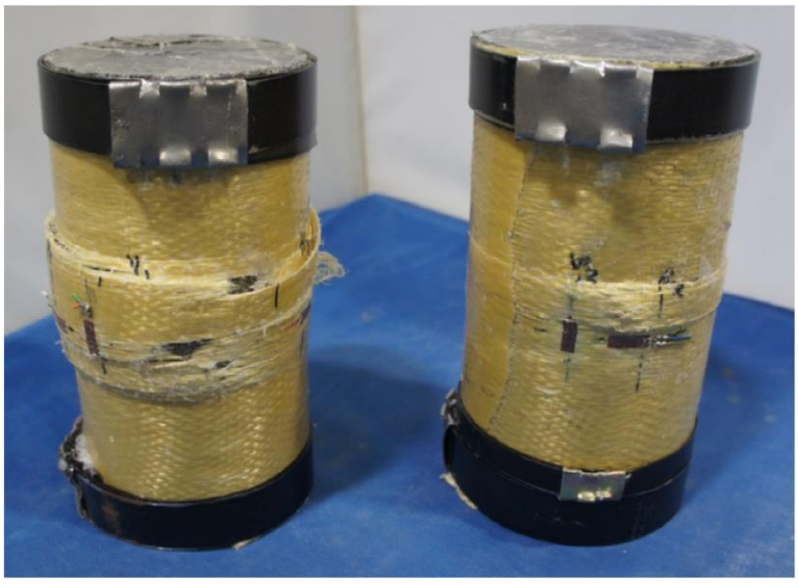

Figure 2.2: Failure of CRuC cylinder by rupture of AFRP (Raffoul et al., 2017)

Similar research work was done on RuC with 50% rubber replacement by volume, confined with various layers of CFRP (Tufail et al., 2019). Similar to Raffoul et al. (2017), Tufail et al. noted that the effectiveness of the confinement was best for aggregate replacement of both fine

and coarse rubber. Despite the relatively higher stiffness of CFRP, the CRuC cylinders sustained up to 4.6% axial strain, at an ultimate compressive strength of 56 MPa. Wang et al. (2019) tested the shear behaviour of CRuC prims with asymmetric shear tests, with shear span-to-depth ratio of 0.5, 0.75, and 1 (Wang et al., 2019). 60% of the total aggregate volume was replaced with fine and crumb rubber particles, and the samples were confined with one layer of CFRP. Wang et al. noted a bilinear shear stress-strain behaviour, with shear deformations up to 40 times those observed in RuC specimens (2.7% shear strain) (Figure 2.3b). In a related study, Wang et al. (2021) examined the axial behaviour of FRP CRuC and compared the experimental results with predictions obtained from stress-strain models developed for FRP confined CC (Wang et al., 2021). The study reported that the confinement effectiveness of CRuC was much higher than that of the confined CC specimen. Also, the CFRP confined specimen, in general, had lower confinement effectiveness than that of AFRP; an ultimate axial strain of 5.7% was measured for the three layers AFRP CRuC (Figure 2.3a). The study also concluded that the FRP confinement models for CC are unable to predict the behaviour of CRuC, specifically for the second branch of its uniaxial compressive bilinear behaviour.

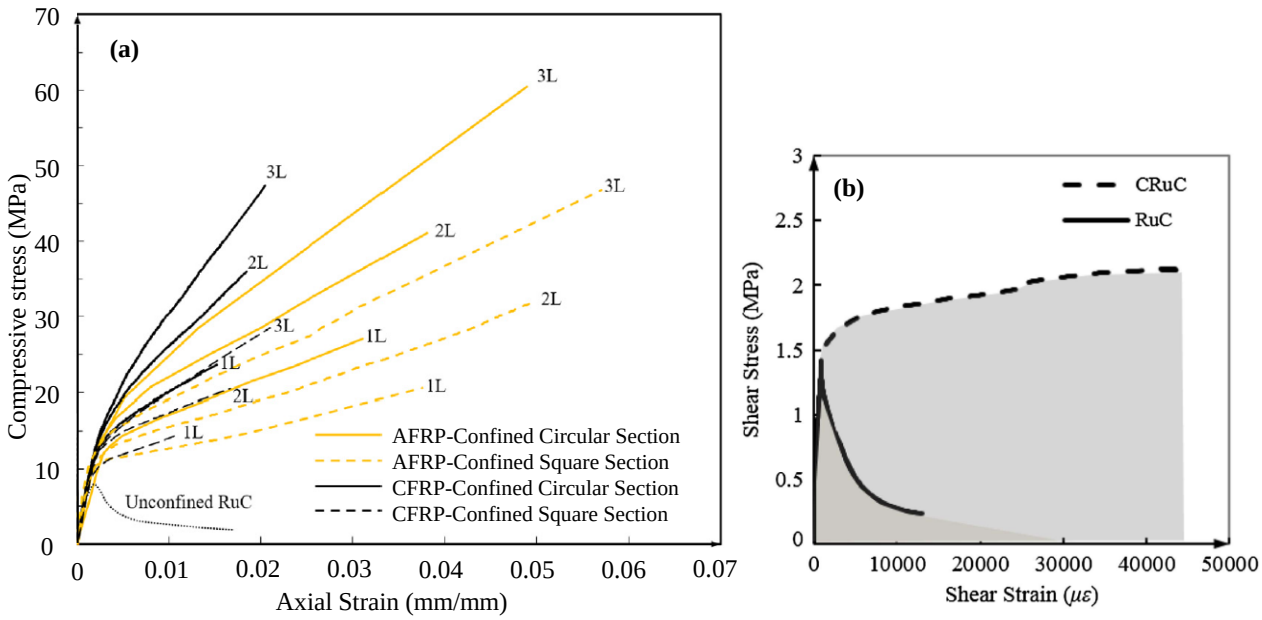

Figure 2.3: (a) Uniaxial compressive stress-strain behaviour of RuC, and AFRP and CFRP CRuC, and (b) shear stress-strain behaviour of RuC and CRuC (Wang et al., 2019, 2021)

The inclusion of rubber particles inside the concrete mix alters the constitutive response of the hardened RuC and affects the way in which lateral confinement is mobilised. For instance, volumetric contraction has been observed in CRuC cylinders with high level of confinement, which is opposite to what is typically observed in comparable confined CC cylinders (Raffoul et al., 2017; Wang et al., 2021).

2.2.2 Uniaxial compressive constitutive models for CRuC

Although, additional research is required to examine in more depth the macro- and micro-characteristics of CRuC, two models have already been proposed to predict with good accuracy the constitutive uniaxial behaviour of CRuC (Raffoul et al., 2019; Bompa & Elghazouli, 2021). The model developed by Raffoul et al., 2019, is an analysis-oriented behaviour model that can predict the axial and lateral stress-strain of FRP-confined CRuC. The model makes use of the confinement model of Mander et al., 1988, and the lateral-to-axial strain relationships developed by Papastergiou, 2010. The stress-strain output requires an incremental iterative procedure based on the previous two models.

The model developed by Bompa & Elghazouli, 2021, is a design-oriented constitutive model for FRP-confined concrete with and without rubber content. Unlike Raffoul's model, this one uses the uniaxial rupture strain of the confining jacket as the ultimate fracture point, with design factors to account for the fact that the actual rupture of the jacket around a cylinder is usually less than the uniaxial rupture strain. This model utilises a constitutive model, developed by the same authors, that predicts with high accuracy the behaviour of RuC cylinders (Bompa et al., 2017).

2.3 STRUCTURAL ELEMENT TESTING OF RUC AND CRUC

Several studies were performed to investigate the behaviour of structural elements incorporating RuC and CRuC:

Columns under uniaxial compression

- Son et al. (2011) explored RuC rectangular reinforced columns with varrying rubber replacement (2.7-5.4%) by volume of fine aggregates under pure axial compressive load. The uniaxial compressive strength of the RuC cylinders decreased with increasing the rubber content, 12-20% reduction, and the elastic modulus also decreased by 10-15%. The compressive load-carrying capacity of the column specimens also decreased with increasing the rubber content by up to 18-32%. However, what was notable is that the RuC columns were able to undergo lateral deformations that were up to two times larger than those of regular concrete columns (Figure 2.4), which provided higher energy dissipation capacity and ductility (Son et al., 2011). The RuC columns exhibited between 45-90% higher curvature ductility than their CC counterparts.

Figure 2.4: Failure mode of RC columns with tyre rubber particles (Son et al., 2011)

Columns under uniaxial compression and cyclic lateral loading

- Youssf et al. (2015) investigated reinforced RuC circular columns under axial and reverse cyclic lateral loading. The rubber replacement by volume of fine aggregates was 20%. Damping, snap-back tests, and a final cyclic test until failure were performed on three columns, including two conventional concrete and one RuC columns. The use of RuC led to an increase in the hysteric damping ratio by 13% and in energy dissipation by 150% as compared to the CC specimens. The ultimate lateral strength and deformability of the three columns was similar, but that is attributed to a relatively low rubber percent replacement (Youssf et al., 2015).

- Youssf et al. (2016) tested the reverse cyclic lateral behaviour of columns made of CC and RuC confined with zero, two and four layers of CFRP (Youssf et al., 2016). The researchers noted that the higher the confinement ratio, the higher the ultimate drift and peak strength of the column were; doubling the confinement thickness increased the peak strength and the ultimate drift of the CRuC columns by 11.5% and 53.8%, respectively, and the plastic hinge length was increased by 19%. Also, the confinement effectiveness for the CRuC columns was 9% higher than that of the CC ones. The rubberised concrete columns increased the maximum tensile and compressive strains measured on the rebar steel by 1.1 and 1.4 times, respectively.

- Elghazouli et al. (2018) investigated the behaviour of RC columns, with 0, 45, and 60% rubber replacement by total volume of aggregates, and confined with 0, 2, and 3 layers of AFRP (Figure 2.5). The columns were tested monotonically under reverse cyclic lateral loading with sustained axial loading. The RuC specimen exhibited softer crushing behaviour than CC, which favoured higher ductility and energy dissipation. The CRuC columns showed a very stable hysteretic response owing to the high

confinement effectiveness. The authors also concluded that RuC columns were 50% more ductile than their CC counterparts, while the CRuC columns were 40% more ductile than the unconfined RuC columns (Elghazouli et al., 2018). Similar to the observation by Youssf et al. (2016), the plastic hinge length varied between 29-39% of the moment length of the members, which was higher than the conventional concrete members.

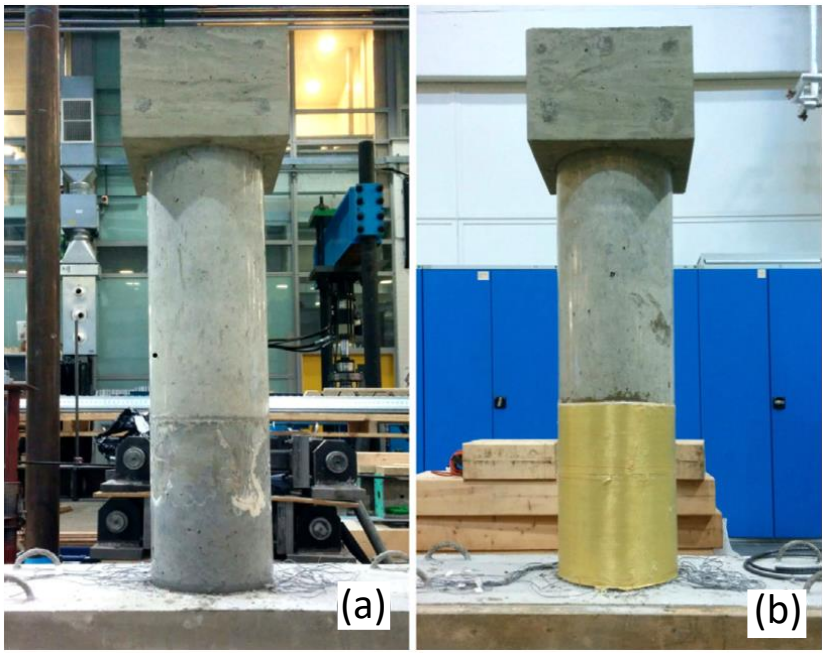

Figure 2.5: (a) RuC column, and (b) CRuC column tested in reverse cyclic loading

Beams under four-point bending

- Ismail and Hassan (2016) investigated the flexural performance of 12 self-consolidating reinforced RuC beams under four-point bending. The rubber replacement by volume of fine aggregates varied from 0-50%. As expected, the added rubber deteriorated the fresh and mechanical properties of the concrete, as well as decreased the flexural stiffness of the beams. It was reported that using up to 10% fine-rubber replacement improved the beam's deformation capacity, ductility and toughness, without affecting the ultimate flexural strength. An increase in rubber replacement up to 20% led to a slight decrease

in the ultimate flexural load, while more that 20% replacement had significant adverse effects on the moment capacity of the beam (Ismail & Hassan, 2016).

Columns under seismic loading (shake-table)

- Moustafa et al. (2017) performed shake-table tests on reinforced CC and RuC columns with 20% replacement by volume of the fine aggregates (Moustafa et al., 2017). The strength of the RuC column was 3% less than the CC column, however, it had a 12.5% higher drift capacity, and a 16.5% more energy dissipation. The RuC column showed higher hysteresis and viscous damping. Interestingly, the fracture of the steel reinforcement was delayed for the RuC and it occurred at a level corresponding to 190% of the design earthquake, compared to 140% for the CC, which allowed the column to maintain its integrity up to 5.4% drift.

Joints under reverse cyclic loading

- AbdelAleem and Hassan (2018) investigated self-consolidating RuC beam-column joints under reverse cyclic loading, with percent rubber replacement from 0-25% (AbdelAleem & Hassan, 2018). The researchers found that for rubber replacements up to 15%, the reduction in load carrying capacity was minimal (up to 10%), whereas the ductility increased by 18.7% and the energy dissipation increased by 20.9%. A rubber replacement of 25%, however, changed the failure mode of the joints from yielding at the beam to joint shear failure, which in turn resulted in limited deformability.

2.4 POSSIBLE APPLICATIONS OF CONFINED RUBBERISED CONCRETE

As discussed in the previous sections, the unique mechanical and physical properties offered by CRuC can enable the development of novel RC structural solutions for applications where large deformations are desirable. Some of the most promising applications for CRuC are discussed in the following.

2.4.1 Coupling beams

Coupling beams are elements that link together two separate items such as shear walls in order to add stiffness to the structure, and enhance its lateral resistance. During events of lateral loading on the structure, these beams undergo large shear deformations and must be able to sustain high shear forces over several cycles (Elghazouli, 2011). Special reinforcement detailing is often required to accommodate the high shear forces that develop in coupling beams and ensure an adequate degree of ductility. One such detailing solution was developed in 1974 by Paulay and Binney (Figure 2.6), which involves the use of heavy diagonal reinforcement, as opposed to the conventionally reinforced coupling beams with horizontal reinforcement (Paulay & Binney, 1974). While some design codes (ACI Committee 318, 2014) have adopted and recommend the use of this detailing solution for coupling beams, it remains a challenge to assemble such complicated steel cages, and the cost of construction increases due to the large amounts of steel used. The brittle nature of CC also needs to be considered carefully as it severely limits the strain capacity of these elements.

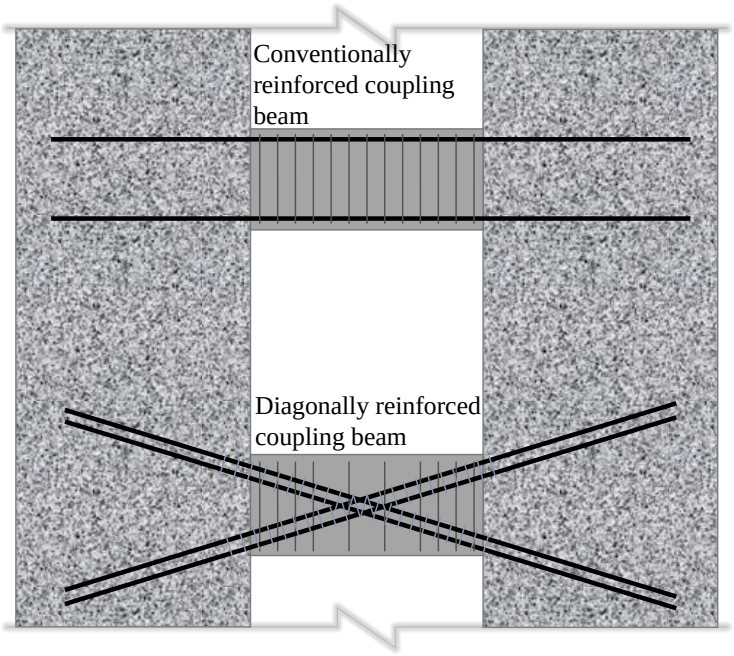

Figure 2.6: Conventionally reinforced versus diagonally reinforced coupling beam

Escolano-Margarit et al. (2017) performed numerical and experimental pushover analyses on coupling beams with 60% rubber replacement by volume of total aggregates and confined with two layers of AFRP (Escolano-Margarit et al., 2017). The beams were tested under reverse cyclic loading and the results showed that CRuC beams can develop up to 4 MPa shear stresses, with a stable hysteresis behaviour. In addition, the CRuC beams exhibited a lower stiffness degradation, and a higher deformation capacity (an ultimate rotation of 8%) than the equivalent CC beams. The energy dissipated by the CRuC beams was up to 20% higher than that of the CC beams.

Although further experimental and numerical research is needed to confirm the benefits of using CRuC in coupling beams, a combination of proper detailing and a highly deformable concrete composite could offer a viable and cost-effective solution.

2.4.2 Short columns

In structures located in seismic-prone areas, the geometry of structural elements and their relative stiffnesses affect significantly load distribution, and can limit structural performance. For instance, short columns are typical examples where the relatively high stiffness of the element could lead to catastrophic failures (Yamada & Furui, 1966). A common classification of short columns is by the relation of the end forces acting on the member as follows: $\alpha_s = \left({}^{M}/_{Vl}\right) \leq 2.5$, where α_s is the shear ratio, M is the end moment, V is the shear force, and l is the width of the column (Wakabayashi & Minami, 1972; Yamada & Furui, 1968; Zhou & Hong, 2000; Moretti & Tassios, 2006). Although design codes advice to avoid short columns, architectural features may necessitate them, e.g. in partially buried basements, stair and platform connections, mezzanine floors, and buildings on sloping grounds (Figure 2.7). Short columns can also be created unintentionally when non-structural partial infill walls or parapets are added between columns. The behaviour of short columns is dominated by shear and therefore (if inadequately detailed) brittle failures can occur, with limited yielding and force redistribution (Figure 2.7,a,b,c,d,e,g) (EERI, 1996).

Hosseini & Mostofinejad studied the seismic performance of RC short columns where they emphasised the danger of the predominant shear failure mode of these columns. The authors indicate that plastic hinges form at low drift ratios for short columns, hence, it is not only enough to provide adequate shear capacity, but it is required to strengthen the flexure capacity as well, in order to transfer the plastic hinges to the beams (Hosseini & Mostofinejad, 2021). FRP confined members support both the shear and flexural behaviour, and with RuC those members can accommodate for large displacements.

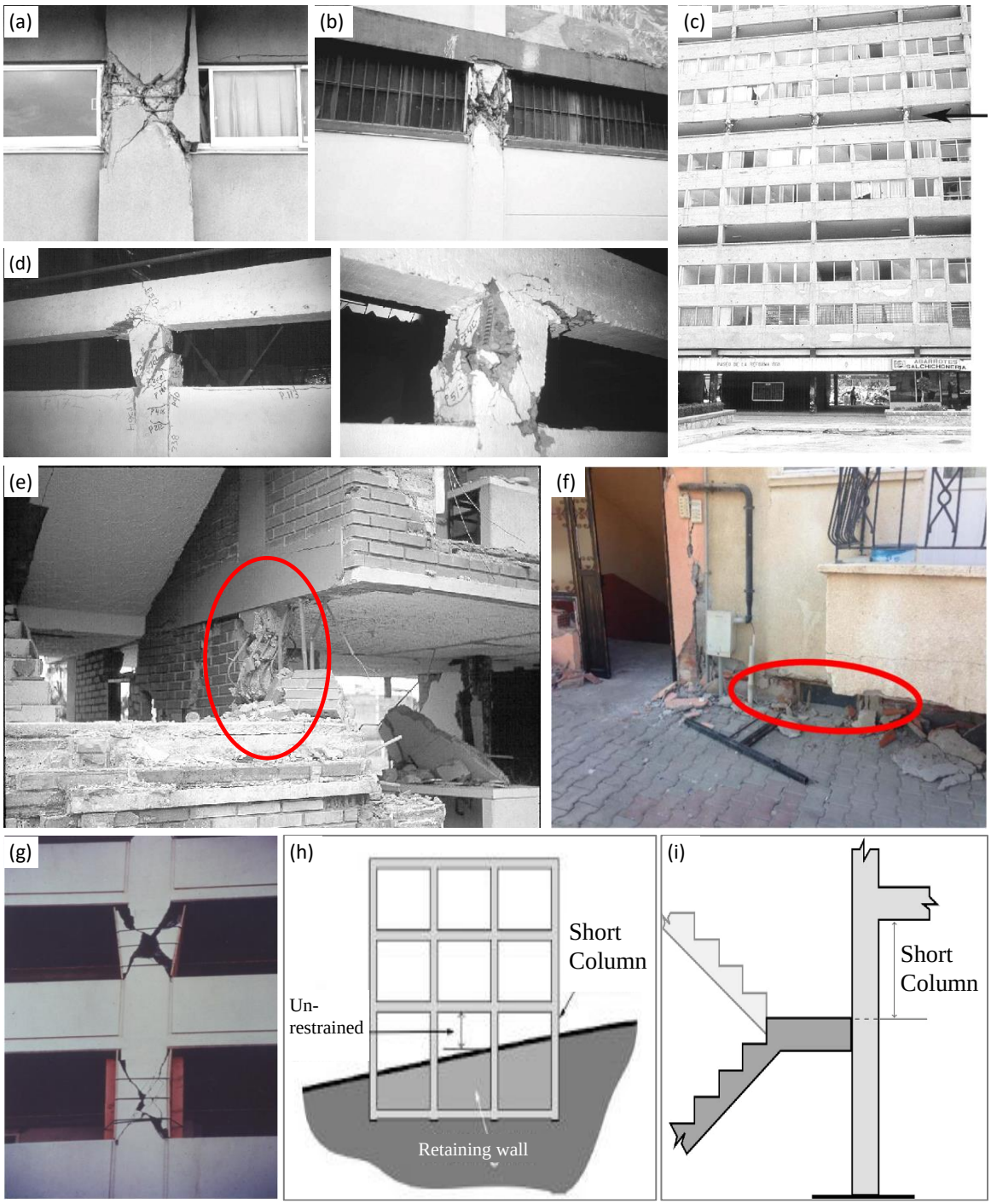

Figure 2.7: (a,b,c,g) Short column failure (crushing, and X-type cracking) during earthquakes caused by partial infill (EERI, 1996; Guevara & García, 2005)*; (d) Experimental test on concrete frame with partial infill under lateral load* (Pineda, 1994)*; (e, i) Short column caused by stair connection; (f,h) Short column caused by partially buried basements* (Duran et al., 2020)

Experimental and analytical tests on partially infilled RC frames, performed by Chiou et al., 1999, show that the partial infill causes a short column effect, and localised the damage in the short column leads to severe shear failure. The partially infilled frame drift was 50% less than that of the bare RC frame at peak strength (Chiou et al., 1999). Similar analytical work was

performed by Tanganelli et al., 2013, to investigate the influence of infill panels on the seismic response of RC buildings, and they concluded that the short column effect increases the shear demand drastically on the column, which increases the complexity of the design.

Modelling the behaviour of short columns is not straightforward due to their short span-to-depth ratio, which makes it difficult to decouple the flexure and shear interaction (Moretti & Tassios, 2006). One method that has been utilised to model structural elements with this complex behaviour, is the global truss model (Y.-A. Li & Hwang, 2017). The truss model is based on the strut and tie method along with defining the load path within the structural element. The behaviour of shear walls, coupling beams, deep beams, and short columns has been modelled with decent accuracy using the truss model (Hwang et al., 2001; Kassem, 2015; Zhi et al., 2017). Further research, however, is needed to develop a strut and tie model that can predict the behaviour of short columns with the post-peak degradation, and be able to accommodate for CC and RuC material input.

If short columns are necessary, the use of construction materials that can develop high deformation and rotational capacity (such as CRuC) would promote force redistribution, increase energy dissipation and lead to a more efficient design. However, research, both experimental and numerical, is needed to verify the potential of CRuC at improving the shear behaviour of short columns under seismic load. Conventional seismic analysis tools based on fibre element cannot efficiently account for the shear dominated behaviour of short columns, hence there is a need for the development of new suitable elements for the analysis of structures with short columns, and adapt those elements to be able to model and analyse structures with CRuC short columns.

2.4.3 Base-isolation

Seismic isolation relies on the concept of decoupling a building from the ground, such that horizontal ground movements are not transmitted to the structure (Naeim & Kelly, 2000). The base-isolation system elongates the fundamental period of vibration of the overall structural system, thus reducing the force demand on the structure during an earthquake (compared to an equivalent fixed-base building). However, while the spectral accelerations are reduced, the base-isolation system increases the displacement demands (Grant et al., 2005). These displacements are localised at the foundation level, and can be accommodated by the isolation system (Figure 2.8 right). Effective base-isolation systems can accommodate these large displacements, dissipate the energy, and transmit minimal accelerations into the structure. As such, the base-isolating units must be ductile enough to sustain significant forces at large deformations, as well as be able to dissipate energy. The higher energy dissipation of the system also lowers the force demand (less acceleration response), but also lowers the displacement demand.

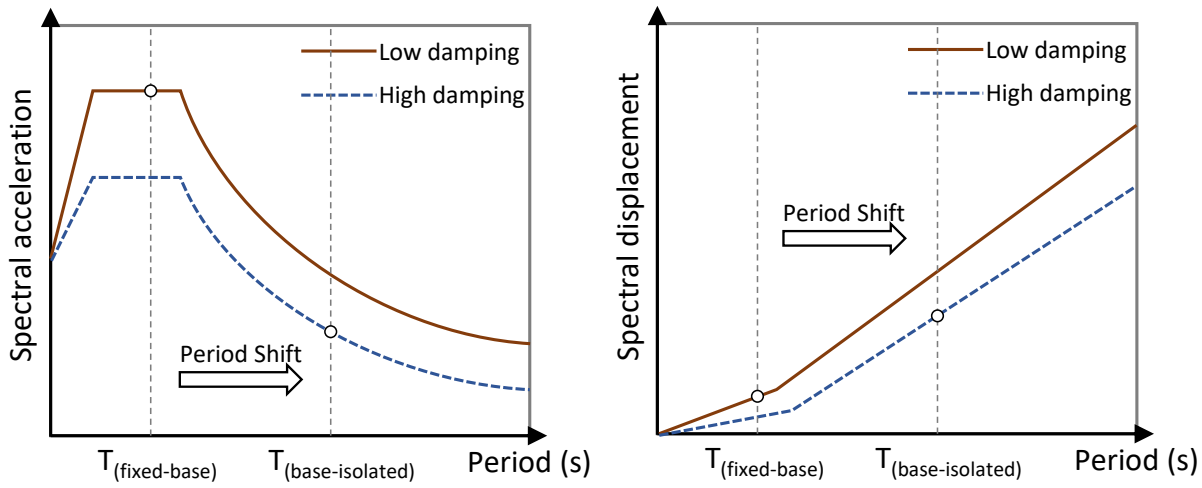

Figure 2.8: Spectral acceleration (left) and displacement (right) for a fixed-base (low damping) versus base-isolated (high damping) building

The most common seismic isolation devices used in buildings are elastomeric bearings (rubber and lead-rubber bearings) and sliding bearings (or friction pendulums) (Figure 2.9). While both

systems aim to achieve the same result of isolating the structure, they each function in a fundamentally different manner (Eröz & Desroches, 2013). The friction pendulum system forces the structure into a pendulum motion, as the plates of the system glide against each other, dissipating hysteretic energy via friction. The curvature of the concave surface of the friction pendulum determines the period of the isolator, regardless of the mass of the superstructure. The elastomeric bearing system relies on the hysteretic plastic deformations of the bearing to dissipate energy. Rubber bearings have layers of rubber and steel; the soft flexible nature of the rubber ensures the elongation of the natural period of the structure, while the steel plates within the bearing ensure adequate load bearing capacity. Lead-rubber bearings (LRB) have a lead cylindrical core in the middle of the bearing. The lead core enhances the initial stiffness and aids with the energy dissipation (Priestley et al., 1996).

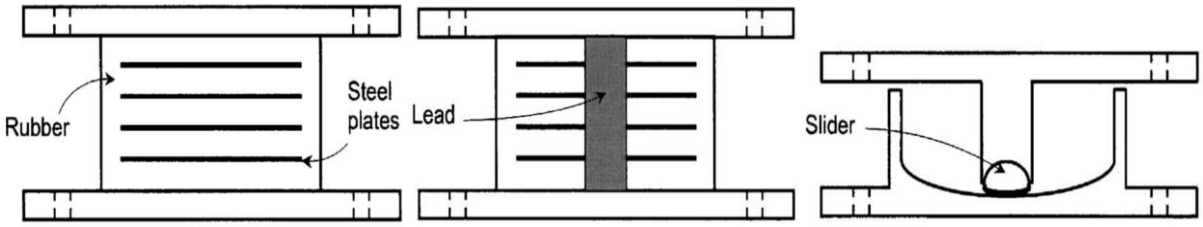

Figure 2.9: Left to right: Rubber bearing, Lead-rubber bearing, and Friction pendulum system (Kunde & Jangid, 2006)

The general consensus on the dynamic properties of RuC, is that it enhances the damping ratio when compared to CC (Skripkiunas et al., 2009; Najim & Hall, 2012; Moustafa & ElGawady, 2013; Xue & Shinozuka, 2013; Rahman et al., 2014; Moustafa & Elgawady, 2015; Faizah et al., 2019; Eltayeb, Ma, Zhuge, Youssf, & Mills, 2020). More importantly, due to its high ductility and its bilinear compressive and shear constitutive behaviour (see Figure 2.3), CRuC could be used as a replacement to LRB, or in conjunction with LRB or other damping devices. The CRuC isolator would have a relatively high initial stiffness (first branch of the bilinear behaviour), but after yielding caused by strong earthquake, the hysteretic behaviour would be dominated by the second branch which can be controlled by the level of confinement.

2.5 CONCLUDING REMARKS

Current research on RuC and CRuC has highlighted the great potential of this novel material. Although the use of large amounts of rubber replacements can reduce the mechanical properties of the resulting concrete, these can be effectively enhanced by providing an adequate level of confinement. CRuC has been shown to possess desirable mechanical properties, which can be exploited to design highly deformable elements and develop effective structural solutions, especially for seismic applications. Amongst the possible applications discussed in the previous sections, the use of CRuC in short columns and base isolation systems has the potential to offer sustainable and cost-effective alternatives to current solutions and systems.

In the case of short columns, research, both experimental and numerical, is needed to verify the potential of CRuC at improving their shear behaviour under seismic load. Although few structural element testings have been performed on columns, most of these had slender aspect ratios, whereas the current work aims at investigating short columns with a low span-to-depth ratio. In addition, this research provides the first instance of the use of CRuC in a scaled down full structure, to study its effect on the structural behaviour. Moreover, conventional seismic analysis tools based on fibre element cannot account for the shear dominated behaviour of short columns, hence there is a need for the development of new suitable elements for the analysis of structures with short columns, and adapt those elements to be able to model and analyse structures with CRuC short columns. As for the base-isolation system, the use of CRuC structural elements as isolators can substitute for more complex and highly technical base-isolating mechanisms, which means it can be used in developing countries.

Both of the aforementioned structural applications will be examined in more details in the following chapters through a series of complementary experimental tests and numerical modelling.

2.6 REFERENCES

AbdelAleem, B. H., & Hassan, A. A. A. (2018). Influence of rubber content on enhancing the structural behaviour of beam–column joints. *Magazine of Concrete Research*, *70*(19), 984–996. https://doi.org/10.1680/jmacr.17.00323

ACI Committee 318. (2014). *Building Code Requirements for Structural Concrete (ACI 318-14) and Commentary*.

Batayneh, M. K., Marie, I., & Asi, I. (2008). Promoting the use of crumb rubber concrete in developing countries. *Waste Management*, *28*(11), 2171–2176. https://doi.org/10.1016/j.wasman.2007.09.035

Bignozzi, M. C., & Sandrolini, F. (2006). Tyre rubber waste recycling in self-compacting concrete. *Cement and Concrete Research*, *36*(4), 735–739. https://doi.org/10.1016/j.cemconres.2005.12.011

Bompa, D. V., Elghazouli, A. Y., Xu, B., Stafford, P. J., & Ruiz-Teran, A. M. (2017). Experimental assessment and constitutive modelling of rubberised concrete materials. *Construction and Building Materials*, *137*, 246–260. https://doi.org/10.1016/j.conbuildmat.2017.01.086

Bompa, D. V, & Elghazouli, A. Y. (2021). Behaviour of confined rubberised concrete members under combined loading conditions. *Magazine of Concrete Research*, 1–19. https://doi.org/10.1680/jmacr.19.00121

Chiou, Y. J., Tzeng, J. C., & Liou, Y. W. (1999). Experimental and analytical study of masonry infilled frames. *Journal of Structural Engineering*, *125*(10), 1109–1117. https://doi.org/10.1061/(ASCE)0733-9445(1999)125:10(1109)

Duran, B., Tunaboyu, O., & Avşar, Ö. (2020). Structural Failure Evaluation of a Substandard RC Building due to Basement Story Short-Column Damage. *Journal of Performance of Constructed Facilities*, *34*(4), 04020053. https://doi.org/10.1061/(asce)cf.1943-

5509.0001455

EERI. (1996). *Northridge Earthquake Reconnaissance Report Earthquake Spectra*.

Elghazouli, A. (2011). *Seismic Design of Buildings to Eurocode 8* (Issue 2). CRC Press. https://doi.org/10.3397/1.3532782

Elghazouli, A., Bompa, D., Xu, B., Ruiz-Teran, A., & Stafford, P. (2018). Performance of rubberised reinforced concrete members under cyclic loading. *Engineering Structures*, *166*(November 2017), 526–545. https://doi.org/10.1016/j.engstruct.2018.03.090

Eltayeb, E., Ma, X., Zhuge, Y., Youssf, O., & Mills, J. E. (2020). Influence of rubber particles on the properties of foam concrete. *Journal of Building Engineering*, *30*(January), 101217. https://doi.org/10.1016/j.jobe.2020.101217

Eltayeb, E., Ma, X., Zhuge, Y., Youssf, O., Mills, J. E., & Xiao, J. (2020). Structural behaviour of composite panels made of profiled steel sheets and foam rubberised concrete under monotonic and cyclic shearing loads. *Thin-Walled Structures*, *151*(November 2019), 106726. https://doi.org/10.1016/j.tws.2020.106726

Eröz, M., & Desroches, R. (2013). A comparative assessment of sliding and elastomeric seismic isolation in a typical multi-span bridge. *Journal of Earthquake Engineering*, *17*(5), 637–657. https://doi.org/10.1080/13632469.2013.771589

Escolano-Margarit, D., Garcia, R., Raffoul, S., Di Benedetti, M., Hajirasouliha, I., Guadagnini, M., & Pilakoutas, K. (2017). Seismic performance evaluation of coupled walls using innovative highly deformable coupling beams. *16th World Conference on Earthquake Engineering (16WCEE), Santiago, Chile*.

Faizah, R., Priyosulistyo, H., & Aminullah, A. (2019). An Investigation on Mechanical Properties and Damping Behaviour of Hardened Mortar with Rubber Tire Crumbs (RTC). *MATEC Web of Conferences*, *258*, 05002. https://doi.org/10.1051/matecconf/201925805002

Ganjian, E., Khorami, M., & Maghsoudi, A. A. (2009). Scrap-tyre-rubber replacement for aggregate and filler in concrete. *Construction and Building Materials*, *23*(5), 1828–1836. https://doi.org/10.1016/j.conbuildmat.2008.09.020

Grant, D. N., Fenves, G. L., & Auricchio, F. (2005). *Modelling and Analysis of High-damping Rubber Bearings for the Seismic Protection of Bridges by Ferdinando Auricchio Professor of Mechanics of Solids* (Issue May).

Guevara, L. T., & García, L. E. (2005). The captive- and short-column effects. *Earthquake Spectra*, *21*(1), 141–160. https://doi.org/10.1193/1.1856533

Habib, A., Yildirm, U., & Eren, O. (2020). Mechanical and dynamic properties of high strength concrete with well graded coarse and fine tire rubber. *Construction and Building Materials*, *246*, 118502. https://doi.org/10.1016/j.conbuildmat.2020.118502

Hosseini, S. M., & Mostofinejad, D. (2021). Seismic Performance of RC Short Columns Retrofitted with a Novel System in Shear and Flexure Using CFRP Composites. *Journal of Composites for Construction*, *25*(5), 04021039. https://doi.org/10.1061/(asce)cc.1943-5614.0001148

Hwang, S.-J., Fang, W., Lee, H., & Yu, H. (2001). Analytical Model for Predicting Shear Strengthof Squat Walls. *Journal of Structural Engineering*, *127*(1), 43–50. https://doi.org/10.1061/(asce)0733-9445(2001)127:1(43)

Ismail, M. K., & Hassan, A. A. A. (2016). Performance of full-scale self-consolidating rubberized concrete beams in flexure. *ACI Materials Journal*, *113*(2), 207–218. https://doi.org/10.14359/51688640

Kassem, W. (2015). Shear strength of squat walls: A strut-and-tie model and closed-form design formula. *Engineering Structures*, *84*, 430–438. https://doi.org/10.1016/j.engstruct.2014.11.027

Khatib, Z. K., & Bayomy, F. M. (1999). Rubberized Portland Cement Concrete. *Journal of*

Materials in Civil Engineering, *11*(03), 206–213. https://doi.org/10.1061/(asce)0899-1561(1999)11:3(206)

Kunde, M. C., & Jangid, R. S. (2006). Effects of Pier and Deck Flexibility on the Seismic Response of Isolated Bridges. *Journal of Bridge Engineering*, *11*(1), 109–121. https://doi.org/10.1061/(asce)1084-0702(2006)11:1(109)

Li, D., Gravina, R., Zhuge, Y., & Mills, J. E. (2020). Bond behaviour of steel-reinforcing bars in Crumb Rubber Concrete (CRC). *Australian Journal of Civil Engineering*, *18*(1), 2–17. https://doi.org/10.1080/14488353.2019.1680073

Li, G., Stubblefield, M. A., Garrick, G., Eggers, J., Abadie, C., & Huang, B. (2004). Development of waste tire modified concrete. *Cement and Concrete Research*, *34*(12), 2283–2289. https://doi.org/10.1016/j.cemconres.2004.04.013

Li, Pang, S.-S., & Ibekwe, S. I. (2011). FRP tube encased rubberized concrete cylinders. *Materials and Structures*, *44*(1), 233–243. https://doi.org/10.1617/s11527-010-9622-8

Li, Y.-A., & Hwang, S.-J. (2017). Prediction of Lateral Load Displacement Curves for Reinforced Concrete Short Columns Failed in Shear. *Journal of Structural Engineering*, *143*(2), 04016164. https://doi.org/10.1061/(asce)st.1943-541x.0001656

Liu, F., Zheng, W., Li, L., Feng, W., & Ning, G. (2013). Mechanical and fatigue performance of rubber concrete. *Construction and Building Materials*, *47*, 711–719. https://doi.org/10.1016/j.conbuildmat.2013.05.055

Mander, J. B., Priestley, M. J. N., & Park, R. (1988). Theoretical stress-strain model for confined concrete. *J. Struct. Eng*, *114*(8), 1804–1826.

Mohammed, B. S., Adamu, M., & Shafiq, N. (2017). A review on the effect of crumb rubber on the properties of rubbercrete. *International Journal of Civil Engineering and Technology*, *8*(9), 599–615.

Moretti, M. L., & Tassios, T. P. (2006). Behavior and ductility of reinforced concrete short

columns using global truss model. *ACI Structural Journal*, *103*(3), 319–327. https://doi.org/10.14359/15309

Moustafa, A., & ElGawady, M. (2013). Dynamic Properties of High Strength Rubberized Concrete. *American Concrete Institute (ACI), 314*, 3.1-3.22.

Moustafa, A., & Elgawady, M. A. (2015). Mechanical properties of high strength concrete with scrap tire rubber. *Construction and Building Materials*, *93*, 249–256. https://doi.org/10.1016/j.conbuildmat.2015.05.115

Moustafa, A., Gheni, A., & ElGawady, M. A. (2017). Shaking-Table Testing of High Energy–Dissipating Rubberized Concrete Columns. *Journal of Bridge Engineering*, *22*(8), 04017042. https://doi.org/10.1061/(asce)be.1943-5592.0001077

Muñoz-Sánchez, B., Arévalo-Caballero, M. J., & Pacheco-Menor, M. C. (2017). Influence of acetic acid and calcium hydroxide treatments of rubber waste on the properties of rubberized mortars. *Materials and Structures/Materiaux et Constructions*, *50*(1). https://doi.org/10.1617/s11527-016-0912-7

Naeim, F., & Kelly, J. M. (2000). *Design of Seismic Isolated Structures: From Theory to Practice*. John Wiley and Sons, Inc.

Najim, K. B., & Hall, M. R. (2010). A review of the fresh/hardened properties and applications for plain- (PRC) and self-compacting rubberised concrete (SCRC). *Construction and Building Materials*, *24*(11), 2043–2051. https://doi.org/10.1016/j.conbuildmat.2010.04.056

Najim, K. B., & Hall, M. R. (2012). Mechanical and dynamic properties of self-compacting crumb rubber modified concrete. *Construction and Building Materials*, *27*(1), 521–530. https://doi.org/10.1016/j.conbuildmat.2011.07.013

Pacheco-Torgal, F., Ding, Y., & Jalali, S. (2012). Properties and durability of concrete containing polymeric wastes (tyre rubber and polyethylene terephthalate bottles): An

overview. *Construction and Building Materials*, *30*, 714–724. https://doi.org/10.1016/j.conbuildmat.2011.11.047

Papastergiou, P. (2010). *A confinement model for concrete wrapped or pretensioned with FRP*. University of Sheffield.

Paulay, T., & Binney, J. R. (1974). Diagonally reinforced coupling beams of shear walls, Shear in Reinforced Concrete. In *American Concrete Institute Structural Journal: Vol. SP-42* (Issue 2, pp. 579–598).

Pham, T. M., Zhang, X., Elchalakani, M., Karrech, A., Hao, H., & Ryan, A. (2018). Dynamic response of rubberized concrete columns with and without FRP confinement subjected to lateral impact. *Construction and Building Materials*, *186*, 207–218. https://doi.org/10.1016/j.conbuildmat.2018.07.146

Pineda, J. C. (1994). *Ensayos Experimentales Sobre Control de Columnas Cortas (in Spanish)*. Universidad de los Andes, Bogota, Colombia.

Priestley, M. J. N., Seible, F., & Calvi, G. M. (1996). Seismic Design and Retrofit of Bridges. In *Seismic Design and Retrofit of Bridges*. John Wiley and Sons. https://doi.org/10.1002/9780470172858

Raffoul, S., Escolano-Margarit, D., Garcia, R., Guadagnini, M., & Pilakoutas, K. (2019). Constitutive Model for Rubberized Concrete Passively Confined with FRP Laminates. *Journal of Composites for Construction*, *23*(6), 04019044. https://doi.org/10.1061/(asce)cc.1943-5614.0000972

Raffoul, S., Garcia, R., Escolano-Margarit, D., Guadagnini, M., Hajirasouliha, I., & Pilakoutas, K. (2017). Behaviour of unconfined and FRP-confined rubberised concrete in axial compression. *Construction and Building Materials*, *147*, 388–397. https://doi.org/10.1016/j.conbuildmat.2017.04.175

Raffoul, S., Garcia, R., Pilakoutas, K., Guadagnini, M., & Medina, N. F. (2016). Optimisation

of rubberised concrete with high rubber content: An experimental investigation. *Construction and Building Materials*, *124*, 391–404. https://doi.org/10.1016/j.conbuildmat.2016.07.054

Rahman, M., Al-Ghalib, A., & Mohammad, F. (2014). Anti-vibration characteristics of rubberised reinforced concrete beams. *Materials and Structures/Materiaux et Constructions*, *47*(11), 1807–1815. https://doi.org/10.1617/s11527-013-0151-0

Rashad, A. M. (2016). A comprehensive overview about recycling rubber as fine aggregate replacement in traditional cementitious materials. *International Journal of Sustainable Built Environment*, *5*(1), 46–82. https://doi.org/10.1016/j.ijsbe.2015.11.003

Rivas-Vázquez, L. P., Suárez-Orduña, R., Hernández-Torres, J., & Aquino-Bolaños, E. (2015). Effect of the surface treatment of recycled rubber on the mechanical strength of composite concrete/rubber. *Materials and Structures/Materiaux et Constructions*, *48*(9), 2809–2814. https://doi.org/10.1617/s11527-014-0355-y

Roychand, R., Gravina, R. J., Zhuge, Y., Ma, X., Youssf, O., & Mills, J. E. (2020). A comprehensive review on the mechanical properties of waste tire rubber concrete. *Construction and Building Materials*, *237*, 117651. https://doi.org/10.1016/j.conbuildmat.2019.117651

Siddika, A., Mamun, M. A. Al, Alyousef, R., Amran, Y. H. M., Aslani, F., & Alabduljabbar, H. (2019). Properties and utilizations of waste tire rubber in concrete: A review. *Construction and Building Materials*, *224*, 711–731. https://doi.org/10.1016/j.conbuildmat.2019.07.108

Siddika, A., Mamun, M. A. Al, Ferdous, W., & Alyousef, R. (2020). Performances, challenges and opportunities in strengthening reinforced concrete structures by using FRPs – A state-of-the-art review. *Engineering Failure Analysis*, *111*(August 2019), 104480. https://doi.org/10.1016/j.engfailanal.2020.104480

Siddique, R., & Naik, T. R. (2004). Properties of concrete containing scrap-tire rubber - An overview. *Waste Management*, *24*(6), 563–569. https://doi.org/10.1016/j.wasman.2004.01.006

Skripkiunas, G., Grinys, A., & Miškinis, K. (2009). Damping properties of concrete with rubber waste additives. *Materials Science (Medziagotyra)*, *15*(3), 266–272.

Son, K. S., Hajirasouliha, I., & Pilakoutas, K. (2011). Strength and deformability of waste tyre rubber-filled reinforced concrete columns. *Construction and Building Materials*, *25*(1), 218–226. https://doi.org/10.1016/j.conbuildmat.2010.06.035

Strukar, K., Kalman Šipoš, T., Miličević, I., & Bušić, R. (2019). Potential use of rubber as aggregate in structural reinforced concrete element – A review. *Engineering Structures*, *188*(February), 452–468. https://doi.org/10.1016/j.engstruct.2019.03.031

Sugapriya, P., & Ramkrishnan, R. (2018). Crumb Rubber Recycling in Enhancing Damping Properties of Concrete. *IOP Conference Series: Materials Science and Engineering*, *310*(1). https://doi.org/10.1088/1757-899X/310/1/012013

Sukontasukkul, P., & Chaikaew, C. (2006). Properties of concrete pedestrian block mixed with crumb rubber. *Construction and Building Materials*, *20*(7), 450–457. https://doi.org/10.1016/j.conbuildmat.2005.01.040

Tanganelli, M., Viti, S., De Stefano, M., & Reinhorn, A. (2013). Influence of Infill Panels on the Seismic Response of Existing RC Buildings: A Case Study. *Seismic Behaviour and Design of Irregular and Complex Civil Structures*.

Toutanji, H. A. (1996). The use of rubber tire particles in concrete to replace mineral aggregates. *Cement and Concrete Composites*, *18*(2), 135–139. https://doi.org/10.1016/0958-9465(95)00010-0

Tufail, R. F., Feng, X., & Zahid, M. (2019). Behavior of unconfined and CFRP confined rubberized concrete. *International Journal of Low-Carbon Technologies*, *15*(1), 65–83.

https://doi.org/10.1093/ijlct/ctz058

Wakabayashi, M., & Minami, K. (1972). *An experimental study on hysteretic characteristics of reinforced concrete columns failing in shear*. 97–112.

Wang, Z., Chen, L., Guadagnini, M., & Pilakoutas, K. (2019). Shear Behavior Model for FRP-Confined and Unconfined Rubberized Concrete. *Journal of Composites for Construction*, *23*(5), 04019039. https://doi.org/10.1061/(asce)cc.1943-5614.0000962

Wang, Z., Hajirasouliha, I., Guadagnini, M., & Pilakoutas, K. (2021). Axial behaviour of FRP-confined rubberised concrete: An experimental investigation. *Construction and Building Materials*, *267*, 121023. https://doi.org/10.1016/j.conbuildmat.2020.121023

Wang, Z., Hu, H., Hajirasouliha, I., Guadagnini, M., & Pilakoutas, K. (2020). Tensile stress-strain characteristics of rubberised concrete from flexural tests. *Construction and Building Materials*, *236*, 117591. https://doi.org/10.1016/j.conbuildmat.2019.117591

Xu, B., Bompa, D. V., Elghazouli, A. Y., Ruiz-Teran, A. M., & Stafford, P. J. (2018). Behaviour of rubberised concrete members in asymmetric shear tests. *Construction and Building Materials*, *159*, 361–375. https://doi.org/10.1016/j.conbuildmat.2017.10.091

Xue, J., & Shinozuka, M. (2013). Rubberized concrete: A green structural material with enhanced energy-dissipation capability. *Construction and Building Materials*, *42*, 196–204. https://doi.org/10.1016/j.conbuildmat.2013.01.005

Yamada, M., & Furui, S. (1966). *Research on the shear resistances of reinforced concrete members subjected to axial load*.

Yamada, M., & Furui, S. (1968). *Shear resistance and explosive cleavage failure of reinforced concrete members subjected to axial load*. 1091–1102.

Yi, O., Mills, J. E., Zhuge, Y., Ma, X., Gravina, R. J., & Youssf, O. (2020). Case Study of the Structural Performance of Composite Slabs with Low Strength CRC Delivered by Concrete Truck. *Case Studies in Construction Materials*, *13*.

https://doi.org/10.1016/j.cscm.2020.e00453

Yi, O., Zhuge, Y., Ma, X., Gravina, R. J., Mills, J. E., & Youssf, O. (2021). Push-off and Pull-out Bond Behaviour of CRC Composite Slabs – An Experimental Investigation. *Engineering Structures*, *228*(April 2020). https://doi.org/10.1016/j.engstruct.2020.111480

Youssf, O., Elgawady, M. A., & Mills, J. E. (2016). Static cyclic behaviour of FRP-confined crumb rubber concrete columns. *Engineering Structures*, *113*, 371–387. https://doi.org/10.1016/j.engstruct.2016.01.033

Youssf, O., ElGawady, M. A., & Mills, J. E. (2015). Experimental Investigation of Crumb Rubber Concrete Columns under Seismic Loading. *Structures*, *3*, 13–27. https://doi.org/10.1016/j.istruc.2015.02.005

Youssf, O., Mills, J. E., Benn, T., Zhuge, Y., Ma, X., Roychand, R., & Gravina, R. (2020). Development of Crumb Rubber Concrete for Practical Application in the Residential Construction Sector – Design and Processing. *Construction and Building Materials*, *260*, 119813. https://doi.org/10.1016/j.conbuildmat.2020.119813

Zheng, L., Sharon Huo, X., & Yuan, Y. (2008). Experimental investigation on dynamic properties of rubberized concrete. *Construction and Building Materials*, *22*(5), 939–947. https://doi.org/10.1016/j.conbuildmat.2007.03.005

Zhi, Q., Guo, Z., Xiao, Q., Yuan, F., & Song, J. (2017). Quasi-static test and strut-and-tie modeling of precast concrete shear walls with grouted lap-spliced connections. *Construction and Building Materials*, *150*, 190–203. https://doi.org/10.1016/j.conbuildmat.2017.05.183

Zhou, W., & Hong, H. P. (2000). Modeling Error of Strength of Short Reinforced Concrete Columns. *ACI Structural Journal*, *97*(3), 427–435.

Chapter 3

Simulating the behaviour of short columns and how to enhance their capacity and ductility

Keywords: Short columns; Reinforced concrete; Shear failure; Highly deformable concrete; Seismic performance.

3.1 INTRODUCTION

Short columns in RC structures are particularly vulnerable to seismic actions and failure of short columns is often seen after earthquakes. This chapter presents an experimental and numerical study on the behaviour of a reinforced concrete frame with short columns subjected to lateral loading. The work reported in the following includes the first phase of an experimental program aimed at examining structural applications for CRuC along with the development of suitable numerical, analytical and simplified design models. A one-story one-bay building with short columns along the loading direction was tested to assess the performance of short columns made of CC and investigate the resulting failure mechanism. A detailed FE analysis (FEA) is then carried out to gain an in-depth understanding of the structural response of the frame with short columns, which is then used to develop a strut and tie model (STM) in OpenSees. The latter allows for the development of more efficient analysis methods to simulate the structural behavior of short columns under seismic loading. Both the FE model, and the STM were adapted to examine the effect of using short columns made with CRuC confined with AFRP on the global seismic performance of the RC frame. The results of this numerical investigation are presented along with a comparison between the behavior of short column with CC and CRuC.

3.2 EXPERIMENTAL PROGRAM

The first phase of the experimental work comprised a benchmark test to examine the structural performance of an RC frame building with short columns under unidirectional cyclic and monotonic loading. The boundary conditions were selected to force the development of a short column mechanism in two of the columns as described in the next section. The primary consideration in the design of the test specimen was to force a local shear failure in the short column, hence the column flexural capacity was sought to be much higher than the shear capacity. The results of this test, along with a complementary numerical study, were used to inform the design of a series of buildings that were tested on a shake-table to study the behaviour of highly deformable short columns.

3.2.1 Design of the test specimen

The structure examined in this study was a scaled down one-bay one-storey reinforced concrete building with a scale factor of 1/2, and it had a story height of 1360 mm, total length of 2550 mm in the direction of loading, and width of 1950 mm. Figure 3.1 shows the building geometry and detailing of the reinforcement. The building was designed according to EC2, however, in order to attain a shear failure in the short columns, the beams were intentionally over strengthened, and the columns' shear reinforcement consisted of mild steel. The four columns had a cross-section of 150×150 mm, a clear length of 1100 mm, and their foundations (220×220 mm) were embedded in a rigid steel frame for a depth of 400 mm. The steel foundation was in-turn bolted to the strong floor of the laboratory. The longitudinal and transverse beams measured 150×260 mm, and the two-way slab was 60 mm thick and measured 2250×1650 mm. The columns' reinforcement consisted of six 14 mm diameter longitudinal bars, and 4 mm diameter shear links spaced at 100 mm centre-to-centre, both of which extended into the foundation and into the joints. The bars were bent at 90 degrees angle for anchoring. The beams in the X-direction were reinforced with six 12 mm diameter longitudinal bars, and 6 mm

diameter stirrups at 200 mm spacing in the middle 800 mm span, and 100 mm spacing at the ends. The beams in the Y-direction were reinforced with four 10 mm diameter longitudinal bars, and 6 mm diameter stirrups at 200 mm spacing in the middle 600 mm span, and 100 mm spacing at the ends. The steel bars of the beams were anchored at a 90 degrees angle into the adjacent beam. The clear cover was 20 mm in all structural elements.

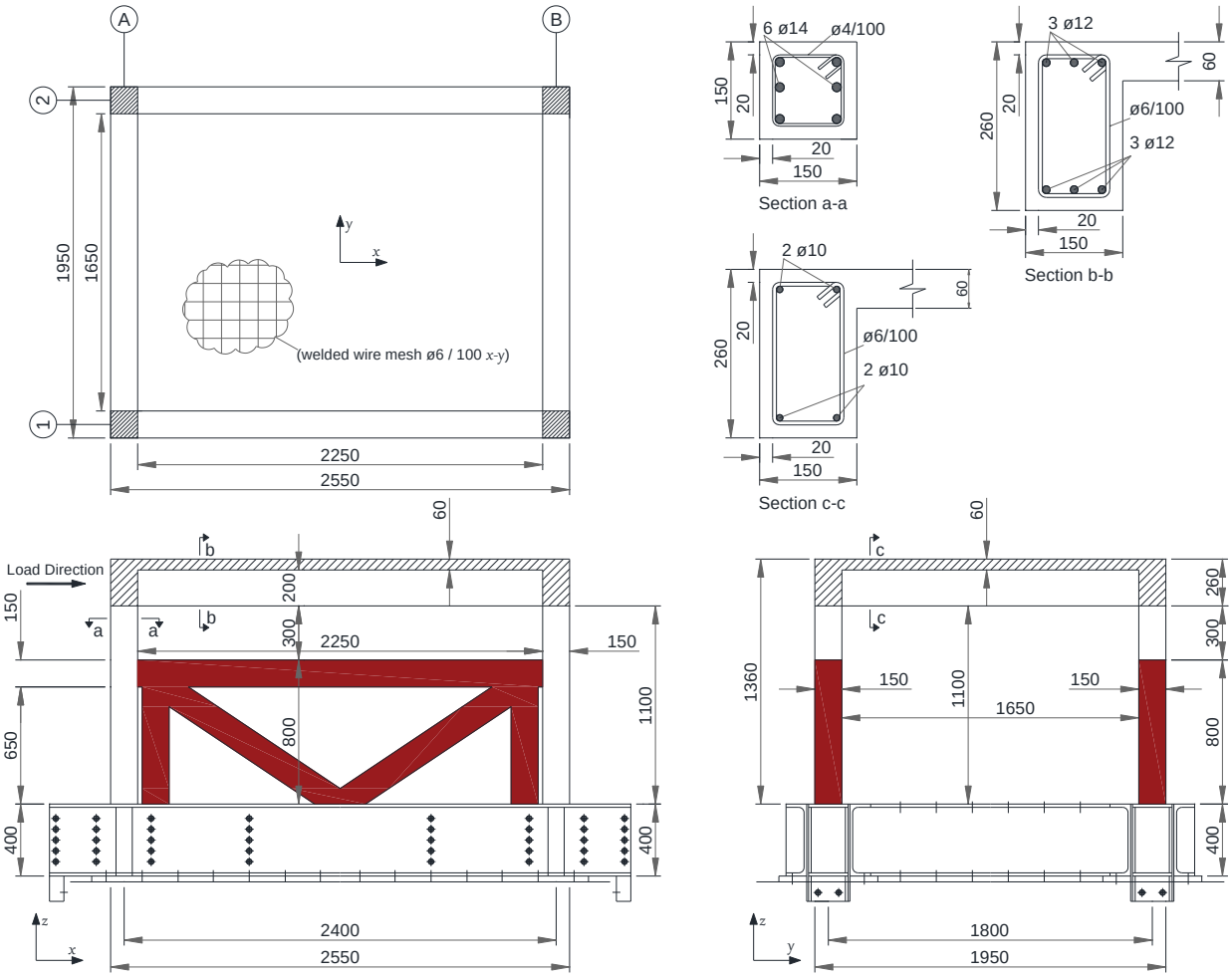

Figure 3.1: Geometry of the tested building and cross-sections of the main structural elements

The columns were intentionally designed to fail in shear within the top region restrained by the external steel frame and the top beams, and had a yielding flexural strength of 23 kNm, an ultimate flexural capacity of 25 kNm and a maximum shear capacity of 28 kN for the concrete alone according to Eurocode 2 (EC2) (EN 1992-1-1, 2004). The shear reinforcement of the column provides an additional 6.9 kN resistance. At the limit of 34.9 kN shear load, the bending

moment exhibited by the short column is 5.2 kNm, which is far from the yielding flexural moment by a big safety margin. The ultimate flexural capacities of the longitudinal beams (X-) and transverse beams (Y-) were 46 and 22 kNm, respectively. The two-way slab of the building was 60 mm thick and was reinforced with a mesh of 6 mm diameter bars at a 100 mm spacing. The structural elements of the building were identified based on their type, location, and orientation. The first letter of the ID indicates the type of structural element (C=column, J=beam-column joint), while the next digit and letter represent the location of the element based on the intersection of the corresponding axes from Figure 1. The fourth letter, if used, determines the direction being referred to. For example, J1A-X refers to the joint situated at the intersection of axes 1 and A, and the face being observed is parallel to the X-axis.

3.2.2 Material properties

The mechanical properties of the concrete were determined by testing five 150×300 mm standard cylinders according to EN 12390 (EN 12390-3, 2019), which resulted in a compressive mean strength $f_{cm} = 37\ MPa$ and elastic modulus $E_c = 30\ GPa$. The tensile strength of the concrete was estimated to be $f_{ct} = 3.3\ MPa$, according to EC2 (EN 1992-1-1, 2004). The longitudinal bars of beams and columns had yield and ultimate strengths of $f_{ly} = 513\ MPa$ and $f_{lu} = 626\ MPa$, respectively, as obtained from five direct tensile coupons tested according to EN 10080 (EN 10080, 2009). The smooth steel wire used for the beams and columns stirrups, as well as for the steel mesh of the slab, had a yield strength of $f_{sy} = 255\ MPa$ according to the manufacturer data.

3.2.3 Test setup, instrumentation, and load sequence

The steel frame that served as the foundation of the RC building was fixed to the strong floor. Since the focus of this experiment is the behaviour of short columns, additional softening effects and failure mechanisms due to the masonry infill were unnecessary and would complicate the structural system. Additionally, the in-plane stiffness of partial infill masonry walls, for a multi-bay building, is relatively much higher than that of the column, and hence the damage will concentrate in the short column region (Chiou et al., 1999). Hence, two stiff steel frames were positioned between the columns of the frames in the X-direction to simulate the presence of partial infill masonry walls and force the development of a short column mechanism within the top region columns C1A and C2A. The steel frames were bolted to the bottom steel foundation.

The clear shear span of the short column region from the bottom of the beam to the top of the restraining system was 300 mm, which gives a shear ratio $\alpha_s = 1$. Ten concrete blocks (total=36 kN) were bolted to the slab to simulate axial load, thus resulting in a 9 kN axial load per column (i.e. approximately 1% of the column's axial capacity). The main reason for the low axial load was Laboratory limitations, in terms of the availability of weight blocks. In addition to that, this test will inform the setup for a shake-table test on a similar building, where the maximum allowed overturning moment on the table is limited, hence, the physical mass on top of the slab was taken as minimum.

The X direction of the building was instrumented with eight horizontal linear variable differential transformers (LVDTs shown as Ln1 to Ln8 in Figure 3.2) located at the top and bottom of the short columns. Four diagonal LVDTs (Incl1 to Incl4) placed at an angle of 45° measured the relative rotation between beams and columns.

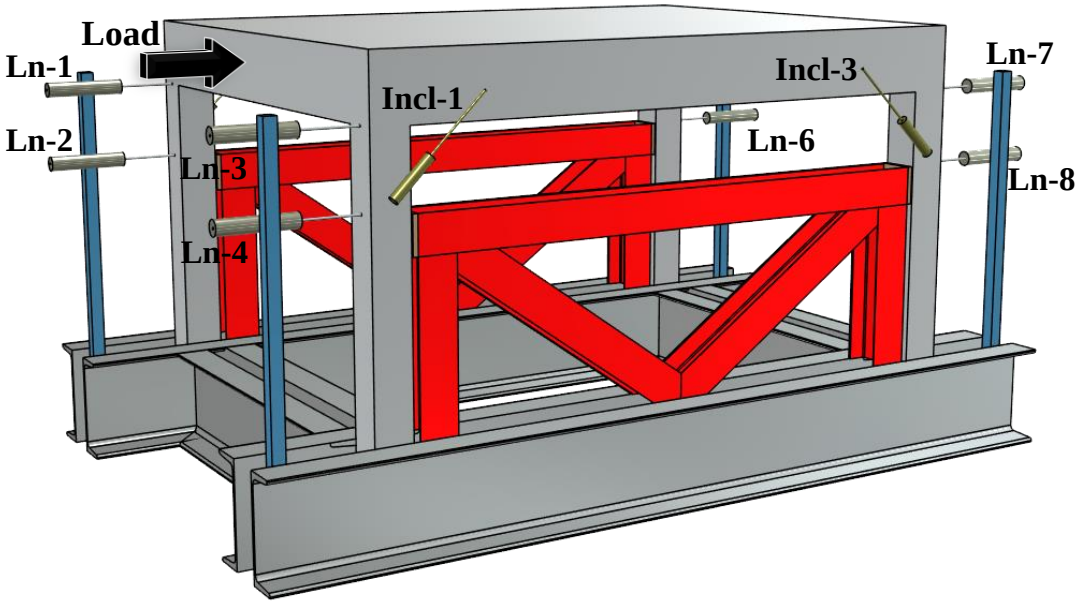

Figure 3.2: Test setup and layout of the external instrumentation

The lateral load was applied to the specimen via a hydraulic actuator and a steel transfer beam connected to the top transverse beam (Figure 3.3). The test was performed in load control at a rate of 6 kN/min. The RC building was subjected to three sets of three cycles: A set performed at 40 kN to capture the first flexural crack, an intermediate set performed at 60 kN, and a set performed at 100 kN to capture the diagonal shear cracking, followed by a final monotonic load up to failure. The test was halted when the maximum load recorded during the test dropped by 20%.

Figure 3.3: RC building with short columns (test initialisation)

3.2.4 Experimental results and discussion

Figure 3.4 shows the lateral load versus displacement obtained from the average of four horizontal transducers, Ln-1, 3, 5, and 7.

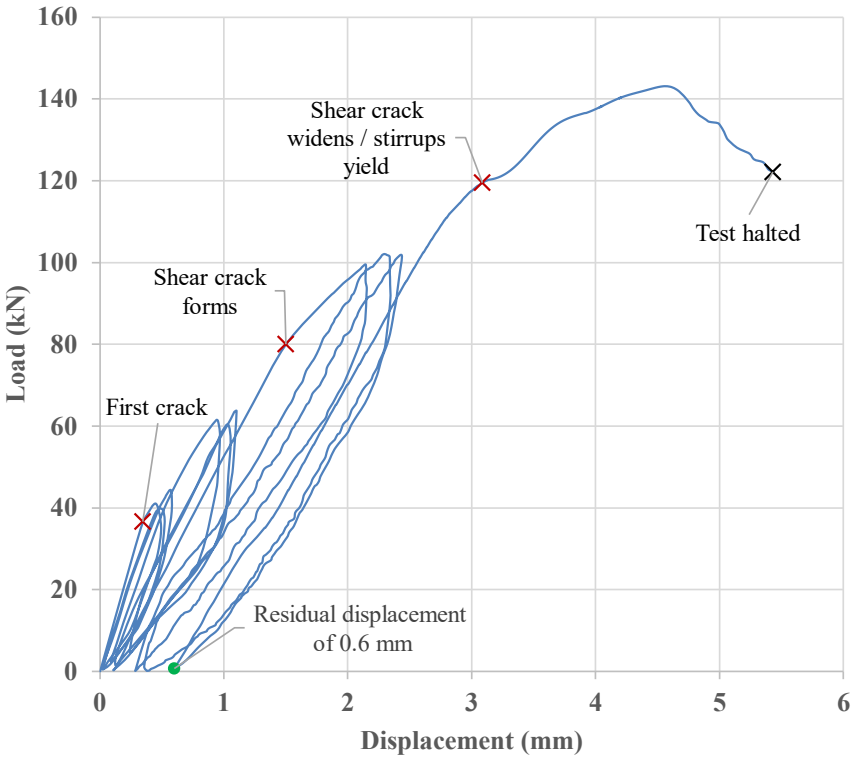

Figure 3.4: Lateral load versus frame displacement response of the tested building

First flexural cracking occurred in the joints J1A and J2A during the first loading cycle at a lateral force of 37 kN. The cracks propagated at an angle of 45° and 70° from the horizontal for J1A-X and J2A-X, respectively. The cracks further propagated through the joints during the subsequent cycles performed at 40 and 60 kN. Few hairline flexural cracks appeared along columns C1A-X and C2A-X during the cycles performed at 100 kN. At a lateral force of 82 kN, shear cracking occurred in the top portion of both columns C1A-X and C2A-X. The shear crack propagated at an angle of 17° from the vertical along the direction connecting the externally applied load to the internal restraining system as the main load transfer mechanism relied on the formation of a diagonal compression strut (Figure 3.5).

Figure 3. 5: Shear cracking along the short column (excessive spalling in C2A occurred post-peak)

Flexural cracking in columns C1B-X and C2B-X initiated during the second cycle at 100 kN at a load of approximately 98 kN. The maximum lateral load capacity of the building (143 kN) was reached at 4.55 mm, and "failure" occurred at a displacement of 5.4 mm (121 kN). Excessive spalling along the top of columns C1A-X and C2A-X occurred at a displacement greater than 5.4 mm, at which point the test was halted and the frame was deemed to have failed. No damage was observed in the slab or the beams. No torsion was recorded as the displacements measured by the LVDTs were similar on both sides of the building. The initial stiffness of the building was 107 kN/mm, measured experimentally from the slope of the load-displacement data up to a load of 30 kN, while the relative decrease in stiffness at the first cycle of every load set is shown in Figure 3.6.

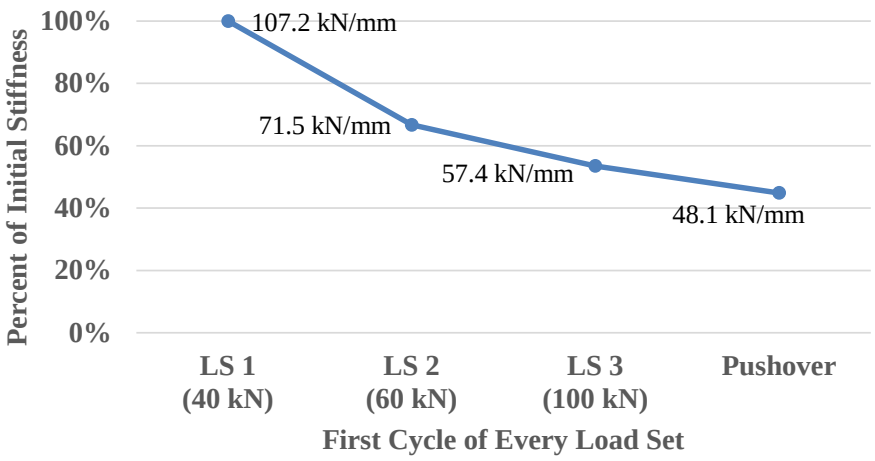

Figure 3.6: Stiffness degradation at first cycle of every load set (LS)

The beam-column relative rotation at axis-A and axis-B is shown in Figure 3.7. The first stiffness change due to flexural cracking can be clearly seen in the rotation at axis-A, whereas the rotation at axis-B does not show any significant stiffness change since the columns and joints at axis B showed no signs of damage until a lateral load of 98 kN.

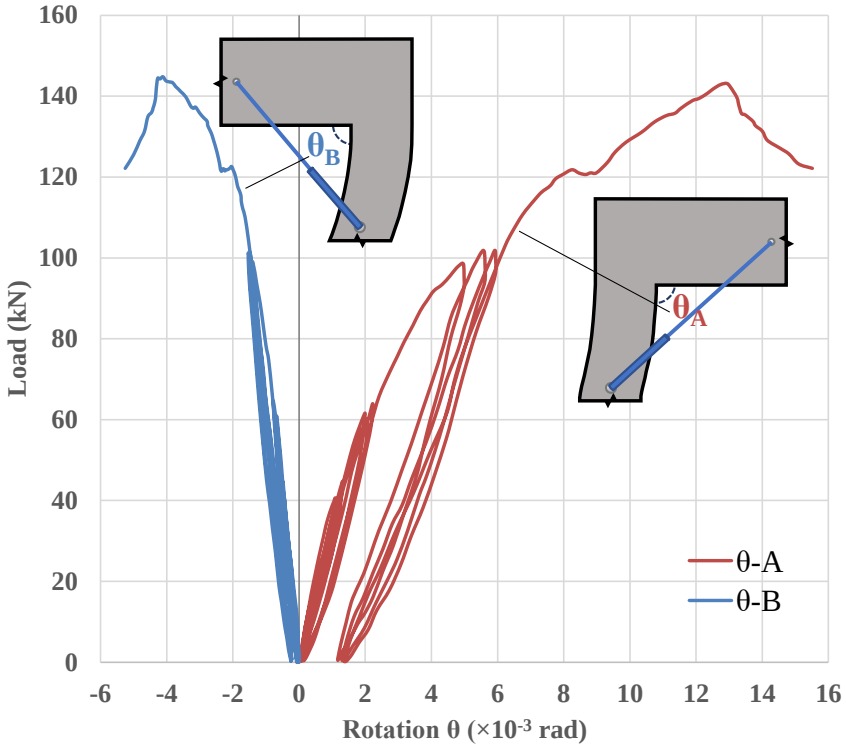

Figure 3.7: The average beam-column relative rotation at axis-A (Joint opening) and axis-B (Joint closing)

In the next section, the results from these tests were used to study, numerically, in more detail the structural response and failure mode of the short columns of the building.

3.3 NUMERICAL MODELLING OF THE FRAME

To study in greater detail the structural response and failure mode of the short columns of the tested building, a numerical investigation was performed using Abaqus (Dassault Systèmes SIMULIA, 2017), a general finite element software.

3.3.1 Modelling approach

Due to symmetry and absence of in-plan torsion during the test, the building was modelled as one frame only. Figure 3.8 shows the model with part of the concrete concealed to show the reinforcement layout. The bottom 400 mm of the columns were fully restrained along the sides to simulate the fixity provided during the tests by the steel footings.

The braced steel frame used in the experiment to provide lateral restraint was modelled as a 3D analytical rigid body. The interaction between this rigid body and the concrete column was simulated by a surface-to-surface hard contact (with no friction) but allowing separation after contact.

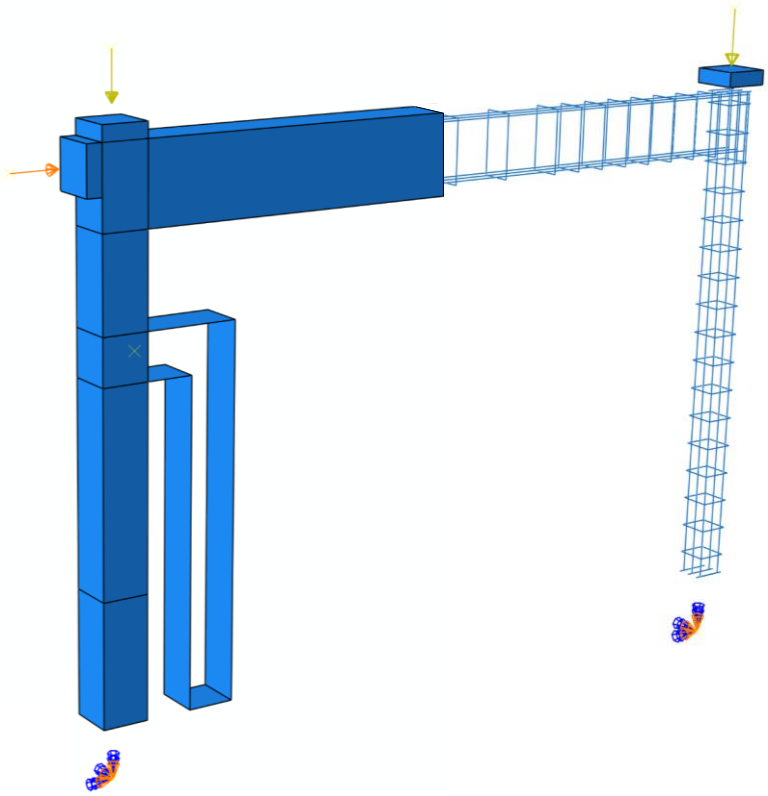

Figure 3.8: Abaqus model of a single frame of the tested building (concrete partially hidden to show reinforcement)

The gravity load was applied as concentrated forces on reference points (control nodes), whereas an increasing displacement was imposed on a reference point connected to J1A. The reference points were connected to their corresponding load transfer steel plate via a Multiple Point Constraint (MPC) tie. Abaqus/Standard was used to perform a static analysis with viscoplastic regularization, using a viscosity parameter of 1×10^{-5}. The frame was pushed monotonically until failure.

3.3.2 Concrete and steel reinforcement models

The built-in concrete damage plasticity model (CDP) in Abaqus/Standard was used in the analysis with the following plasticity parameters: dilation angle ψ=37°; eccentricity ϵ=0.1; stress ratio σ_{b0}/σ_{c0}=1.16; and shape factor of the yield surface K_c=0.667. The compressive stress-strain behaviour was defined according to the Krätzig and Pölling (Krätzig & Pölling, 2004) elasto-plastic damage model, whereas the tensile softening function was defined based on the stress-crack opening relation of Hordijk (Hordijk, 1992). The CDP damage parameters, for both compression and tension, were defined using the damage evolution model proposed by Alfarah et al. (Alfarah et al., 2017). The adopted framework implements a fracture energy-based regularization and should ensure mesh independent results (see Appendix A1). The fracture energy of concrete was calculated using Eq. (3.1) (Bažant & Becq-Giraudon, 2002):

$$G_F = 2.5\alpha_0 \left(\frac{f_{cm}}{0.051}\right)^{0.46} \left(1 + \frac{d_a}{11.27}\right)^{0.22} \left(\frac{w}{c}\right)^{-0.3} \quad (3.1)$$

where G_F is the fracture energy in N/m; α_0 is 1 for round aggregates; d_a is the maximum aggregate size; and w/c is the water-cement ratio by weight.

Adopting α_0=1, f_{cm}=37 MPa, d_a=15 mm, and w/c=0.4, the fracture energy was calculated as 82 N/m. The crushing energy G_C was taken to be 100 times the fracture energy (Nana et al., 2017). All the concrete parts of the model were meshed with an 8-node linear 3D brick element with reduced integration (C3D8R).

The longitudinal steel bars and stirrups were modelled as 2-node linear 3-D truss elements (T3D2) assuming an elastic-perfectly plastic behaviour. All reinforcement was fully embedded in the concrete assuming perfect bond. The steel loading plates were modelled as 3D solid C3D8R elements assuming an elastic behaviour.

3.3.3 Numerical results and discussion

Mesh sensitivity analysis was performed on the model using a different number of elements across the width of the column equal to 4, 5, 6 and 8, resulting in mesh sizes of 37.5, 25, 30, and 18.75 mm, respectively. Figure 3.9 compares the lateral load versus frame displacement results obtained for each case.

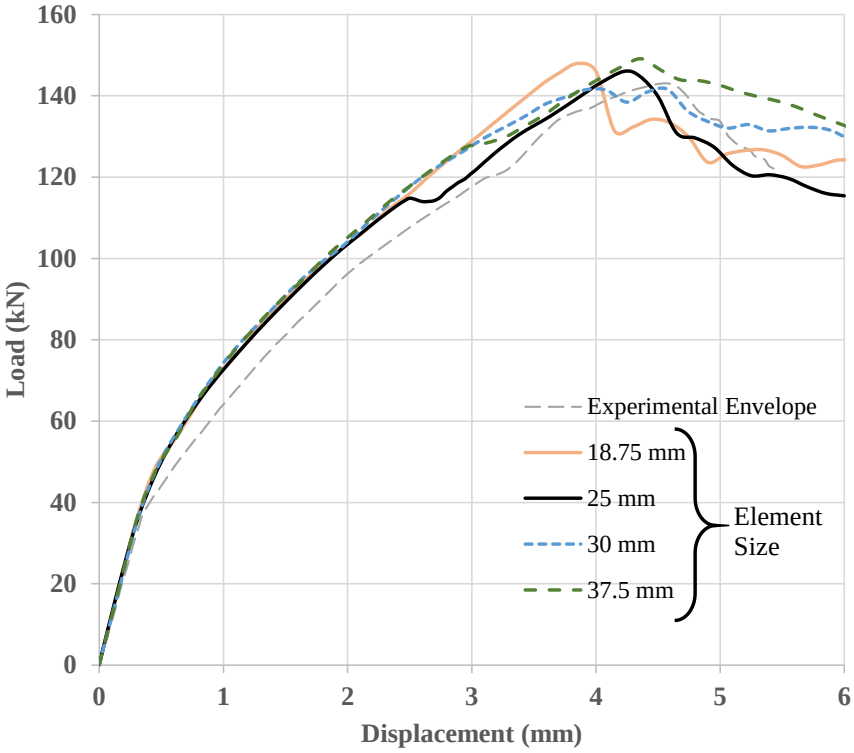

Figure 3.9: Mesh sensitivity analysis of the Abaqus model (lateral load vs. frame displacement)

Although small differences can be observed in terms of both peak load and displacement, the initial stiffness and subsequent degradation of all models are similar. The results from the 25 mm mesh are considered to best fit the experimental results and are discussed herein. The peak lateral resistance and displacement predicted by the model were 146 kN and 4.2 mm,

respectively, which compare well with the experimental values of 143 kN and 4.55 mm. The initial stiffness of the model (120 kN/mm) was 12% higher than the initial experimental stiffness (107 kN/mm). The higher stiffness of the model can be attributed to minor unintended damage caused to the building while positioning it on the testing rig. At a load of 43 kN, flexural cracking occurred simultaneously in joint J1A-X and along the external face of column C1A-Y, at the level of the restraining system. The stiffness reduction after 43 kN was less severe than that in the experiment (see Figure 3.9), which led to a stiffer response. A sudden increase in lateral displacement was observed at 114 kN, possibly as a result of yielding of the top stirrup in column C1A just below the joint. A similar behaviour is seen in the experimental results but at 120 kN. This fact, along with the large observed crack widths and the additional evidence provided by the numerical analysis, confirms yielding of the stirrups along the short column. However, the longitudinal column bars remained elastic.

The minimum principal stress field along the column and the joint at a frame displacement of 3.75 mm, shown in Figure 3.10, displays the compressive force path within the short column.

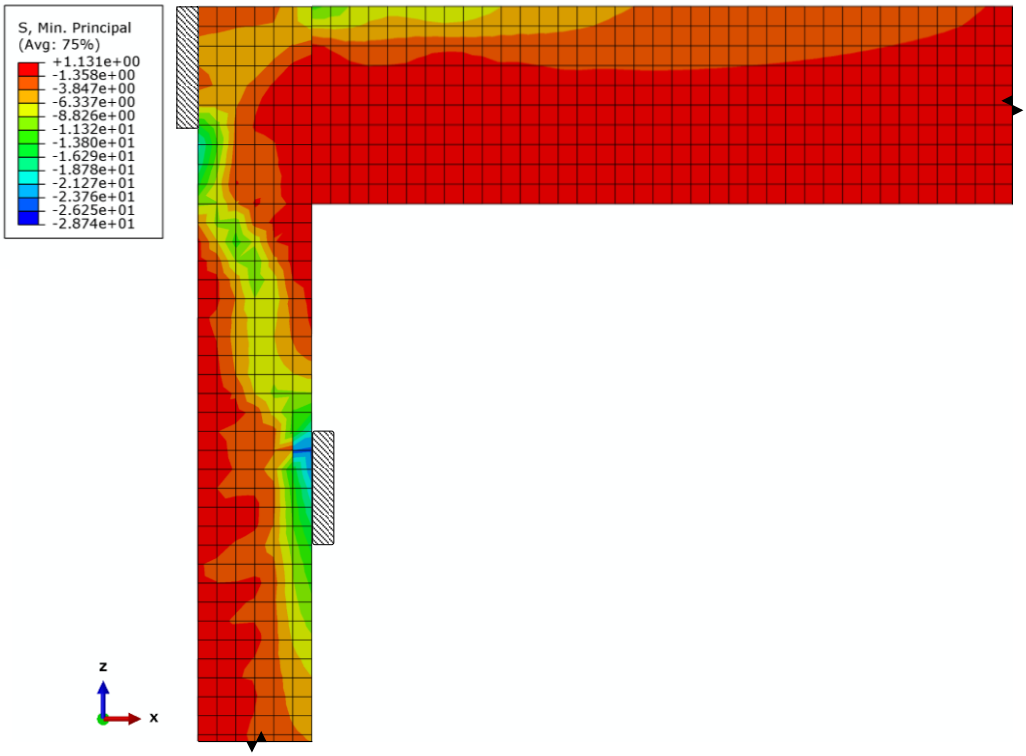

Figure 3.10: Minimum principal stress field along the short column and the joint at a frame displacement of 3.75 mm

The results show that the analytical stress distribution agrees well with the experimental cracking pattern. Consequently, the frame model can provide details of the evolution of the main load transfer mechanism within the short column. A diagonal concrete strut connecting the bottom of the beam at the loading side to the top of the lateral restraint system clearly formed at a frame displacement of about 1.2 mm. The dimensions of the nodes of the strut were estimated from the numerical model to be 65 mm and 45 mm for the top and bottom nodes, respectively. These dimensions, which agree with simpler cross-section analysis calculations, were used to determine the geometry of nodes and strut implemented in a new analytical model presented in the following section.

3.4 STRUT AND TIE MODELLING AND FRAME ANALYSIS

Although the FEA presented in the previous section matched well the experimental results, this type of analysis method is computationally intensive to analyse large buildings and/or dynamic loading effects. As a consequence, this section presents a more practical analytical model (implemented in OpenSees software (Mazzoni et al., 2009)) that simplifies the analysis of buildings with short columns.

3.4.1 Frame geometry and element type

The tested structure was modelled as a single 2-D frame made of displacement beam-column elements. The elements had a fibre cross-section with three materials: unconfined concrete (concrete cover), confined concrete (core concrete) based on Chang and Mander's confinement model, and steel (reinforcing bars). Six strut and tie elements were used to model the shear load-transfer mechanism within the short column, as detailed below.

3.4.2 Short column model

The geometry of the elements of the short column macro element (SCME) (Figure 3.11c) was determined using a strut-and-tie approach (Figure 3.11a), based on experimental observations (Section 3.2), numerical analyses of crack patterns, and principal load/stress paths (Section 3.3).

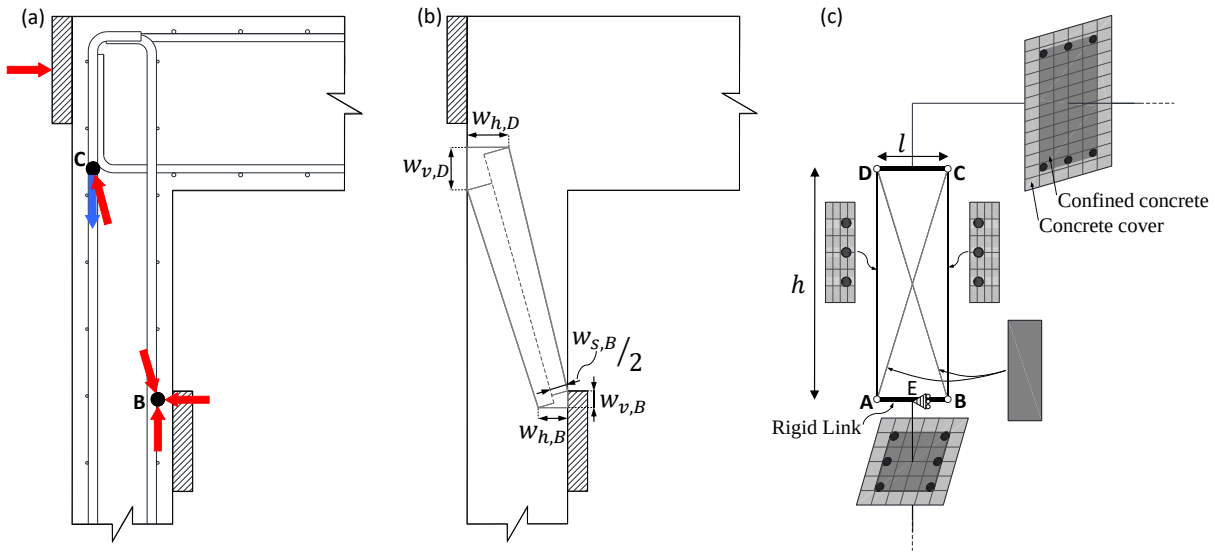

Figure 3.11: Development of the Short Column Macro Element (SCME) to model the shear-flexure behaviour of concrete short columns: a) Force distribution, b) Strut and node formation, and c) SCME topology

The bottom right node, B, is a CCC node, created by three compression forces: the reaction at the bearing face, the cross-sectional force at the back-face, and the force imposed by the strut. The width of the bearing face, ($w_{v,B}$ in Figure 3.11b), was taken to be 25 mm based on the stress distribution at the interface between the column and the short-column boundary condition, as determined from the FEA (see Figure 3.10 in section 3.3.3). The effect of the width of the bearing face on the strut angle and its size is minimal, however, it was considered here to get a more precise location of the centroid of node B. For design, a more straightforward approach can be considered by assuming a negligible $w_{v,B}$, hence, the node centroid will be at the bottom of the clear height of the short column (300 mm down from the beam). Appendix A2 describes the latter in more detail.

Likewise, the width of the back face $w_{h,B}$ was chosen to be the neutral axis depth at the yielding moment of the column (44 mm), based on the centre of gravity of compressive stress of the section. The width of the strut at node B ($w_{s,B}$) was taken as the width normal to the centreline according to Eq. (3.2).

$$w_{s,B} = w_{h,\mathrm{B}} \sin\alpha + w_{v,B} \cos\alpha = 50 \text{ mm} \tag{3.2}$$

where $\alpha = \tan^{-1} h/l$ is the inclination of the strut, and h and l are the height and width of the SCME, respectively. $h = 343.5\ mm$ and $l = 96\ mm$, so $\alpha = 74°$.

The width of the back-face of node A ($w_{h,A}$) was equal to $w_{h,B}$. The width of strut AC ($w_{s,A}$) was taken as the projection of $w_{h,A}$ onto the axis perpendicular to the strut.

$$w_{s,A} = w_{h,A} \sin\alpha \tag{3.3}$$

The top left node D (Fig. 3.11c) is a CCT node, created by the compression from the external load, the compression imposed by the strut, and the tension along the column longitudinal reinforcement (Fig. 3.11a). Node D was located at the intersection of the centrelines of the column and beam bottom longitudinal reinforcement. The width of the horizontal ($w_{h,D}$) and

vertical ($w_{v,D}$) faces of node D was taken as twice the distance from the centreline of the reinforcement to the concrete face. Accordingly, $w_{v,D} = 62\,mm$, and $w_{h,D} = 64\,mm$. A constant strut width equal to the minimum width (i.e. $w_{s,C} = 50\,mm$) was considered in the analysis to ensure appropriate maximum strength capacity. The depth of all SCME elements was equal to the column depth (150 mm).

3.4.3 Material and element assignment for the SCME

The diagonal struts AC and BD were modelled as truss elements made of plain concrete, using *ConcreteCM* material. The negative effect of transverse tension on the concrete strength was considered using Eurocode 2 (EN 1992-1-1, 2004), as shown in Eq. 3.4:

$$f_{cm}^{e} = 0.6\left(1 - \frac{f_{cm}}{250}\right) f_{cm} \tag{3.4}$$

where f_{cm}^{e} is the effective compressive strength of concrete in the strut in Mega Pascales. To account for the effect of confinement provided by the stirrups, the effective strength of the confined concrete (f_{cc}^{e}) was calculated using Mander et al.'s model (Mander et al., 1988) (Eq. 3.5).

$$f_{cc}^{e} = \varphi f_{c}^{e} \tag{3.5}$$

where φ is a confined strength ratio, found to be 1.10 (see Appendix A3), and $f_{cc}^{e} = 21\,MPa$. The post peak stress-strain behaviour of the strut was modified to take into account its aspect ratio (Palmquist & Jansen, 2001; Watanabe et al., 2004; Tung & Tue, 2015). The Chang and Mander concrete model in OpenSees allows for the post peak branch to be adjusted by defining a shape factor r_c, which was originally proposed by Tsai's uniaxial compressional model (Tsai, 1988; Chang G. A. & Mander, 1994). The factor r_c was calibrated based on the relationship proposed by Palmquist and Jansen (Palmquist & Jansen, 2001) and was found to be equal to 10 (see appendix A4).

The vertical elements AD and BC were modelled as truss elements made of reinforced concrete, with a width of $w_{h,A}$, and $w_{h,B}$, respectively. The concrete in these elements was modelled using the *ConcreteCM* material definition in OpenSees. The effect of the stirrup confinement was ignored for these edge vertical elements and therefore the concrete compressive and tensile strengths were taken as $f_{cm} = 37\ MPa$ and $f_{ct} = 3.3\ MPa$, respectively. Each element had three reinforcing bars according to the cross-section geometry (Figure 3.1). The bars were modelled using the *Steel02* material model with material properties as described in the experimental section of this study.

The horizontal elements AB and DC were modelled as rigid links to allow the transfer of moments and forces from the frame elements to the SCME.

3.4.4 Frame analysis

3.4.4.1 Load and boundary conditions

The columns were fully fixed at the bottom. To simulate the short column, node E was restrained against displacement in the X-direction. A gravity nodal load of 13 kN (including self-weight) was applied at the top of each column under load control. A lateral pushover was performed under displacement control via a nodal force at the top node of the left column, up to a maximum displacement of 6 mm.

3.4.4.2 Results and discussion

Figure 3.12 compares the results of the OpenSees and Abaqus simulations, as well as the backbone curve of the experimental cycles. The results indicate that the frame modelled in OpenSees had an initial stiffness of 119 kN/mm, which is similar to that obtained from the FEA.

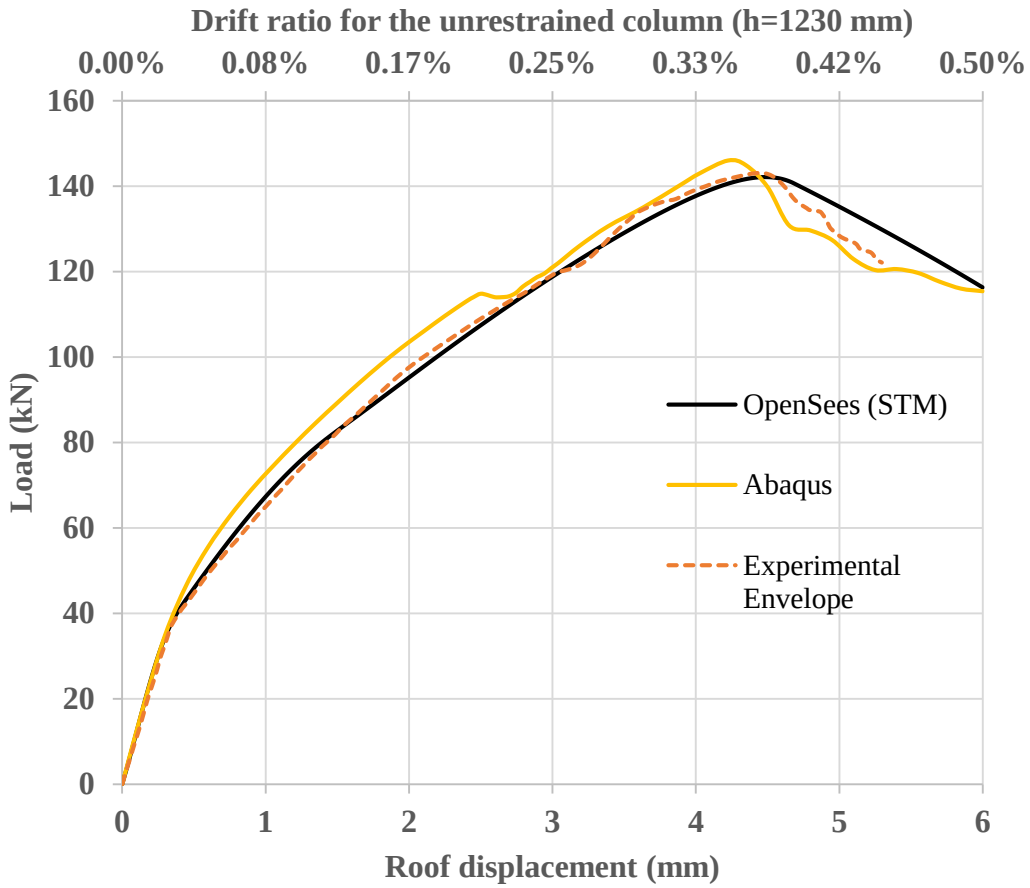

Figure 3.12: Comparison of experimental results (envelope) and OpenSees and FE model

The model reached a peak load of 142 kN at a displacement of 4.48 mm. Failure of the model was caused by the compressive failure of strut DB, which agrees well with the experimental observations. It is also evident that the OpenSees load-displacement curve agrees better with the experimental envelope compared to that obtained from the FEA. As the shear links were not explicitly modelled in OpenSees, however, the horizontal shift in displacement recorded during the test and captured by the FEA at the onset of stirrup yielding, could not be reproduced. In the developed STM, the shear deformation is a function of the stiffness of the shear transfer mechanisms within the SCME.

Figure 3.13 shows the percentage of shear displacement (δ_s) (as % of the local short column deformation) within the short column for both OpenSees and Abaqus models. The shear displacements were decoupled from the flexural ones using Massone and Wallace's model (Massone & Wallace, 2004). The results show that both models calculate an initial δ_s to be 45% of the short column deformation. However, it is also shown that δ_s increases faster in the SCME (OpenSees) as the global frame displacement increases. This is due to the fact that the SCME itself was specifically designed to deform in shear, whereas the strut and tie mechanism in Abaqus can only form after the structure has undergone an initial amount of deformation. At higher displacements (>2.6 mm), however, both models give similar estimate of the shear and flexural components of deformation. This indicates that the new/proposed SCME can predict efficiently the load-displacement behaviour of short columns throughout the entire load history. The run time for the OpenSees simulation was 2 minutes, whereas that of Abaqus was 5 hours.

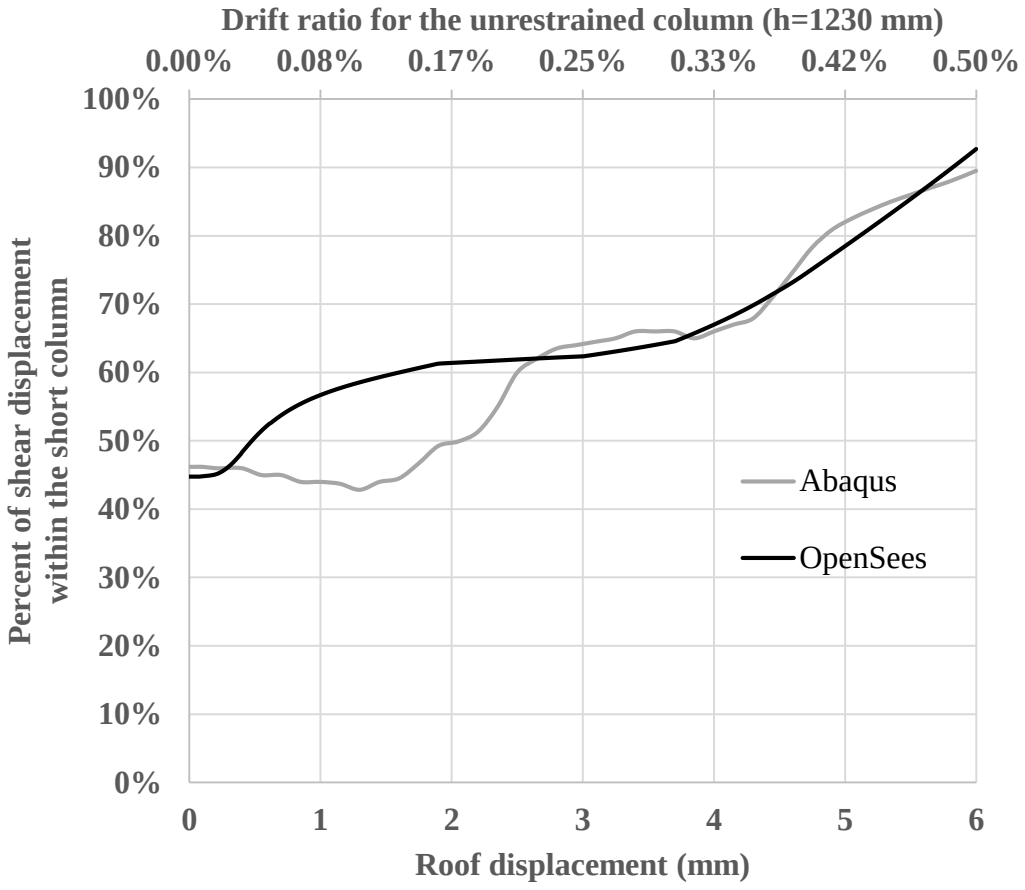

Figure 3.13: Decomposition of the shear-flexural displacement of the short column (conventional concrete)

3.5 NUMERICAL INVESTIGATION OF HIGHLY DEFORMABLE CONCRETE IN SHORT COLUMNS

A series of numerical analyses were carried out to examine the overall structural response of buildings with short columns made of FRP CRuC. A RuC with rubber content of 60% was assumed in the investigation. Such level of aggregate replacement proved suitable to ensure high deformability while maintaining an acceptable compressive strength (Raffoul et al., 2016). AFRP was selected as confining material as it provides a good tensile strength at higher ultimate elongation than other confining materials (Raffoul et al., 2017). The AFRP rupture strain was taken as 65-70% of the ultimate sheet strain given by the manufacturer. The reduced ultimate strain is less than the uniaxial rupture strain of the sheet due to the fact that the jacket might have imperfections and stress concentrations (Raffoul et al., 2017).

3.5.1 Numerical simulation of FRP CRuC short columns in Abaqus

The FE model described in Section 3.3 was modified to carry out this analysis. The corner of the RuC short columns were rounded (radius = 25 mm) to prevent stress concentrations at the corners. The RuC and FRP confinement were modelled separately. The RuC stress-strain behaviour was obtained from the uniaxial compressive constitutive material model proposed by Bompa et al. (Bompa et al., 2017) for the selected type and percent of rubber replacement (Table 3.1). The latter model was developed based on testing cylinders made of RuC under uniaxial compression and it was adopted in this research as it is, without applying a shape factor to account for a rectangular section.

The dilation angle in the CDP model was increased to ψ=45° to consider RuC's high lateral dilation (Youssf et al., 2014; Duarte et al., 2015). The AFRP confinement was modelled as a shell-membrane with the Abaqus user defined Lamina material model (material properties given in Table 3.1). A tie constraint was used to connect the FRP to the concrete surface, assuming perfect bond between the two surfaces.

Three frames were simulated with varying number of AFRP layers around the short column: 1, 2, and 3 layers (ID: CRuC-1L, CruC-2L, & CRuC-3L, respectively). A lateral displacement was imposed at the top of the column until failure of the frame.

Table 3.1: RuC material properties using Bompa et al.'s model and AFRP properties

Conventional Concrete	f_{cm}					
Base concrete mix	63					
Rubberized Concrete	ρ_{vr} (%)	λ	E_{rc}	f_{rc}	ε_{rc}	$f_{rc,t}$
60% volume replacement	60	2.9	9.2	6.7	0.105	0.92
Confined RuC	f_{cr}	ε_{cr}	f_{crc}	ε_{crc}	f_{crc}^{e}	ε_{crc}^{e}
CRuC-1L (1 Layer of AFRP)	8	0.14	28	3.00	26	2.77
CRuC-2L (2 Layer of AFRP)	10	0.17	47	4.34	44	4.00
CRuC-3L (3 Layer of AFRP)	12	0.19	66	5.42	61	5.00
Aramid FRP	t (mm)	E_f	f_u	ε_{fu}		
S&P A120/290	0.2	116	2400	2.5		

Strength *f* in (MPa), Young's Modulus *E* in (GPa), and Strain ε in (%)

In table 3.1 above, adapted from Bompa et al.'s model, ρ_{vr} is the percentage of rubber replacement by volume, λ is a factor for the type of rubber used and is equal 2.9 for a coarse and fine mix, E_{rc}, f_{rc}, ε_{rc}, and $f_{rc,t}$ are the young's modulus, peak compressive strength, strain at peak compressive stress, and peak tensile strength, for unconfined rubberised concrete, respectively. For the confined RuC part of the table, f_{cr} and ε_{cr} are the critical stress and strain, respectively, as defined by Raffoul et al., 2019. f_{crc} and ε_{crc} are the ultimate compressive strength and strain of confined rubberised concrete, respectively. f_{crc}^{e}, and ε_{crc}^{e} are the effective ultimate compressive strength and strain of confined rubberised concrete, respectively, to account for the inclination of the strut in the SCME model as shown in section 3.5.2.

The Aramid FRP properties, t, E_f, f_u, and ε_{fu}, are the sheet thickness, stiffness, ultimate rupture strength, and strain at rupture, respectively, as given by the manufacturer.

3.5.1.1 Results and analysis of numerical simulations

As shown in Figure 3.14, the load displacement curves of the three building models have a similar behaviour, which can be summarized in four phases:

1) Elastic Phase I, which is not affected by the level of confinement as the AFRP is not yet activated at this stage. The initial stiffness of all frames was around 83 kN/mm.
2) Transition Phase II, where the loss in stiffness is due to the development of cracking at the short column/beam interface. At the onset of this phase, the compressive stresses developed within the short column cause its lateral expansion, which in turn activates the AFRP confinement. This phase ends when the RuC reaches its peak strength, which occurs at higher strain values for increasing values of confinement stiffness. This phase ends at a lateral load of 83 kN, 94 kN, and 102 kN for the frames with 1, 2, and 3 layers of AFRP, respectively.
3) Linear hardening Phase III, the stiffness of which is determined by the level of confinement along with the resistance from all other structural elements. The stiffness of this branch was 4.3, 5.4, and 6 kN/mm for the frames with 1, 2, and 3 layers of AFRP, respectively.
4) A further reduction in stiffness (Phase IV) is observed as a result of yielding of the longitudinal reinforcement at the bottom of the unrestrained column C1B, which occurs at a lateral displacement of approximately 19 mm for all three confinement levels.

Phase IV ends with the failure of the frame. Frames CRuC-1L and CRuC-2L failed when the AFRP along the face of the column parallel to the loading direction reached its rupture strain of 1.75%, which occurred at a lateral displacement of 36 mm and 57 mm, respectively. Frame CRuC-3L failed following the formation of a plastic hinge mechanism when the longitudinal reinforcement in column C1A yielded at the short column restraint level at a frame

displacement of 52 mm and a lateral load of 272 kN. At this stage, the strain in the AFRP was 1.3%. Experimental asymmetric shear tests on rectangular prisms with CRuC in the shear zone, performed by Zhao et al. (Wang et al., 2019), have shown similar behaviour to the four-phase model described above (see Appendix A5, Figure A.9-a). Despite the complexity of the frame, the general trend is dominated by the short column. The load-displacement experimental envelope of the conventional concrete experiment is shown in Figure 3.14 only for the purpose of displaying the relative improvement in terms of frame ductility that the CRuC short columns can provide.

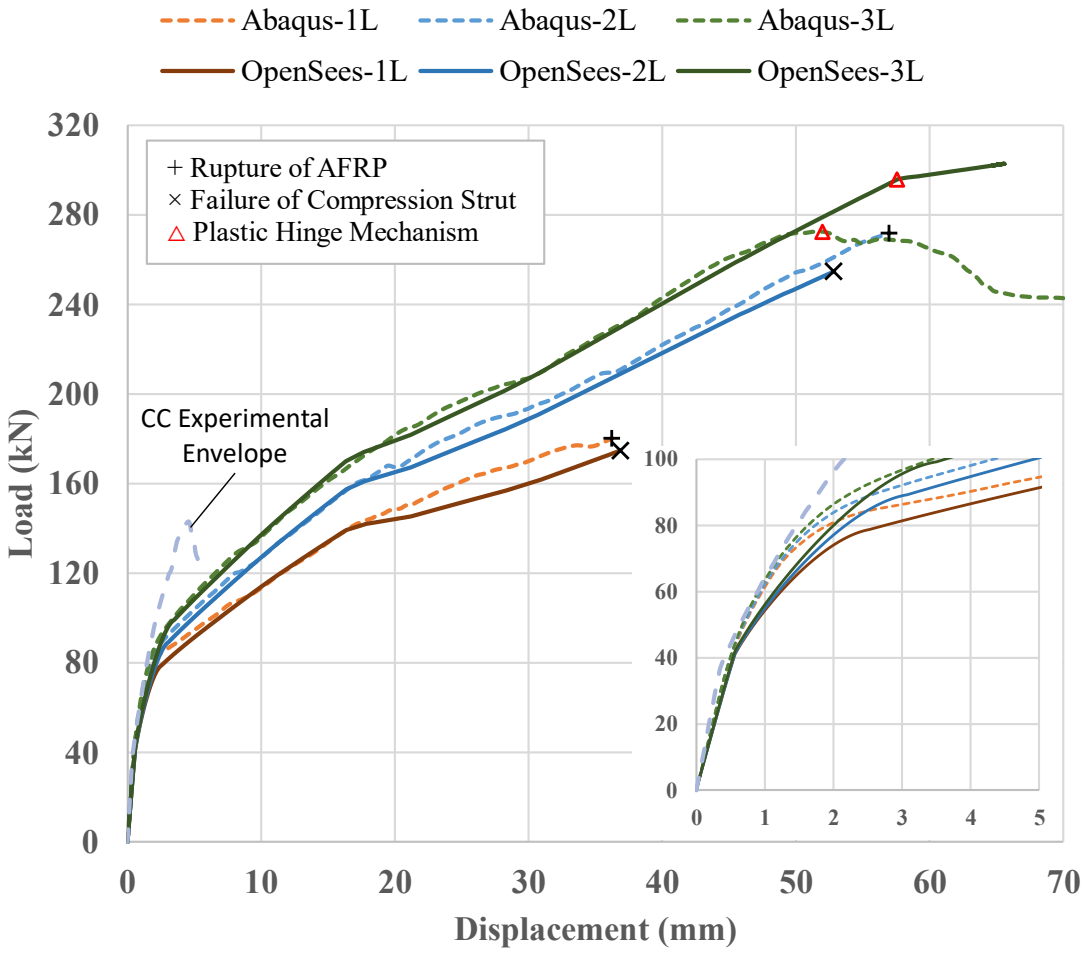

Figure 3.14: Numerical lateral load versus frame displacement of buildings with confined Rubberized Concrete short columns

Figure 3.15 shows the AFRP strain results profile at the centre of the sheet along the faces of the column parallel and perpendicular to the loading direction. The FRP strains in the loading direction were higher than the strain in the transverse direction as the fibres resist the development of diagonal cracking. However, the ratio between the strains on the adjacent faces of the column reduces with the increase in the applied lateral load as the expansion of the cross-section further mobilizes the FRP along the entire column perimeter. It is also shown that, as expected, the FRP strains decrease as the amount of FRP layers increase, which in turn leads to a more uniform distribution of strains around the column perimeter. For example, at a drift ratio of 2.5% for the unrestrained column (30 mm frame displacement), the strain in the AFRP along the face parallel to the loading direction reached 1.4% for 1-layer, while strain levels of 1.03%, and 0.82% were recorded for the 2- and 3-layer configurations, respectively.

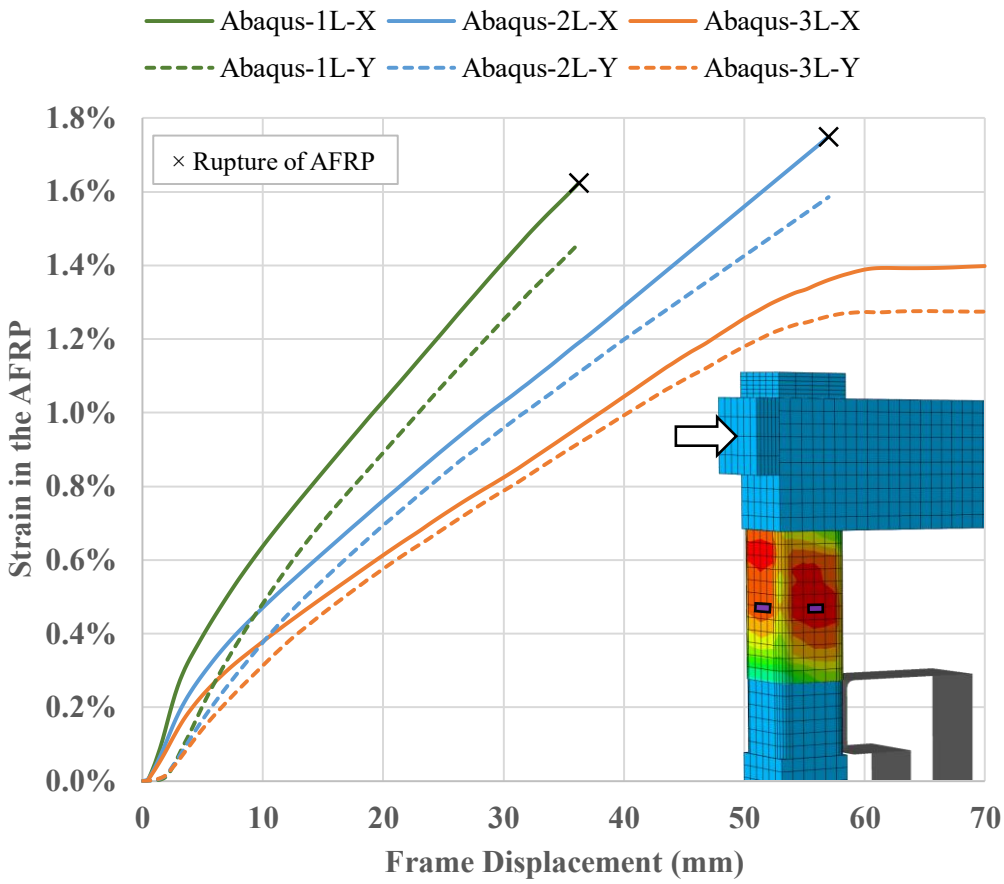

Figure 3.15: Hoop strain profile at the centre of the AFRP confining jacket in the direction parallel and perpendicular to the loading direction

3.5.2 Modelling FRP CRuC short columns using the proposed SCME

The proposed SCME was adopted to model the CRuC short column and examine its effect on the overall behaviour of the frame. The constitutive model developed by Raffoul et al. (Raffoul et al., 2019) was used to define the uniaxial compressive behaviour of CRuC, which implicitly considers the effect of different confinement stiffnesses (i.e., different thickness and type of FRP confinement). The relevant parameters of the constitutive behaviour were used as input in the *Concrete01* material model in OpenSees.

Since the fibres of the confining jacket are horizontal (parallel to the ground and loading direction), and the strut is inclined at an angle of $\alpha = \tan^{-1} h/l$ as per Equation 3.2, then the effectiveness of the confinement to the compressive strut is reduced. To account for the reduced effectiveness of the confinement due to the relative inclination between the confining FRP fibres and the strut, the ultimate strength of the CRuC was reduced according to Equation 3.6.

$$f_{crc}^{e} = (f_{crc} - f_{cr}) \sin^2 \alpha + f_{cr} \tag{3.6}$$

where f_{crc} and f_{cr} are defined by Raffoul et al. (Raffoul et al., 2019) as the compressive strength and critical stress of CRuC, respectively (see Appendix A5, Figure A.10).

Consequently, the effective ultimate strain, ε_{crc}^{e}, was reduced at a ratio that maintains the second linear stiffness of the CRuC stress-strain (Table 3.1). For the vertical elements of the SCME, AD and BC, the material input was used without any reduction. The same boundary conditions and dimensions of the CC SCME were also used for the CRuC SCME.

3.5.2.1 Results and analysis of the CRuC SCME simulations

Figure 3.14 above shows the lateral load versus displacement of the frame with the CRuC SCME obtained from the OpenSees simulations. Although the transition phase is slightly softer in the OpenSees simulations, up to the peak strength of the RuC, the general trend agrees well with the results of the more detailed FEA in Abaqus. The elastic stiffness for all three frames was around 77 kN/mm, whereas the stiffness of the linear hardening phase (phase III) was 4.4, 5.2, and 5.6 kN/mm for the frames with 1, 2, and 3 AFRP layers, respectively. At 16.8

mm lateral frame displacement, the steel at the bottom of the unrestrained column yielded for all three frames, indicating the start of phase IV. Frames CRuC-1L and CRuC-2L failed when the strut reached its maximum strength, corresponding to rupture of the AFRP at a lateral displacement of 37 mm and 52 mm, respectively. Frame CRuC-3L failed as a result of the formation of a plastic hinge mechanism as also obtained from the FEA, at a displacement of 57 mm and lateral load of 295 kN. The ductility of the frames was assessed based on the bilinear idealization of the force-displacement curve according to FEMA 356 (FEMA & ASCE, 2000). The ductility obtained from OpenSees were 18.9, 22.9, and 22.3 for the CRuC-1L, CRuC-2L and CRuC-3L frames, respectively (see Appendix A6 for idealised force-displacement curves). Although the AFRP is not explicitly modelled in the SCME, an estimation of the jacket lateral strain is attainable from the uniaxial compressive strain levels of the strut and the adopted confinement constitutive model (Papastergiou, 2010; Raffoul et al., 2019). Figure 3.16 compares the AFRP strain values for the CRuC-2L frame obtained from Abaqus and the STM model. A good correlation can be seen between the two curves until the rupture strain.

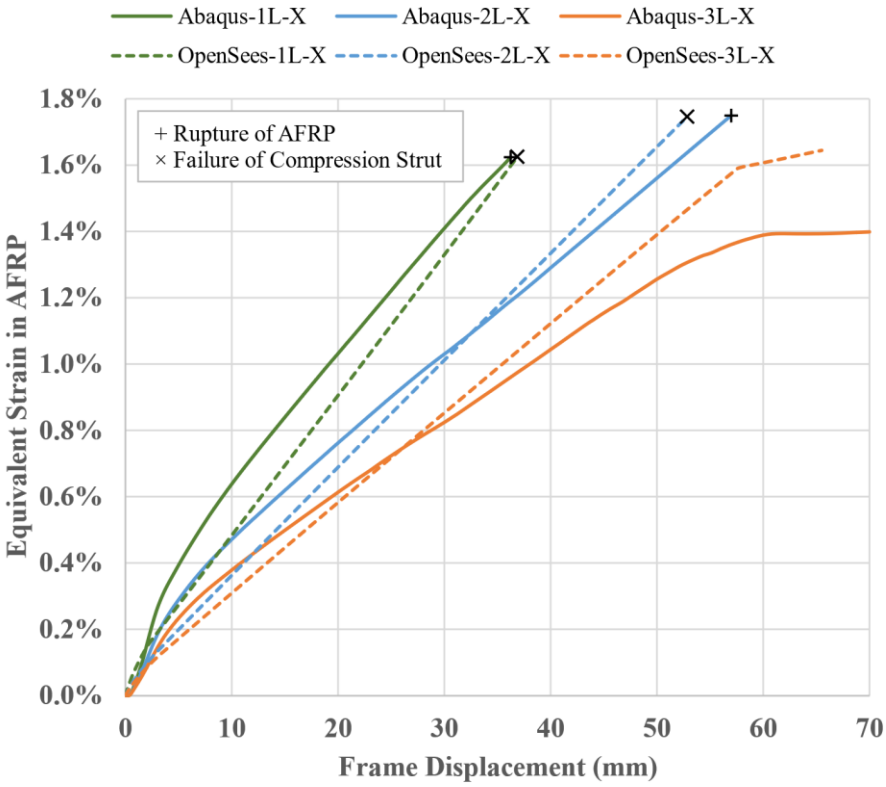

Figure 3.16: Equivalent lateral strain in the AFRP obtained from Abaqus and the SCME model implemented in OpenSees

3.5.3 Comparison between models with CRuC and CC short columns

The results from the numerical simulations prove that high shear demand short columns made of CRuC can develop higher ductility than CC counterparts. This also leads to a better utilization of the resistance of other structural elements in the building model as damage distributes more unfirmly among them, rather than being concentrated in the short columns. While the use of CC in the short column limits the deformability of the frame model and prevents yielding of the longitudinal reinforcement, yielding of the reinforcement in column C1B occurs for all 3 configurations of CRuC. At high confinement levels (CRuC-3L), yielding of the longitudinal reinforcement occurs at the short column restraint level. The higher ductility of the AFRP CRuC frames is mainly due to the unique mechanical properties of CRuC, which enable the short column element to undergo higher shear deformations (Wang et al., 2019). Figure 3.17 shows the shear-flexure displacement decomposition of the CRuC short column for both the detailed numerical analysis and the STM. It is shown that the shear deformation of the short column accounts for 80-90% of the total frame deformations after 0.5 mm global displacement, which is when the frame enters the transition phase and the FRP is activated.

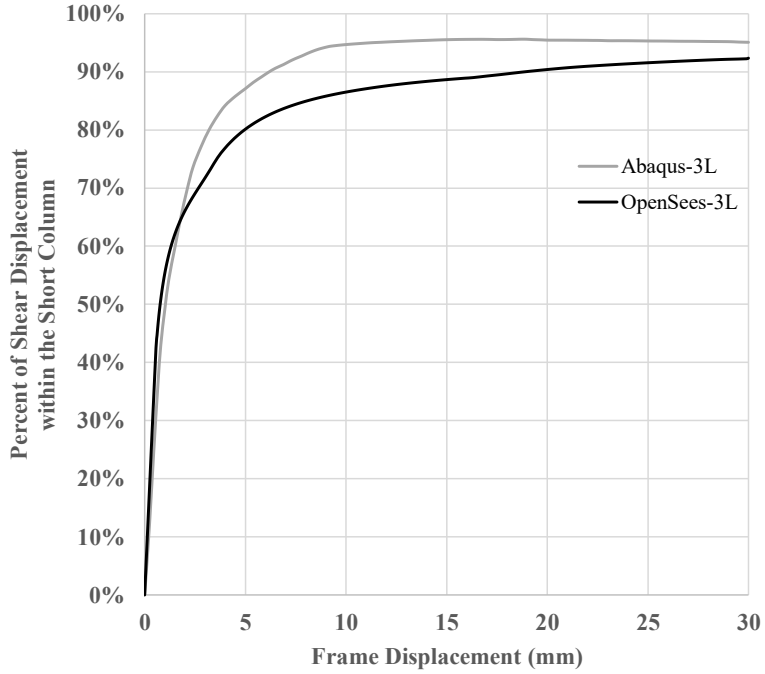

Figure 3.17: Decomposition of the shear-flexural displacement of the short column (CRuC-3L up to 30 mm lateral displacement of the frame)

3.6 CONCLUDING REMARKS

This article presented an experimental and numerical study aimed at examining the behaviour of RC frames with short columns subjected to lateral loading. The experimental observations and the results of a detailed finite element analysis were used to develop a simplified macro element to model the behaviour of short columns and assess the potential of CRuC to develop more deformable structural elements. Based on the results of this study and the discussions presented above, the following conclusions can be drawn:

- The failure of the tested building made of conventional RC was dominated by the brittle shear failure of the short columns. Failure occurred at a small drift of 0.37% (4.55 mm) for the unrestrained column.
- A simplified approach to determine the geometry of a short column macro element based on the strut and tie method was proposed. This was able to capture accurately the shear dominated response of the tested short columns and their effect on the global response of the frame.
- The proposed SCME was extended to account for the use of CRuC in short columns, which significantly improved the performance of the frame. For instance, the use of two layers of AFRP CRuC led to ultimate drift value of 4.23% (52 mm) for the unrestrained column, i.e. more than 11 times that of the CC frame. This also enabled a more efficient use of the other structural elements in the model.

The numerical investigation into confined rubberized concrete confirms the hypothesis that using this material in high shear demand regions of the frame, can lead to a more ductile behaviour when compared to conventional concrete.

A series of large-scale experimental tests have been conducted as part of the larger experimental programme to examine the performance of CRuC elements under seismic load and are reported in the following chapters.

3.7 REFERENCES

Alfarah, B., López-Almansa, F., & Oller, S. (2017). New methodology for calculating damage variables evolution in Plastic Damage Model for RC structures. *Engineering Structures*, *132*, 70–86. https://doi.org/10.1016/j.engstruct.2016.11.022

Bažant, Z. P., & Becq-Giraudon, E. (2002). Statistical prediction of fracture parameters of concrete and implications for choice of testing standard. *Cement and Concrete Research*, *32*(4), 529–556. https://doi.org/10.1016/S0008-8846(01)00723-2

Bompa, D. V., Elghazouli, A. Y., Xu, B., Stafford, P. J., & Ruiz-Teran, A. M. (2017). Experimental assessment and constitutive modelling of rubberised concrete materials. *Construction and Building Materials*, *137*, 246–260. https://doi.org/10.1016/j.conbuildmat.2017.01.086

Chang G. A., & Mander, J. B. (1994). Seismic energy based fatigue damage analysis of bridge columns: Part I - Evaluation of seismic capacity. Technical Report NCEER-94-0006. In *State University of New York. Buffalo, New York*.

Chiou, Y. J., Tzeng, J. C., & Liou, Y. W. (1999). Experimental and analytical study of masonry infilled frames. *Journal of Structural Engineering*, *125*(10), 1109–1117. https://doi.org/10.1061/(ASCE)0733-9445(1999)125:10(1109)

Dassault Systèmes SIMULIA. (2017). *ABAQUS Software and Documentation* (Ver 6.14).

Duarte, A. P. C., Silva, B. A., Silvestre, N., De Brito, J., & Júlio, E. (2015). Mechanical characterization of rubberized concrete using an image-processing/XFEM coupled procedure. *Composites Part B: Engineering*, *78*, 214–226. https://doi.org/10.1016/j.compositesb.2015.03.082

EN 10080. (2009). *Steel for the reinforcement of concrete: Weldable reinforcing steel, General*. Comité Européen de Normalisation (CEN).

EN 12390-3. (2019). *Testing hardened concrete Part 3: Compressive strength of test specimens*. Comité Européen de Normalisation (CEN).

EN 1992-1-1. (2004). *Eurocode 2: Design of concrete structures - Part 1-1: General rules and*

rules for buildings. Comité Européen de Normalisation (CEN).

FEMA, & ASCE. (2000). Prestandard and Commentary on the Seismic Rehabilitation of Buildings. *Federal Emergency Management Agency, Report No. 356*.

Hordijk, D. A. (1992). Tensile and tensile fatigue behaviour of concrete; experiments, modelling and analyses. In *Heron* (Vol. 37, Issue 1).

Krätzig, W. B., & Pölling, R. (2004). An elasto-plastic damage model for reinforced concrete with minimum number of material parameters. *Computers and Structures*, *82*(15–16), 1201–1215. https://doi.org/10.1016/j.compstruc.2004.03.002

Mander, J. B., Priestley, M. J. N., & Park, R. (1988). Theoretical stress-strain model for confined concrete. *J. Struct. Eng*, *114*(8), 1804–1826.

Massone, L. M., & Wallace, J. W. (2004). Load-Deformation Responses of Slender Reinforced Concrete Walls. *ACI Structural Journal*, *101*(1), 103–113. https://doi.org/10.14359/13003

Mazzoni, S., McKenne, F., Scott, M. H., & Fenves, G. L. (2009). *Open System for Earthquake Engineering Simulation User Manual, Version 2.0*. Pacific Earthquake Engineering Center, University of California. http://opensees.berkeley.edu

Nana, W. S. A., Bui, T. T., Limam, A., & Abouri, S. (2017). Experimental and Numerical Modelling of Shear Behaviour of Full-scale RC Slabs Under Concentrated Loads. *Structures*, *10*, 96–116. https://doi.org/10.1016/j.istruc.2017.02.004

Palmquist, S. M., & Jansen, D. C. (2001). Postpeak strain-stress relationship for concrete in compression. *ACI Materials Journal*, *98*(3), 213–219. https://doi.org/10.14359/10275

Papastergiou, P. (2010). *A confinement model for concrete wrapped or pretensioned with FRP*. University of Sheffield.

Raffoul, S., Escolano-Margarit, D., Garcia, R., Guadagnini, M., & Pilakoutas, K. (2019). Constitutive Model for Rubberized Concrete Passively Confined with FRP Laminates.

Journal of Composites for Construction, *23*(6), 04019044. https://doi.org/10.1061/(asce)cc.1943-5614.0000972

Raffoul, S., Garcia, R., Escolano-Margarit, D., Guadagnini, M., Hajirasouliha, I., & Pilakoutas, K. (2017). Behaviour of unconfined and FRP-confined rubberised concrete in axial compression. *Construction and Building Materials*, *147*, 388–397. https://doi.org/10.1016/j.conbuildmat.2017.04.175

Raffoul, S., Garcia, R., Pilakoutas, K., Guadagnini, M., & Medina, N. F. (2016). Optimisation of rubberised concrete with high rubber content: An experimental investigation. *Construction and Building Materials*, *124*, 391–404. https://doi.org/10.1016/j.conbuildmat.2016.07.054

Tsai, W. T. (1988). Uniaxial Compressional Stress-Strain Relation of Concrete. *Journal of Structural Engineering*, *114*(9), 2133–2136. https://doi.org/10.1061/(asce)0733-9445(1988)114:9(2133)

Tung, N. D., & Tue, N. V. (2015). Post-peak behavior of concrete specimens undergoing deformation localization in uniaxial compression. *Construction and Building Materials*, *99*, 109–117. https://doi.org/10.1016/j.conbuildmat.2015.09.013

Wang, Z., Chen, L., Guadagnini, M., & Pilakoutas, K. (2019). Shear Behavior Model for FRP-Confined and Unconfined Rubberized Concrete. *Journal of Composites for Construction*, *23*(5), 04019039. https://doi.org/10.1061/(asce)cc.1943-5614.0000962

Watanabe, K., Niwa, J., Yokota, H., & Iwanami, M. (2004). Experimental study on stress-strain curve of concrete considering localized failure in compression. *Journal of Advanced Concrete Technology*, *2*(3), 395–407. https://doi.org/10.3151/jact.2.395

Youssf, O., Elgawady, M. A., Mills, J. E., & Ma, X. (2014). An experimental investigation of crumb rubber concrete confined by fibre reinforced polymer tubes. *Construction and Building Materials*, *53*, 522–532. https://doi.org/10.1016/j.conbuildmat.2013.12.007

Chapter 4

Shake-table tests on frames with short columns made with conventional concrete and FRP-confined rubberised concrete

Keywords: Short columns; Reinforced concrete; Shear failure; Confined Rubberised concrete; Seismic performance; FRP; shake-table.

4.1 INTRODUCTION

Although Pseudo-dynamic and quasi-static tests give a good assessment of the lateral capacity and performance of a structure, they cannot capture the effect of loading rate induced during a real earthquake on the overall structural behaviour and local/global damage accumulation. On the other hand, shake-table tests can simulate seismic excitations more realistically, within the limitations of the shake-table (see Appendix B2 for properties of the shake-table). This chapter discusses the shake-table tests that were performed on two RC frames similar to that described in chapter 3 to investigate experimentally the performance of CRuC short columns.

4.2 DESIGN, MANUFACTURE, AND SEISMIC TESTING OF THE BUILDINGS

The building geometry for the shake-table tests was adopted from the 1/2-scale 1-bay 1-storey structure tested under lateral cyclic loading (CC-STC) as described in Chapter 3. However, to avoid issues that rose during assembling the steel cage and casting of the CC-STC building caused by the large amount of reinforcement in the beam-column joints, the sections were redesigned to reduce the amount of reinforcement, while maintaining a relatively high flexural capacity of the columns compared to their shear capacity. The columns of the conventional concrete building tested on the shake-table (CC-EQ) had a flexural reinforcement of four 14 mm diameter longitudinal bars, and the beams in the X-direction were reinforced with four 12 mm diameter longitudinal bars (Figure 4.1). This new reinforcement layout provides an ultimate moment capacity of 17.3 kNm and 34 kNm for the column and beam, respectively. The shear reinforcement of all structural elements was the same as for the CC-STC building, also, the slab and beams in the Y-direction were not altered (Figure 3.1 in Chapter 3).

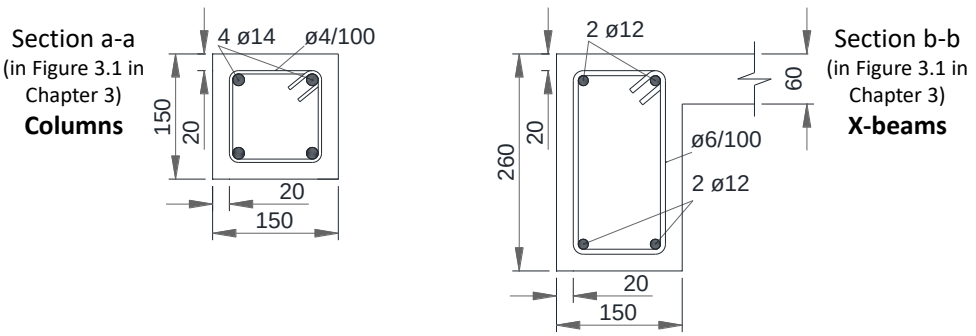

Figure 4.1: Cross-section dimensions and reinforcement layout of columns and beams in x-direction

The building with Confined Rubberized Concrete short columns tested on the shake-table (CRuC-EQ) had the same reinforcement layout as CC-EQ. The frame was cast in three stages (Figure 4.2-a): 1) CC concrete was cast into the foundation footing and up to a clear height of 800 mm; 2) RuC was cast on top of the 800 mm level to reach the bottom level of the beams at a height of 1100 mm, forming the short columns (300 mm high). 3) CC concrete was used for all beams and the slab. All stages were cast within less than 30 minutes from each other to avoid the formation of cold joints and the CC mix was kept rotating in the mixer during the RuC casting. After 28 days of curing, the top 300 mm of the clear height of the columns, which will form the short column during the test, was confined with three layers of AFRP, with the final overlap of the sheet laid on the column side transverse to the shaking direction. The 150 mm section of the column below the short column was also confined with two layers of AFRP to protect it from the impact with the stiff steel frame boundary condition, as well as prevent any failure at the construction joint. Finally, the beam column joints were strengthened with one layer of L-shaped CFRP to prevent excessive damage at the beam/joint interface and concentrate the damage in the short columns (see Appendix B1 for steps of application of FRP).

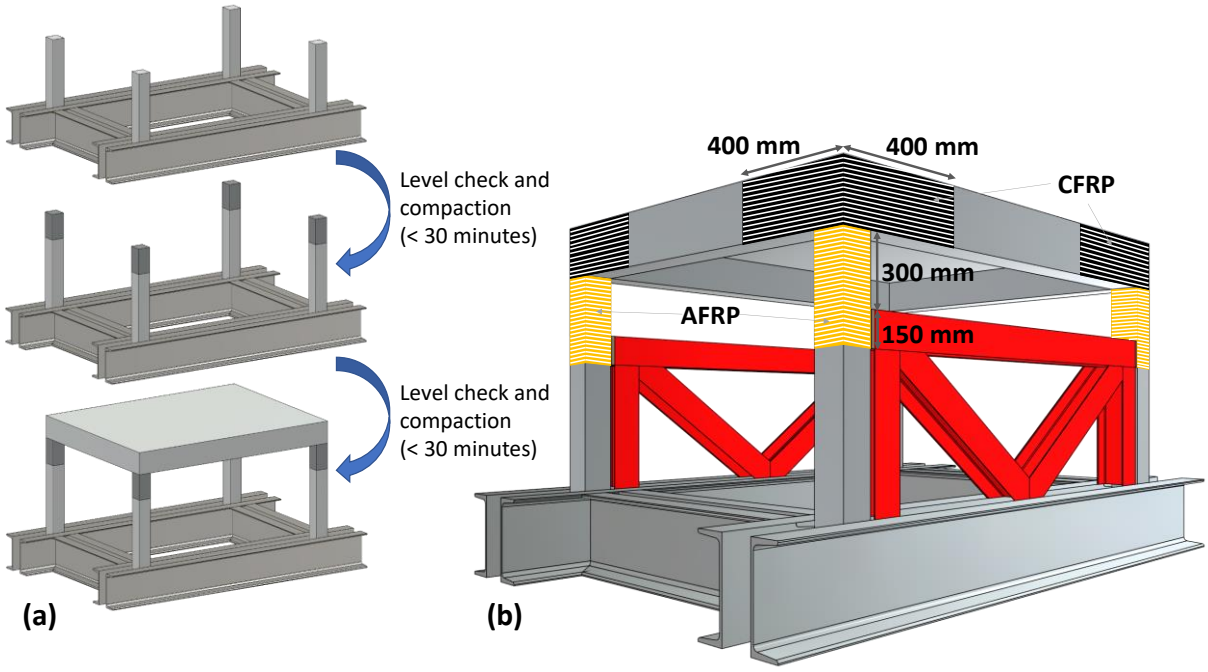

Figure 4.2: (a) Casting phases of the CRuC-EQ building, and (b) FRP layout

4.2.1 Material properties

The concrete mix was done in the laboratory and both CC-EQ and CRuC-EQ buildings were cast off the shake-table then moved onto the shake-table after 28 days of curing. The RuC mix used in the short columns was prepared using the original mix of CC with 5% less water content, and replacing 60% by volume of both the sand and coarse aggregates with rubber particles. Table 4.1 shows the mix design properties of the CC and RuC.

Table 4.1: Mix design properties of the CC and RuC

Mix designation	Cement CEM I-42.5R (kg/m^3)	Water (kg/m^3)	Sand 0-4 mm (kg/m^3)	Coarse Aggregates 4-8 mm (kg/m^3)	Coarse Aggregates 8-16 mm (kg/m^3)	Rubber particles 0-5 mm (kg/m^3)	Rubber particles 5-15 mm (kg/m^3)
CC	489	250	582	388	647	-	-
RuC	489	230	233	155	259	103	187

The compressive mechanical properties of the concrete were determined by testing twelve CC and nine RuC standard 150×300 mm cylinders in uniaxial compression according to EN 12390. Out of the twelve CC cylinders, six were from the CC-EQ casting, and six were from the CRuC-EQ casting. The same steel bars and stirrups used in the CC-STC building were used to reinforce both buildings tested on the shake-table. S&P A120/290 AFRP sheets were used to confine the columns, and MapeWrap C Uni-Ax CFRP sheets were used to confine the beam-column joints. Table 4.2 and 4.3 show the properties of the concrete and the aramid and carbon fibre sheets, respectively.

Table 4.2: Mechanical properties of the CC and RuC

Building ID	Concrete type	f_{cm} (MPa)	ε_c (mm/m)	E_c (GPa)	f_{ct}* (MPa)
CC-EQ	CC	38	2.06	30	3.39
CRuC-EQ	CC	39	2.06	31	3.45
	CC$^+$	44	2.12	31.5	3.74
	RuC	5.8	1.19	9.2	0.84

* Concrete tensile strength calculated based on EC2 for CC, and Bompa et al.'s model for RuC (Bompa et al., 2017)
$^+$ Conventional concrete base mix that was used for the rubberised concrete.

Table 4.3: Properties of the dry Aramid and Carbon fibre confining sheets according to the manufacturer

Sheet ID	Fibre type	t (mm)	E_f (GPa)	f_u (MPa)	ε_{fu} (%)
S&P A120/290	Aramid	0.2	116	2400	2.5
MapeWrap C Uni-Ax	Carbon	0.16	252	4900	2

4.2.2 Test Setup

The buildings were lifted by the steel foundation and bolted on the ANCO R3123 tri-axial shake-table platform (see Appendix B2 for table characteristics). The same stiff-steel frames used in CC-STC to force the short column boundary condition were used in both CC-EQ and CRuC-EQ. The stiff-steel frames were fabricated with a length of 2180 mm, which is 70 mm shorter than the clear distance between the columns in the longitudinal X-direction. The gap at each end, between the column and stiff frame, was filled with precisely cut high density wood pieces each with a width of 35 mm. A total gravity load of 40 kN was applied via 15 600×400×100 mm lead blocks that were spread evenly and bolted onto the slab (Figure 4.3).

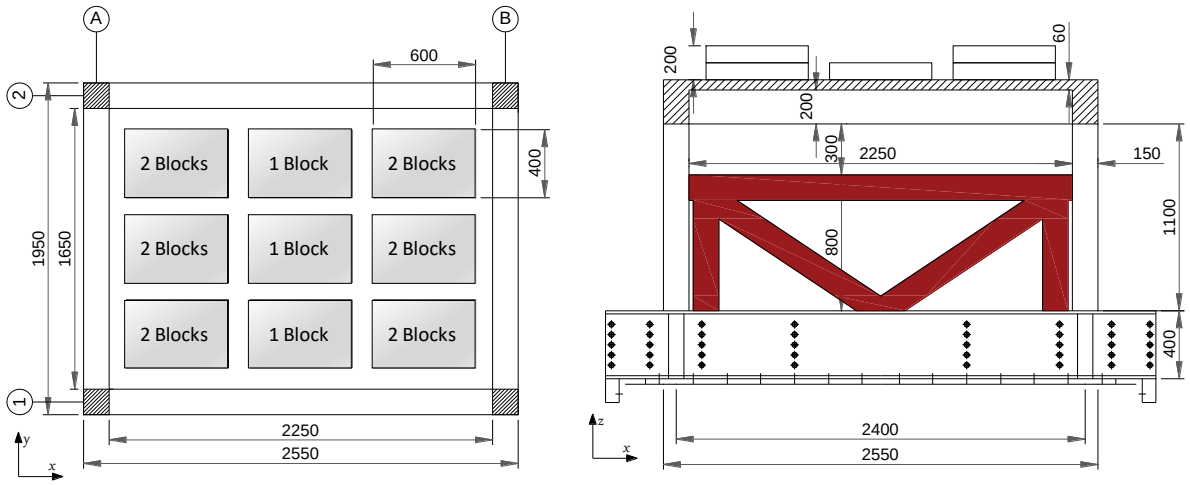

Figure 4.3: Positioning of the lead blocks on top of the slab

The high density of lead relative to the concrete blocks used in the CC-STC building reduced the volume/height of the blocks added on top of the slab, which allowed for the centre of mass to be closer to the slab, hence reducing the over-turning moment on the shake-table. Non-structural wooden beams were fixed to the top of the stiff-steel frame in the CRuC-EQ building

to support the concrete beams and slab in case the structure collapses. Figure 4.4 and 4.5 show the CC-EQ and CRuC-EQ buildings, respectively, mounted on the shake-table prior to seismic testing.

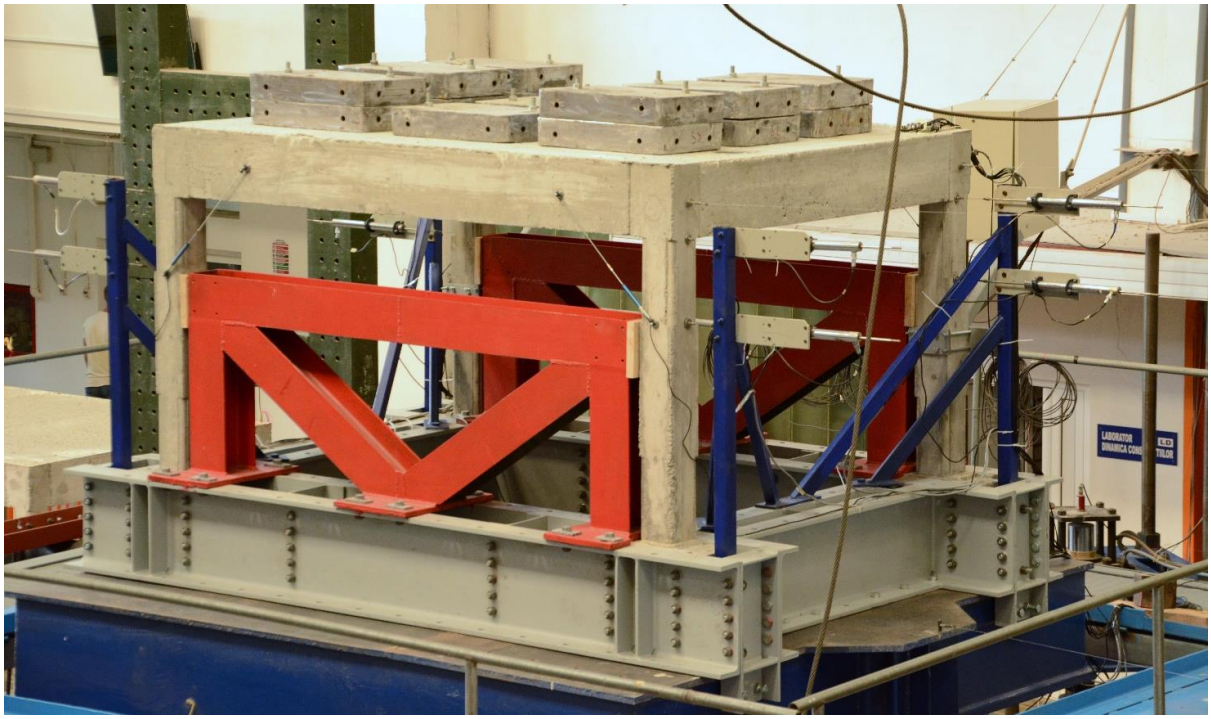

Figure 4.4: CC-EQ building bolted on the shake-table before testing

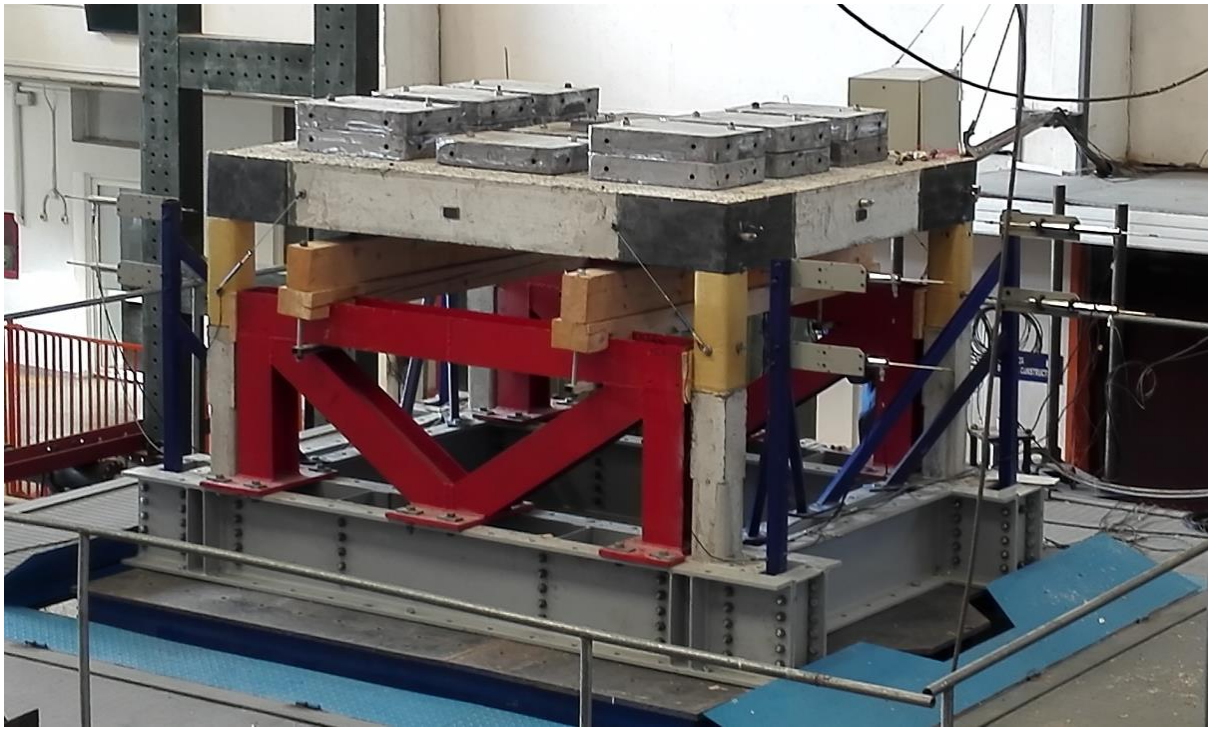

Figure 4.5: CRuC-EQ building on the shake-table before testing

4.2.3 Instrumentation

The CC-EQ building was instrumented with four piezoelectric accelerometers that recorded accelerations in the X and Y direction at the level of the beams. Another three accelerometers were connected to the shake-table to record ground accelerations in the X-Y-Z axis. Eight displacement transducers (Ln1-8) fixed on the building foundation, recorded the relative displacement in the X direction of the top of each column and at the level of the short column restraint. Four inclined LVDTs (Incl1-4) were used to measure the beam-column joint opening in the X direction. Three wire displacement transducers, connected to a fixed outside frame, measured the absolute displacement of the shake table (xA-T) and the top of both sides of the frame (xA-1,2). Figure 4.6 shows the external instrumentation used for the CC-EQ building.

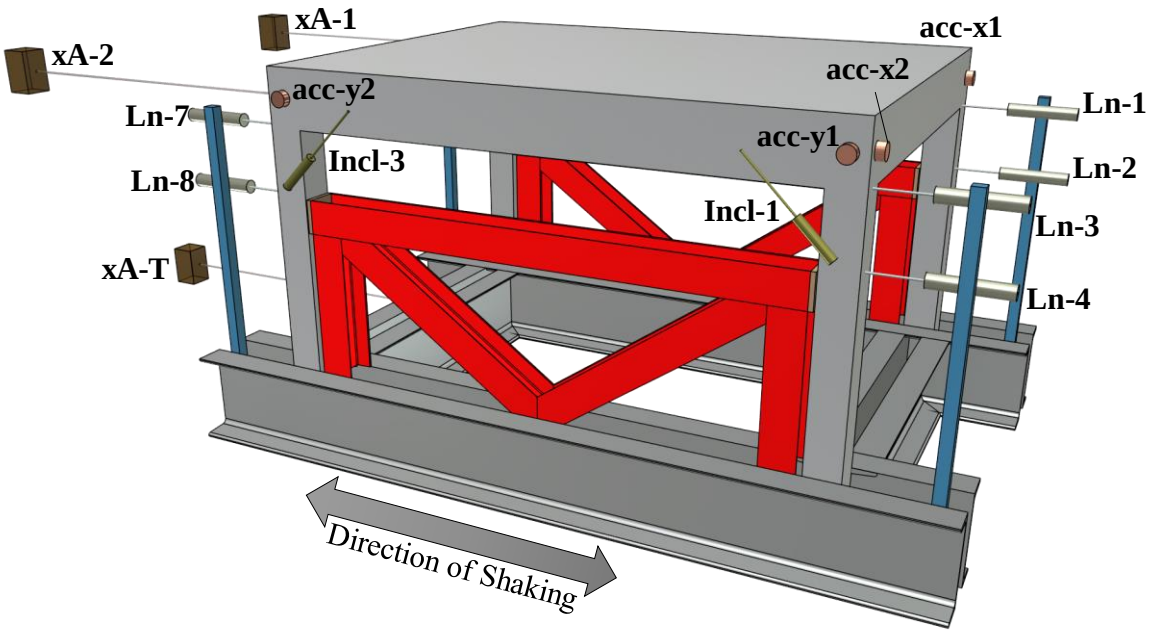

Figure 4.6: External instrumentation of the CC-EQ building

Sixteen strain gauges were fixed on the reinforcement: two on the outside longitudinal reinforcement of the short column and two on the inside ones, one on each of the three stirrups in the short column span, and one on the bottom longitudinal bar of the beam 50 mm away from the column. The same strain gauge distribution was replicated on the opposite column in the X direction (Figure 4.7).

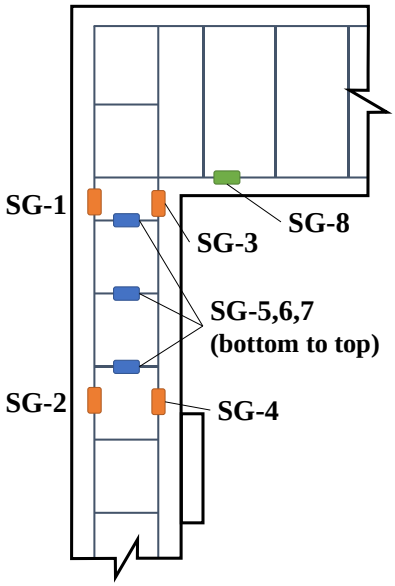

Figure 4.7: Strain gauge location on the steel reinforcement

The CRuC-EQ building had the same instrumentation as CC-EQ, with the addition of one accelerometer to record the roof X-accelerations, and two wire transducers (xA-3 and xA-4) to track the movement of the column at the level of the short column restraint (Figure 4.8).

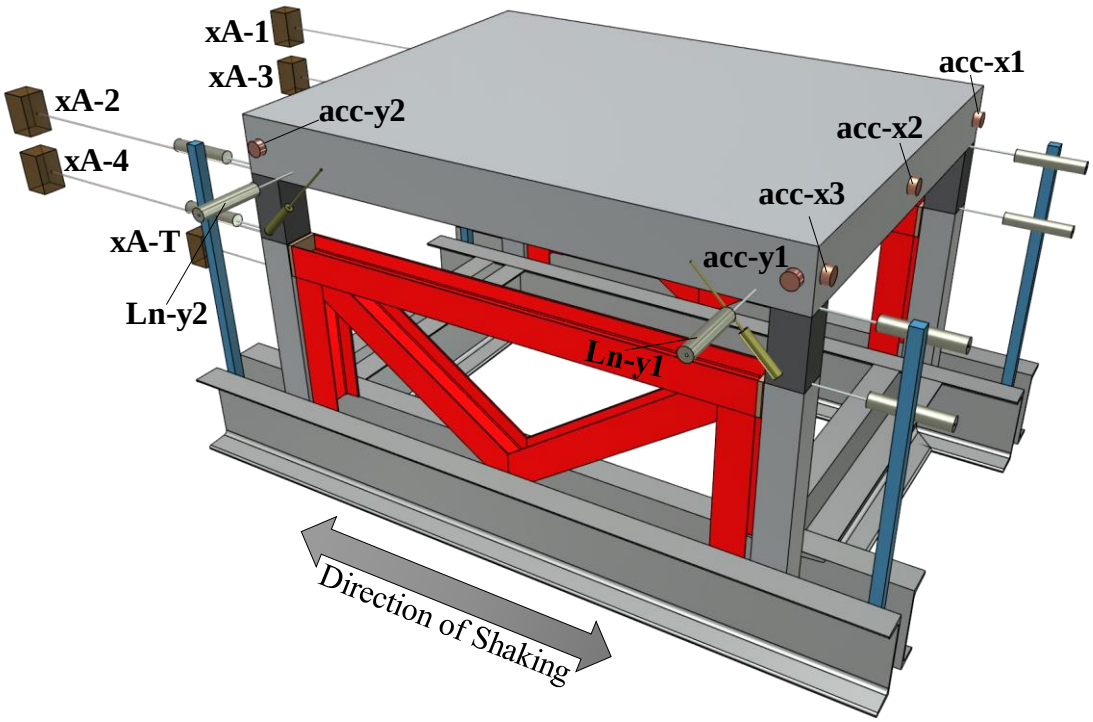

Figure 4.8: External instrumentation of the CRuC-EQ building

The strain on the AFRP was monitored by three strain gauges on each short column wrap, two along and one transverse to the direction of the shaking and positioned 50 mm down from the bottom of the beam. No gauges were placed on the side of the column with AFRP overlap (Figure 4.9). The sampling frequency for data acquisition for the CC-EQ test was set to 200 Hz, however, it was increased to 500 Hz in the CRuC-EQ test.

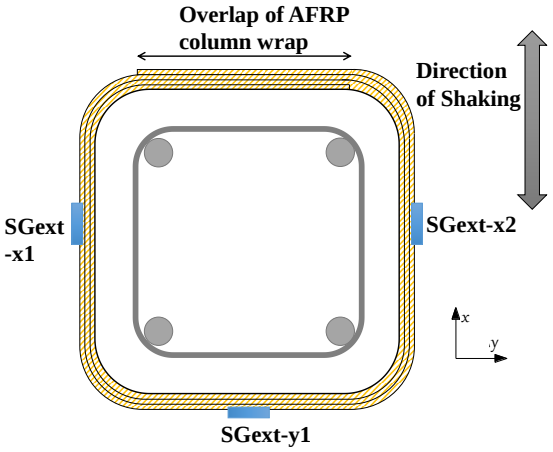

Figure 4.9: Strain-gauge layout on the AFRP jacket of the short column

4.2.4 Seismic record and test sequence

The shake table input for both buildings, consisted of a unidirectional horizontal record with increased level of Peak Ground Accelerations (PGAs). The record was an artificial earthquake based on the Eurocode 8 (EC8) soil type C spectrum (Figure 4.10-right). Figure 4.10 shows the spectral acceleration (Sa) matching of the input record response spectrum to that of the EC8.

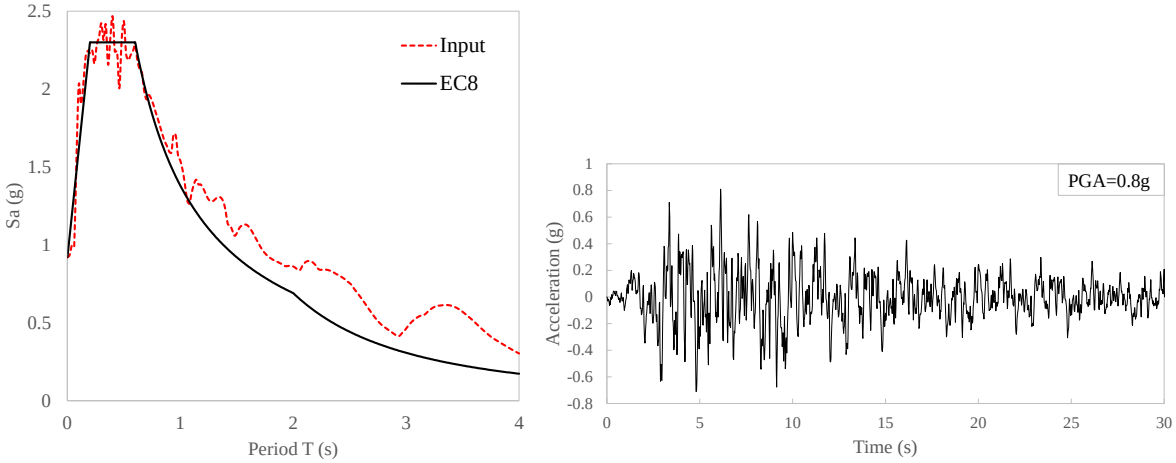

Figure 4.10: Left: Elastic response spectrum, and earthquake spectrum; Right: Time history acceleration of the artificial earthquake

The time history acceleration was compressed in time to respect similitude requirements with the scaled down geometry. Based on similitude, the scale factor for time is a function of the geometry factor λ_L, and acceleration factor λ_a (Eq. 4.1).

$$\lambda_t = \sqrt{\lambda_L / \lambda_a} = \sqrt{1/2 / 1} = 0.707 \tag{4.1}$$

The reference peak ground acceleration ($a_{g,R}$) was taken from the seismic intensity area map of Iasi, Romania, and was equal to 0.2g at a reference return period (T_{NCR}) of 100 years (Figure 4.11) (Solomos et al., 2008).

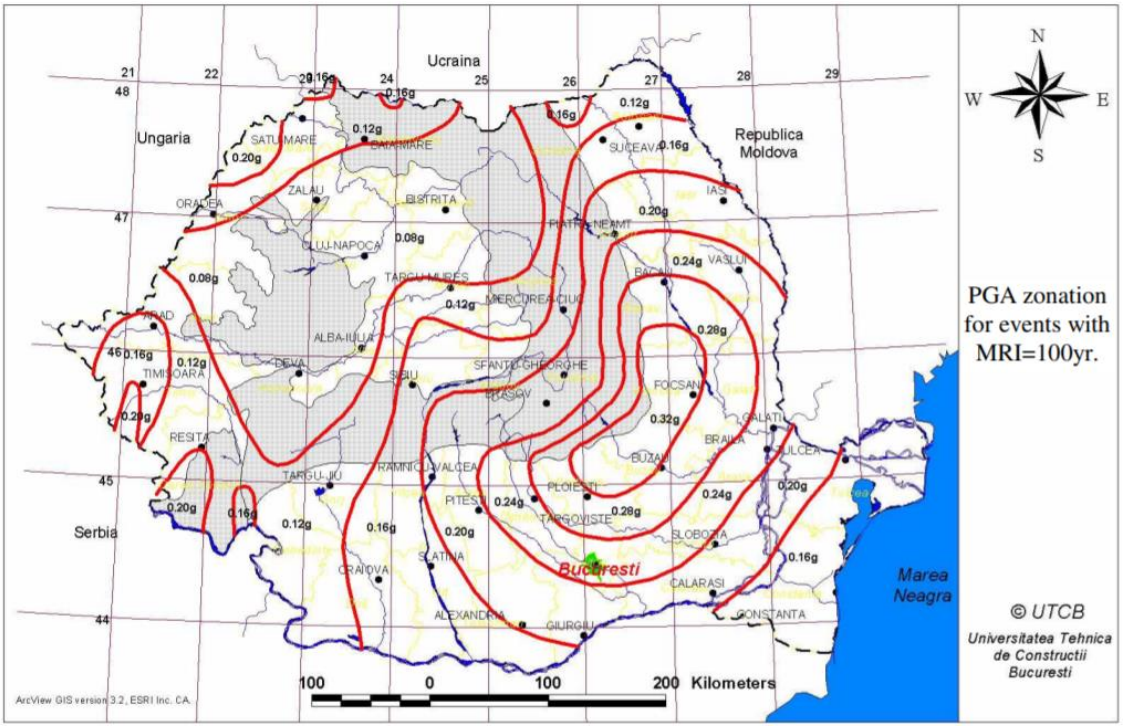

Figure 4.11: Seismic zonation map of Romania (PGA given correspond to reference return period of 100 years

The acceleration input was scaled in amplitude to apply 70%, 100%, 140%, 200%, and 400% of the reference PGA, which can be associated with a return period (T_R) of 50, 100, 200, 400, and 1600 years, based on EC8-Part 2. The corresponding applied PGAs are 0.14g, 0.2g, 0.28g, 0.4g, and 0.8g. A final PGA input of 1.6g was applied, which should ensure collapse through failure of the short columns.

A white-noise input, with a frequency range of 0.5-40 Hz, a duration of 30 seconds (s) and amplitude of 0.025g, was applied to the table before and after every shaking test, to help with the identification of the natural frequencies of the building.

The natural frequencies of the undamaged CC-EQ model were determined by fixing a vibration generator on the roof of the building, oriented along the X and Y axis, as well as at 45° angle (Figure 4.12).

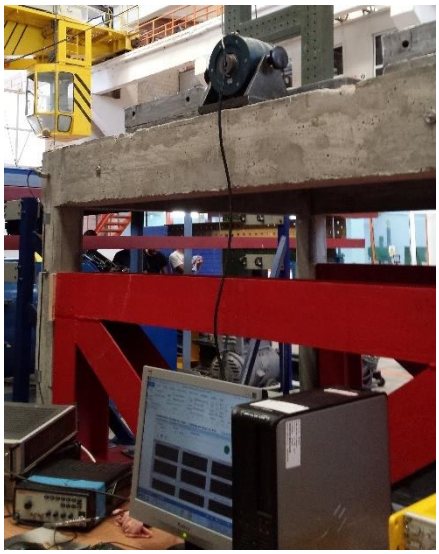

Figure 4.12: Vibration generator fixated on top of the building to determine natural frequencies

The excitation signal was applied with variable frequency, ranging from 0.1 to 50 Hz, and the response of the model was recorded through the four accelerometers attached to the beams. The natural frequencies were 25 Hz in the direction of shaking, 14.2 Hz in the unrestrained transverse direction, and 33.5 Hz for the torsional twisting. A more accurate natural frequency of 22.2 Hz in the X-direction was later obtained from a white-noise test before the first PGA excitation of 0.14g. The natural frequency of the undamaged CRuC-EQ model along the shaking direction (X-direction) was determined from the white-noise test and was found to be 17 Hz.

4.2.5 Time-history performance of the CC-EQ building

Table 4.4 summarises the seismic performance of the CC-EQ building in terms of natural frequency, period, equivalent stiffness, maximum roof displacement and acceleration, and strain measurement at key locations. The equivalent stiffness was obtained from the natural frequency of the structure with an estimated total mass of 5400 kg.

Table 4.4: Seismic performance parameters of the CC-EQ building

Test ID / PGA level	f (Hz)	T (s)	K_{equiv} ($^{kN}/_{mm}$)	Max roof displacement (mm)	Max roof acceleration (g)	Max SG-1 (με)	Max SG-3 (με)	Max SG-7 (με)	Max SG-8 (με)
Undamaged	22.8	0.044	111	-	-	-	-	-	-
0.14g	22.3	0.045	106	0.11	0.167	65	74	18	103
0.2g	21.1	0.047	95	0.28	0.35	193	170	65	299
0.28g	19.3	0.052	80	0.52	0.497	301	238	101	501
0.4g	17.3	0.058	64	1.08	0.718	427	346	214	677
0.8g	14.1	0.071	42	3.35	1.52	1109	1117	3500	1470
1.6g*	9.7+	0.108	22	8.11	4.564	-	-	-	-

* Collapse of the CC-EQ building
+ Average frequency value from windowed FFT throughout the response signal

The CC-EQ building had a natural frequency of 22.8 Hz (T=0.044 s), or an equivalent stiffness of 111 kN/mm, which is comparable to the CC-STC building initial stiffness of 107 kN/mm. The period of the structure was located in the first ascending branch of the design acceleration spectrum. The response acceleration, recorded at the top of the building, increased with progression of the tests due to the period lengthening caused by damage to the structural elements.

The first two PGA levels applied of 0.14g and 0.2g imposed a roof displacement of 0.11 and 0.28 mm, respectively, which were still within the elastic displacement range of the building, hence a negligible reduction in stiffness was measured. Few hairline flexural cracks appeared after the 0.28g excitation, which imposed a maximum roof displacement of 0.52 mm. At that PGA level, the maximum strain was recorded in the bottom longitudinal bar of the beam (SG-8) and was equal to 501 με. The relatively higher strain was mostly due to slight unintentional yawing motion of the shake-table which applied vertical acceleration on the building causing

further bending in the beams. Further stiffness reduction occurred after the 0.4g PGA test, with new flexural hairline cracks appearing in the columns and the beams along the X-direction. During the 0.8g test, a roof displacement of 3.35 mm and acceleration of 1.52g was recorded, and yielding of the reinforcement occurred in the top stirrup of the C1A-X short column, SG-7 (Figure 4.13). Although some noise was present in the results, the high frequency content observed in the time-history is due to the relatively high stiffness of the structure.

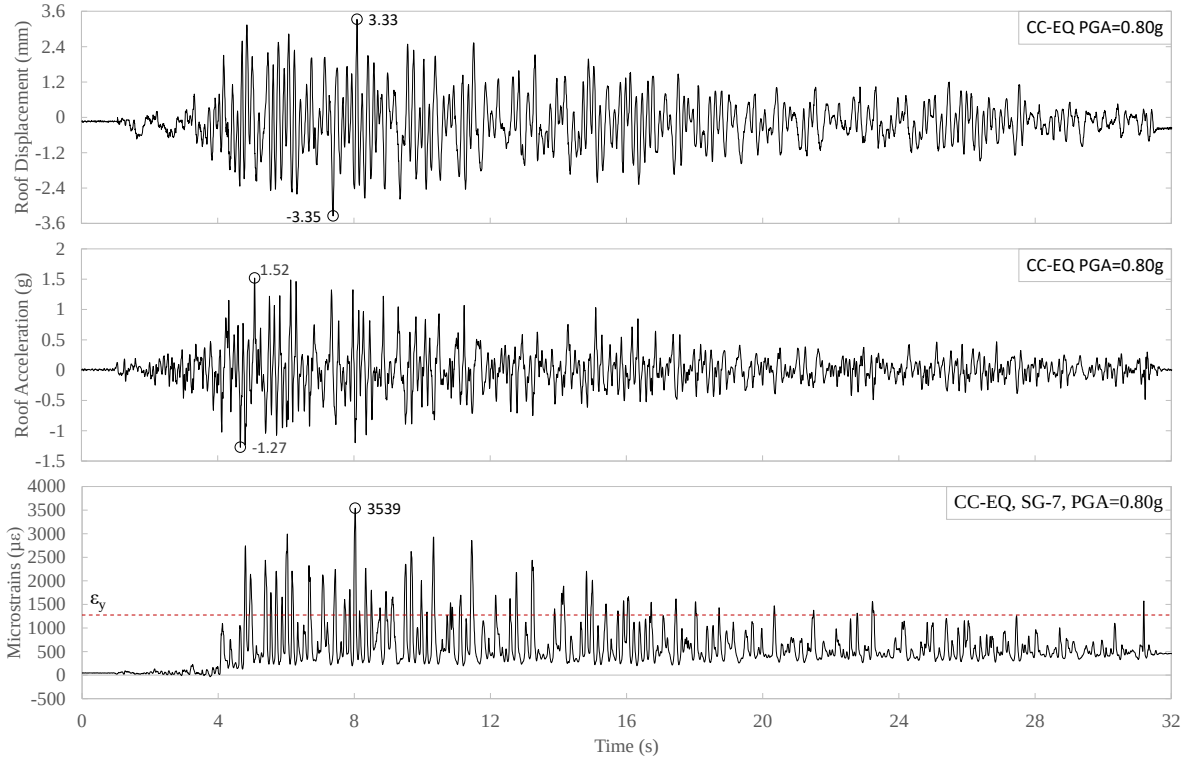

Figure 4.13: Roof displacement(top) and acceleration(bottom) for the CC-EQ building (PGA=0.80g)

A discontinuous hairline shear crack was observed along the middle of joint J1A-X crossing to the centre and inner side of the C1A-X short column, as well as a visible joint opening crack crossing to the top of the short column at the same location (Crack-J in Figure 4.14). The maximum strain in the middle and lower stirrups of the short column was less than 200 με, and the column longitudinal reinforcement had a strain of around 1109 με, while SG-8 recorded 1470 με. The equivalent stiffness of the building after the 0.8g test was 47 kN/mm.

The CC-EQ building collapsed during the 1.6g PGA test after shear failure occurred in the short columns following extensive cracking. Video footage from the cameras mounted on the

short columns showed that the shear crack in C1A that developed in the 0.8g test widened 5 seconds into the 1.6g test (Crack-A in Figure 4.14). At this stage, the top and middle stirrups had yielded, as well as the external longitudinal bar of the column at the level of the short column restraint, SG-2 (Figure 4.15).

Figure 4.14: Shear crack (crack-A) developing in column C1A during 1.6g test for the CC-EQ building

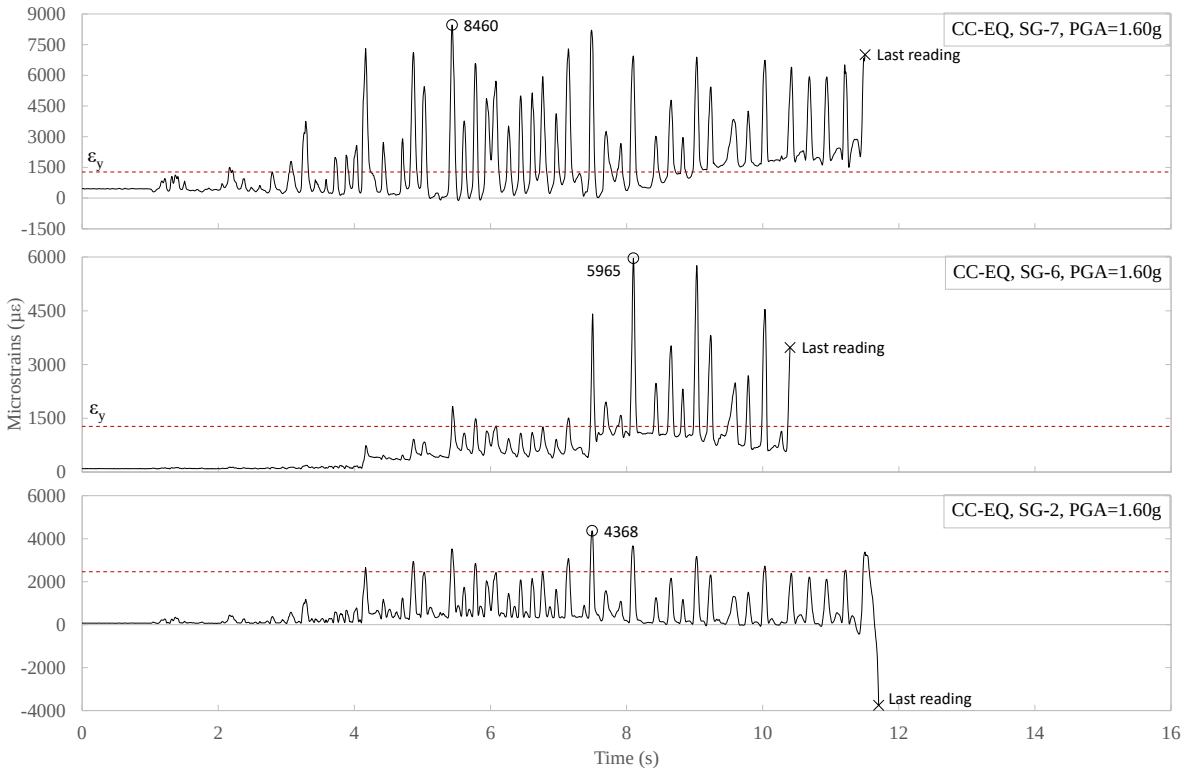

Figure 4.15: Shear stirrup strain reading (SG-7 and SG-6), and longitudinal bar strain SG-2 (CC-EQ, PGA=1.60g)

At 8.8 s, the short columns at C1B and C2B exhibited an S-shaped shear crack spanning from the middle of the beam-column joint (J1B & J2B) to the top of the short column restraint (Crack-C in Figure 4.16-C1B, and Figure 4.17 for C2B). At the same time, a smaller shear crack formed into the middle of J1B and crossed to the top of the short column (Crack-D, Figure 4.16-C1B). An S-shaped shear crack, spanning the 300 mm short column and causing yielding of the bottom stirrup of the short column, appeared 9 s into test (Crack-B, Figure 4.16-C1A). At that same time, the first crack coming from the joint into the column at C1A opened and spalling of concrete was observed (Crack-A, Figure 4.16-C1A). Collapse of the short column C1A occurred at 10.3 s into the test.

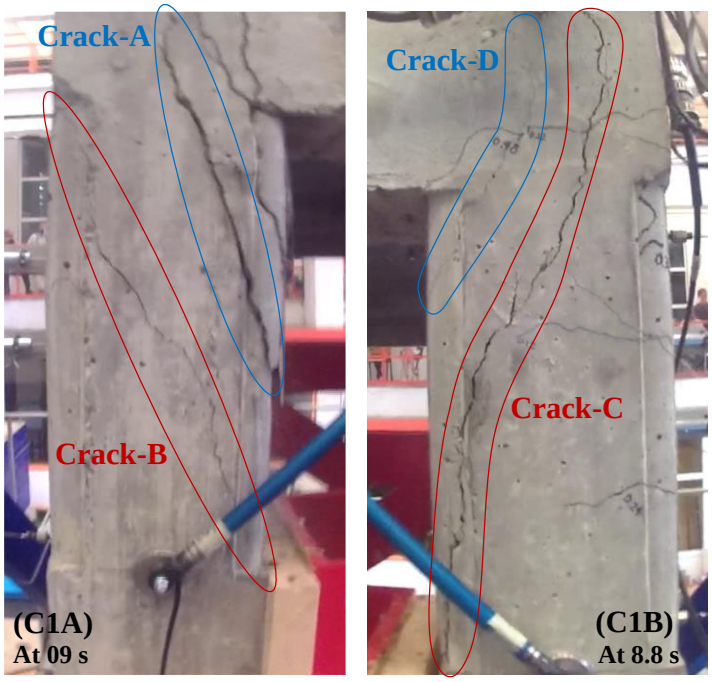

Figure 4.16: Crack development in the short columns C1A and C1B during the 1.60g PGA test (CC-EQ building)

Short column C1B and C2B collapsed at 11 s into the test (Figure 4.18). The test was halted at 15 s to avoid any damage to the shake-table or nearby equipment. The maximum displacement recorded prior to collapse, was 8.3 mm, which includes the shear crack widening at the short columns. The natural frequency was obtained using Fast Fourier Transform (FFT) of the full response before failure, as well as windowed FFT at different time segments to note the

frequency degradation leading up to failure. The range of frequencies was between 12.1 and 7.4 Hz (T=0.082-0.135 s, K=31-12 kN/mm).

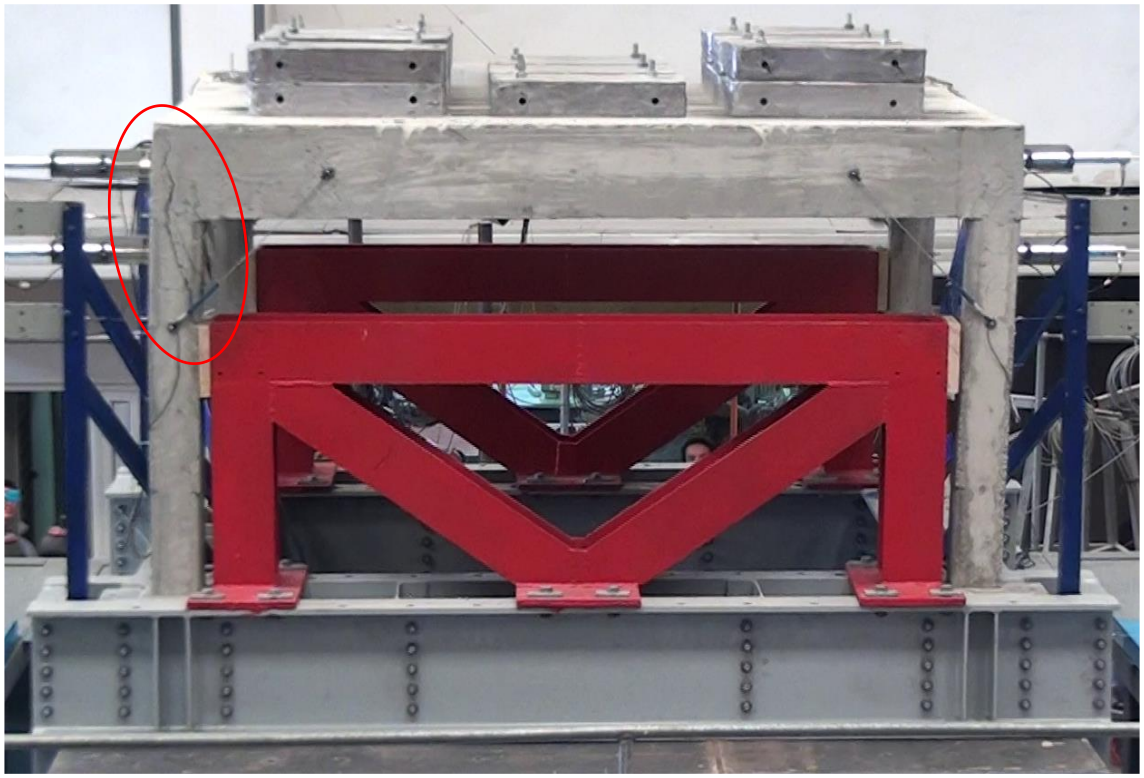

Figure 4. 17: Shear crack development in column C2B during the 1.60g PGA test (CC-EQ building) (Opposite view to the mounted cameras on the short columns)

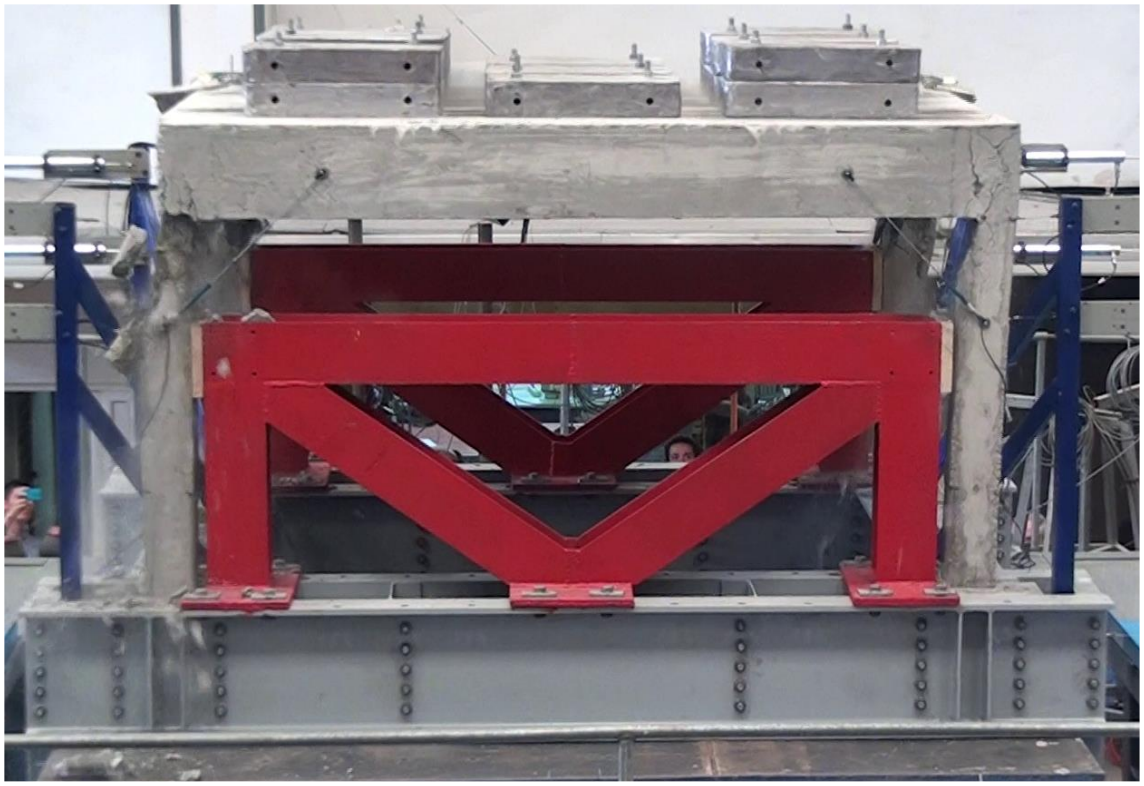

Figure 4. 18: Collapse of the CC-EQ building during the 1.60g PGA excitation

4.2.6 Time history performance of the CRuC-EQ building

Table 4.5 summarises the seismic performance of the CRuC-EQ building, with the same parameters as described for the CC-EQ building, in addition to strain measurements of the AFRP confinement along the X-direction and Y-direction. The maximum roof displacement of the CC-EQ building are also shown between parenthesis for comparison.

Table 4.5: Seismic performance parameters of the CRuC-EQ building

Test ID / PGA level	f (Hz)	T (s)	K_{equiv} ($^{kN}/_{mm}$)	Max roof displacement* (mm)		Max roof acceleration (g)	Max SG-1 (με)	Max SG-3 (με)	Max SG-6 (με)	Max SG-8 (με)	Max SGext-x (με)	Max SGext-y (με)
Undamaged	18.55	0.054	73	-	CC-EQ	-	-	-	-	-	-	-
0.14g	17.0	0.059	62	0.21	(0.11)	0.25	184	144	36	124	46	27
0.2g	15.9	0.063	54	0.36	(0.28)	0.43	274	198	51	274	70	35
0.28g	13.6	0.074	39	0.62	(0.52)	0.63	363	247	79	407	114	52
0.4g	9.8	0.102	20	2.01	(1.08)	0.88	411	426	100	626	444	195
0.8g	5.5	0.182	6	6.65	(3.35)	1.72	727	599	258	1107	1249	525
1.6g	4.3	0.233	3.9	17.1	(8.11)	2.56	1401	1030	1090	2236	2530	1209
2.0g	4.24	0.236	3.8	23.2		3.26	1709	-	2327	3035	3646	1970

***** The maximum roof displacement of CC-EQ is provided for comparison.

The CRuC-EQ building had an undamaged natural frequency of 18.6 Hz, or an equivalent stiffness of 73 kN/mm. Similar to the CC-EQ building, the natural period of the CRuC-EQ building, T=0.054 s, was located in the first ascending branch of the design acceleration spectrum, however, the slightly longer period meant that the response acceleration of CRuC-EQ was higher up on the ascending branch relative to that of CC-EQ.

The first two PGA levels applied of 0.14g and 0.2g imposed a roof displacement of 0.21 and 0.36 mm, respectively, which were still within the elastic displacement range of the building based on the numerical analysis done in the previous chapter. A roof displacement of 0.62 mm was recorded during the 0.28g excitation, after which the equivalent stiffness of the frame decreased from 54 kN/mm to 39 kN/mm after the test.

The strain recording in the AFRP showed that the confinement started being activated during the 0.4g PGA test, with a maximum strain of 444 με along the shaking-direction, and 195 με on the transverse side (Figure 4.19).

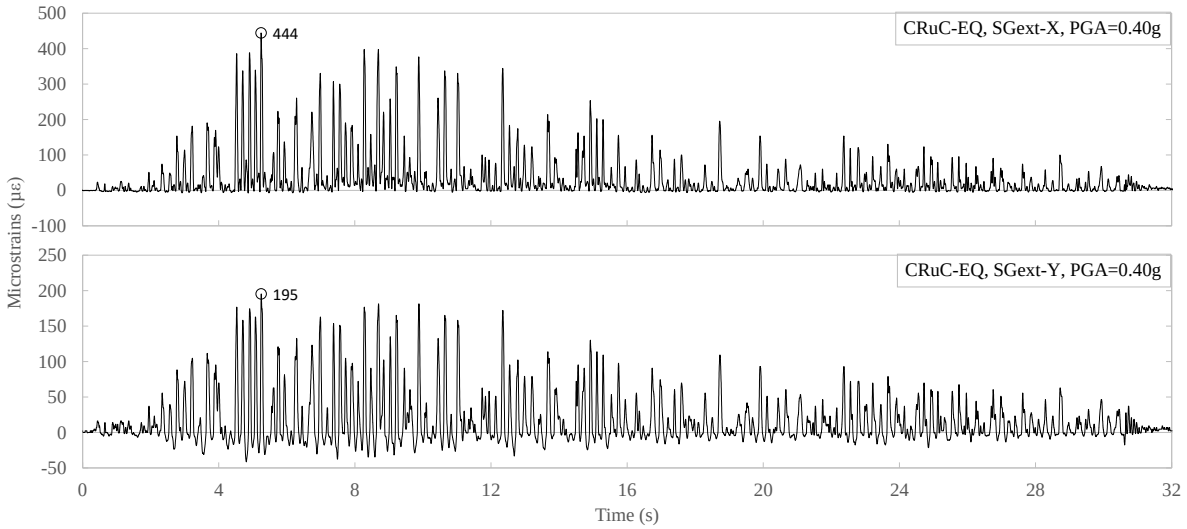

Figure 4.19: Strain on the AFRP along the shaking direction (top), and transverse side (bottom)

The strain in the internal and external longitudinal bars at the top of column were 426 and 411 με, respectively. The maximum strain in the shear links within the short column span was recorded in the middle stirrup, SG-6, and was equal to 100 με which is relatively small due to

the confining jacket. Further reduction in the stiffness occurred after the 0.8g PGA test, which imposed a roof displacement of 6.65 mm and roof acceleration of 1.72g. The maximum strain recorded in the steel was 1107 με in the bottom longitudinal bar of the beam, SG-8, and the maximum strain in the AFRP was 1249 με in the X-direction.

The CRuC-EQ building was able to survive the 1.6g PGA excitation, level at which the CC-EQ building collapsed. The maximum recorded roof displacement was 17 mm (Figure 4.20).

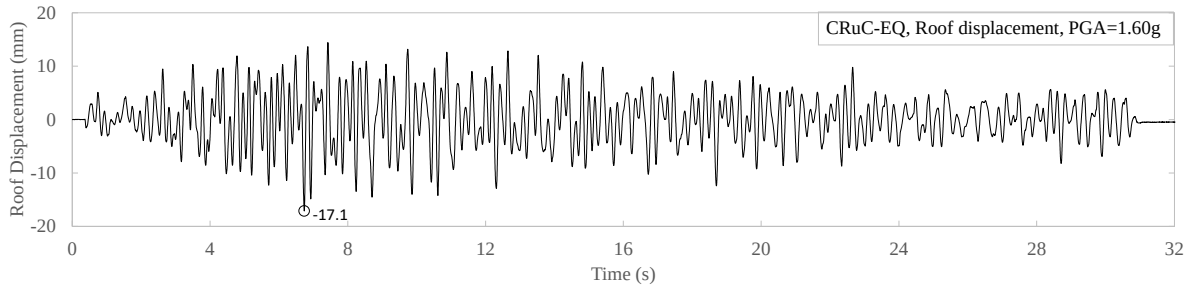

Figure 4.20: Roof displacement of the CRuC-EQ building during the 0.40g PGA excitation

Although no yielding was recorded in any of the reinforcement, the middle stirrup of the short column recorded a relative high strain of 1090 με, while the top stirrup was at 713 με. The strain in the beam reinforcement, SG-8, was close to yielding at 2236 με due to the unintentional yawing motion of the shake-table. The strain in the AFRP along the shaking direction (2530 με) was almost double the AFRP strain in the transverse side (1209 με). At the end of the 1.6g test, the building had a natural period of 0.23 s, or an equivalent lateral stiffness of 3.9 kN/mm. This low stiffness indicates that the building was in the linear hardening phase, or phase III as described in the previous chapter, in which the estimated numerical stiffness of the modelled building at a similar damaged state was 5.6 kN/mm.

An excitation of PGA=2.0g was finally applied to the CRuC-EQ building. As the safe working parameters were exceeded under this level of excitation, however, the input signal was automatically dampened after 12 seconds and the test was halted. The maximum roof displacement recorded was 23 mm, at which point yielding occurred in the top and middle

stirrup of the short column at 1693 με and 2327 με, respectively (Figure 4.21). The bottom reinforcement of the beam also yielded with a maximum strain of 3035 με.

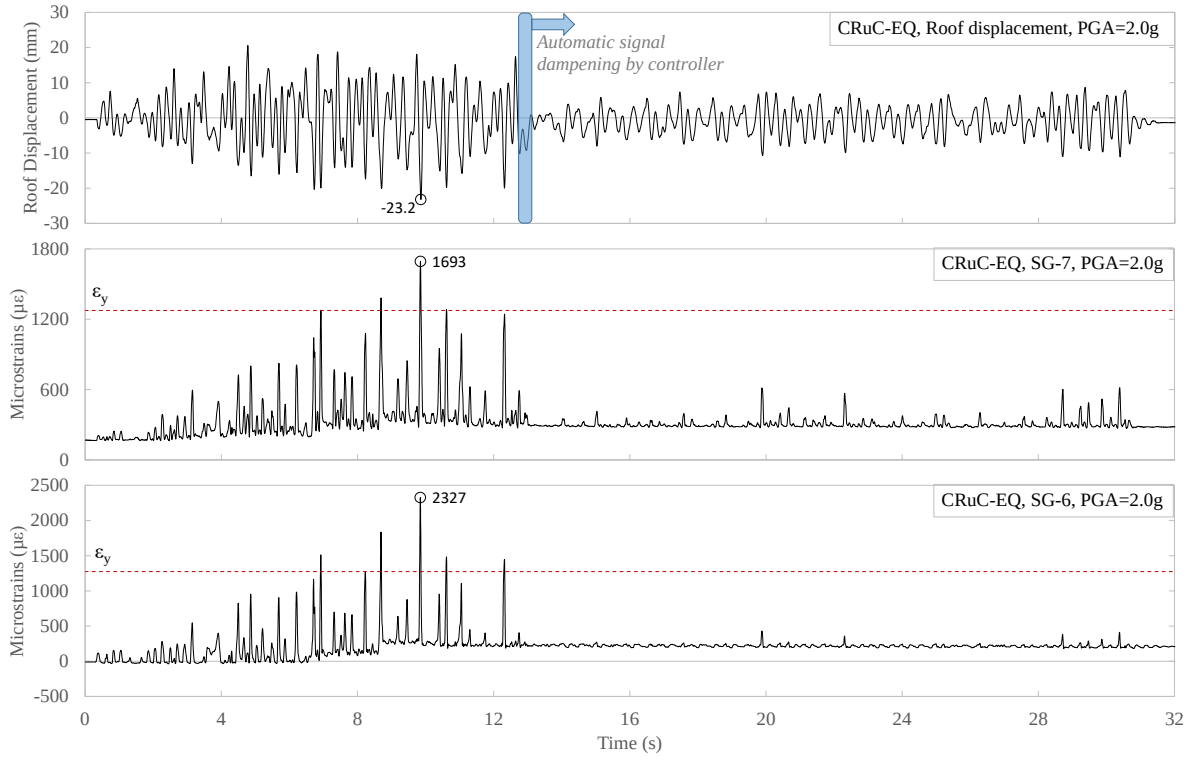

Figure 4.21: Roof displacement and top and middle stirrup strain gauge reading (CRuC-EQ, PGA=2.0g)

The strain in the AFRP along the shaking direction was 3646 με, which is significantly less than the estimated rupture strain of 17,000 με (around 70% of the manufacturer's rupture strain). The structural period after the 2.0g test was 0.24 s, while the corresponding lateral stiffness was 3.8 kN/mm, which confirms that the building was in the linear hardening phase, with negligible stiffness reduction from the previous excitation levels (3.9 kN/mm after the previous test). The observed behaviour provides evidence that a 4-phase bilinear behaviour, as observed in the numerical simulations performed in the previous chapter, can capture accurately the behaviour of the buildings with short columns made of confined rubberised concrete.

4.2.7 Comparison of the damage evolution through period elongation

Figure 4.22 shows the structural period elongation of both the CRuC-EQ and CC-EQ buildings normalised with respect to their corresponding undamaged period (T_i). The period shift for both buildings was very small after the first two PGA levels. The maximum short column drift (displacement/300 mm) achieved after the 0.2g test was 0.09% and 0.12% for the CC-EQ and CRuC-EQ building, respectively. The 0.28g and 0.4g PGA caused additional elongation in the period, with the CC-EQ building showing a 32% increase from the undamaged period, compared to 90% increase for the CRuC-EQ building. The 0.8g PGA test further increased the difference in the response of the two buildings. The CC-EQ exhibited 62% increase in the structural period with a maximum recorded drift ratio of 1.12%, whereas the CRuC-EQ building period increased by 237% of the undamaged one, with a maximum drift ratio of 2.22%. The period elongation of the CC-EQ building, in the 1.6g PGA test, ranged from 88% to 208% after which the building collapsed. The ultimate drift recorded was 2.7%, however the peak capacity drift prior to the major crack opening and spalling of the concrete was estimated from the video recording to be between 1.6-2%. The CRuC-EQ building had a period elongation of 331 and 338% for the 1.6g and 2.0g PGA tests, respectively. The maximum recorded drift of the confined short column was 7.74%.

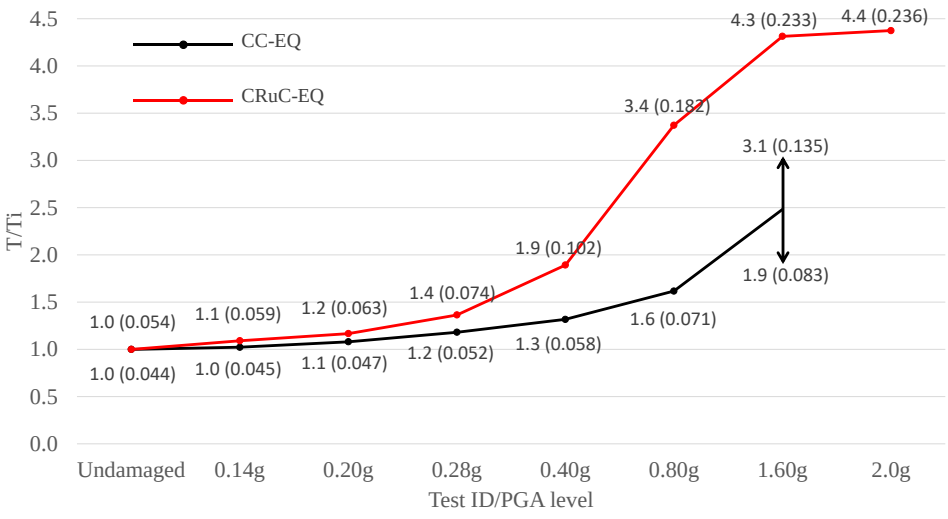

Figure 4.22: Structural period elongation with test progression of CC-EQ and CRuC-EQ building

4.3 DYNAMIC FRAME ANALYSIS OF THE CC-EQ AND CRuC-EQ BUILDINGS USING THE SCME

To assess the ability of the strut and tie model developed in Chapter 3 to capture the behaviour of short columns subjected to dynamic loading, the two buildings tested on the shake-table, CC-EQ and CRuC-EQ, were each modelled as a single 2-D frame in OpenSees. While during the experiment both columns were not attached to the short column fixity, and hence an impact was generated every time the frame hit the stiff internal support, the boundary conditions of the modelled frames were modified to aid convergence while maintaining an appropriate level of restraint. To avoid the numerical divergence issues that arise from impact, one of the columns was modelled with a roller fixity at the short column base, preventing any movement along the X-direction, while the other column only had an encastre fixity at the foundation. The frame stiffness in both lateral directions was governed by the two independent diagonal struts of the short column macro-element in compression, where each strut in the SCME accounts for the capacity of the corresponding short column. Figure 4.23 illustrates the deformation profile of the analytical frame modelled in OpenSees and that of the building tested (struts in red).

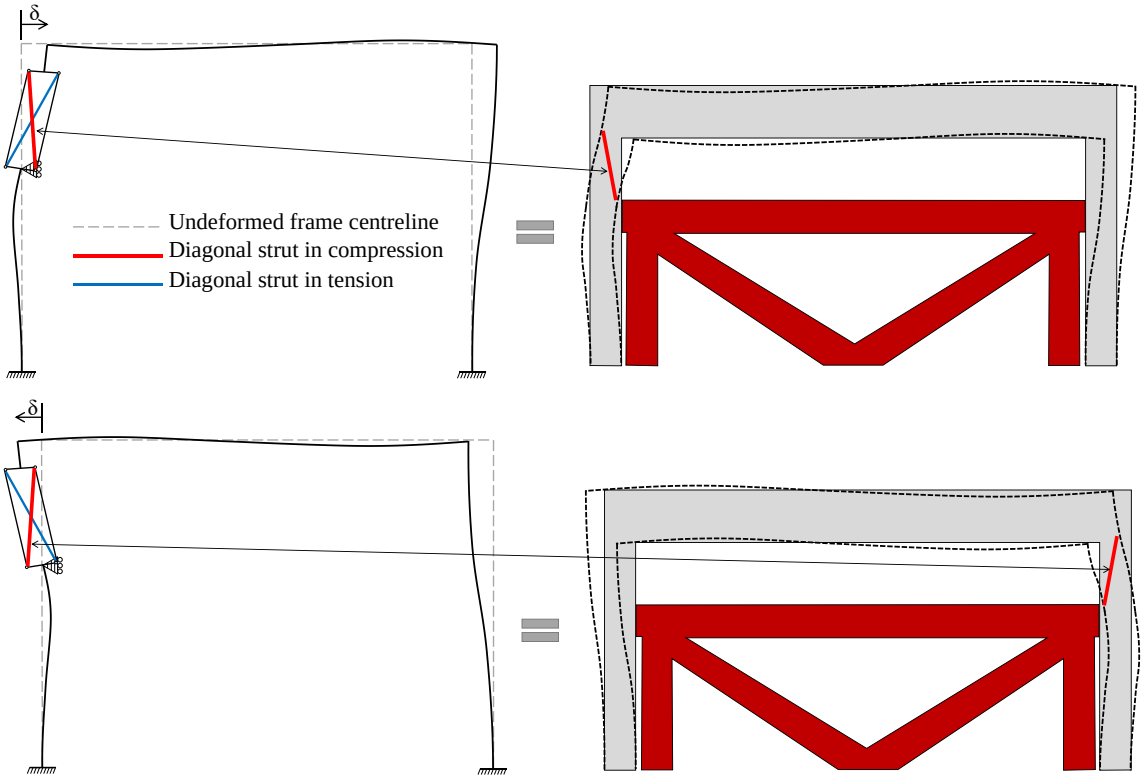

Figure 4.23: Deformation profile of the analytical STM OpenSees model and that of the tested building

The nodal mass of the analytical model was allocated at four locations as shown in Figure 4.24. The different tiers of weight allocation are important to capture more precisely the transfer of forces along the frame. The mass of the slab, beams, and the top 50% of the 300 mm short column span was allocated at the beam-column joint (345 kg at each node). The mass of the column below the short column restraint has no effect on the seismic response. The added mass on top of the slab was aligned with the actual centre of mass of the lead plates to replicate more realistically the location of the point of application of the inertial forces acting on the structure. The lead plate nodal mass was connected vertically at the beam-column joint with a rigid element (1000 kg at each column). The centre of gravity of the lead plates was 83 mm above the top surface of the slab, which makes the length of the rigid element equal to 213 mm (83 + 260/2).

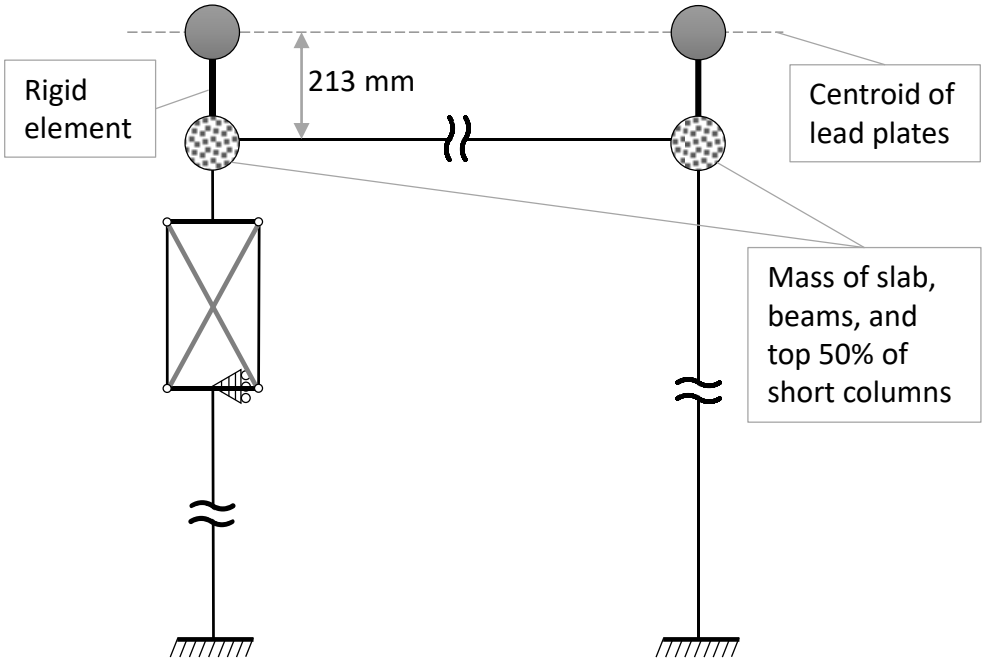

Figure 4.24: Nodal mass locations on the analytical model

The layout and dimensions of the struts and ties was based on the methodology outlined in the previous chapter. The width of the bearing face at node B, $w_{v,B}$, was assumed to be the same as in the static pushover setup and was equal to 25 mm. The reduction in the reinforcement ratio affected the width of the back face, $w_{h,B}$, which was equal to 38 mm and 47 mm for the

CC-EQ and CRuC-EQ building, respectively. The resultant width of the strut, $w_{s,B}$, was equal to 44 mm and 52 mm based on a strut inclination angle of 72° and 73° for the CC-EQ and CRuC-EQ building, respectively. The effective strength of the concrete strut for the CC-EQ building, f_{cc}^{e}, was equal to 21.2 MPa. The CRuC cylinder properties were obtained based on the constitutive model of Raffoul et al. (Raffoul et al., 2019) using the mean unconfined rubberised concrete strength and strain (Table 4.6). It was assumed that the strut that formed within the concrete is well confined as it is in the centre of the cross-section, and hence no shape-factor was applied to account for the rectangular section of the strut. To account for the inclination of the strut, Equation 3.6 in Chapter 3 was used to get the effective strength of the CRuC strut:

$$f_{crc}^{e} = (64 - 10.5)\sin^2 73 + 10.5 = 59\ MPa$$

and the effective ultimate axial strain, ε_{crc}^{e} was found to be 5.9%.

Table 4.6: RuC and CRuC mechanical properties

Rubberized Concrete	f_{rc}	ε_{rc}				
60% volume replacement	5.8	0.119				
Confined RuC	f_{cr}	ε_{cr}	f_{crc}	ε_{crc}	f_{crc}^{e}	ε_{crc}^{e}
CRuC (3 Layers of AFRP)	10.5	0.2	64	6.5	59	5.9

Strength f in (MPa), and Strain ε in (%)

The modelled frames were subjected to a successive series of PGA excitations as per the experiments, and the damage state of the frames after each test was used as input for the subsequent test to simulate the damage accumulation observed in the experimental tests. The roof displacement time history of the CC-EQ frame model obtained from OpenSees is plotted against the corresponding experimental results in Figure 4.25.

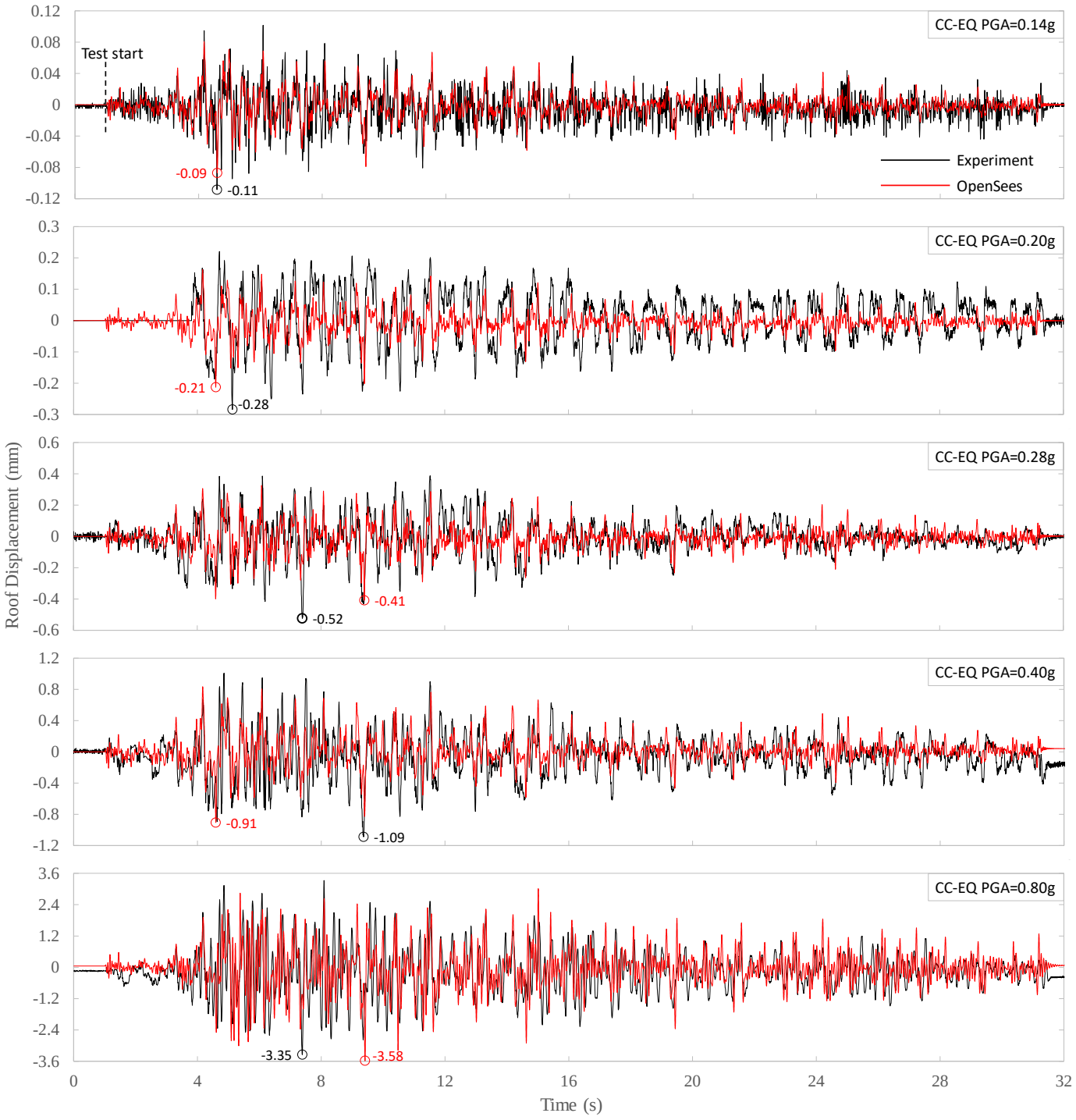

Figure 4.25: OpenSees vs. experimental displacement time history (CC-EQ)

A good correlation can be seen between the OpenSees dynamic analysis and the shake-table results of the CC-EQ building. However, a slight stiffer response for OpenSees is observed for the PGA test levels below the 0.8g. The higher stiffness of the analytical model can be attributed to the modified boundary conditions at the short column.

The OpenSees analytical model failed at an imposed excitation level of 1.6g PGA (Figure 4.26). Figure 4.27 shows the stress time history for both diagonal struts and indicates the peak compressive strength. Strut A reached its peak capacity at around 4 s into the test; however, the residual capacity of the concrete model prevented the total collapse of the frame. After the ultimate strength point was reached, the strut compressive capacity became negligible, and this can be seen in both figures where the compressive stress decays to zero, and the stiffness of the frame reduces due to the degradation of the short columns.

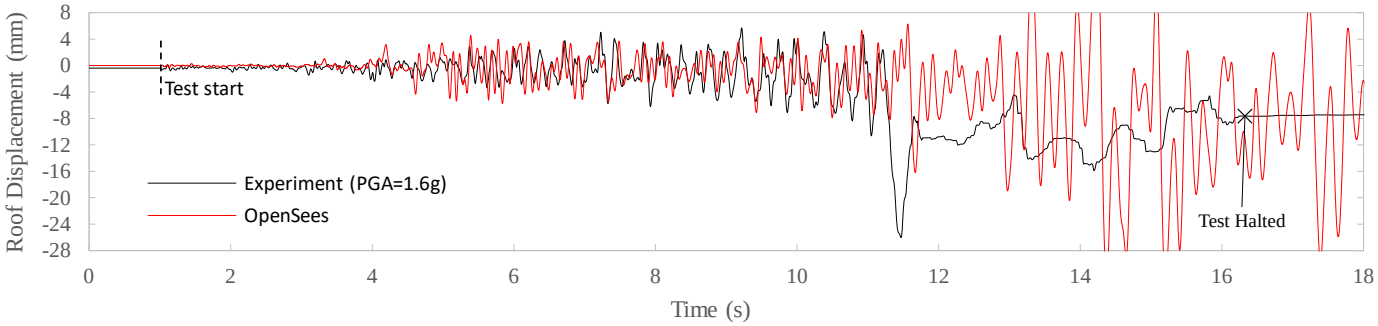

Figure 4.26: OpenSees vs. experiment displacement time-history for the 1.60g test (CC-EQ)

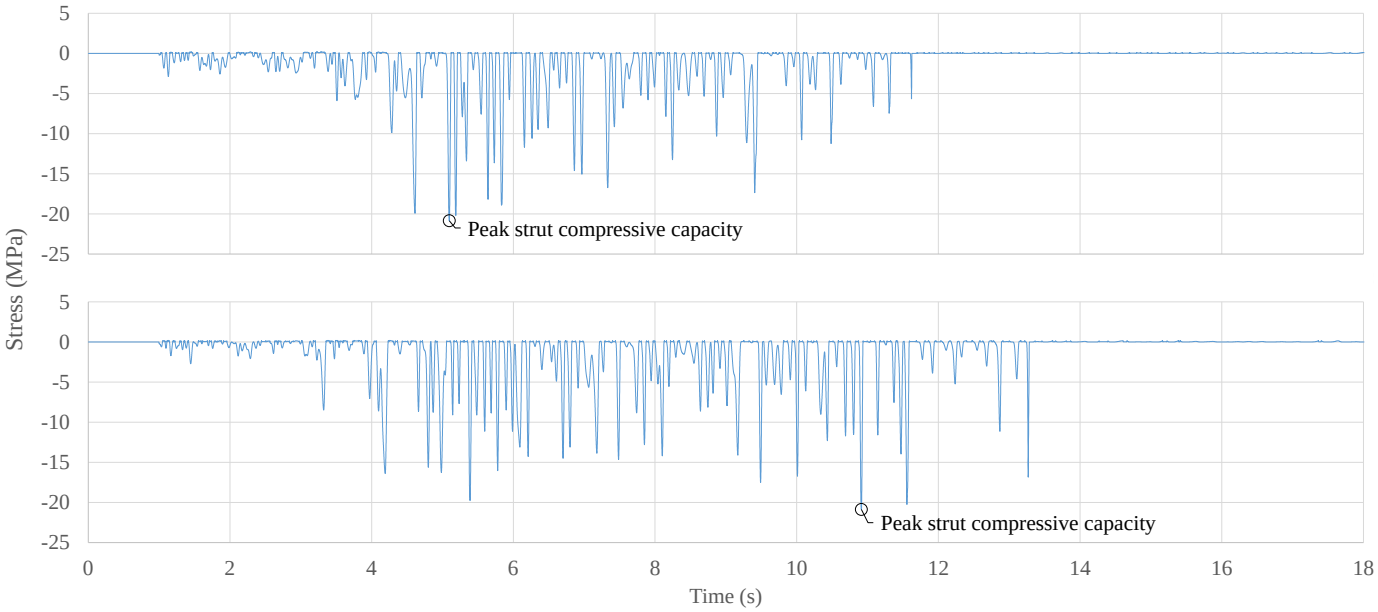

Figure 4. 27: Stress in the struts during the 1.60g PGA excitation of the analytical model (CC-EQ)

Figure 4.28 below shows the analytical model displacement time-history plotted against the experimental results for the CRuC-EQ building.

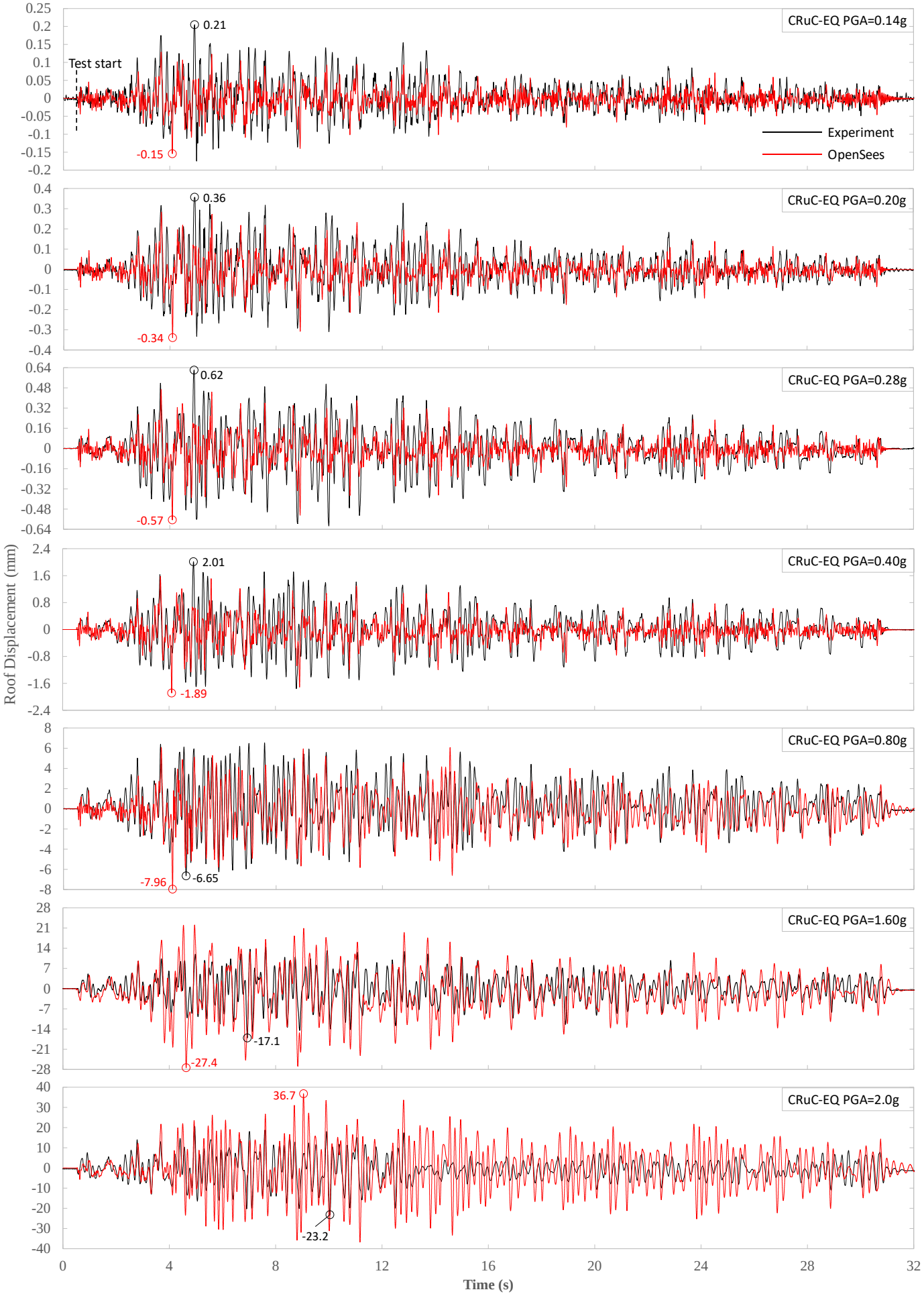

Figure 4.28: OpenSees vs. experimental displacement time history (CRuC-EQ)

The roof displacement of the CRuC dynamic analysis for the first PGA level of 0.14g was lower than that of the experiment by 29%. This can be attributed to the compression of the AFRP sheet wrapped around the column due to its impact with the short column restraint. However, the general trend of the analyses results matches the response from the shake-table tests. The response of the CRuC dynamic analyses for PGA levels 1.6g and 2.0g exhibited up to 60% higher roof displacement when compared to the experimental results. At the end of the 2.0g PGA excitation, the equivalent stiffness of the modelled CRuC frame was around 1.5 kN/mm, which is less than the 3.8 kN/mm stiffness of the CRuC-EQ building. However, the unrestrained column reinforcement at this stage yielded, which meant the frame was in the Phase IV of its lateral behaviour (see Section 3.5 for the full four-phase lateral behaviour). Also, unlike the experiment which was halted for safety, the simulation delivered the full 2.0g earthquake time-history, which imposed higher damage on all the structural elements of the frame, while the short column remained intact.

4.4 CONCLUDING REMARKS

The seismic performance of two buildings was compared experimentally to assess the behaviour of CRuC. The CC-EQ building collapsed after the short columns exhibited explosive shear failure. The maximum drift attained before the failure test was 3.35 mm, or 1.1% drift ratio. The building with short columns made of CRuC was able to withstand higher accelerations than the CC-EQ building. More importantly, the CRuC short columns demonstrated higher ductility, with a drift ratio of up to 7.7% (23.2 mm). The strain time-history results of CRuC-EQ indicate damage progression along all structural members of the frame. The enhanced global behaviour of the building, as well as the notable improvements at the local short column level suggest that CRuC can be utilised in short columns and in other high shear demand regions.

The two shake-table tests were modelled and analysed using the SCME STM model described in Chapter 3. The short column boundary condition of the analytical model was modified to assist with the numerical convergence. The lumped mass was allocated at two different levels, to precisely capture the level at which the inertial forces were acting in the experiment. The model was simulated with the full load-protocol. Good correlation was seen between the analytical and experimental results, which validates the model to be used in seismic analysis.

4.5 REFERENCES

Bompa, D. V., Elghazouli, A. Y., Xu, B., Stafford, P. J., & Ruiz-Teran, A. M. (2017). Experimental assessment and constitutive modelling of rubberised concrete materials. *Construction and Building Materials*, *137*, 246–260. https://doi.org/10.1016/j.conbuildmat.2017.01.086

Raffoul, S., Escolano-Margarit, D., Garcia, R., Guadagnini, M., & Pilakoutas, K. (2019). Constitutive Model for Rubberized Concrete Passively Confined with FRP Laminates. *Journal of Composites for Construction*, *23*(6), 04019044. https://doi.org/10.1061/(asce)cc.1943-5614.0000972

Solomos, G., Pinto, A., & Dimova, S. (2008). A REVIEW OF THE SEISMIC HAZARD ZONATION IN NATIONAL BUILDING CODES IN THE CONTEXT OF EUROCODE 8. *JRC Scientific and Technical Reports*.

Chapter 5

Experimental and numerical investigation of the performance of confined rubberised concrete base-isolators

Keywords: Base-isolation; Confined Rubberised concrete; Seismic performance; FRP; shake-table.

5.1 INTRODUCTION

This chapter discusses the concept of a base-isolation system consisting of CRuC deformable micro-columns. The first part of the chapter describes the shake-table tests performed on a building (CRuC-EQ building tested in Chapter 4) mounted on four circular columns made of CRuC. The superstructure performance is compared to that of the fixed-base. The second part provides a seismic analysis example of a building, modelled in OpenSees, with a fixed-base and with base-isolation made with CRuC.

5.2 SHAKE-TABLE TEST ON A STRUCTURE BASE-ISOLATED WITH SLENDER CRUC COLUMNS

The building with CRuC short columns discussed in Chapter 4 (CRuC-EQ) was mounted on top of four micro-columns which were proposed to act as a base-isolation system. Even though the CRuC-EQ building was mildly retrofitted before this third testing phase, it was heavily damaged after the last test of the second phase (2.0g excitation) and had a lateral stiffness of 3.8 kN/mm (T=0.24 s) (the undamaged stiffness was 73 kN/mm). This meant that a comparative evaluation between the fixed-based building (CRuC-EQ) and the base-isolated one (CRuC-ISO), at least in terms of drift, was not possible due to the different initial stiffness of the superstructures. Nevertheless, this phase of the experimental program aimed at examining the ductile behaviour of CRuC columns under seismic loading, and its ability to attenuate the seismic excitation, as well as the mode of failure of the slender CRuC isolators.

5.2.1 Design and manufacture of the base-isolated building

The damaged CRuC-EQ building was retrofitted by injecting grout in the flexural cracks that developed in the beams and base of the columns, as well as in the slab. Grout was also injected in the cracks that developed on the inner side of the joints underneath the slab. A layer of resin was applied to the edges of the CFRP sheets of the joints to prevent any debonding at the ends.

The base-isolators comprised of a cylindrical column made of rubberised concrete with a height of 600 mm and a diameter of 110 mm (Figure 5.1-a). The column's reinforcement consisted of six 12 mm diameter longitudinal bars, and a 4 mm diameter shear spiral with a pitch of 50 mm (Figure 5.1-b). The top and bottom 50 mm of the column were cast into a 5 mm thick hollow steel cap in order to provide a solid footing for the column. The column was confined with AFRP sheets with varying thickness (i.e. number of layers) along its height: four layers at the top and bottom 150 mm, two layers at the centre 100 mm, and three layers at the rest (Figure 5.1-c). The four layers of confinement at the ends were intended to provide extra safety and ductility, as the plastic hinge was expected to form within that portion of the base-isolaor. The ultimate moment capacity of the columns was found to be approximately 13 kNm, from section analysis, while the shear resistance of the unconfined section was estimated to be 15 kN (according to EC2, (EN 1992-1-1, 2004)), with an additional contribution of 10 kN from the shear spiral reinforcement.

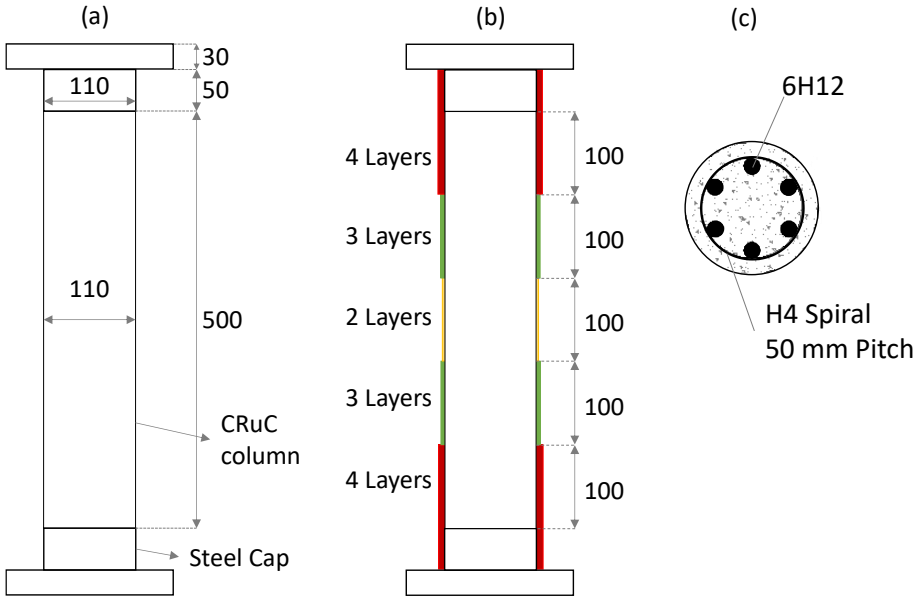

Figure 5.1: a) Geometry of the CRuC base-isolator, b) AFRP layout, c) Detailing of the reinforcement (units in mm)

The steps below describe the process of manufacturing the CRuC base-isolators (Figure 5.2):

1. The top and bottom 30 mm thick steel plates were positioned via four removable steel rods to give a clear height of 600 mm for the column.

2. Six holes were drilled into both plates to insert the longitudinal reinforcement. Additionally, a central 40 mm hole was drilled for casting the concrete.

3. The steel caps were positioned in the centre of the plates followed by the shear spiral reinforcement and the whole assembly was then welded into place (Figure 5.2-a).

4. The longitudinal bars were then inserted into the pre-drilled holes and welded at the top and at the bottom (Figure 5.2-b).

5. The spiral reinforcement was tied to the longitudinal bars and the strain gauges were placed on the reinforcement.

6. A polyvinyl chloride (PVC) pipe was cut open on its long side and then secured tightly around the steel caps (Figure 5.2-c).

7. RuC was cast through the casting hole in the steel plate. The PVC formwork was removed and the column was allowed to cure.

8. The RuC column was confined with AFRP sheets using the wet lay-up process described in Appendix B1 (Figure 5.2-d).

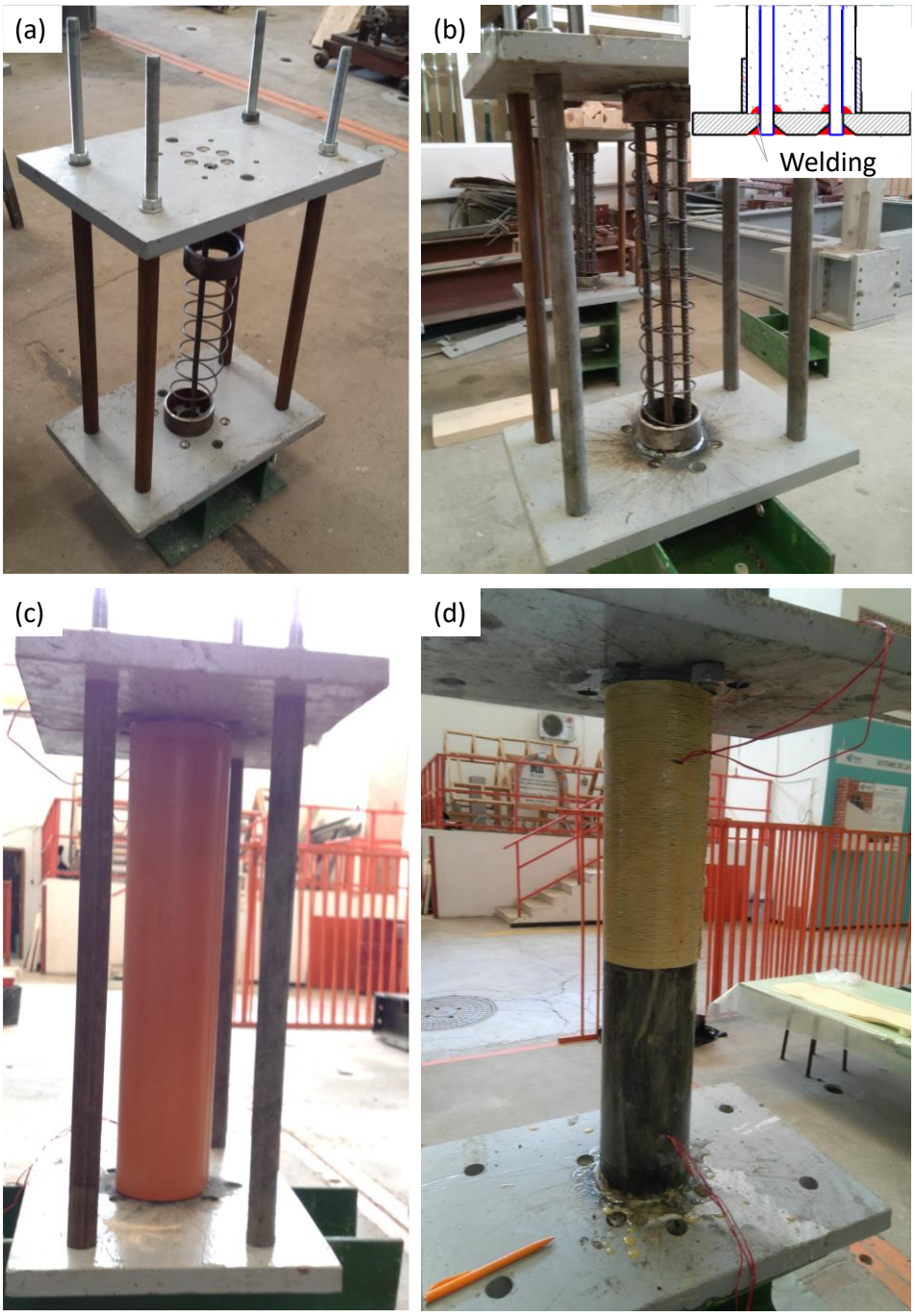

Figure 5.2: Manufacture of the CRuC base-isolator: a) Positioning of steel plates, caps, and reinforcement, b) Welding of reinforcement, c) Formwork and casting, d) AFRP confinement

5.2.2 Material Properties

The same CC base mix described in chapter 4 was used with 60% by volume of fine and coarse aggregates replaced with rubber particles. However, due to the small cross-section size of the base-isolator the size of the coarse aggregates was limited to 8 mm. Table 5.1 summarizes the compressive mechanical properties of the CC base mix (average of three cylinders), and the RuC mix (average of five cylinders) tested in uniaxial compression according to EN 12390. The same steel described in chapter 3 for the longitudinal bars and transverse stirrups was used to reinforce the base-isolators. S&P A120/290 AFRP sheets were used to confine the base-isolators.

Table 5. 1: Mechanical properties of the concrete mixes used for the base-isolators

Building ID	Concrete type	f_{cm} (MPa)	ε_c (mm/m)	E_c (GPa)	f_{ct}* (MPa)
CRuC-ISO	CC^{+}	42	2.08	31	3.62
	RuC	5.4	1.14	7.1	0.84

* Concrete tensile strength calculated based on Bompa et al.'s model for RuC (Bompa et al., 2017)
$^{+}$ Conventional concrete base mix that was used for the rubberised concrete.

5.2.3 Test setup, instrumentation, and test sequence

The CRuC-EQ building was mounted on four CRuC base-isolators by bolting the steel foundation to the top steel plate, while the bottom steel plate was bolted to the shake-table (Figure 5.3). Each of the base-isolators was positioned concentrically under the columns of the superstructure. A stack of wooden planks was fixed on the shake-table underneath the steel foundation to safeguard from heavy impact in the case of collapse of the base-isolating system. The additional gravity load was the same as in the CRuC-EQ test: 40 kN provided by bolting 15 lead plates on the slab. The total mass of the superstructure along with the foundation was estimated to be 7 tons.

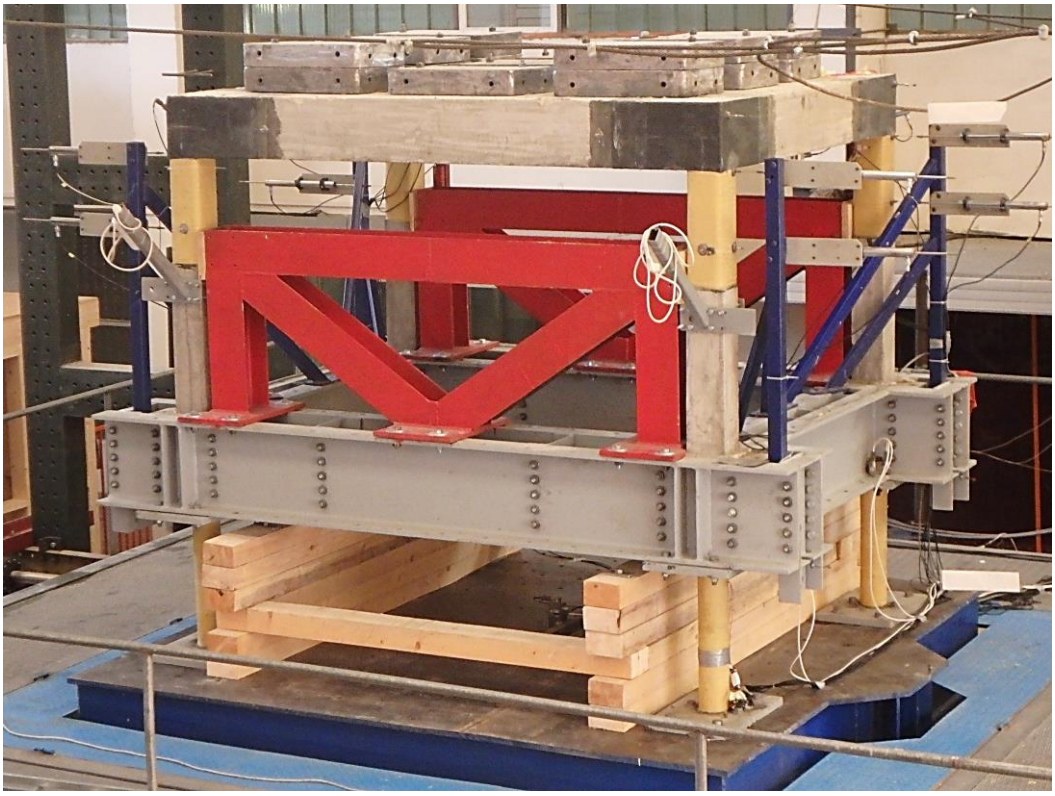

Figure 5.3: CRuC-ISO building positioned on the shake-table prior to testing

The CRuC-ISO building was instrumented with eight piezoelectric accelerometers, four at the top level of the base-isolators, and four at the top of the superstructure, which recorded accelerations in the X and Y direction. Additional three accelerometers were connected to the shake-table to record ground accelerations in the X-Y-Z axis. Five wire displacement transducers, connected to a fixed outside frame, measured the absolute displacement of the shake-table (xTable), the top of the base-isolators (xIso-1,2), and the top of the building (xTop-1,2). Figure 5.4 shows the external instrumentation used for the CRuC-ISO building.

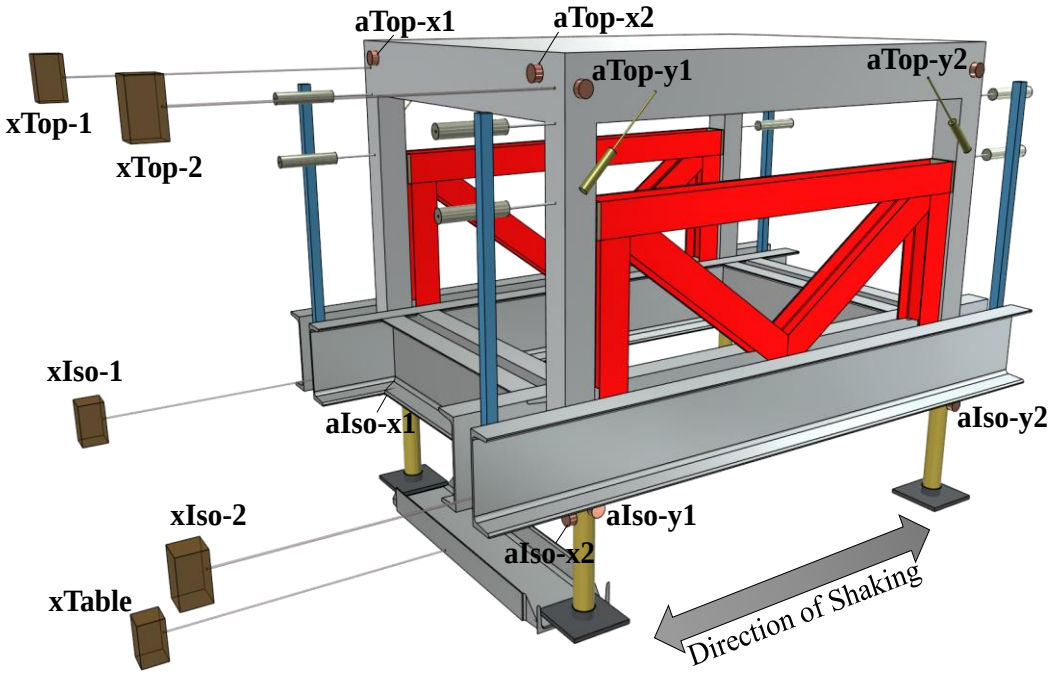

Figure 5.4: Instrumentation of the CRuC-ISO building

In addition to the displacement and acceleration instrumentation, two diagonally opposite base-isolators were instrumented with seven strain gauges each. Four strain gauges attached 70 mm away from the top and bottom of the longitudinal reinforcement (SG1-4), one attached on the spiral reinforcement (SG5), and two strain gauges attached at the top and bottom of the AFRP sheet (Figure 5.5).

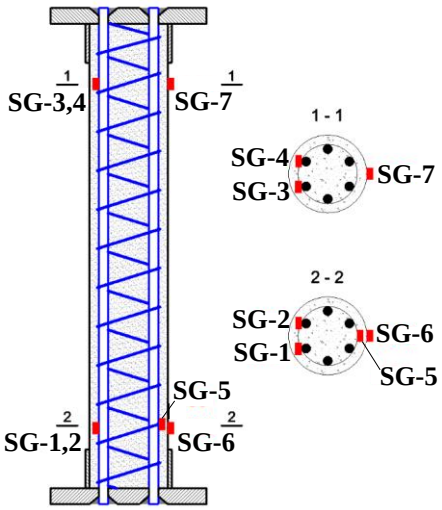

Figure 5.5: Strain gauge instrumentation of the base-isolator

The seismic record and test sequence described in chapter 4 were used to perform the shake-table test on the CRuC-ISO building.

5.2.4 Numerical modelling of the CRuC base-isolator

The CRuC base-isolator column was modelled in Abaqus in order to examine its ductility and general behaviour. The top and bottom round steel cap were not modelled, as a perfect tie bond was assumed at the top and bottom surfaces. The column had a clear height of 500 mm and diameter of 110 mm. The shear links were modelled as circular hoops at a spacing of 50 mm each, which should confine the core RuC in a similar way to the shear spiral. The longitudinal bars were extended and embedded into a top and bottom load plates (Figure 5.6). The column was confined with three layers of AFRP modelled as a skin reinforcement with elastic lamina material.

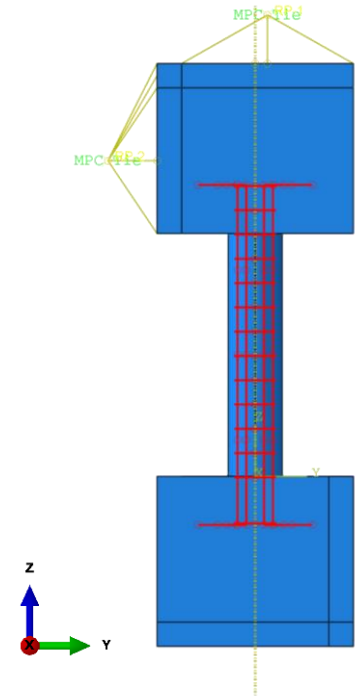

Figure 5.6: Steel embedded into the CRuC base-isolator modelled in Abaqus

The RuC stress-strain behaviour was obtained from the constitutive material model proposed by Bompa et al. (Bompa et al., 2017) based on the RuC mean cylinder strength (Table 5.1). The default parameters for the CDP material model were used, with a dilation angle of 45°, and a viscosity parameter of 1×10^{-5}. A gravity load of 17.5 kN, which was the estimated experimental axial load, was applied as a concentrated force on the reference point tied to the top load plate. The column was pushed laterally under a double-curvature boundary condition.

Figure 5.7-a below shows the lateral load-displacement of the CRuC column, with drift values at the top x-axis. The CRuC base-isolator had an initial stiffness of 6 kN/mm. Yielding of the first and second layer of longitudinal reinforcement (i.e. the most external reinforcing bar, and the adjacent two reinforcing bars closer to the middle of the section) occurred at 36 and 44 mm, respectively. The ultimate lateral resistance of the base-isolator was 44 kN at lateral displacement of 115 mm (23 % drift). At that level, the AFRP jacket reached its rupture strain at the bottom compression side of the base-isolator. The shear demand on the fibres, along with extra stress from the local crushing and expansion of the RuC caused a high stress concentration on the compression side at the bottom and top level of the base-isolator (Figure 5.7-b).

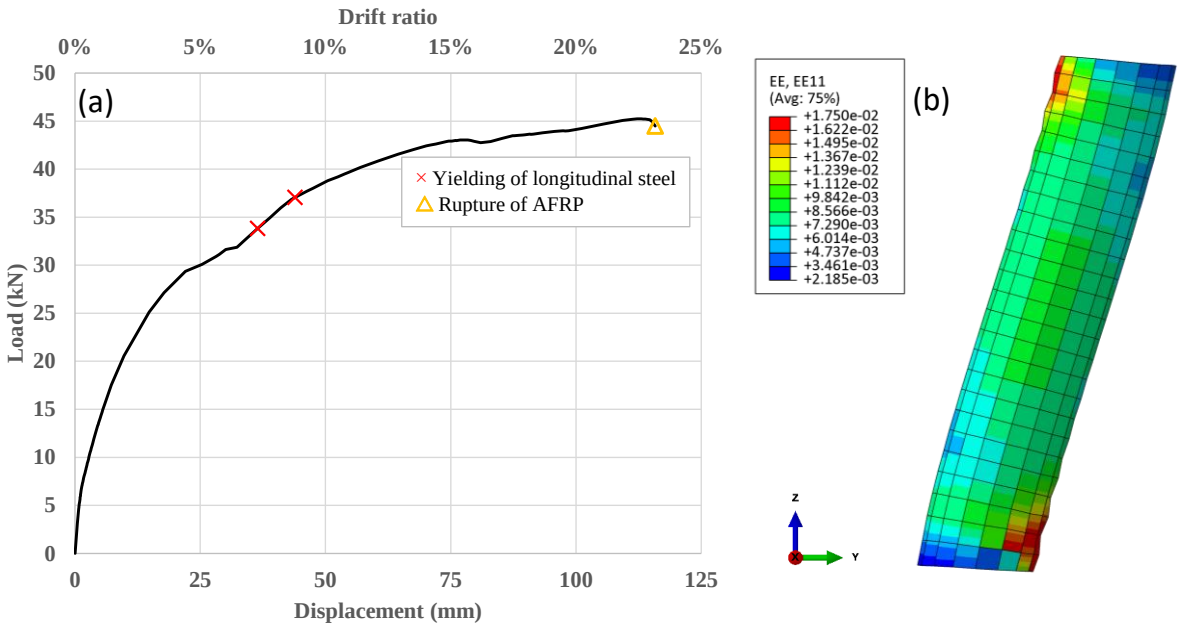

Figure 5.7: a) Lateral load-displacement response of the CRuC base-isolator Abaqus model, b) AFRP Jacket hoop strain (EE11) at the pre-defined rupture strain level

5.2.5 Time history performance and analysis of the CRuC-ISO building

Table 5.2 summarises the seismic performance of the CRuC-ISO building in terms of natural frequency, period, equivalent stiffness, maximum displacement and acceleration at the isolator level and top of superstructure, as well as maximum strain measurement at the flexural reinforcement and AFRP confinement of the base-isolator. Unfortunately, the strain gauge placed on the shear spiral reinforcement was damaged during casting and did not provide any reading. Plots of all the data recorded during the seismic test are placed in *Appendix C1: Time history results of the CRuc-iso shake-table test.*

Table 5.2: Summary of the time history performance parameters of the CRuC-ISO building

Test ID / PGA level	f (Hz)	T (s)	Maximum relative displacement (mm) (drift %)		Maximum acceleration (g)		Maximum flexural reinforcement strain (με)	Maximum AFRP strain (με)
			Top of CRuC isolator	Top of Structure	Top of CRuC isolator	Top of Structure		
Undamaged	4.90	0.204	-	-	-	-	-	-
0.14g	4.71	0.212	1.97 (0.33%)	2.47 (0.82%)	0.23	0.33	245	176
0.2g	4.32	0.231	3.21 (0.54%)	4.02 (1.34%)	0.32	0.55	416	239
0.28g	3.86	0.259	4.55 (0.76%)	6.21 (2.07%)	0.46	0.83	727	518
0.4g	3.25	0.308	7.51 (1.25%)	8.84 (2.95%)	0.69	1.11	1503	724
0.8g	2.41	0.415	23.0 (3.84%)	14.2 (4.73%)	1.54	1.86	3673	1927
1.6g	1.32	0.756	60.5 (10.1%)	17.8 (5.93%)	2.02	2.10	>10000	7902
2.0g*	0.84	1.198	105 (17.6%)	16.3 (5.44%)	2.07	1.98	-	11628

The drift for the base-isolator and short column at top of structure were considered based on the 600 mm height, and 300 mm clear height, respectively.

* During the 2.0g PGA test, the building failed by rupture of the AFRP in the base-isolators.

It was estimated from a Fast Fourier Transform (FFT) of the relative response of the superstructure that its natural period (T) was between 0.21 and 0.23 seconds (equivalent stiffness ranging between 10 to 5 kN/mm), which was slightly stiffer than the last state attained after the second phase of testing, owing to the repair of the cracks through grout injection. The natural period of the CRuC-ISO system (0.204 s) was marginally smaller than that of the superstructure, which is opposite to the purpose of base-isolation where the natural period is increased and the acceleration response of the structure is decreased. The latter can be attributed to the fact that the base-isolators were stiffer than originally designed, due to the use of a top and bottom steel cap which reduced the bending height, as well as the use of a large reinforcement ratio of 7.2%. However, these adjustments were deemed necessary to prevent local rupture or slippage that could cause collapse of the superstructure and compromise the safety of the operators. A natural period of 0.204 s meant that the CRuC-ISO building was located at the plateau of the response spectrum of the applied acceleration record. This increased the response acceleration of the CRuC-ISO specimen by a factor of almost 2.5 for the tests up to and including the 0.8g excitation.

During the 0.4g PGA test, a 0.69g acceleration was recorded at the top of the CRuC isolator, whereas the top of the superstructure experienced a 1.13g acceleration. This high response is owed mostly to the spectral amplification factor. The latter test imposed a drift ratio of 1.25% for the base-isolators, and a 2.95% (8.84 mm) for the shear dominated short columns at the top of the structure. In comparison, during the 0.8g test on the fixed-base CRuC-EQ building (Chapter 4), a roof acceleration of 1.72g caused a maximum roof displacement of 6.65 mm (2.22%). However, the CRuC-EQ building had a stiffness of 20 kN/mm prior to that test, which limited the resultant drift compared to the significantly less stiff CRuC-ISO superstructure. A more detailed comparison between the CRuC-EQ and CRuC-ISO experimental tests is provided in Section 5.2.6.

During the 0.8g PGA test, the response acceleration and displacement at the top of the superstructure were 1.86g and 14.2 mm (4.73%), respectively. The CRuC base-isolators were subjected to a drift ratio of 3.84% (23 mm), at which point the first yielding occurred in the flexural reinforcement (3673 με) (Figure 5.8), and the maximum strain recorded on the AFRP was 1927 με. The yielding of the reinforcement softened the CRuC base-isolators, which in turn shifted the natural period of the CRuC-ISO system to 0.415 s, almost double the undamaged T. Despite the longer period, the system was still inherently stiff, and the building T was still located at the plateau of the response spectrum, which can explain the high acceleration response at the top of the base-isolators (1.54g).

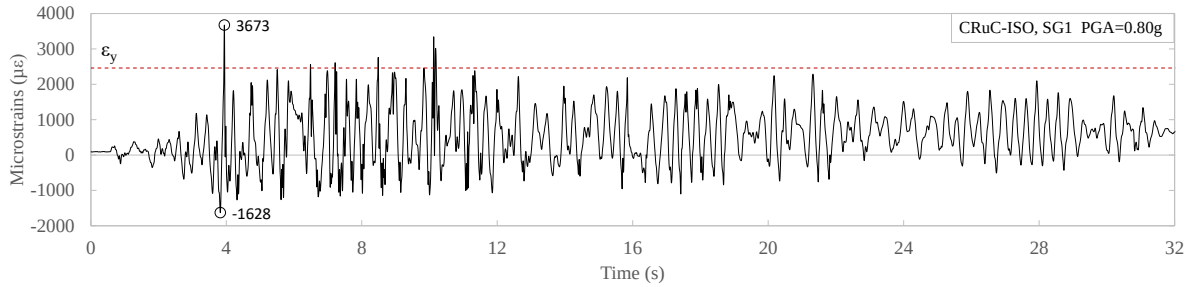

Figure 5.8: Strain time history of the base-isolator flexural reinforcement (PGA=0.80g)

During the 1.6g PGA test, the CRuC base-isolators further lost stiffness, which pushed the natural period of the CRuC-ISO building to 0.76 s. This is evident in the reduced amplification of the acceleration from the ground (up to 1.6g) to the top of the base-isolating foundation, which was around 1.26, compared to the amplification for the 0.8g test of around 1.9. The maximum drift recorded in the base-isolators was 10% (60 mm) (Figure 5.9), and the strain gauge on the longitudinal reinforcement reached its measurement limit of 25000 με (Figure 5.10), which indicates high plasticity of the reinforcement. The maximum AFRP strain recorded was 7902 με (0.79%), which was only about 45% of the rupture strain (1.75%) (Figure 5.11). Visual inspection of the AFRP after this test, however, showed mild whitening of the fibres at the top and bottom of the base-isolators, indicating substantial strain concentration at that level, as well as debonding due to the high flexural deformation in the plastic hinge zone

(Figure 5.12). The results of the numerical simulation of the base-isolator (Section 5.2.4) show similar stress concentration in the AFRP at the same location, due to the expansion of concrete at that level, as well as possible buckling of the longitudinal reinforcement.

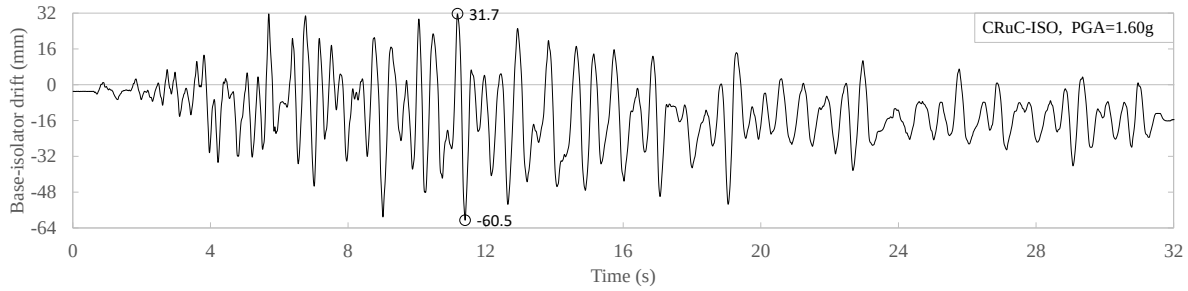

Figure 5.9: Base-isolator drift time history for the CRuC-ISO building (PGA=1.60g)

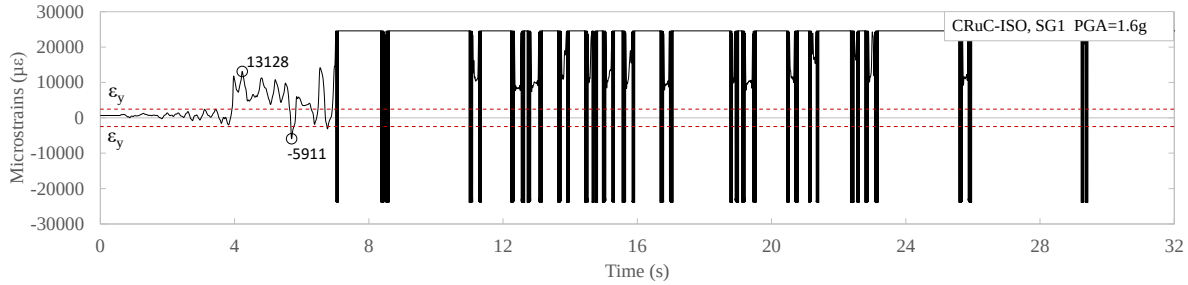

Figure 5.10: Strain time history of the base-isolator flexural reinforcement (PGA=1.60g)

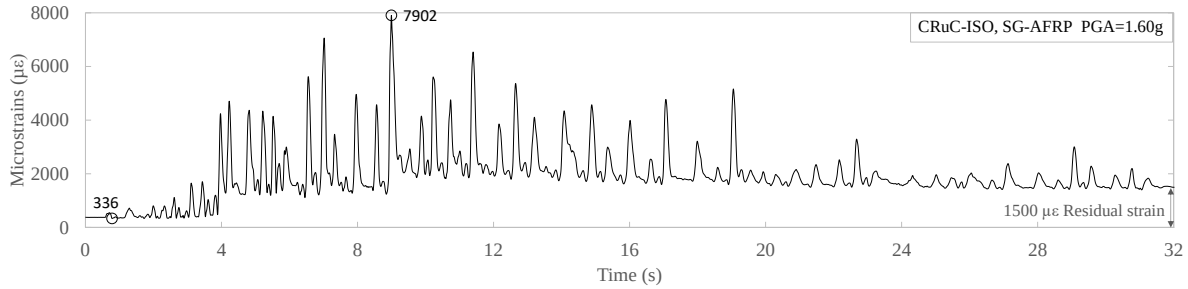

Figure 5.11: Strain time history of the base-isolator AFRP jacket (PGA=1.60g)

Figure 5.12: Strain concentration in the AFRP at the bottom of the CRuC base-isolator

The 2.0g PGA test imposed a drift of around 17.6% (105 mm) on the CRuC base-isolators which lead to the rupture of the AFRP (see Figure 5.14). The maximum recorded strain in the AFRP was 11628 με (Figure 5.13). At the end of the 2.0g PGA test, the natural period of the CRuC-ISO building was around 1.2 s. The maximum recorded acceleration at the top of the base-isolator was 2.07g, which is a negligible amplification from the ground PGA of 2.0g, hence, demonstrating the reduction in the response acceleration due to shifting of the natural period of the structure.

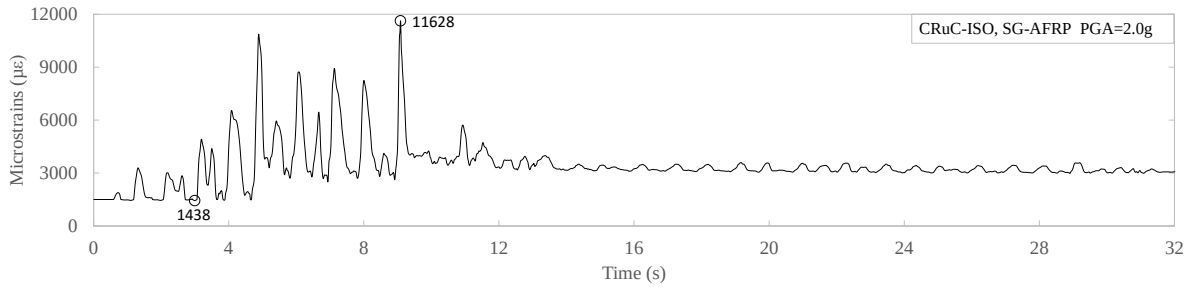

Figure 5. 13: Strain time history of the base-isolator AFRP jacket (PGA=2.0g)

Figure 5.14: Rupture of the AFRP jacket of the base-isolators after the 2.0g PGA test

5.2.6 Comparative evaluation of the CRuC-EQ and CRuC-ISO building response

Table 5.3 summarises the maximum roof displacement and acceleration recorded during the CRuC-EQ and CRuC-ISO shake-table tests for every excitation level.

Table 5.3: Comparison of the maximum roof displacement and acceleration between the CRuC-EQ and CRuC-EQ building

Test ID / PGA level	Maximum roof displacement (mm)			Maximum roof acceleration (g)			Acceleration at level of base-isolator
	CRuC-EQ (Fixed base)	CRuC-ISO (Base-isolated)	Ratio*	CRuC-EQ (Fixed base)	CRuC-ISO (Base-isolated)	Ratio	
0.13g	0.21 (0.07%)	2.47 (0.82%)	11.8	0.25	0.33	1.32	0.23g
0.2g	0.36 (0.12%)	4.02 (1.34%)	11.2	0.43	0.55	1.28	0.32g
0.28g	0.62 (0.21%)	6.21 (2.07%)	10.0	0.63	0.83	1.31	0.46g
0.4g	2.01 (0.67%)	8.84 (2.95%)	4.40	0.88	1.11	1.26	0.69g
0.8g	6.65 (2.22%)	14.2 (4.73%)	2.14	1.72	1.86	1.08	1.54g
1.6g	17.1 (5.71%)	17.8 (5.93%)	1.04	2.56	2.10	0.82	2.02g
2.0g	23.2 (7.74%)	16.3 (5.43%)	0.70	3.26	1.98	0.61	2.07g

*Ratio of the CRuC-ISO performance parameter to that of the CRuC-EQ

The drift ratio (shown between parenthesis) was considered based on the 300 mm clear height of the short column

The drift in the short column at the top of the superstructure of CRuC-ISO was significantly larger than that of the CRuC-EQ building (up to 11.8 times), at least for the first four PGA tests. This can be attributed to two main reasons:

1) As mentioned earlier, the CRuC-ISO superstructure was much softer than that of the CRuC-EQ at the initial stage of testing, due to the permanent damage sustained. While CRuC-EQ had an estimated lateral stiffness of 73 kN/mm, the CRuC-ISO superstructure stiffness ranged between 5-12 kN/mm. This meant that the displacement response was much higher for the CRuC-ISO superstructure for the same level of inertial force.

2) The other main factor that caused the much higher drift in the CRuC-ISO superstructure was the fact that the natural period of the CRuC-ISO system (around 0.2 seconds) was located at the constant acceleration branch of the response spectrum, while that of the CRuC-EQ structure (around 0.05 seconds) was located at the very start of the ascending

acceleration branch (Figure 5.15). This meant that the response amplification factor for the CRuC-ISO building was much higher than that of the CRuC-EQ building. This is evident in the response acceleration at the top of the base-isolators, which underwent higher accelerations than the ground PGA (Table 5.3).

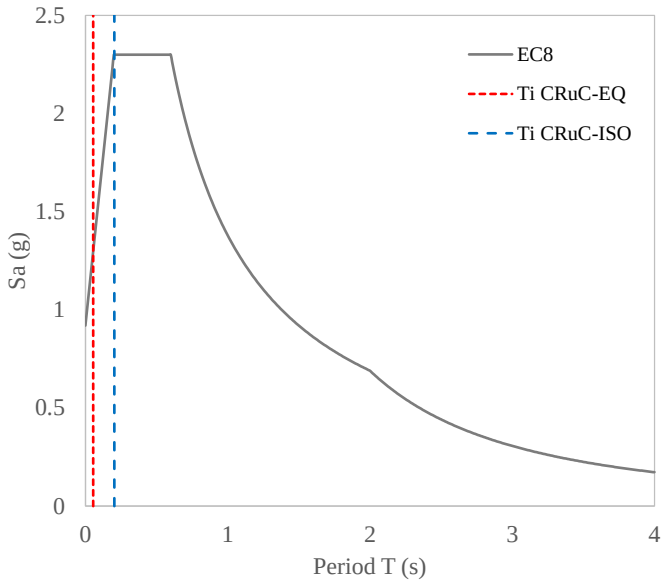

Figure 5.15: Undamaged natural period of CRuC-ISO and CRuC-EQ and the EC8 elastic spectrum for the 0.8g excitation

Due to the aforementioned reason of the response amplification factor, the acceleration recorded at the top of the CRuC-ISO superstructure was on average 25% more than the acceleration recorded on the roof of the CRuC-EQ building, for the first 5 excitation level tests. However, during the 1.6g and 2.0g tests, the natural period of the CRuC-ISO building shifted towards the descending acceleration branch, at T=0.76 and 1.2 s, respectively. This reduced the response acceleration of the structure, and in turn reduced the imposed displacement (drift) at the superstructure. This is evident in the reduction of the roof acceleration for the CRuC-ISO superstructure by 18% and 39% at the 1.6g and 2.0g PGA test, respectively. The short column drift, however, was 4% larger for the CRuC-ISO superstructure during the 1.6g test, due to the fact that the CRuC-EQ building at that stage still had a higher lateral stiffness (K=6 kN/mm).

5.3 COMPARATIVE EVALUATION OF THE PERFORMANCE OF A FIXED-BASE BUILDING AND A CRuC BASE-ISOLATED BUILDING

In order to gain a better understanding of the capability of CRuC as a base-isolating material, an analytical model was built to examine the seismic response of a reinforced concrete frame with a fixed base and with a base-isolation system made of a series of CRuC micro-columns.

5.3.1 Description and design of the superstructure RC frame

A four-storey three-bay reinforced concrete frame was designed in SAP2000 (CSI, 2021) according to the provisions of Eurocode 8 (EN 1998-1, 2004) (See Appendix C2). The building was considered to be of importance factor = 1, with a viscous damping ratio of 5%, designed as a medium class ductility system for a PGA=0.3g, and ground type B. The external bays were 4.5 m wide, while the internal bay had a width of 5 m. The ground floor had a height of 3.6 m, while all the other floors were 3.3 m high, with a total structure height of 13.5 m. The RC frame considered in this design was an internal frame of a building with an out-of-plane bay width of 6 m (Figure 5.16).

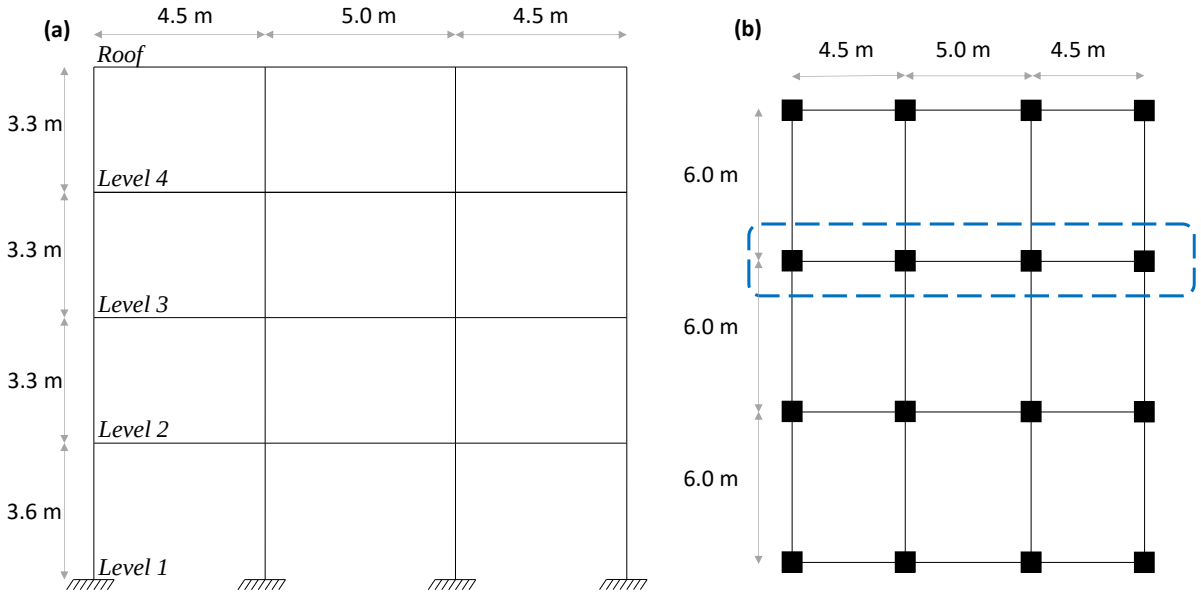

Figure 5.16: a) Elevation view of the designed RC frame, b) Plan view of the building with the internal frame highlighted

The thickness of the slab was 180 mm for all floors. An unfactored permanent load g_k of 1.0 kN/m^2 was assumed for finishes, while an unfactored imposed load q_k of 1.0 and 2.5 kN/m^2 was taken for the roof and all other storeys, respectively. The concrete strength class was C35/45, while all flexural and shear reinforcement were Grade B500B with a characteristic yield strength f_{yk}=500 MPa. The distribution of the applied gravity loads onto the beams and column nodes was done using a tributary area distribution, were all the lines were assumed to bisect the corners at 45° (Figure 5.17).

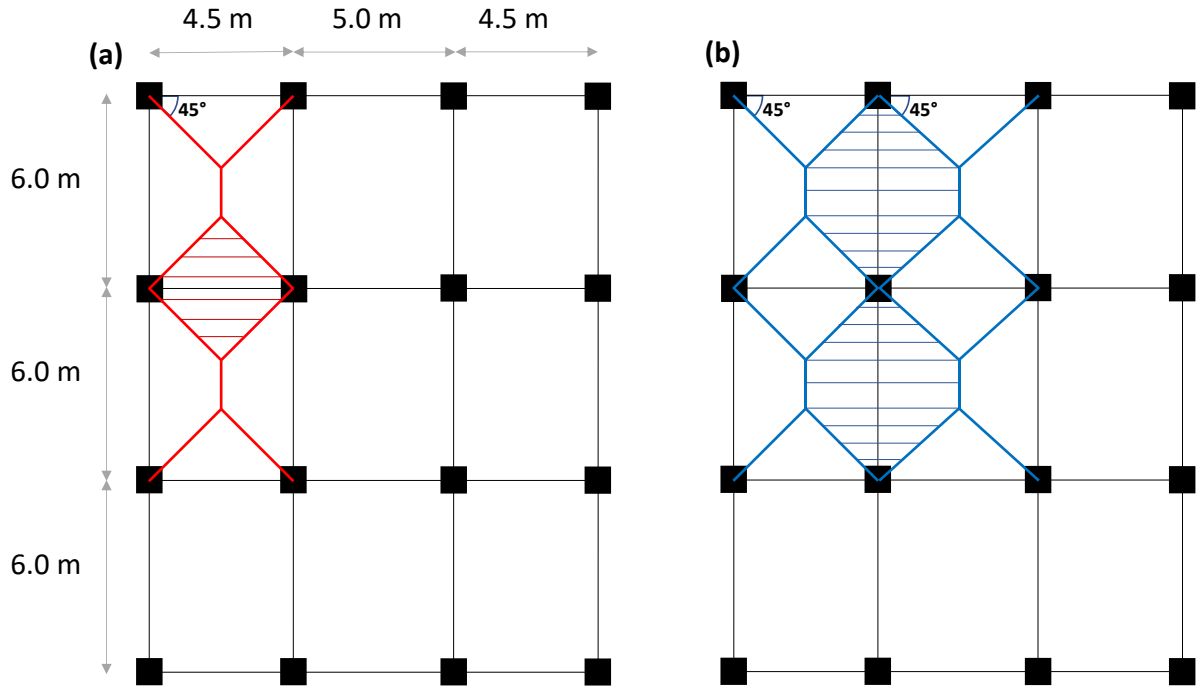

Figure 5.17: Distribution of the applied gravity loads on a) the beams and on b) the column nodes of the RC frame

The seismic design considered here was the linear-elastic multimodal response spectrum method. The latter reduces the seismic forces obtained from linear analysis by using a design spectrum, which is obtained by reducing the elastic response spectrum by the behaviour factor q (Eq. 5.1):

$$q = q_0 K_w \tag{5.1}$$

where q_0 is the basic value of the behaviour factor and is equal to $3(\alpha_u/\alpha_1)$ for a ductility class medium (DCM) moment resisting frame system, and K_w reflects the prevailing failure mode

in structural systems and is taken as 1.0 for frame systems. α_u/α_1 is the overstrength factor and is equal to 1.3 for a regular multi-storey multi-bay RC frame building. (hence $q = 3.9$)

The linear elastic response spectrum was considered for an earthquake with a reference PGA on rock ground (a_{gR}) equal to 0.25g. The spectrum type I was chosen, with a building of importance factor = 1.0 (importance class II), located on soil type B, and with a damping ratio of 5%. Figure 5.18 below shows the elastic response spectrum, the design spectrum, as well as the time history acceleration of the artificial earthquake to be applied and its spectrum.

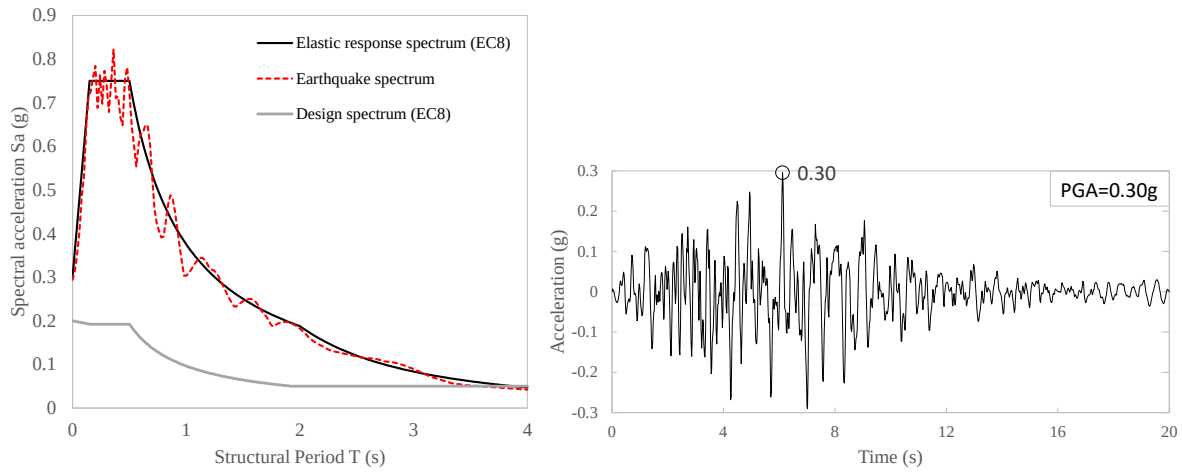

Figure 5.18: Left: Elastic response spectrum, design spectrum and earthquake spectrum; Right: Time history acceleration of the artificial earthquake

Nodal mass was assessed according to the modal analysis based on the applied axial load to the beams and joint nodes. Figure 5.19 shows the vibration mode shapes of the superstructure and the natural period and effective modal mass for each of these vibration modes. The joint mass obtained from the load combination including dead, live, and seismic loads, was used in OpenSees to define the mass along the x-direction, or the direction of the horizontal ground motion. Precise allocation of the joint mass gives accurate results in terms of natural period of the structure, as well as proper distribution of the inertial forces along the building.

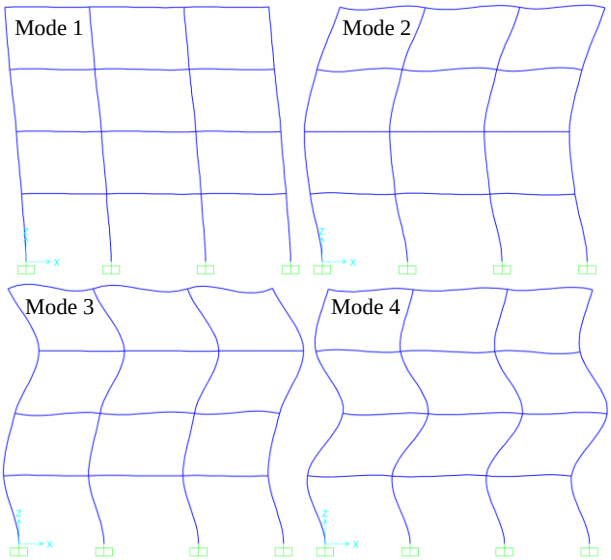

Vibration Mode	Natural period (s)	Effective modal mass (%)
1	0.67	80
2	0.25	15
3	0.13	3
4	0.09	2

Figure 5.19: Left: Vibration mode shape of the superstructure and Right: Mode shape periods and effective modal mass

The cross-section check option in SAP2000 was used after the load combination analysis to design and optimize the RC beams and column size, as well as the reinforcement layout. The final beams and column cross-section layouts are shown in Figure 5.20 below.

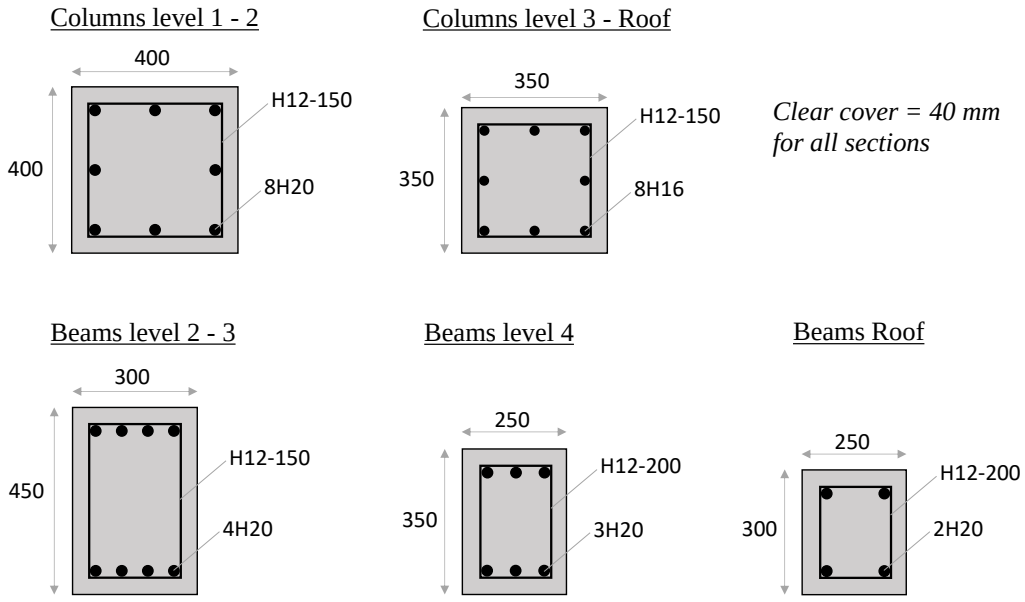

Figure 5.20: Cross-section layouts of the columns and beams of the superstructure RC frame (units in mm)

The cross-sections were designed such that all joints met the Eurocode 8 condition on ductility and the prevention of a soft storey. As such, the sum of design moment resistances of the columns connecting at any joint (M_{Rc}), was at least 1.3 times that of the beams intersecting the same joint (M_{Rb}).

5.3.2 Design of the CRuC base-isolators

The superstructure designed for the 0.30g reference PGA was placed on a set of micro-columns made of confined rubberised concrete, which formed the base-isolating system. Each column is considered to be a CRuC base-isolator with a height of 1.5 m (Figure 5.21-a). The latter had a circular cross-section to ensure maximum efficiency of the FRP confinement. The diameter of the cross-section, amount of reinforcement, as well as the number of the CRuC base-isolators were calibrated to ensure a total moment capacity at least greater than the moment capacity of the 1st floor columns (210 kNm). Twenty CRuC base isolators were chosen with a diameter of 200 mm and 6H16 longitudinal bars (Figure 5.21-b), each with a moment capacity of 44 kNm. The base isolators were confined with three layers of AFRP. The mechanical properties of RuC were taken as those of the material used for the CRuC-ISO building (Table 5.1). A rigid stiff beam was assumed at the ground level connecting the footings of the first-floor columns. The twenty base-isolators were connected at the top node to the rigid beam, and had a full fixity boundary condition at the bottom node. The seismic response results of the latter described model can be found in Appendix C3.

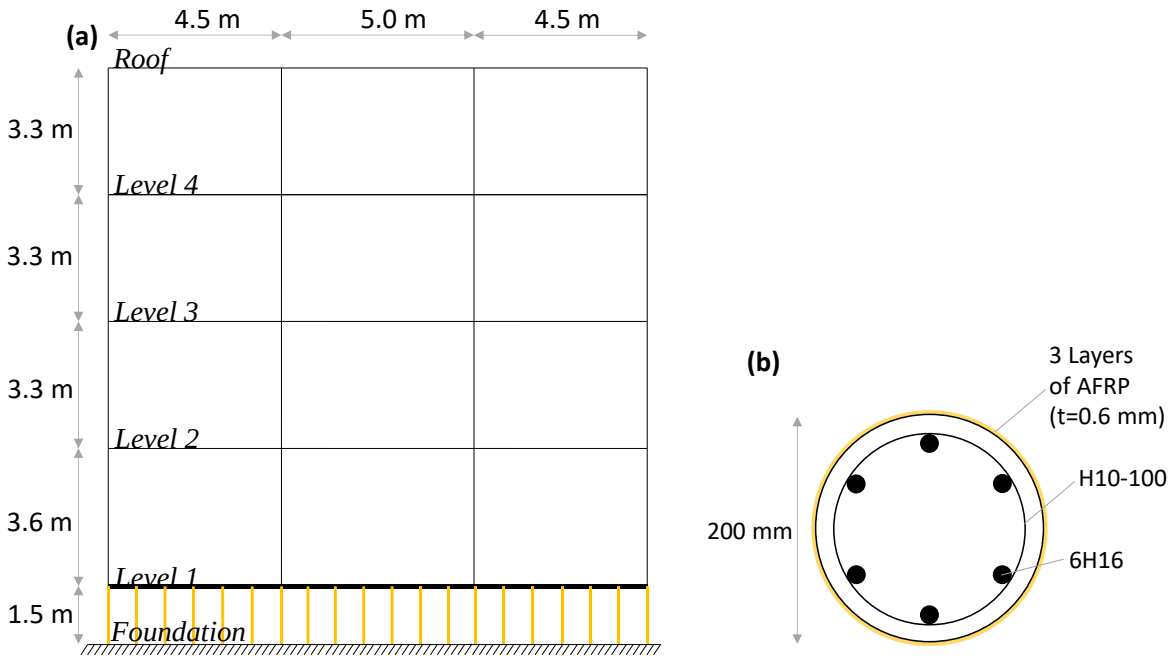

Figure 5.21: a) Elevation view of the base-isolated building, and b) Cross-section description of the CRuC base-isolator

The latter design was based on the equivalent moment capacity of the superstructure ground level columns. The analysis showed a much lower moment demand on the CRuC base-isolation system, up to 61% decrease in the over-turning moment imposed at the base. Hence, the base-isolation system was changed by decreasing the number of the base-isolators used to 13 instead of 20, as well as increase their height from 1.5 m to 1.8 m. This will reduce the stiffness of the base-isolation system, elongating the natural period of the whole structure which will reduce the acceleration response. The base-isolators are spaced at 1.15 to 1.2 m apart. The cross-section dimensions and reinforcement layout were unchanged. The design of the superstructure was the same for the fixed-base case. Figure 5.22 shows the elevation view of the new structure referred to as "Base-isolated*#2*".

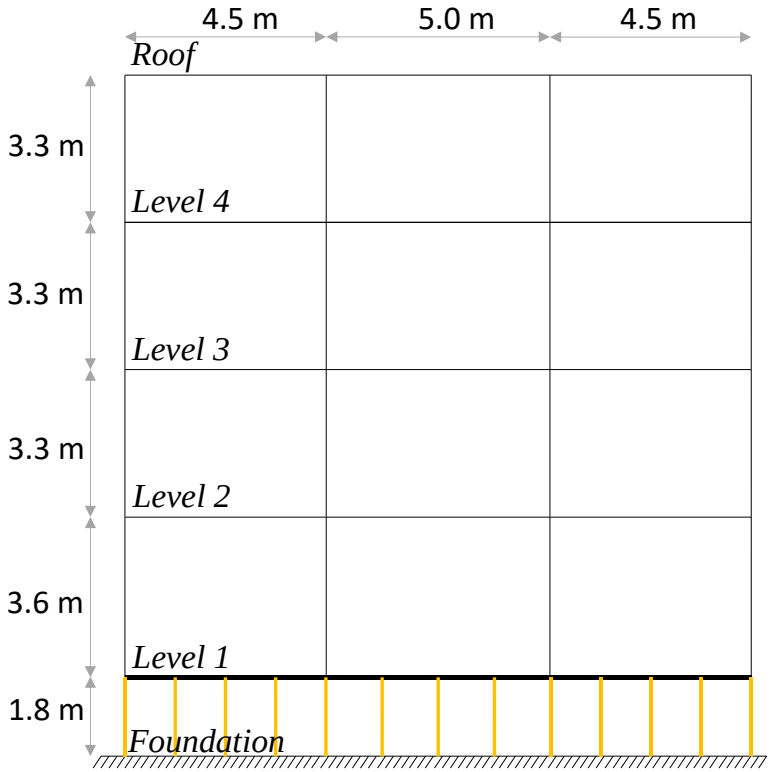

Figure 5. 22: Elevation view of the base-isolated#2 building

5.3.3 Fixed-base versus CRuC base-isolated*#2* seismic response

The fixed-base and base-isolated buildings were modelled in OpenSees. All structural elements were modelled as force beam-column elements. The fixed-base building was fully fixed at the bottom node of the first-floor columns, while the base-isolated building was fully fixed at the bottom nodes of the base-isolators. The concrete in the beams and columns of the superstructure had *Concrete02* material definition, with the core having additional capacity to account for the confinement provided by the stirrups. The confined rubberised concrete was modelled using *Concrete01* material; the full biaxial behaviour was obtained using the experimental strength value f_{cm}=5.4 MPa as input (Raffoul et al., 2019). The longitudinal reinforcement was modelled with *Steel02* material definition in OpenSees.

The two buildings were subjected to the earthquake excitation shown in Figure 5.18, at 50%, 100%, and 150% of the PGA value of 0.30g, which corresponds to the return period of 475 years according to Eurocode 8 design provisions. The nonlinear time-history dynamic response of the two buildings was recorded and compared in terms of natural period, inter-storey drift, maximum roof displacement and acceleration, as well as maximum base shear and moment.

5.3.3.1 Natural period and global damage index

The global damage index (GDI) provides a quantitative method to assess the global damage taken by a building after an earthquake by comparing the natural period of the structure before and after the earthquake. This study uses the global damage index proposed by DiPasquale et al. (Dipasquale et al., 1990). The natural period elongation of a building provides an estimate of the global damage sustained by the building during an earthquake (Garcia et al., 2017).

$$GDI = 1 - \left(\frac{T_i}{T_f}\right)^2 \tag{5.2}$$

where T_i and T_f are the natural structural period before and after the earthquake, respectively. The natural periods are obtained from a modal analysis by obtaining the eigenvalues.

A GDI value ranges between zero and one, with zero indicating no change in the natural period and accordingly no damage to the structure, whereas a GDI value of one indicates theoretical collapse of the building. Table 5.4 below shows the undamaged natural period of the two buildings, the period after the application of the excitation record, and the corresponding GDI.

Table 5.4: Natural period evolution of the fixed-base and base-isolated#2 building, and corresponding damage index

PGA	Fixed-base			Base-isolated#2		
	T_i (s)	T_f (s)	GDI	T_i (s)	T_f (s)	GDI
0.15g	0.643	0.873	0.458	1.014	1.058	0.081
0.30g	0.643	1.115	0.667	1.014	1.152	0.225
0.45g	0.643	1.152	0.688	1.014	1.174	0.254

The base-isolated*#2* building had an undamaged natural period of 1.014 s, which is 58% longer than that of the fixed-base, and 30% longer than the natural period of the first designed base-isolated building. The GDI indicates that the global damage taken by the base-isolated*#2* building is significantly smaller than in the fixed-base, and also smaller than the base-isolated building (Figure 5.23). This result confirms that the new system with a smaller number of isolators, and higher clear height, attains a longer structural period, which reduces the acceleration response of the structure, hence the less damage indicated by the GDI. This confirms the need to optimise the CRuC base-isolation system to deliver a designed target period which will provide the safest protection/isolation from the seismic wave and energy.

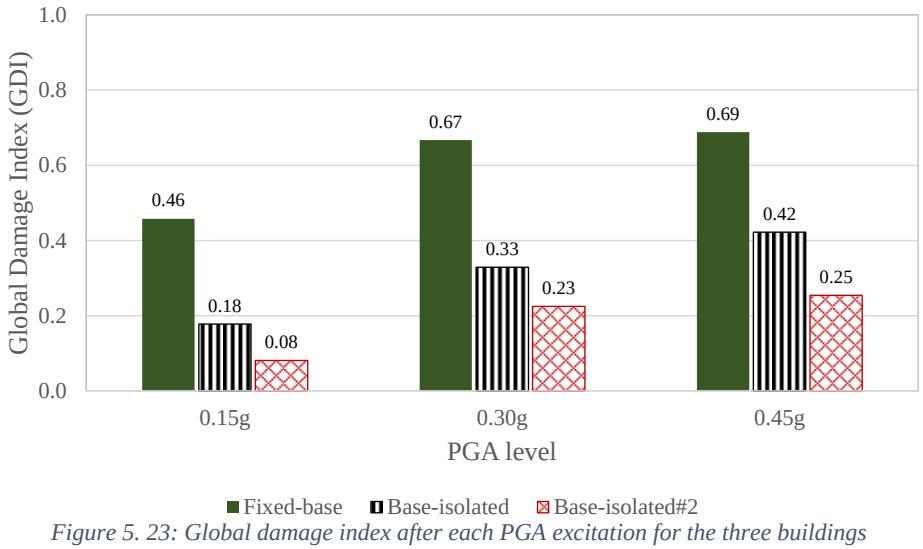

Figure 5. 23: Global damage index after each PGA excitation for the three buildings

5.3.3.2 Inter-storey drift ratio

Table 5.5 shows the maximum inter-storey drift ratio (IDR) at the various levels of the superstructure for both fixed-base and base-isolated#2 structure for all PGA excitations.

Table 5.5: Maximum inter-storey drift ratio for the fixed-base and base-isolated#2 building

PGA	Fixed-base				Base-isolated#2*			
	Level 1	Level 2	Level 3	Roof	Level 1	Level 2	Level 3	Roof
0.15g	0.39	0.45	0.55	0.48	0.24 (37%)	0.29 (35%)	0.30 (46%)	0.26 (47%)
0.30g	0.89	1.06	1.40	1.24	0.43 (51%)	0.49 (54%)	0.63 (55%)	0.51 (59%)
0.45g	1.32	1.71	2.22	1.79	0.53 (60%)	0.63 (63%)	0.73 (67%)	0.63 (65%)

Drift ratio is in percent.

* The percent reduction in drift for the base-isolated building is shown in parenthesis.

The new base-isolated*#2* building had between 35% to 67% less drift ratio compared to the fixed-base building, for various floors and PGA excitations.

It is evident from the results that for a more efficient base-isolation system, there is more reduction in the drift ratio experienced by the building for stronger earthquakes. The latter could be attributed to the early softening of the CRuC base-isolators due to high force demand. The softer branch of the CRuC bilinear stress-strain behaviour possess higher damping and a lesser acceleration response.

Eurocode 8 prevents excessive damage by limiting the inter-storey drift ratio (IDR) for the frequent earthquake (10% probability of exceedance in 10 years) as shown in Equation 5.3:

$$d_r v \leq \alpha_i h \tag{5.3}$$

where d_r is the design storey drift calculated from the difference of the top and bottom storey displacement at that storey, v is the reduction factor which accounts for the frequent earthquakes associated with serviceability and is equal to 0.5 for buildings with importance class I and II, α_i is equal to 0.01 for buildings without non-structural elements, and h is the storey height. Table 5.6 shows the values of $(d_r \cdot v)/\alpha$ values and the corresponding check against the corresponding storey height.

Table 5.6: Eurocode 8 inter-storey drift limitation check; values in table are (dr·ν)/α

PGA	Fixed-base				Base-isolated#2			
	Level 1 (3.6 m)	Level 2 (3.3 m)	Level 3 (3.3 m)	Roof (3.3 m)	Level 1 (3.6 m)	Level 2 (3.3 m)	Level 3 (3.3 m)	Roof (3.3 m)
0.30g	1.60 ✓	1.75 ✓	2.31 ✓	2.04 ✓	0.77 ✓	0.81 ✓	1.04 ✓	0.84 ✓

(dr·ν)/α values shown are in meters, and compared to 3.6 or 3.3 m depending on storey height.

The limitation of inter-storey drift of the fixed-base building is safe for the frequent earthquake. The base-isolated#2 building passes the inter-storey drift check for all levels with a better safety margin than the fixed-base building.

Figure 5.24 shows the time-history IDR of the third storey (Level 3), for the three PGA excitations, along with drift limits as given by VISION 2000 (SEAOC, 1995). VISION 2000 specifies an IDR of 0.2% as fully operational (FO), 0.5% imposes minor damage to the building but still operational (O), 1.5% is heavy damage with possible risk to life safety (LS), and an IDR of 2.5% indicates the building is in a near collapse (NC) state due to severe damage.

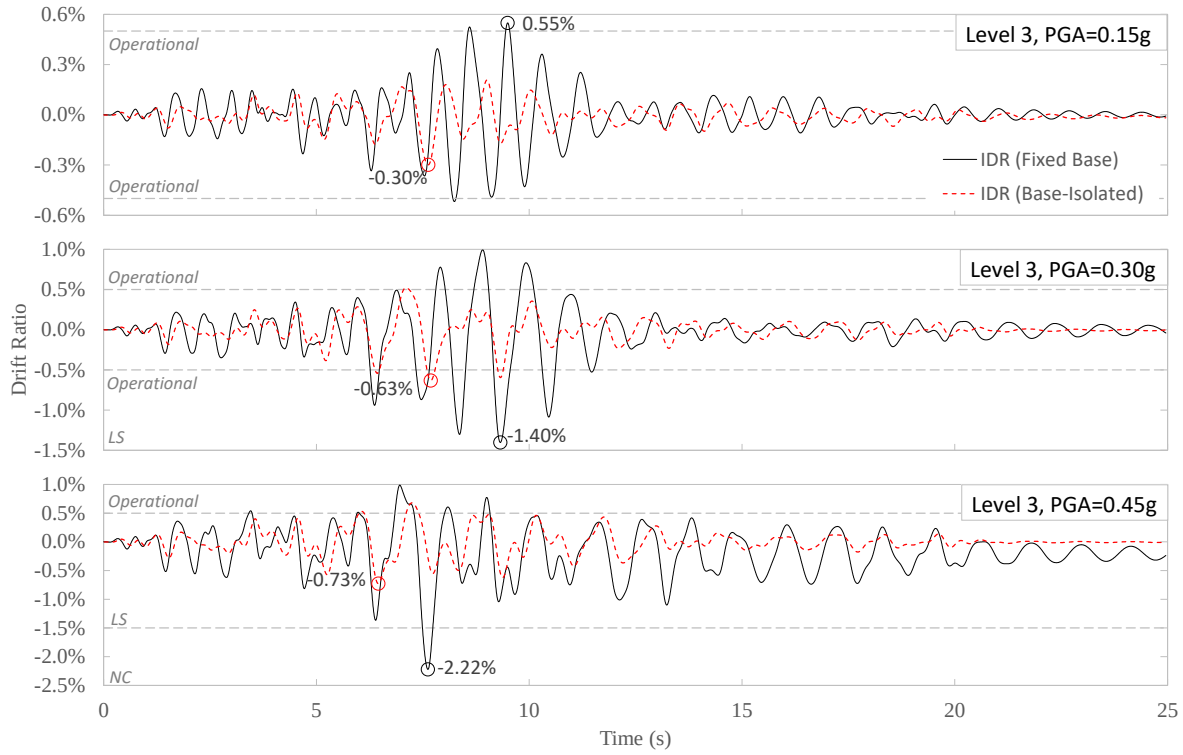

Figure 5.24: Time-history inter-storey drift of the third floor

In general, the time-history response of the base-isolated building had less inter-storey drift. However, few peaks were out-of-phase due to the different structural period and this led to higher IDR for the base-isolated building at some instances. That being said, the maximum drift recorded for all PGA excitations was always higher for the fixed-base building. Due to the change of stiffness between the second and third floor, the third floor IDR is the biggest among the other floor. Although none of the buildings reached a near collapse condition, an IDR of 2.22% was reached at Level 3 of the fixed-base building, during the 0.45g PGA earthquake, which indicates heavy to severe damage of the structure. The base-isolated*#2* level 3 drift only crosses the operational drift limit during the 100% and 150% of the design PGA, at 0.63% and 0.73% drift ratio, respectively.

Figure 5.25 shows the time-history inter-storey drift ratio, and drift value in mm, for the base-isolation foundation level. The latter seismic results are not compared against any drift limits, as the foundation level is supposed to accommodate for large drifts, and the base-isolator columns are designed for this, unlike regular structural elements.

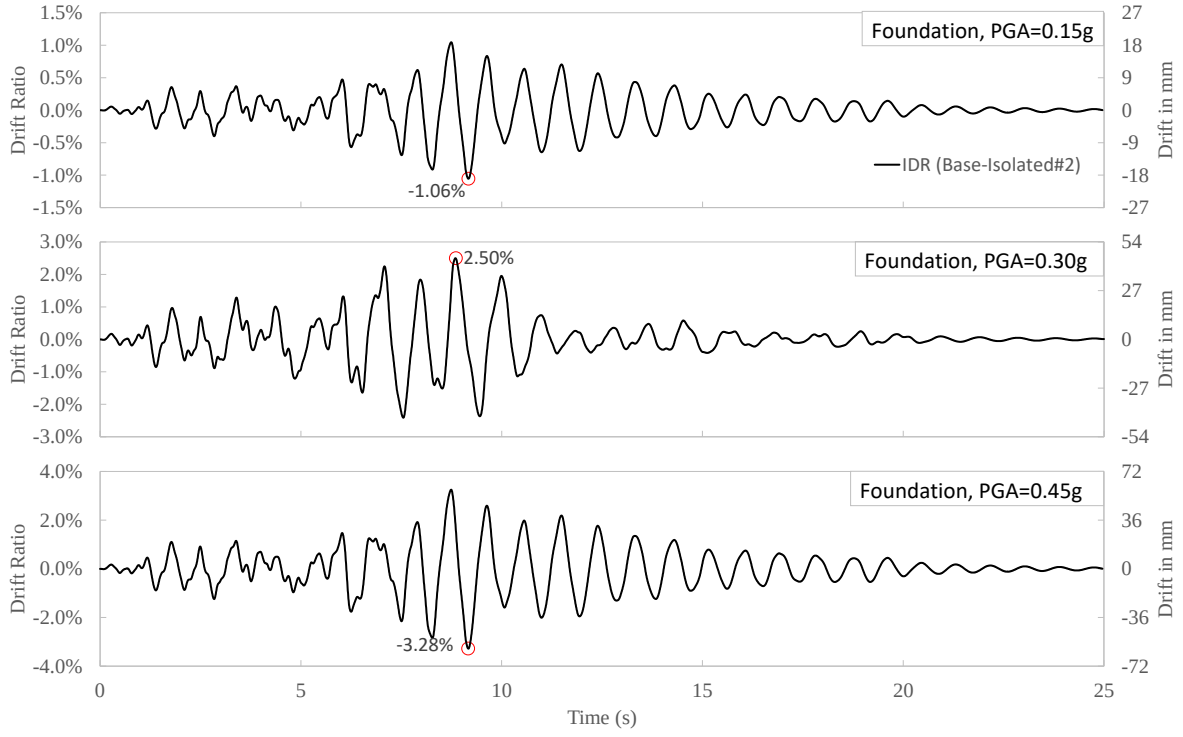

Figure 5. 25: Time-history inter-storey drift of the base-isolation foundation level

5.3.3.3 Second order effects

Eurocode 8 provides the criterion for considering second order effects (or P-Δ effects) based on the inter-storey drift sensitivity coefficient "θ" for the ultimate limit state (rare/design earthquake with 10% probability of exceedance in 50 years). Theta (θ) is defined according to the following equation.

$$\theta = \frac{P_{tot} \cdot d_r}{V_{tot} \cdot h} \tag{5.4}$$

where d_r is the inter-storey drift as described in Equation 5.3, h is the storey height, P_{tot} is the total gravity load at and above the storey as per the seismic design (DeadLoad + 0.3*LiveLoad), and V_{tot} is the total seismic storey shear obtained from the analysis.

If Theta (θ) is less than 0.1, then P- Δ can be neglected, and if $0.1 < \theta < 0.2$, then second order effects need to be accounted by multiplying the seismic action by $1/(1-\theta)$.

Table 5.7 show the input needed for the calculation of the inter-storey drift sensitivity coefficient, for the 0.30g excitation which has a return period of 475 years.

Table 5. 7: Determination of the inter-storey drift sensitivity coefficient θ (PGA=0.30g)

	Fixed-base					Base-isolated#2				
	d_r (m)	P_{tot} (kN)	h (m)	V_{tot} (kN)	θ	d_r (m)	P_{tot} (kN)	h (m)	V_{tot} (kN)	θ
Roof	0.041	407	3.3	196	0.026	0.017	407	3.3	127	0.016
Level 3	0.046	850	3.3	331	0.036	0.021	850	3.3	222	0.024
Level 2	0.035	1322	3.3	404	0.035	0.016	1322	3.3	272	0.024
Level 1	0.032	1799	3.6	493	0.032	0.015	1799	3.6	336	0.023
Foundation	-	-	-	-	-	0.045	2279	1.8	362	***0.157***

Figure 5.26 and 5.27 show graphically the storey drift, cumulative axial load, storey shear, and the inter-storey drift sensitivity coefficient θ for the Fixed-base and Base-isolated#2 building, respectively, for the 0.30g excitation which has a return period of 475 years.

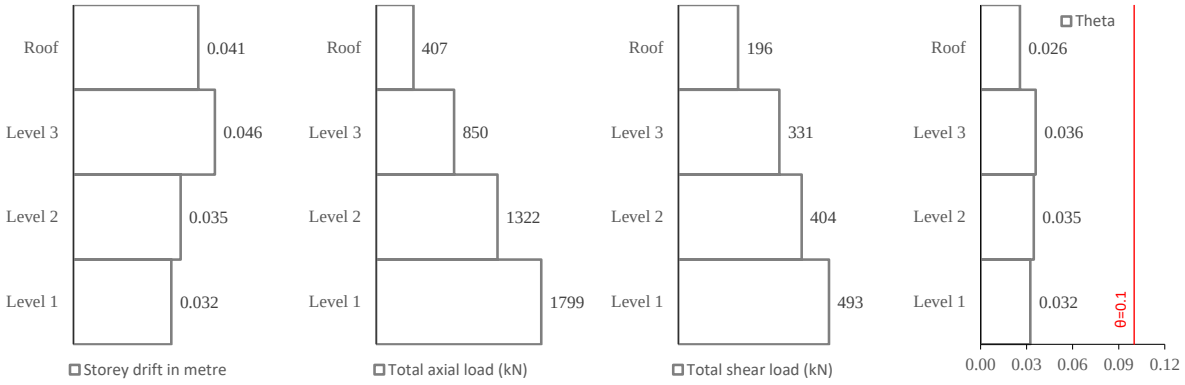

Figure 5. 26: Storey drift (m), cumulative axial load (kN), storey shear (kN), and sensitivity coefficient θ (Fixed-base, PGA=0.30g)

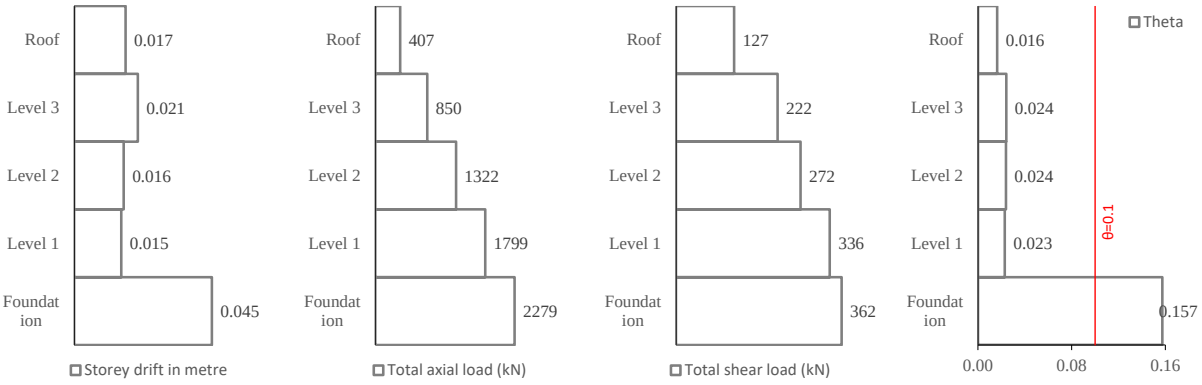

Figure 5. 27: Storey drift (m), cumulative axial load (kN), storey shear (kN), and sensitivity coefficient θ (Base-isolated#2, PGA=0.30g)

In the case of the fixed-base building, the second order effects may be neglected as the inter-storey drift sensitivity coefficient is smaller than 0.1 for all storeys. The same is true for the base-isolated building, except for the foundation level, or the base-isolator level. θ = 0.197 for the 0.45g PGA excitation. However, as the foundation level acts as a base-isolation system that decouples the structure from the ground, it is permissible to have θ higher than 0.1, since the elements are designed for this high drift and shear capacity. The Eurocode 8 check for P-Δ effects applies to the main structural elements.

5.3.3.4 Maximum roof displacement and acceleration

Table 5.8 shows the maximum roof displacement relative to the ground level, and the maximum roof acceleration for the fixed-base and base-isolated#2 building.

Table 5.8: Maximum roof displacement relative to ground, and maximum roof acceleration

PGA	Maximum roof displacement (cm)			Maximum roof acceleration		
	Fixed-base	Base-Isolated#2	Ratio*	Fixed-base	Base-Isolated#2	Ratio
0.15g	5.35	3.47	0.65	0.39g	0.28g	0.72
0.30g	13.1	6.62	0.50	0.65g	0.45g	0.69
0.45g	20.8	7.20	0.35	0.84g	0.58g	0.69

*Ratio of the base-isolated building's performance parameter to that of the fixed-base building.

The base-isolated building experienced on average, between 35-65% less roof displacement compared to the fixed-base building, as well as 28-31% less roof acceleration, significantly less than the response of the first isolation design (Figure 5.28). The reduction is more evident throughout the middle of the excitation time-history, which could be owed to the CRuC base-isolators getting more activated at high accelerations.

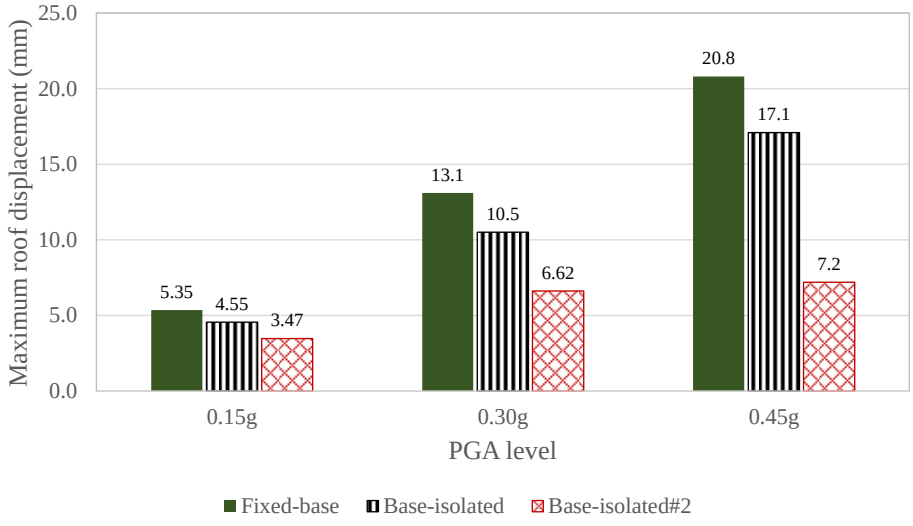

Figure 5. 28: Maximum roof displacement for the three buildings

Figure 5.29 and 5.30 show the time-history maximum roof displacement and maximum roof acceleration, respectively.

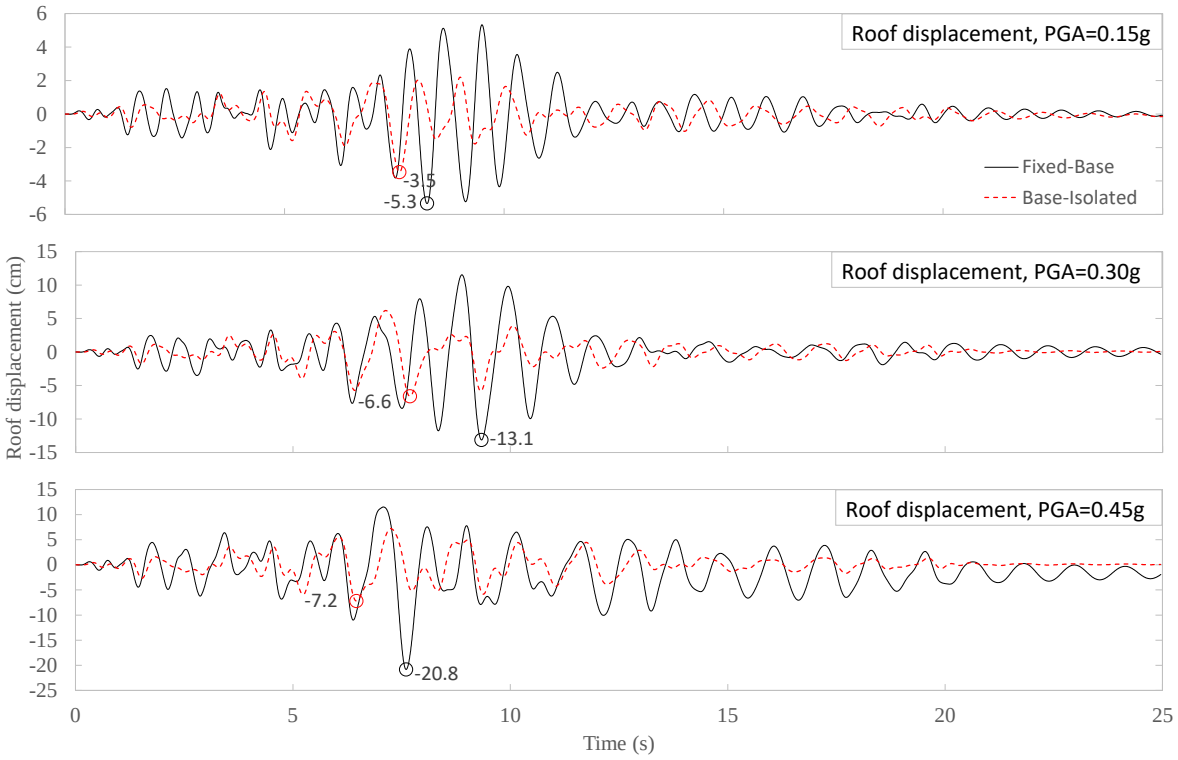

Figure 5.29: Time-history roof displacement relative to ground (Base-isolated#2)

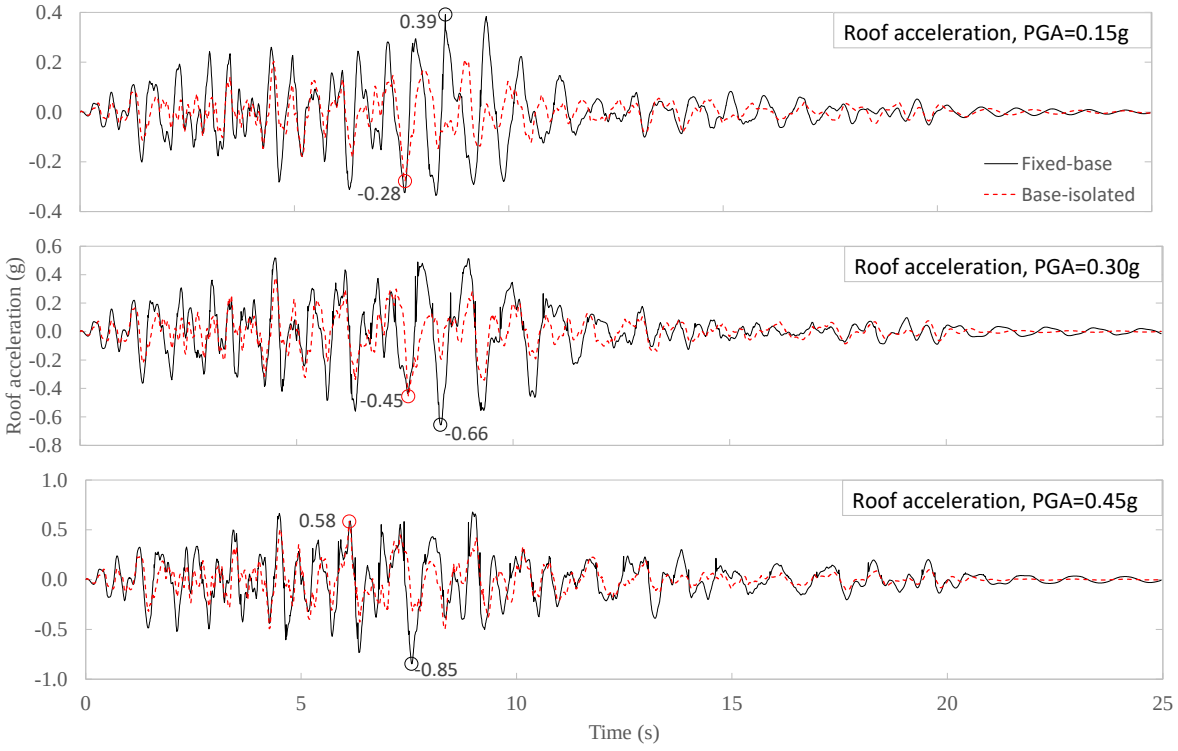

Figure 5.30: Time-history roof acceleration (Base-isolated#2)

5.3.3.5 Maximum base shear and moment

Table 5.9 shows the maximum base-shear and base-moment recorded for the fixed-base and base-isolated#2 buildings.

Table 5.9: Maximum base-shear and base-moment for the fixed-base and base-isolated#2 building

PGA	Maximum base-shear (kN)			Maximum base moment (kNm)		
	Fixed-base	Base-Isolated#2	Ratio*	Fixed-base	Base-Isolated#2	Ratio
0.15g	338	249	0.73	728	280	0.38
0.30g	493	362	0.73	1003	431	0.43
0.45g	566	385	0.68	1005	459	0.46

*Ratio of the base-isolated building's performance parameter to that of the fixed-base building.

The base-isolated building experienced on average, between 28-32% less base-shear compared to the fixed-base building. This is mainly attributed to the lesser spectral acceleration response of the base-isolated building due to the period shift. The base-shear reduction of the base-isolated*#2* building was higher than the first isolation setup, which is expected due to the less force demand imposed on the structure.

The base-moment of the base-isolated*#2* building was significantly less than that of the fixed-base (54-62% reduction), however, more than the original base-isolated building setup (63-71% reduction). That is mainly due to the higher base-isolators which increased the moment resisted at the base, also due to the lower number of the isolators. None of the CRuC base-isolators reached their ultimate/maximum moment capacity.

Figure 5.31 and 5.32 compare the maximum base-shear and base-moment recorded for the fixed-base building, and the two base-isolated buildings.

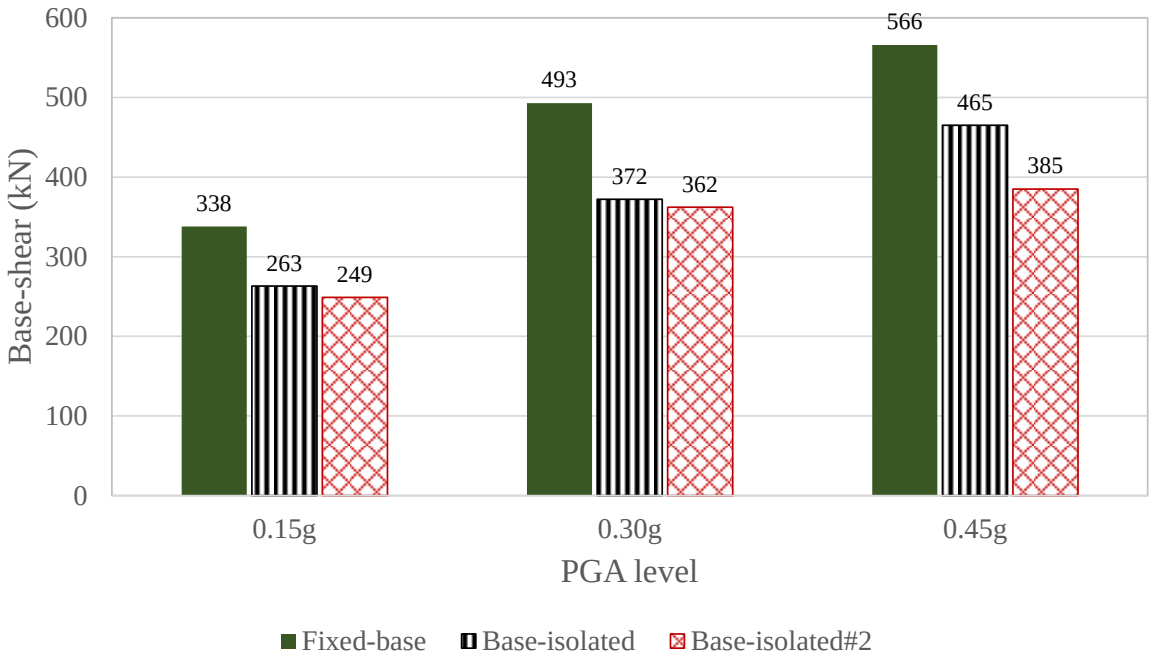

Figure 5. 31: Maximum base-shear for the three buildings

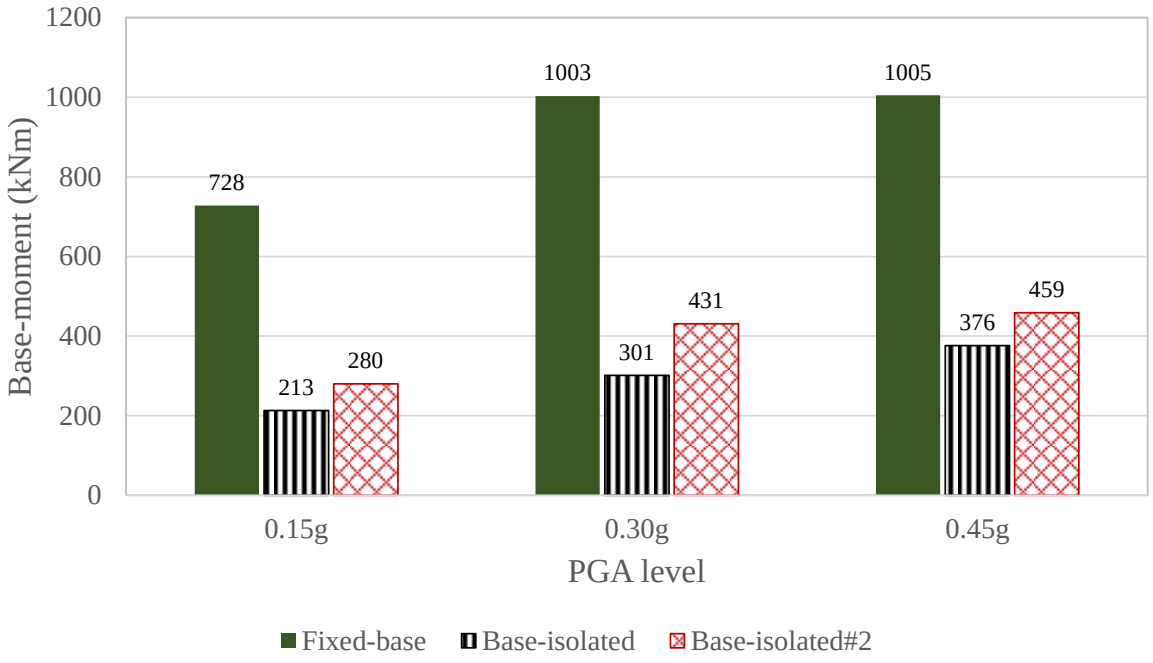

Figure 5. 32: Maximum base-moment for the three buildings

Figure 5.33 and 5.34 show the time-history base-shear and base-moment, respectively.

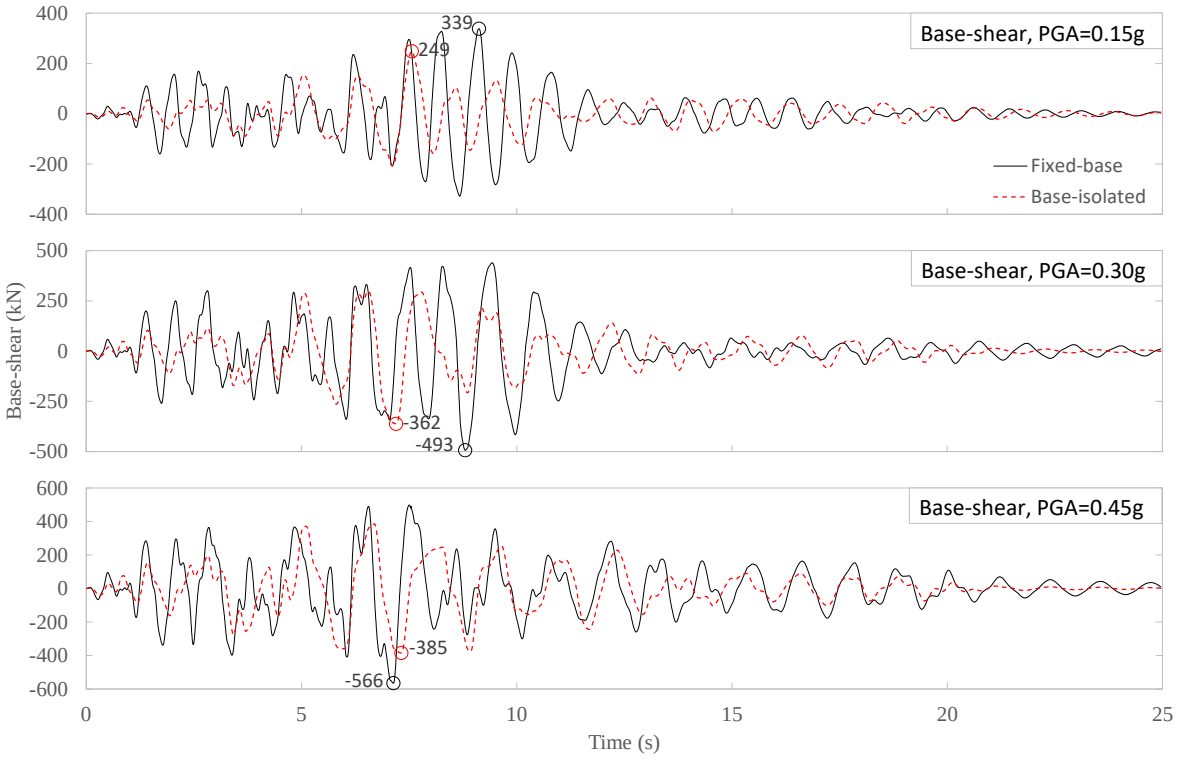

Figure 5.33: Time-history base-shear response in kN (base-isolated#2)

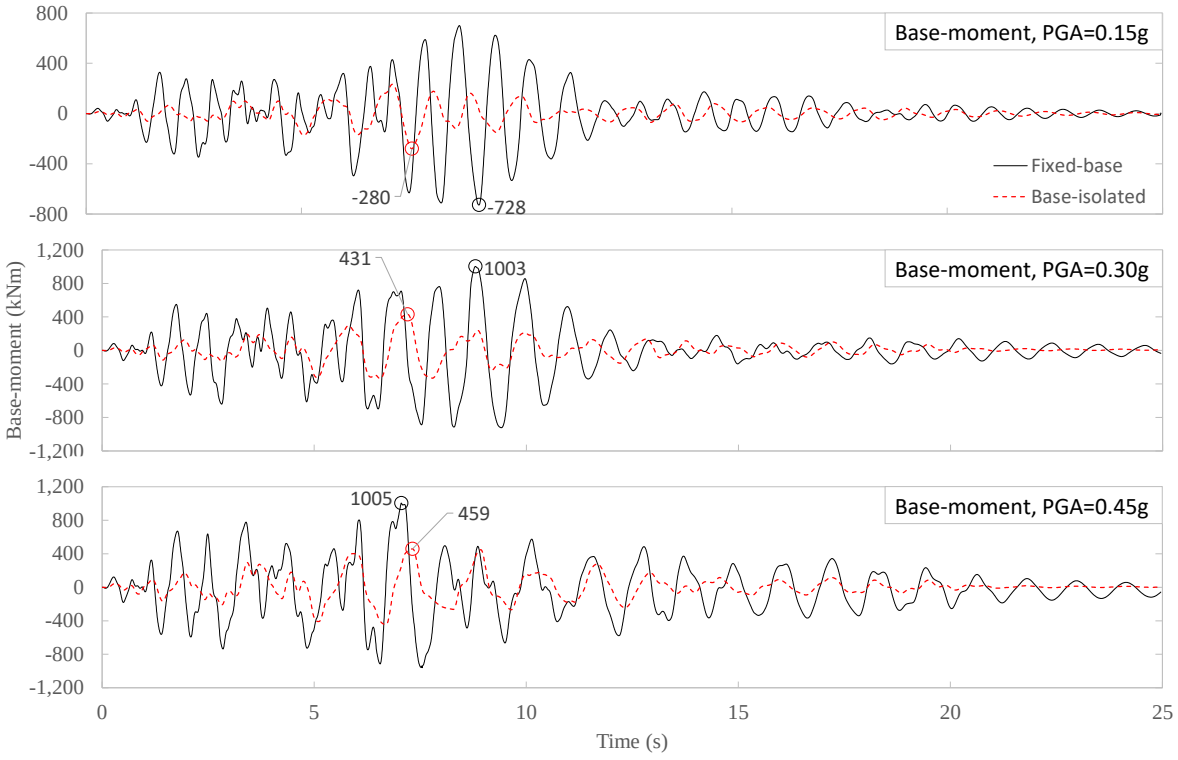

Figure 5.34: Time-history base-moment response in kNm (base-isolated#2)

5.4 CONCLUDING REMARKS

The CRuC-EQ building discussed in Chapter 4 was mounted on four columns made of CRuC, which were supposed to act as base-isolators. However, for the first four PGA excitations (0.14,0.2,0.28, and 0.4g), the drift in the base-isolated building (CRuC-ISO) was larger than that of the fixed-base building (CRuC-EQ) tested in Chapter 4. The main reason for that was the damaged state of the superstructure in the CRuC-ISO system; a much softer superstructure meant higher displacement response. Also, the natural period of the CRuC-ISO system was found to be on the plateau of the elastic response spectrum, which meant the response amplification factor was much higher. During the 1.6g and 2.0g PGA tests, the CRuC base-isolators were pushed towards the linear hardening phase of their hysteresis behaviour, due to the large applied ground acceleration. This reduced the isolators' stiffness and hence shifted the natural period of the system; 0.76 and 1.2 s after the 1.6g and 2.0g tests, respectively. This in turn reduced the response acceleration and imposed displacement of the structure, when compared to the fixed-base experimental results (CRuC-EQ in Chapter 4).

The response of a fixed-base building, was compared to the response of the same building with two different base-isolation systems made of CRuC. In both isolated buildings, the response was better than the fixed-base, in terms of IDR, roof acceleration and displacement, and base-shear and moment. As the softer CRuC isolation system was able to shift the natural period of the initial system to a longer period, the building with less CRuC isolators and 20% larger height exhibited a significantly better performance than the stiffer base isolation system design. The results of these simulations provide enough evidence that a base-isolation system made of CRuC is feasible. While the proof-of-concept of such a system was provided, the design and optimisation of each system should be, site, and structure specific, and should be addressed in future research. Furthermore, the direct displacement-base design method may be used to obtain the required stiffness of the isolators, based on a target design displacement.

5.5 REFERENCES

Bompa, D. V., Elghazouli, A. Y., Xu, B., Stafford, P. J., & Ruiz-Teran, A. M. (2017). Experimental assessment and constitutive modelling of rubberised concrete materials. *Construction and Building Materials*, *137*, 246–260. https://doi.org/10.1016/j.conbuildmat.2017.01.086

CSI. (2021). *SAP2000 Integrated Software for Structural Analysis and Design* (23.0.0). Computers and Structures Inc.

Dipasquale, E., Ju, J., Askar, A., & Cakmak, A. S. (1990). RELATION BETWEEN GLOBAL DAMAGE INDICES AND LOCAL STIFFNESS DEGRADATION. *Journal of Structural Engineering, ASCE*, *116*(5), 1440–1456.

EN 1992-1-1. (2004). *Eurocode 2: Design of concrete structures - Part 1-1: General rules and rules for buildings*. Comité Européen de Normalisation (CEN).

EN 1998-1. (2004). Eurocode 8: Design of structures for earthquake resistance - Part 1: General rules, seismic actions and rules for buildings. In *Comité Européen de Normalisation (CEN)*.

Garcia, R., Pilakoutas, K., Hajirasouliha, I., Guadagnini, M., Kyriakides, N., & Ciupala, M. A. (2017). Seismic retrofitting of RC buildings using CFRP and post-tensioned metal straps: shake table tests. *Bulletin of Earthquake Engineering*, *15*(8), 3321–3347. https://doi.org/10.1007/s10518-015-9800-8

Raffoul, S., Escolano-Margarit, D., Garcia, R., Guadagnini, M., & Pilakoutas, K. (2019). Constitutive Model for Rubberized Concrete Passively Confined with FRP Laminates. *Journal of Composites for Construction*, *23*(6), 04019044. https://doi.org/10.1061/(asce)cc.1943-5614.0000972

SEAOC. (1995). *Vision 2000: Performance Based Seismic Engineering of Buildings*.

Chapter 6

Summary and conclusions, and recommendations for future work

6.1 SUMMARY AND CONCLUSIONS

The main aim of this research work was to examine the behaviour of CRuC in structural elements with high deformation demand. A series of experimental tests, both monotonic and dynamic, were carried out along with complementary numerical and analytical modelling to evaluate the performance of CRuC short columns and base-isolators. This section summarises the main aspects of this research work and draws the main conclusions from the relevant chapters.

6.1.1 Behaviour of CC short columns

The behaviour of CC short columns was examined experimentally by testing two equivalent buildings. One building was tested under monotonic lateral loading, while a similar building was tested on a shake table under dynamic loading. Both buildings failed at the location of the short columns in a brittle shear failure. The crack pattern that developed in the short columns of both tests was similar, thus confirming the development of a similar load transfer mechanism (ie. compression strut and tie). The results from these experimental test phases were used to develop a strut-and-tie macro element, which was then implemented in a series of analytical models.

At the point of failure of the CC-STC short columns, there were no signs of damage to any other structural elements. Similarly, the CC-EQ building showed no signs of yielding in the steel before reaching the PGA excitation that caused collapse. The latter can also be inferred from the relatively small increase in the natural period of CC-EQ with test progression. This is mainly due to the relatively high stiffness of the short columns, which attracts higher load, and limits the global deformability of the building, which in turn prevents the utilization of the resistance of other structural elements in the building. The CC-STC building reached its peak capacity at a drift ratio for the short columns of 1.5%, which is equivalent to 0.37% for the unrestrained column.

6.1.2 Behaviour of CRuC short columns

A one-bay one-storey building with short columns made of CRuC was tested dynamically on a shake-table. The CRuC-EQ building was softer than its CC-EQ counterpart due to the low stiffness of the rubberised concrete, which led to a slightly higher roof displacement. The building was able to withstand all the excitations of the seismic load protocol, up to 2.0g PGA, after which the test had to be halted as the limit of the table was reached.

The stiffness of the CRuC-EQ building after the 1.60g and 2.0g PGA tests was 3.9 and 3.8 kN/mm, respectively. This indicates that the CRuC short columns developed a bilinear hysteresis behaviour as described in the four-phase model discussed in Chapter 3. The natural period of the CRuC-EQ building after the end of the testing was 4.4 times the undamaged period.

The CRuC short column sustained a maximum drift of 7.7% during the 2.0g PGA test, which supports the hypothesis of using CRuC in high ductility/deformability demand regions of the structure.

6.1.3 Numerical and analytical modelling of short columns

A FE model of the CC-STC building was built and validated against the experimental results. Good agreement was found in the global behaviour of the building, as well as the local stress concentration (ie. strut formation) in the short column. To overcome the high computational cost of FE models, a STM was proposed to simulate the behaviour of short columns and carry out comprehensive dynamic analyses. The model was implemented in OpenSees and was validated against the experimental results obtained from the test on the CC-STC building.

The FE model was then modified to replace the CC in the short column with RuC and confine it, explicitly, with AFRP sheets. The SCME was also modified to account for CRuC material, making use of constitutive models for CRuC. The lateral response of the frame with CRuC

short columns could be summarised in a four-phase model: an Elastic phase (I), a Transition phase (II), a Linear hardening phase (III), and finally a Yielding phase (IV).

The analytical model was then validated against shake-table tests on buildings with CC and CRuC short columns. Good agreement was achieved, which demonstrates the seismic analysis capability of the developed SCME.

The FE models and analytical STM allow for parametric studies to be performed on the different percent replacement of rubber, or number and type of layers of FRP.

Guidelines on how to determine the geometry and dimension of the elements of the STM (SCMEs) were presented and a strength reduction formulation was also proposed to account for the effect of the inclination of the strut on its strength (for CC and CRuC).

6.1.4 Base-isolation using CRuC elements

6.1.4.1 Experiment: CRuC-ISO

The CRuC-EQ building was retrofitted and mounted on top of four circular columns made of CRuC which constituted the base-isolation system. The CRuC base-isolators were able to safely undergo 10% drift (60 mm displacement), and up to 17.6% drift during the 2.0g PGA that caused the rupture of the AFRP. The maximum recorded AFRP strain during the 2.0 PGA test was 1.16%. The isolators were able to reduce the roof acceleration and displacement by a factor of 0.61 and 0.70 as compared to the fixed-base response (for the PGA=2.0g level).

6.1.4.2 Analytical comparative evaluation

Although the CRuC-ISO experiment proved the base-isolators to be highly ductile/deformable, due to the nature of the setup and using pre-tested building, a direct comparison between fixed-base and base-isolated buildings was not possible. To gain additional insights, an analytical model was built to examine the seismic response of a reinforced concrete frame designed according to EC8, with a fixed base and with a base-isolation system made of a series of CRuC slender columns.

The base-isolated building's natural period was 21% longer than that of the fixed-base. As the damage was mainly concentrated in the base-isolators, the GDI of the superstructure of the base-isolated solution ranged between 0.18-0.42, while a higher GDI (0.46-0.69) was observed for the fixed-base building. The inter-storey drift of the base-isolated building was up to 25% less than that of the fixed-base. The base-shear was also less, between 18-25%, for the base-isolated building and the base-moment was reduced by 71%.

Due to the significantly less base-moment and shear demand on the first design of the base-isolation system, a second, softer, design was analysed. The softer system was achieved by increasing the height of the isolators to 1.8 m, and decreasing their number to 13 isolators. The overall performance of the softer base-isolation system was better than the initial design. The new T was 58% longer than that of the fixed-base. The damage measured through the GDI ranged between 0.08-0.25. More noteworthy was the reduction in IDR, up to 67%, as well as the roof displacement, up to 65%. The base-shear and base-moment were also reduced, up to 32% and 62%, respectively.

The experiment and analytical models in Chapter 5 prove that CRuC can be used as a cost-effective alternative to conventional base-isolating systems.

6.2 RECOMMENDATIONS FOR FUTURE WORK

This section outlines recommendations for future research work related to this thesis.

6.2.1 Elements with high shear and deformation demand

1) This research work provides an experimental and numerical proof-of-concept that CRuC can be used in structural elements that have a high shear demand and need to accommodate large deformations. While short columns are one example of these elements, there are other scenarios where CRuC could replace CC to solve the problem of brittle failures. One such example would be in the short-beam section of eccentrically braced frames. Experimental tests should be carried out to validate the feasibility of constructing such an element out of CRuC, while the numerical and analytical models developed in this thesis can be easily extended to fit similar structural elements.

2) A parametric study could be performed using the SCME described in this thesis to study the effect of different types of confinement, number of layers of FRP sheets, and different rubber replacement percentage.

3) The SCME analytical model implemented in OpenSees could be used to model a full-scale building with multiple storeys with short columns on all or some of the storeys. While the benefit of CRuC short columns over CC ones was proven in this thesis, the global performance of a multiple-bay multiple-storey building needs to be studied to further the effect of CRuC short columns, and propose design guidelines for using this novel solution in buildings.

6.2.2 Design and optimisation of CRuC base-isolators

The key idea behind a base-isolation system is to shift the global structural period to longer periods where the response accelerations are reduced, at the expense of larger displacements. However, the displacements are ensured to be contained in the base-isolating system/foundation where they are able to accommodate for large drifts. To ensure this period shift is efficient, the base-isolators have to be relatively soft.

1) This research work uses a RuC material with 60% by volume replacement of aggregates with rubber crumb and finer particles. One way to ensure a softer CRuC base-isolator is to use higher percentage of rubber replacement, which would lower the young's modulus of the RuC as well as its strength. However, with adequate confinement, the strength could be restored to acceptable levels, while maintaining high deformability.

2) Another way to create a soft foundation for base-isolation is to reduce the number of the base-isolators. The work presented in Chapter 5 proved that the CRuC base-isolation foundation reduces the shear and moment demand significantly, and this means that less base-isolators are needed. This opens up the research work to be done on properly designing the base-isolator cross-section on an individual level, as well as the global design pertaining to the number of base-isolators and their distribution at the foundation level.

3) The base-isolation system investigated in this thesis was completely made of CRuC base-isolators, ie. a full replacement of a typical lead rubber bearing system. It is worth investigating a combination of systems that comprise CRuC base-isolators alongside other damping devices such as viscous dampers. The latter will ensure high damping of the system, while the low stiffness and high deformability of the CRuC base-isolators will keep the system stable. Another hybrid system could include LRB with CRuC base-

isolators, or a friction pendulum with CRuC. All of these options could have special merits over the others, with the high ductility of CRuC being the common factor with all of them.

This page is intentionally left blank

Appendix A

Material related to Chapter 3

A1: MESH INSENSITIVITY VERIFICATION

To check that the concrete material model used produces results that are near mesh independent, a 150×150 mm cube with three different mesh sizes – 25, 50, and 150 mm – was simulated under uniaxial tension (displacement control).

Table A1.1 shows the parameters of the model outlined by Alfarah et al. (2017), which were calculated for the concrete properties described in Chapter 3. An iterative procedure is performed to obtain the value of "b", which is a constant equal to the average of plastic compressive strain (ε_c^{pl}) divided by the inelastic compressive strain (ε_c^{in}). The latter is part of the compressive constitutive model used in Alfarah et al.'s model in this study, and it was originally developed by Krätzig and Pölling (2004) (Alfarah et al., 2017; Krätzig & Pölling, 2004).

Table A.1: Parameters for defining the concrete material model in Abaqus

Mesh ID	L_{eq} (mm)	f_{cm} (MPa)	f_{ct} (MPa)	G_F (N/mm)	G_C (N/mm)	b	a_c	a_t	b_c	b_t
Fine	25	37	3.3	0.13	13	0.95	7.87	1	103	885
Medium	50	37	3.3	0.13	13	0.89	7.87	1	208	1770
Coarse	150	37	3.3	0.13	13	0.64	7.87	1	623	5310

The parameters in Table A.1 are used to generate the CDP material model relation in compression and in tension, which was used as input to the cube material. L_{eq} is the characteristic length of the finite element, and in the case of a cubic brick element it is equal the length of the side. a_c, a_t, b_c, and b_t are dimensionless parameters used in the definition of the model parameters and iteration.

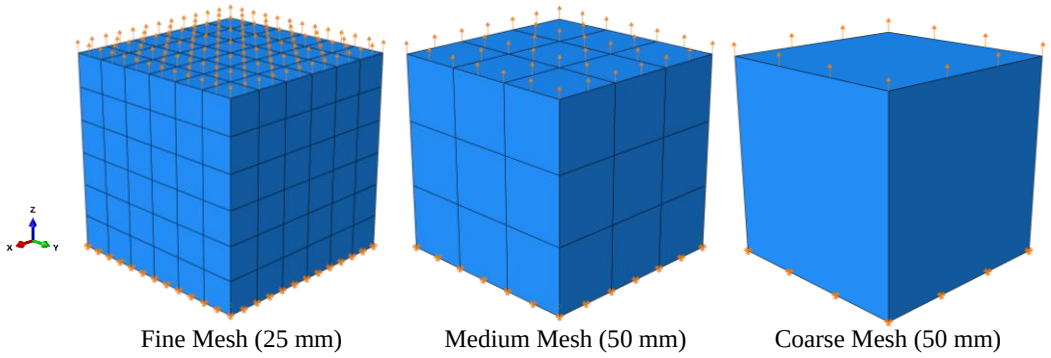

Figure A. 1: Load and boundary condition of the cube numerical test

The constitutive stress-strain relationships are in terms of L_{eq} which means different mesh sizes will have different shape for the material input, to give the precise energy (crushing or cracking) per one finite brick element. Figure A.2 shows the material input for this mesh insensitivity verification.

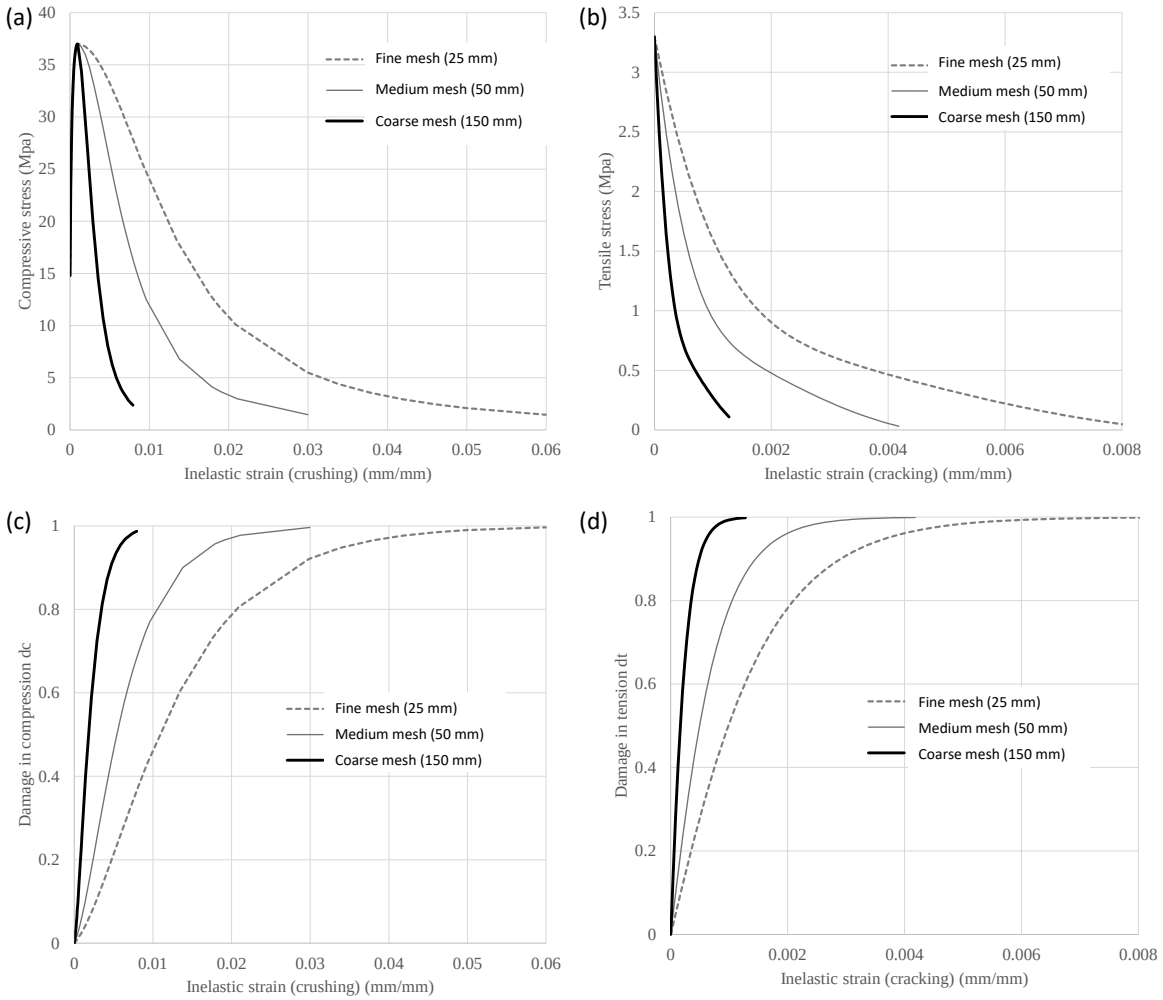

Figure A. 2: (a) Compressive stress-strain; (b) Tensile stress-strain; (c) Compressive damage vs. crushing strain; (d) Tensile damage vs. cracking strain

The load-displacement of the cube tensile analysis are shown in Figure A.3. The results are compared against the closed-form solution of this exercise. The closed-form solution provides the theoretical exact response of such a cube under pure uniaxial tension; it can be derived from equation A.1:

$$\frac{\sigma_t(w)}{f_t} = \left[1 + \left(c_1 \frac{w}{w_c}\right)^3\right] e^{-c_2 \frac{w}{w_c}} - \frac{w}{w_c}(1 + c_1^3) e^{-c_2} \tag{A.1}$$

$$w_c = 5.14 \frac{G_F}{f_t} \tag{A.2}$$

where w is the crack width, wc is the critical crack opening, c1 and c2 are cohesion parameters given by Hordijk (1992) as 3, and 6.93, respectively (Hordijk, 1992).

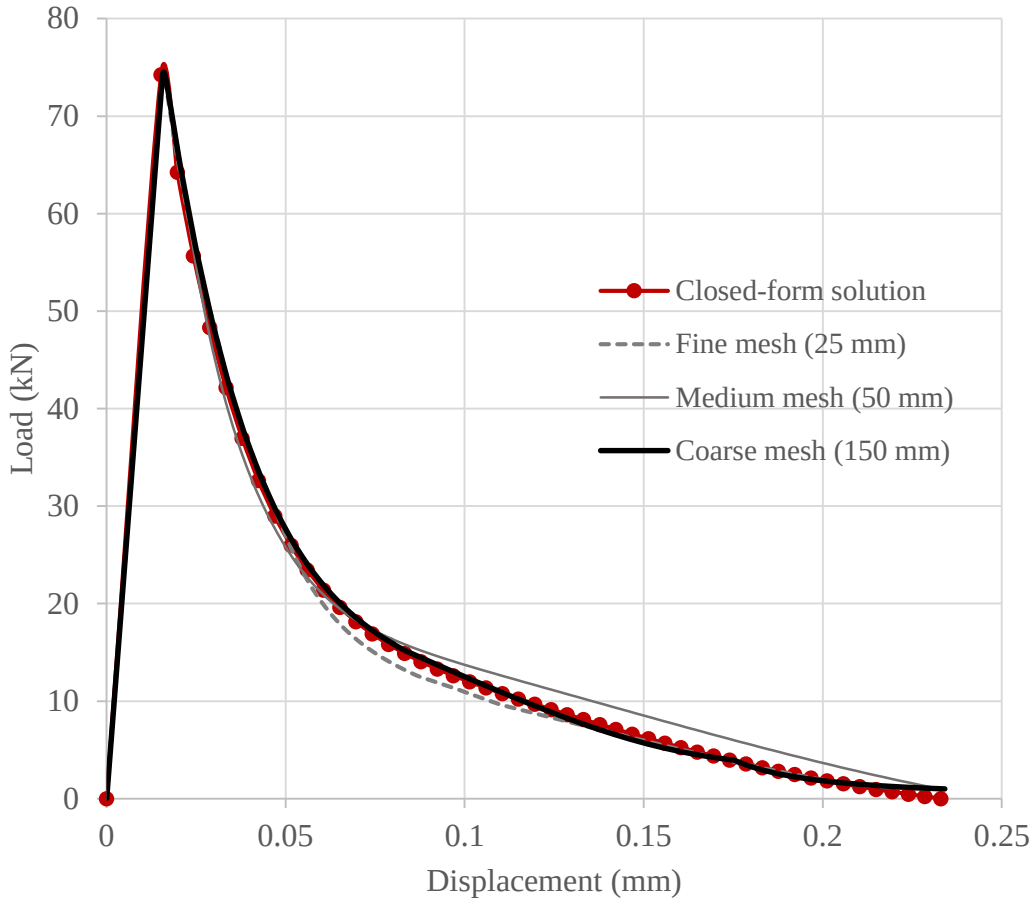

Figure A. 3: Load-dispalcement of the cube tensile analysis

A good agreement can be seen between the closed-form solution and the results of the various mesh size analysis. Figure A.4 below shows the damage in tension in the three cubes with different mesh sizes. For the fine and medium mesh, a single plane of elements reached the maximum permissible tensile damage indicating the crack plane.

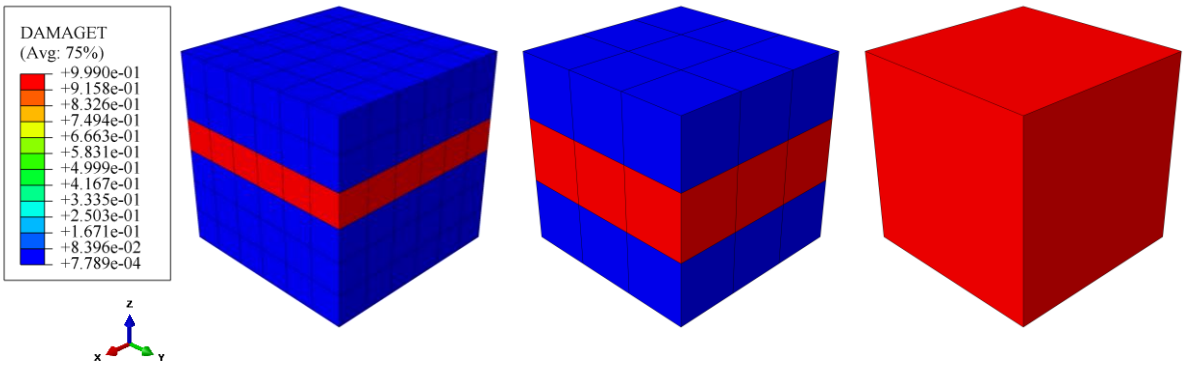

Figure A. 4: Damage in tension for the fine, medium, and coarse mesh

A2: SIMPLIFIED STM NODE POSITIONING FOR THE SCME

The research work on the SCME developed in Chapter 3 of this thesis included information gathered from FEA performed using Abaqus. The latter allowed for extra precision in the location of the centroid of the nodes, however, a more straightforward approach can be taken for general design procedures that do not require FE modelling.

Figure A.5 shows a schematic of the top and bottom nodes as well as the strut formation in a short column. The centroid of the bottom node can be taken along the top of the infill level, with the width w1 taken as the neutral axis depth at the yielding moment of the column (same as $w_{h,B}$ in section 3.4.2). The centroid of the top node can be taken as the intersection of the bottom longitudinal reinforcement of the beam, with the longitudinal reinforcement of the column opposite to the bottom node. The width of the top node can be taken as twice the distance from the centreline of the reinforcement to the concrete face (same as $w_{h,D}$ in section 3.4.2).

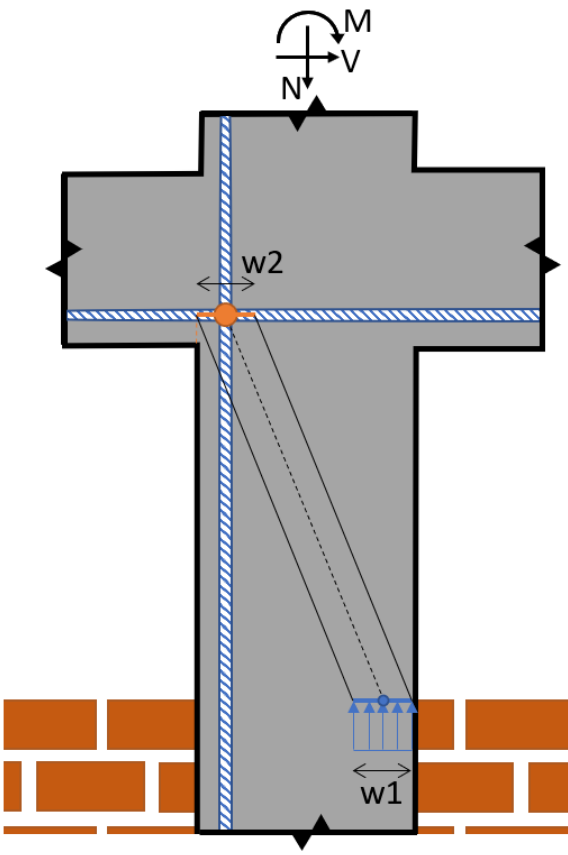

Figure A. 5: Schematic of the top and bottom node of the strut within a short column

A3: CONFINED STRENGTH RATIO USING MANDER'S CONFINEMENT MODEL

Mander et al.'s model (Mander et al., 1988), provides a framework to determine the confined strength ratio for rectangular sections based on the lateral confining stresses. The following is a worked example to get the ratio that was used in Chapter 3.

Due to symmetry of the square cross-section, only the calculation for the confining stresses in the x-direction are shown, and by symmetry they are equal to the ones in the y-direction.

Number of transverse shear bars running in the x-direction A_{sx}:

$$A_{sx} = \pi \cdot n_x \cdot \frac{d_{sx}^2}{4} \tag{A1}$$

where n_x is the number of transverse shear bars in the cross-section along the x-direction (= 2), and d_{sx} is the diameter of confining hoops in the x-direction (= 4 mm). $A_{sx} = 25\ mm^2$.

The area ratio of transverse reinforcement in the x-direction, ρ_x:

$$\rho_x = \frac{A_{sx}}{d_c \cdot s} = \frac{25}{106 \cdot 100} = 0.0024 \tag{A2}$$

$$d_c = b - 2 \cdot cover - d_{sx} = 150 - (2 \cdot 20) - 4 = 106\ mm \tag{A3}$$

where d_c is the core dimension to centrelines of perimeter hoop in y-direction (=b_c dimension in the x-direction), and s is the centre-to-centre spacing of the transverse reinforcement and is equal to 100 mm.

The confinement effectiveness coefficient K_e:

$$K_e = \frac{A_e}{A_{cc}} \tag{A4}$$

where A_e is the area of effectively confined concrete core, and A_{cc} is the area of the confined concrete within the core of the cross-section.

For one single rectangular shear hoop, without middle links, A_e is:

$$A_e = (d_c \cdot b_c)(1 - \frac{s'}{2b_c})(1 - \frac{s'}{2d_c}) \quad \text{(A5)}$$

Where s' is the clear spacing between two stirrups and is equal to (100-4=96 mm). Hence, $A_e = 3364\ mm^2$.

$$A_{cc} = A_c(1 - \rho_{cc}) \quad \text{(A6)}$$

where A_c is the area of the core section assumed to be defined by the centreline of the longitudinal reinforcement, and ρ_{cc} is the ratio of area of longitudinal reinforcement to the area of the core section.

For 6 longitudinal bars, each with a diameter of 14 mm:

$$A_c = (150 - 2 \cdot (20 + 4 + 7))^2 = 7744\ mm^2$$

$$A_{cc} = 7744\left(1 - \frac{6 \cdot \pi 7^2}{7744}\right) = 6820\ mm^2$$

Therefore, $K_e = 0.49$.

The lateral pressure from the transverse reinforcement in the x-direction f_{lsx}:

$$f_{lsx} = \rho_x \cdot f_{sy} = 0.0024 \cdot 255MPa = 0.61\ MPa \quad \text{(A7)}$$

The effective lateral confining pressure in the x-direction f'_{lsx}:

$$f'_{lsx} = f_{lsx} \cdot K_e = 0.61 \cdot 0.49 = 0.29\ MPa \quad \text{(A8)}$$

The confining stress ratio in the x-direction equals that in the y-direction:

$$f'_{lsx}/f_{cm} = f'_{lsy}/f_{cm} = 0.29/19 = 0.015 \quad \text{(A9)}$$

Using the correlation given in Mander et al., 1988, between the two confining stress ratios in the x- and y-directions, the confined strength ratio φ is obtained graphically as shown in Figure A6 below and found to be $\varphi = 1.1$:

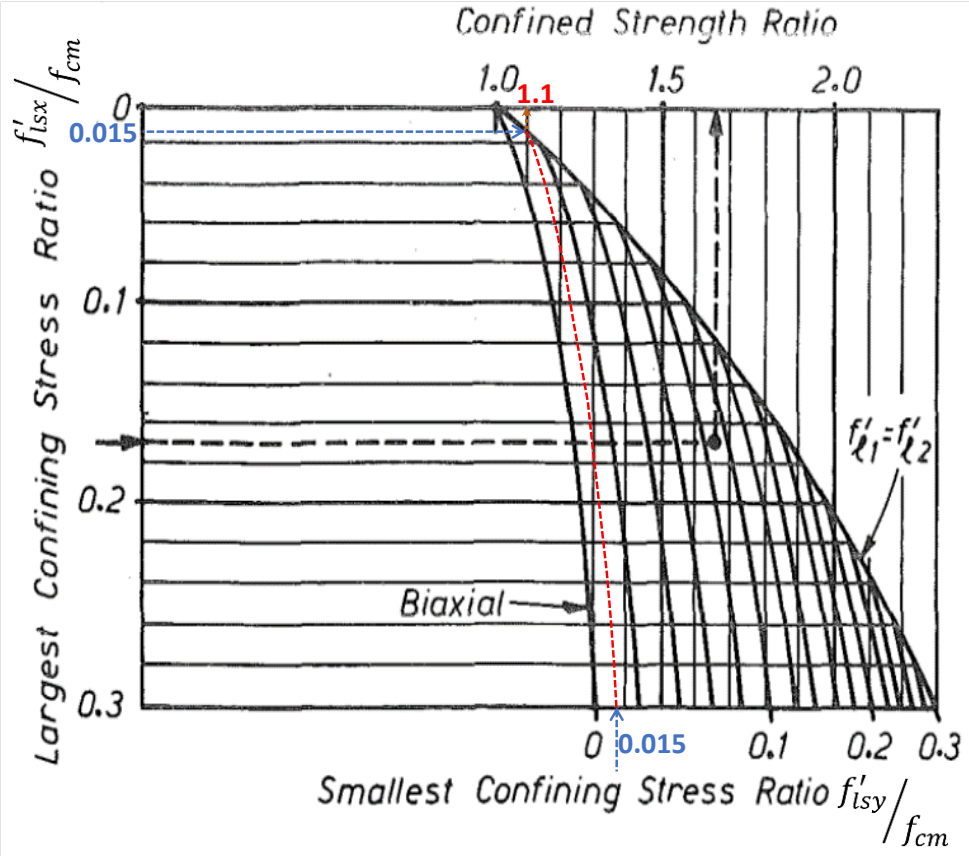

Figure A. 6: Confined strength determination from lateral confining stresses for rectangular sections based on Mander's confinement model

A4: CALIBRATION OF THE SHAPE FACTOR r_c IN CHANG AND MANDER'S CONCRETE STRESS-STRAIN MODEL

Equation A10, developed by Tsai and implemented in Chang and Mander's model, gives the stress-strain relation for unconfined concrete (Chang G. A. & Mander, 1994; Tsai, 1988).

$$y = \frac{nx}{1 + \left(n - \frac{r_c}{r_c - 1}\right)x + \frac{x^{r_c}}{r - 1}} \tag{A10}$$

$$x = \frac{\varepsilon_c}{\varepsilon_{cm}} \tag{A11}$$

$$y = \frac{\sigma_c}{f_{cm}} \tag{A12}$$

ε_c and σ_c are the compressive strain and stress, respectively. ε_{cm} is the compressive strain at peak stress. n and r_c are parameters that control the shape of the stress-strain curve and are defined by Chang and Mander as follows.

$$n = \frac{7.2}{f_{cm}^{3/8}} \tag{A13}$$

$$r_c = \frac{f_{cm}}{5.2} - 1.9 \tag{A14}$$

Formulae A10-A14 provide the cylinder full stress strain given the peak strength and strain. Palmquist and Jansen developed equation (A15) for post-peak strain that takes into account the aspect ratio of the element under compression (Palmquist & Jansen, 2001).

$$\varepsilon = \left(\varepsilon_{cm} + \frac{\sigma_c - f_{cm}}{E_c}\right)\frac{H_B}{H} + \frac{1}{V}\left(\frac{f_{cm}}{\sigma_c} - N\right)^M \frac{H_D}{H} \tag{A15}$$

$$H_B = H - H_D \tag{A16}$$

$$H_D = W\left(2 - \frac{\sigma_c}{f_{cm}}\right) \tag{A17}$$

H is the height of the specimen, H_D is the height of the damage zone in the specimen, and $H_B$is the height of the bulk zone beyond the damage zone (Figure A.7).

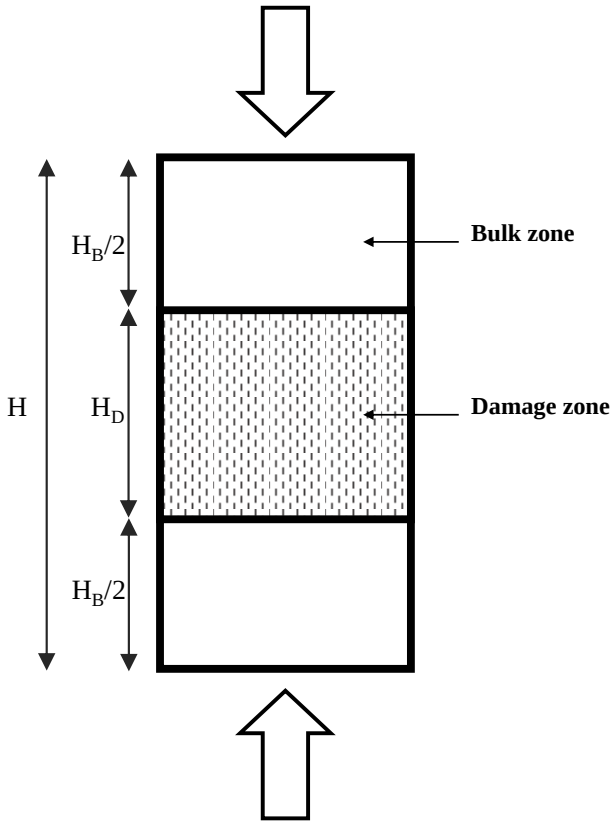

Figure A. 7: Definition of the compression damage zone according to Palmquist and Jansen

M, N, and V are empirical constants calibrated for each type of concrete based on the full stress-strain curve.

Palmquist and Jansen's post-peak strain model was calibrated to fit the stress-strain curve of Chang and Mander for a standard 100×200 mm cylinder (see Figure A.8, for $r_c = 5.2$). The empirical constants were found to be equal 0.145, 0.992, and 225 for M, N, and V, respectively. The post-peak behaviour was then modified according to the aspect ratio of the strut, which was calculated based on the equivalent diameter of the rectangular area, equal to 97 mm, and an element length of 358 mm. The shape factor r_c was then calibrated to fit the new post-peak behaviour for the strut (see Figure A.8, for $r_c = 10$).

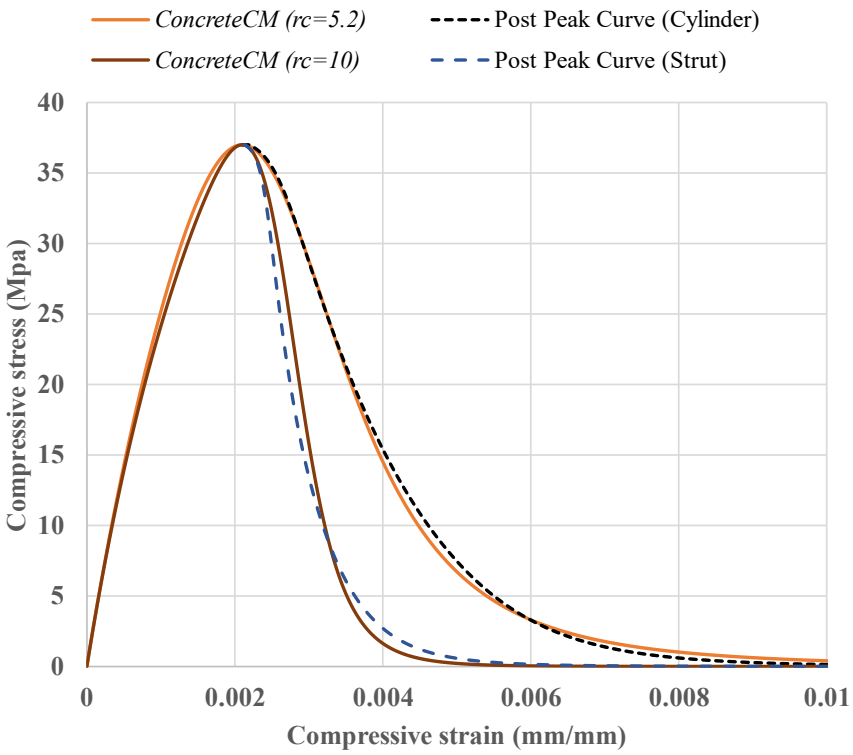

Figure A. 8: Calibration of the Shape Factor (rc) in Chang and Mander's compressive stress-strain model to account for the slenderness ratio of the concrete strut

A5: THE AXIAL, LATERAL, AND SHEAR STRESS-STRAIN BEHAVIOUR OF CRUC

Figure A.9-a describes the shear stress-strain behaviour of RuC and CRuC. The latter was obtained from an experimental setup on rectangular prismatic samples under asymmetric shear loading (see Figure A.9-b,c) (Wang et al., 2019).

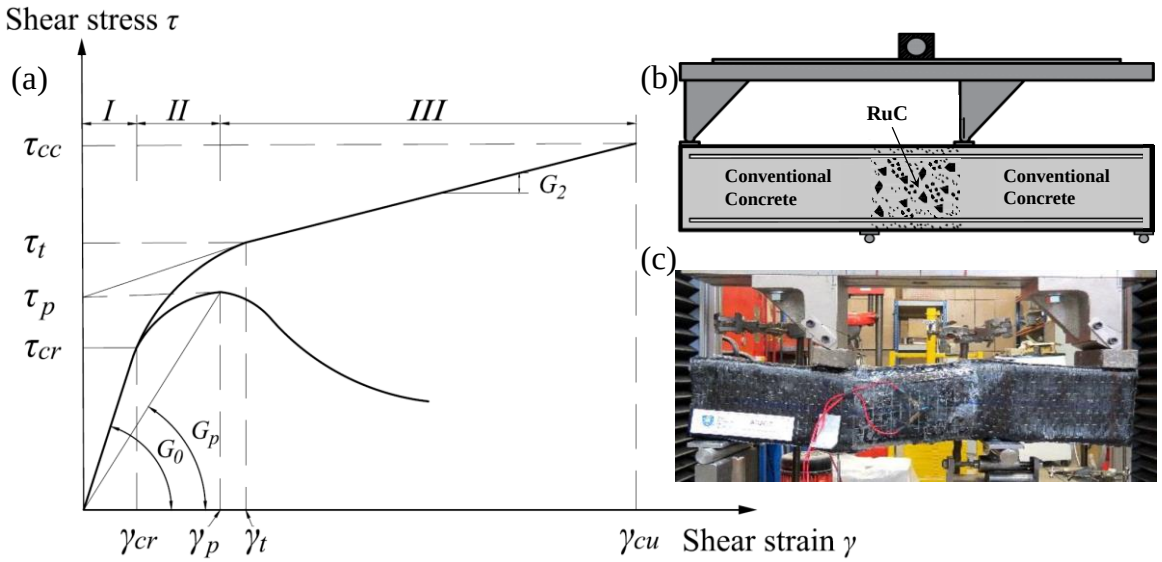

Figure A. 9: (a) Shear stress-strain model for CRuC, (b) Asymmetric shear test configuration, and (c) Asymmetric shear test of CRuC with Carbon FRP

Figure A.10 describes the axial and lateral stress-strain model for CRuC. The latter constitutive model was calibrated based on 38 cylinders of confined RuC under uniaxial compression (Raffoul et al., 2019).

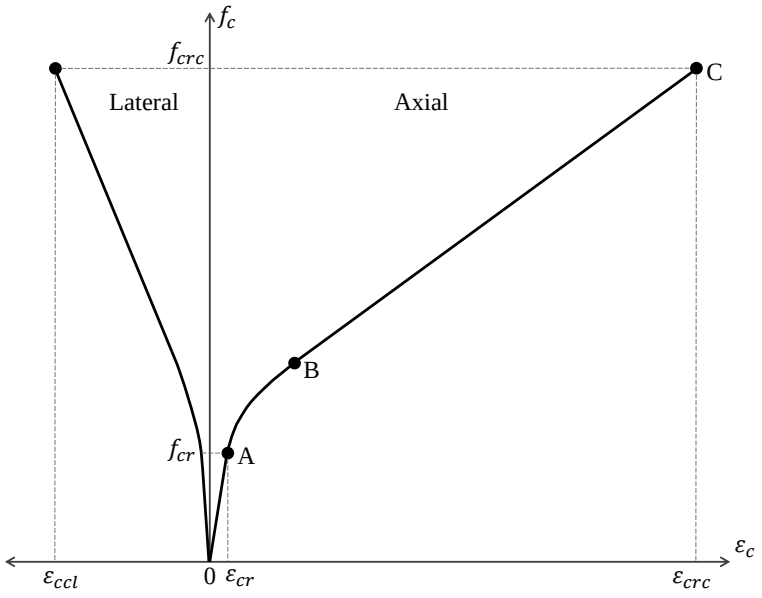

Figure A. 10: Schematic axial and lateral stress-strain behavior of CRuC

A6: FEMA 356 IDEALISED FORCE-DISPLACEMENT CURVE

FEMA 356 proposes a method of producing an idealised force-displacement curve from lateral pushover experiments, which allows for a unified way of determining the yield point of structures. Knowing the structure yield point, and choosing the ultimate point, a measure of ductility can be taken and is comparable to other structures. Figure A.11 describes the FEMA 356 idealisation process via balancing the area between the actual and idealised curve.

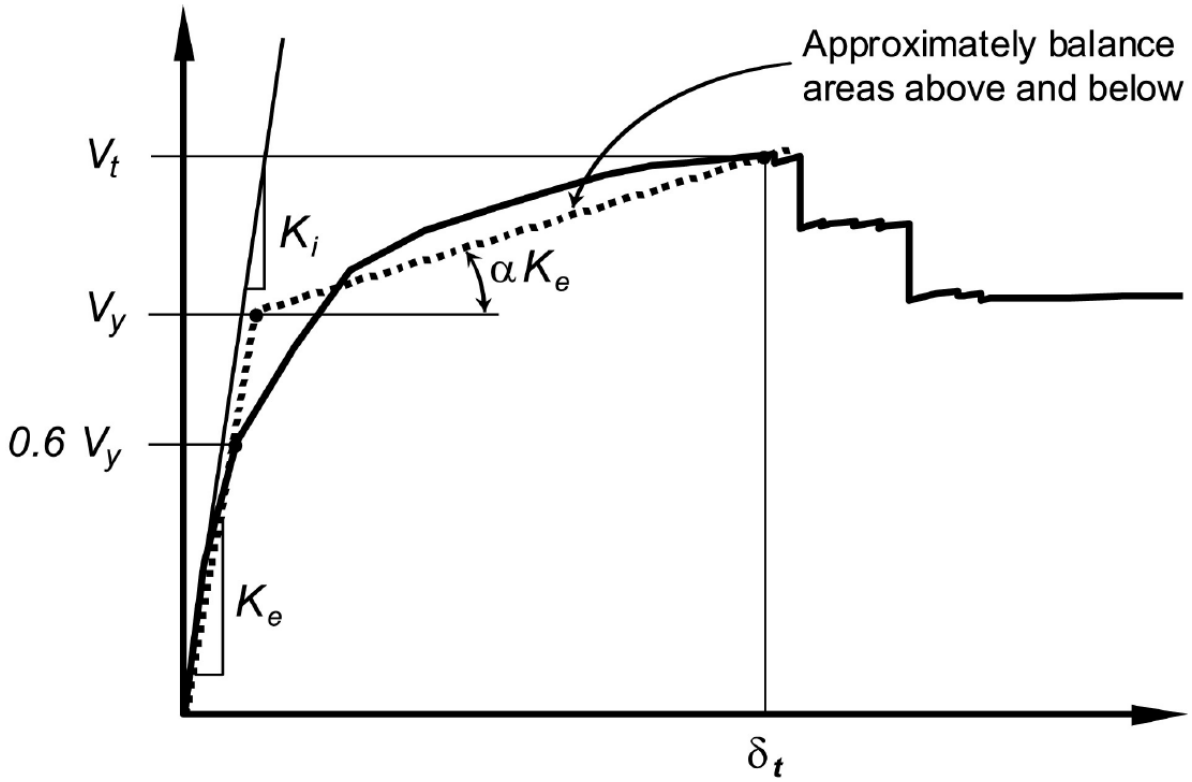

Figure A. 11: FEMA 356 idealised force-displacement curve

The process was applied on the lateral force-displacement results obtained from the OpenSees analysis using CRuC (see section 3.5.2). The area balance was achieved using the "Goal seek" function in Microsoft Excel.

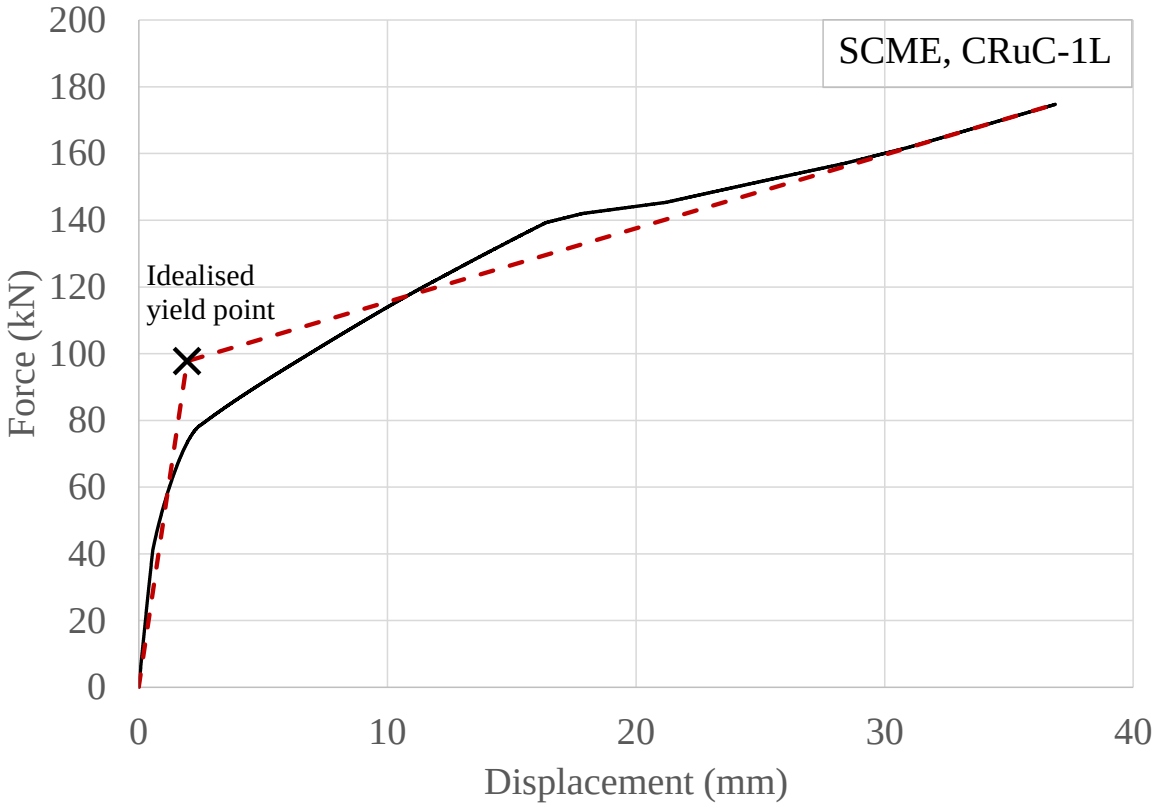

Figure A. 12: FEMA 356 force-displacement idealisation curve for the CRuC-1L SCME analysis

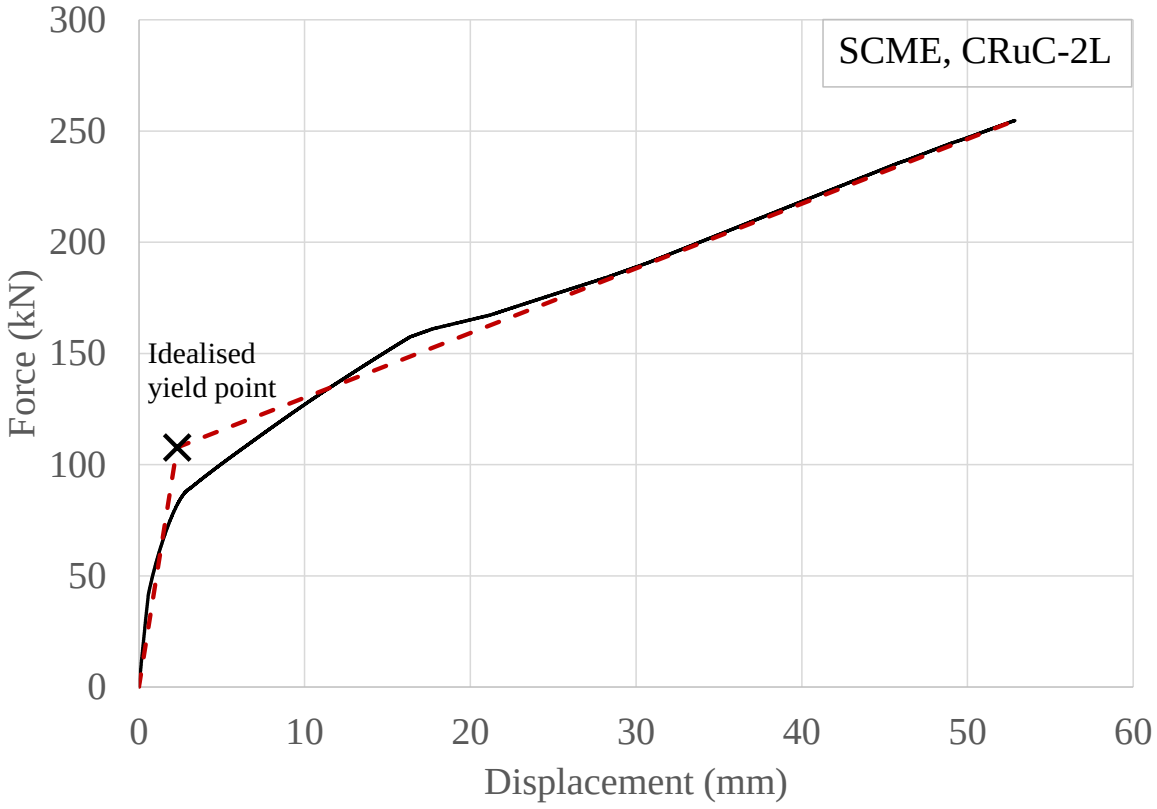

Figure A. 13: FEMA 356 force-displacement idealisation curve for the CRuC-2L SCME analysis

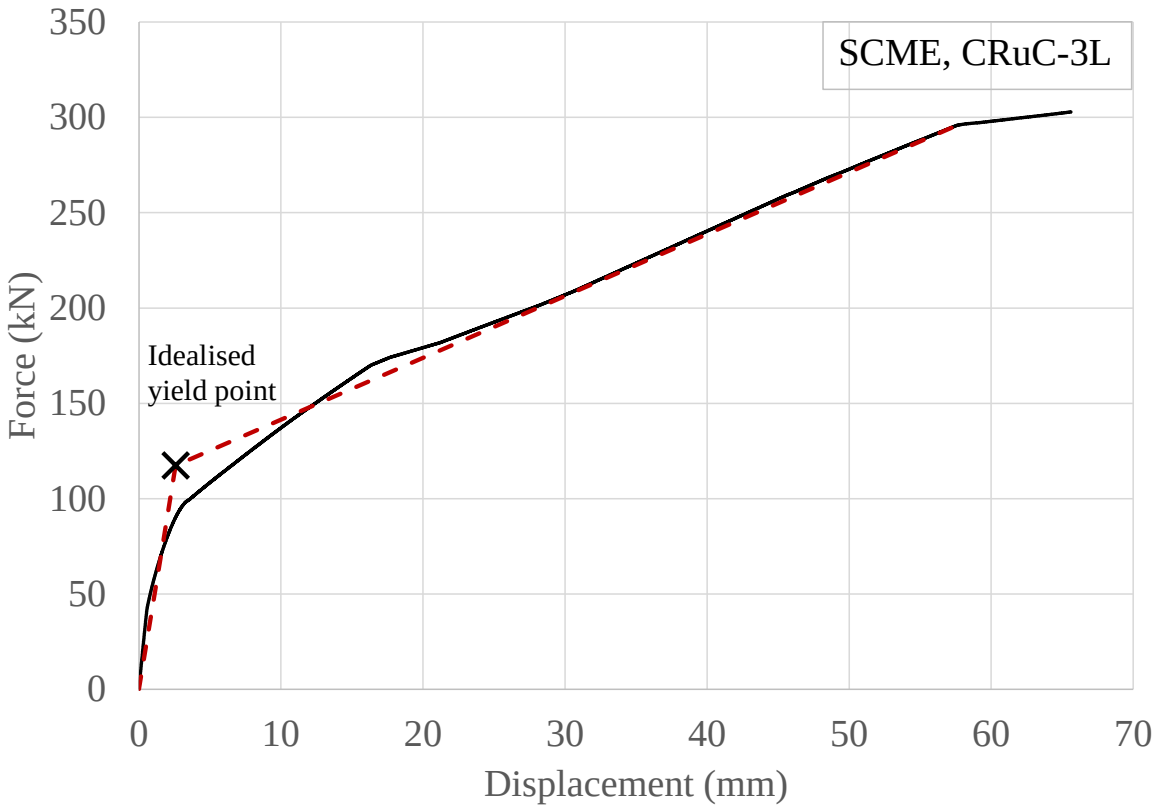

Figure A. 14: FEMA 356 force-displacement idealisation curve for the CRuC-3L SCME analysis

Appendix B

Material related to Chapter 4

B1: APPLICATION OF THE FRP TO THE CONCRETE SURFACE

In order to have rounded corners along the columns' height where FRP is to be placed, round battens, 450 mm long with a radius of 25 mm, were attached to the top corners of the casting formwork.

The following steps were taken to apply the FRP to the concrete surface of the building:

1) The concrete surfaces (450 mm top span of the columns, and the 400 mm in the X and Y direction at each joint) were wire brushed to scratch the surface. Then, the surfaces were blasted with air to clean any dust and debris and then dried for better adherence.
2) A layer of primer was then applied on the surfaces, followed by a coat of epoxy resin, in order to seal the concrete surface.
3) Three layers of AFRP were wrapped around the top 300 mm of the columns, with the final overlap being placed on the outer side of the column transverse to the shaking direction. A two-component epoxy resin was rolled over every layer during wrapping to insure proper impregnation.
4) Two layers of AFRP were wrapped around the 150 mm span of the column below the short column level.
5) One layer of CFRP, 800 mm in length, was bonded horizontally to the beam-column joints. A small strip of CFRP was bonded vertically to the ends of each 800 mm sheet to prevent premature debonding at the ends.
6) All laid out sheets were rolled over in the direction of the fibres with a roller to remove any trapped air and align the fibres in the corresponding load resisting orientation.
7) A final layer of epoxy resin was applied to all the sheets.

B2: SHAKE-TABLE CHARACTERISTICS

The ANCO R250-3123 shake-table was used, which is a tri-axial vibration shake-table driven by three servo-hydraulic actuators.

Characteristics of the shake-table:

- Table size: 3.05×3.05 m
- Three 70 ton servo-hydraulic actuators with 6 ball joints to deliver the tri-axial motions (2 horizontal and 1 vertical).
- Three torque tubes with 18 ball joints to guide table motion and prevent pitch, roll, and yaw motion.
- Displacement range: ± 150 mm
- Peak velocity: 0.8 m/s
- Peak acceleration (with a 10 ton test specimen): 3.0 g
- Digital iterative acceleration controller to achieve desired acceleration signal

Figure B. 1: ANCO R250-3123 shake-table

B3: TIME HISTORY RESULTS OF CC-EQ AND CRUC-EQ SHAKE-TABLE TESTS

The following are the time history results of the shake-table tests performed on the CC-EQ and CRuC-EQ buildings.

Results of the CC-EQ shake-table tests

Roof displacement

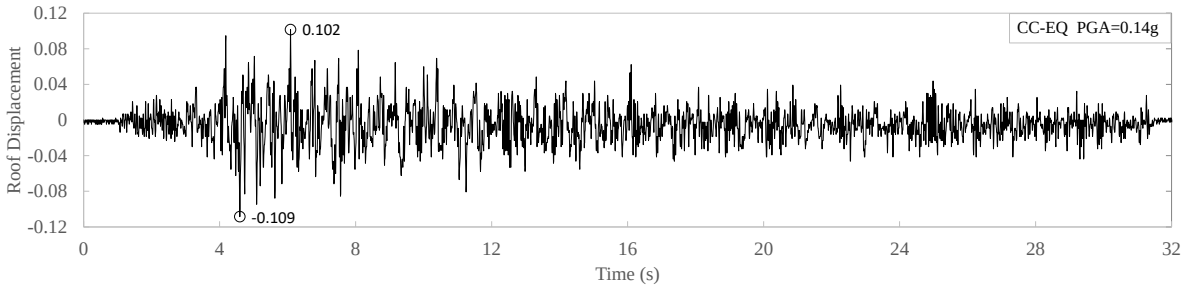

Figure B. 2: Roof displacement time history of the CC-EQ building (PGA=0.14g)

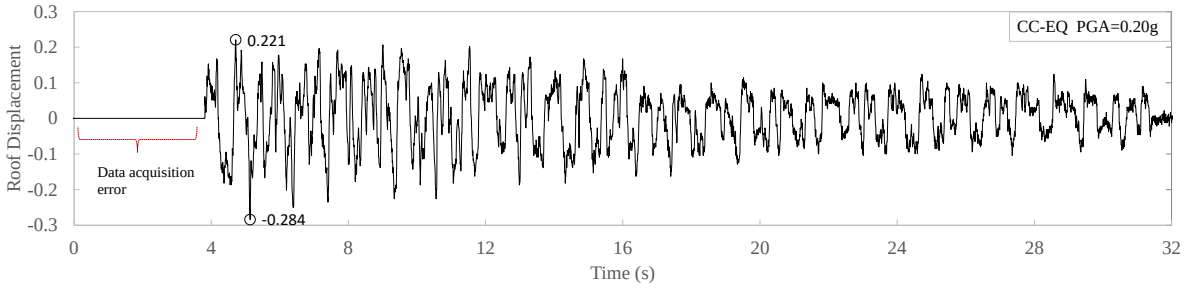

Figure B. 3: Roof displacement time history of the CC-EQ building (PGA=0.20g)

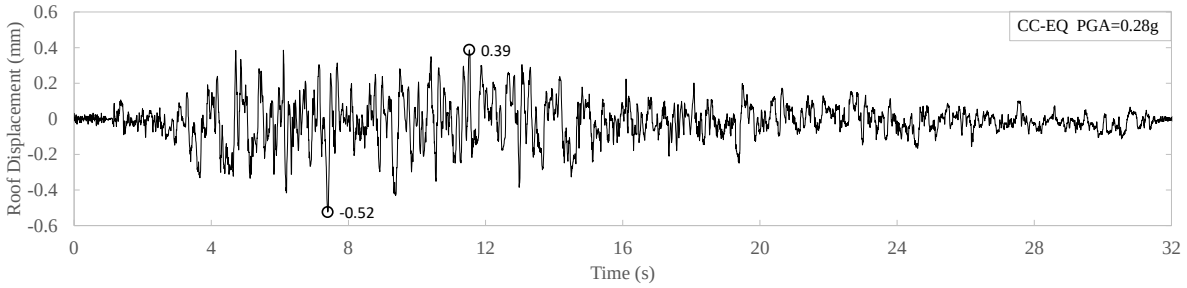

Figure B. 4: Roof displacement time history of the CC-EQ building (PGA=0.28g)

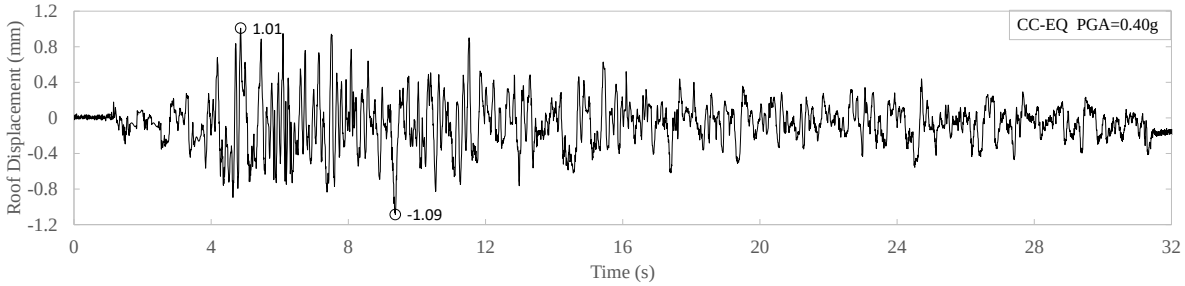

Figure B. 5: Roof displacement time history of the CC-EQ building (PGA=0.40g)

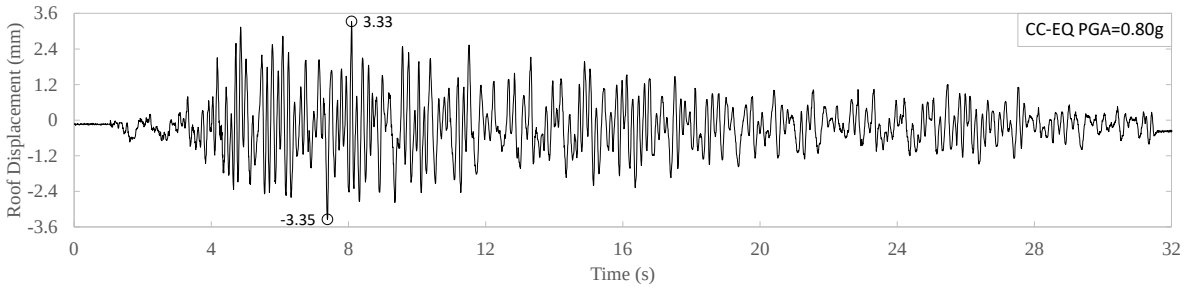

Figure B. 6: Roof displacement time history of the CC-EQ building (PGA=0.80g)

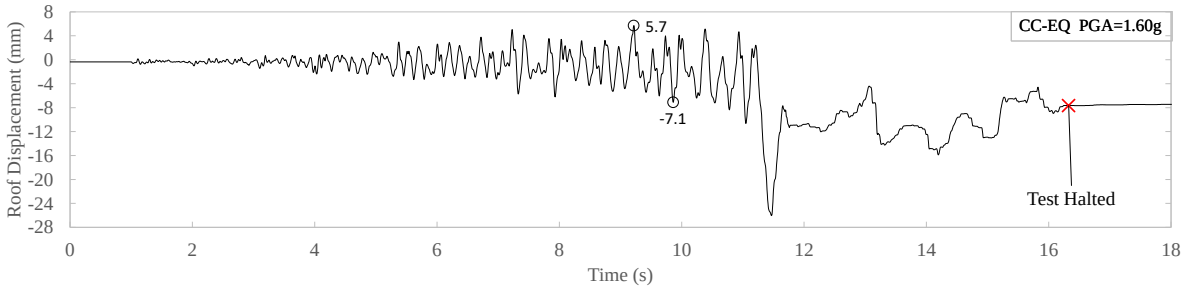

Figure B. 7: Roof displacement time history of the CC-EQ building (PGA=1.60g)

Accelerations

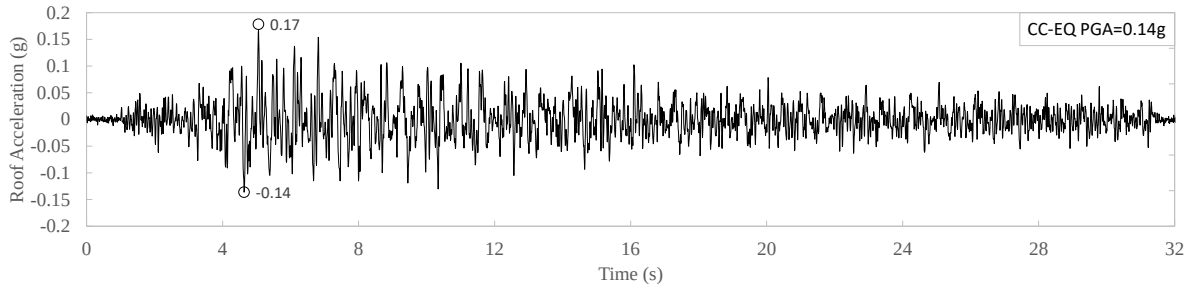

Figure B. 8: Roof acceleration time history of the CC-EQ building (PGA=0.14g)

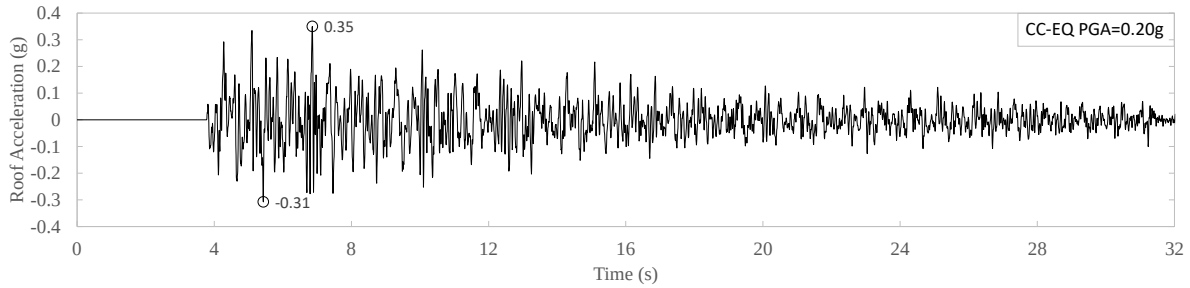

Figure B. 9: Roof acceleration time history of the CC-EQ building (PGA=0.20g)

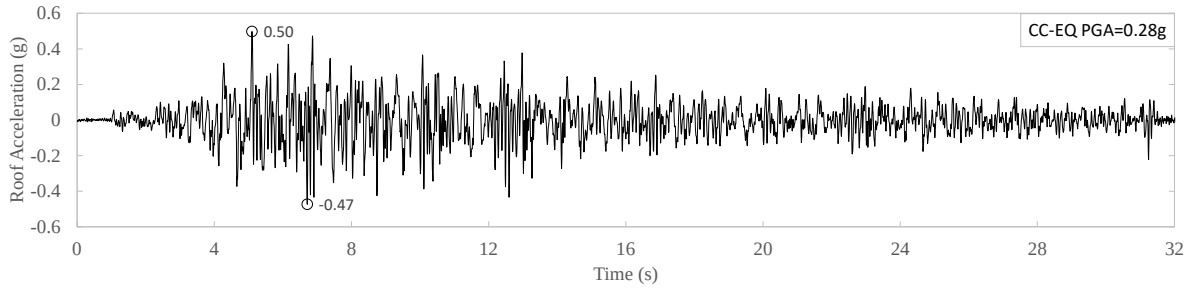

Figure B. 10: Roof acceleration time history of the CC-EQ building (PGA=0.28g)

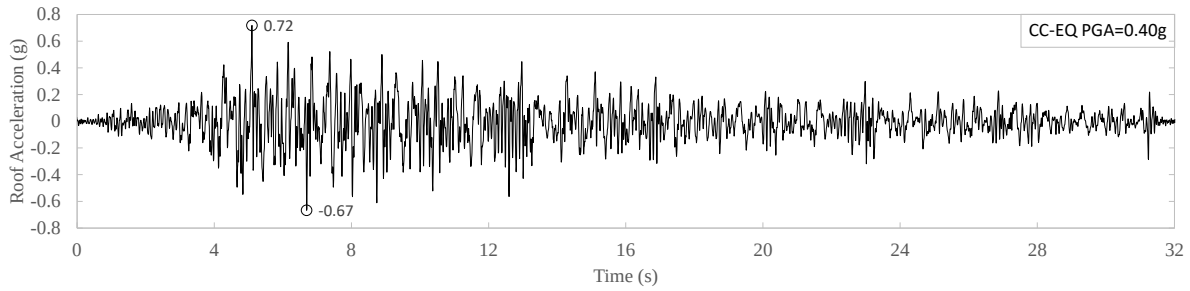

Figure B. 11: Roof acceleration time history of the CC-EQ building (PGA=0.40g)

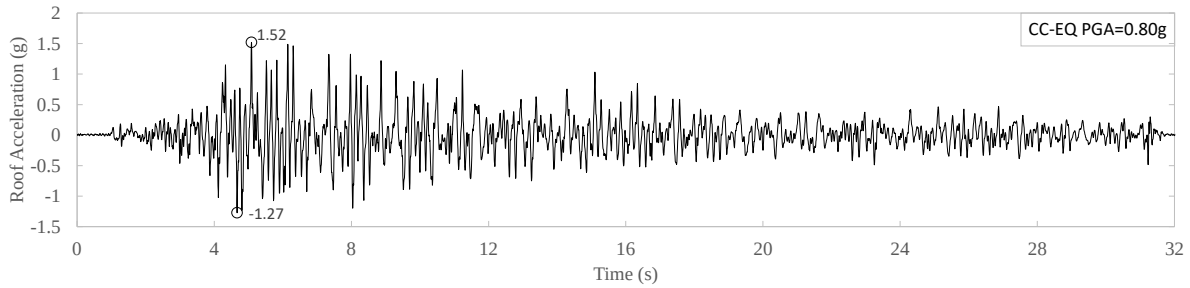

Figure B. 12: Roof acceleration time history of the CC-EQ building (PGA=0.80g)

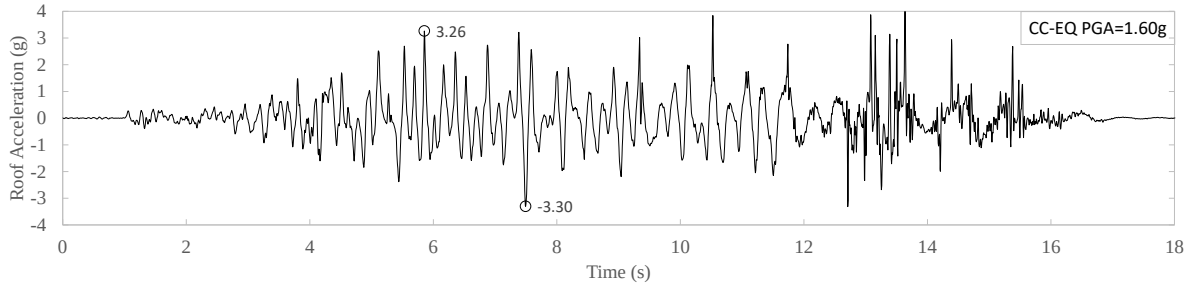

Figure B. 13: Roof acceleration time history of the CC-EQ building (PGA=1.60g)

Strains (steel reinforcement)

The figure below (taken from Chapter 4) is for reference and gives the location and name of the strain gauges located on the reinforcement.

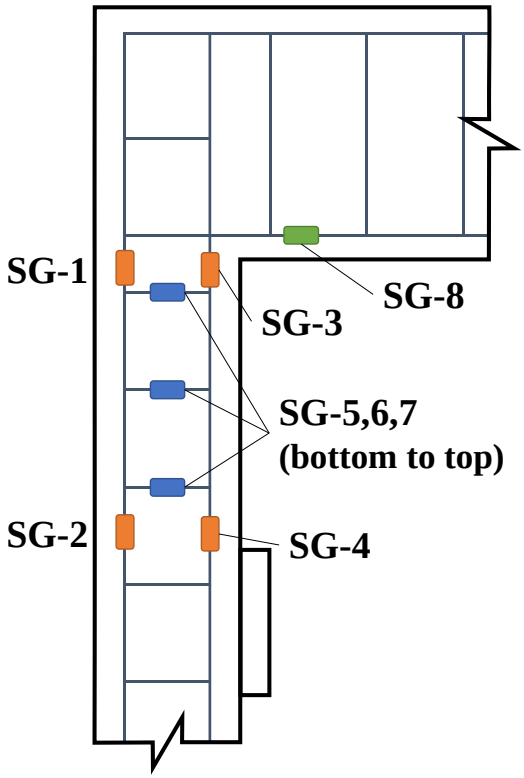

Figure B. 14: Strain gauge location on the steel reinforcement

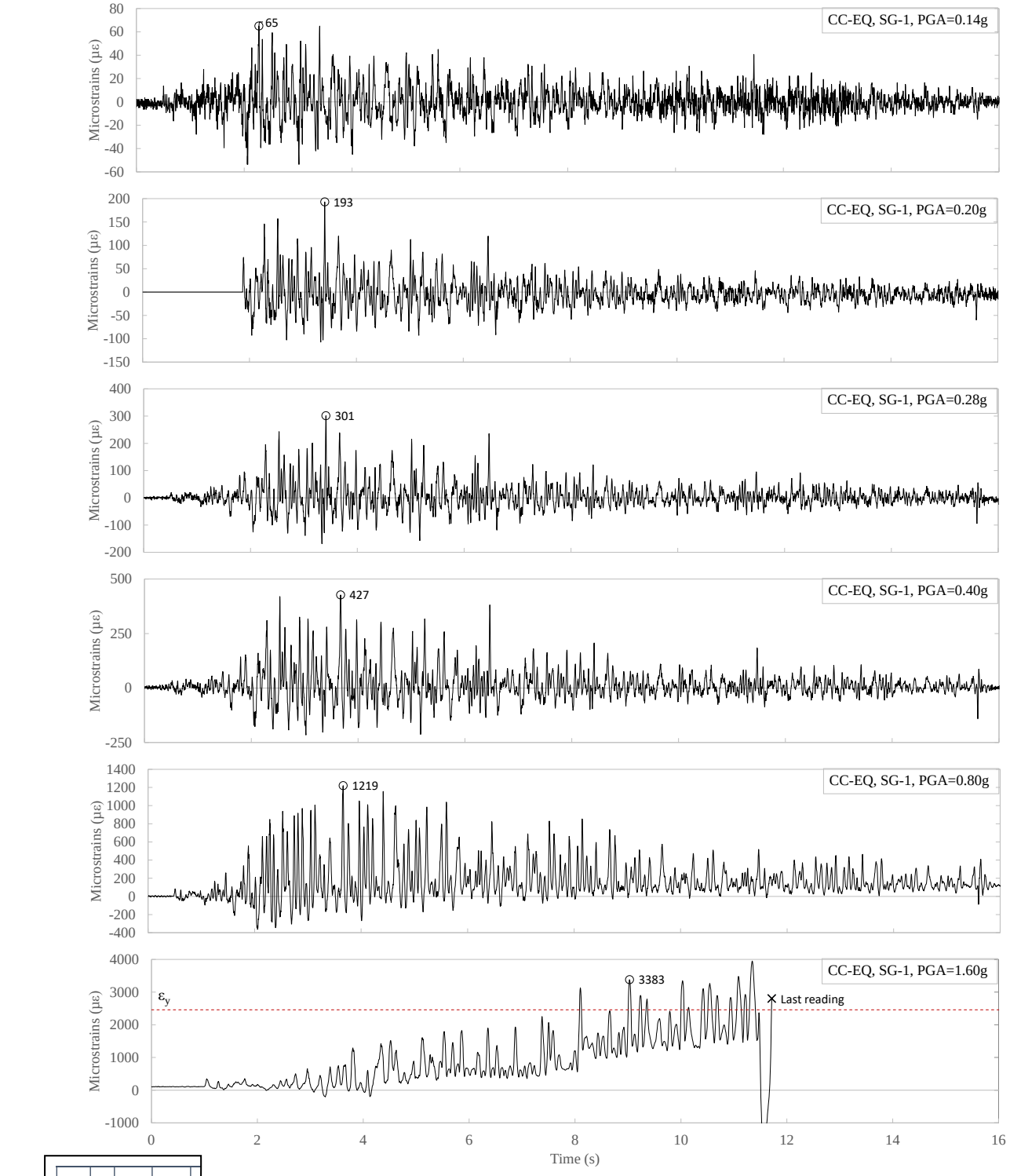

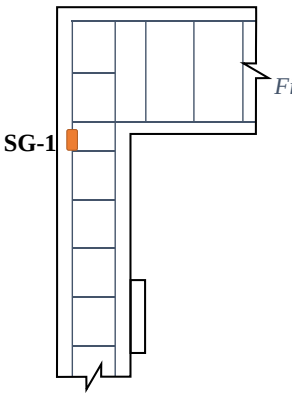

Figure B. 15: Time history strain for CC-EQ column longitudinal reinforcement (SG-1)

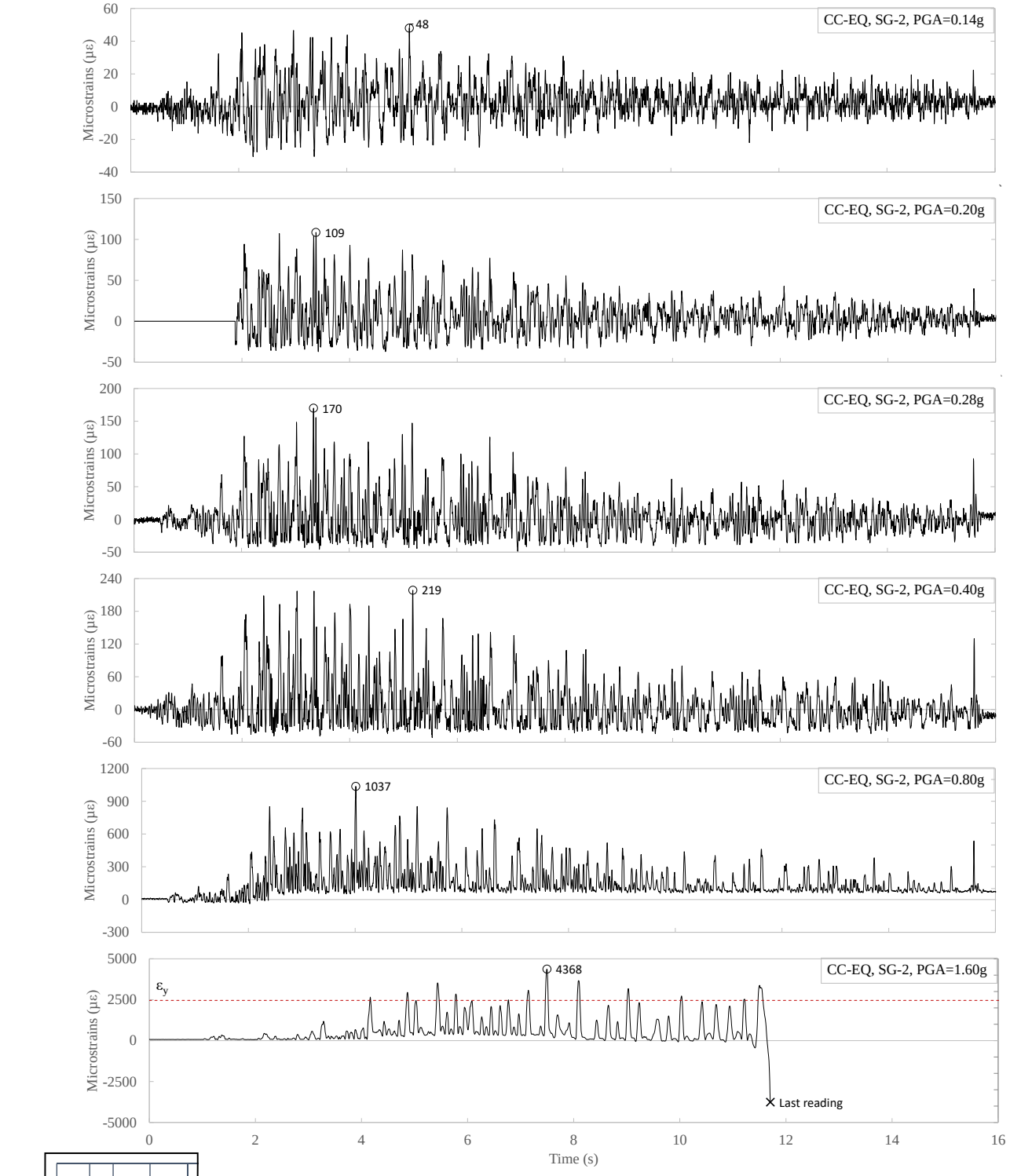

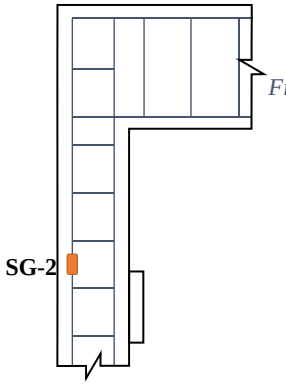

Figure B. 16: Time history strain for CC-EQ column longitudinal reinforcement (SG-2)

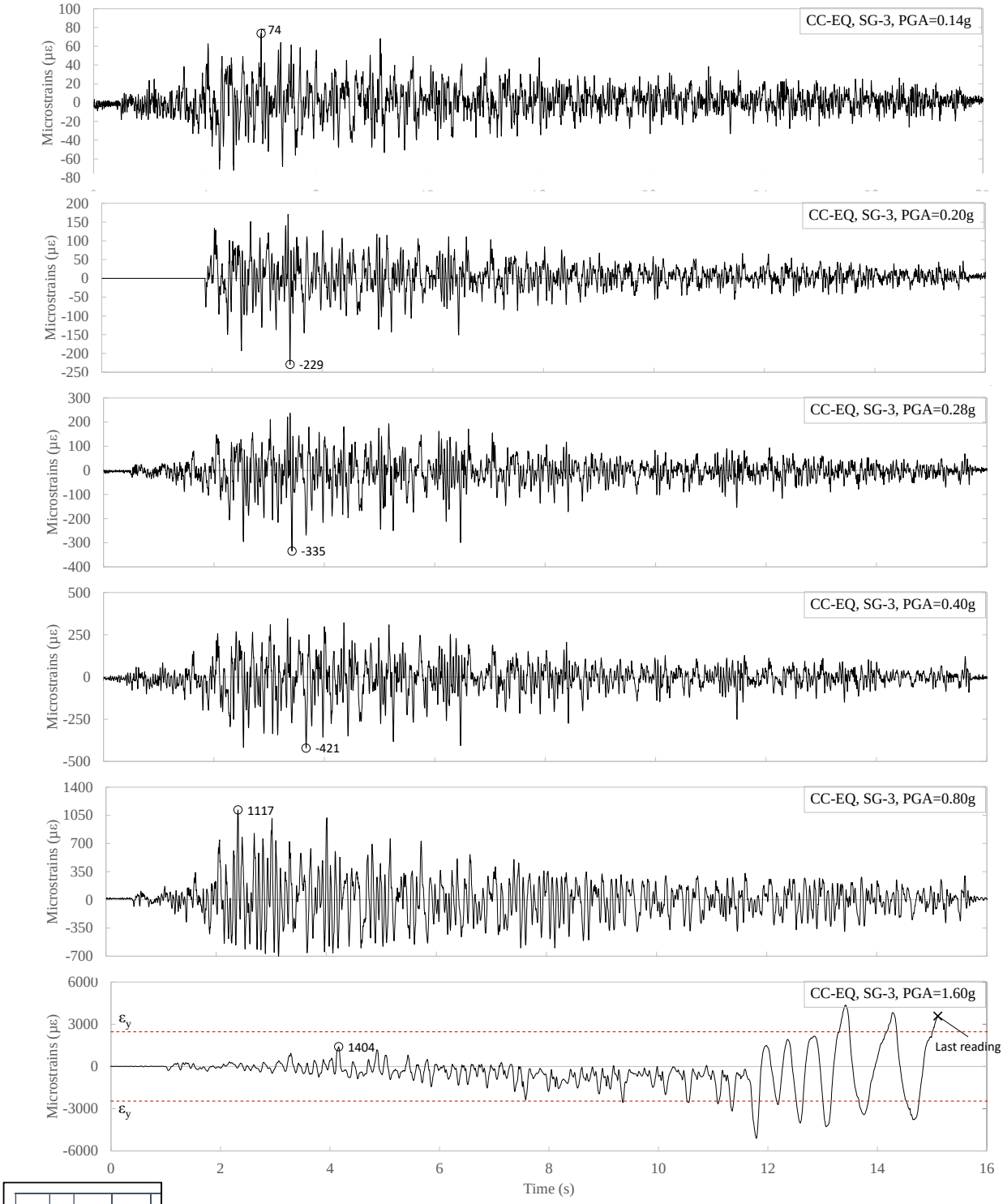

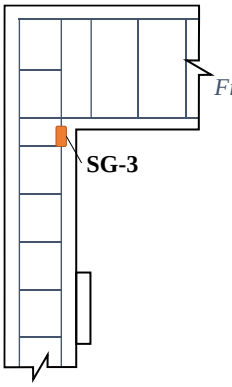

Figure B. 17: Time history strain for CC-EQ column longitudinal reinforcement (SG-3)

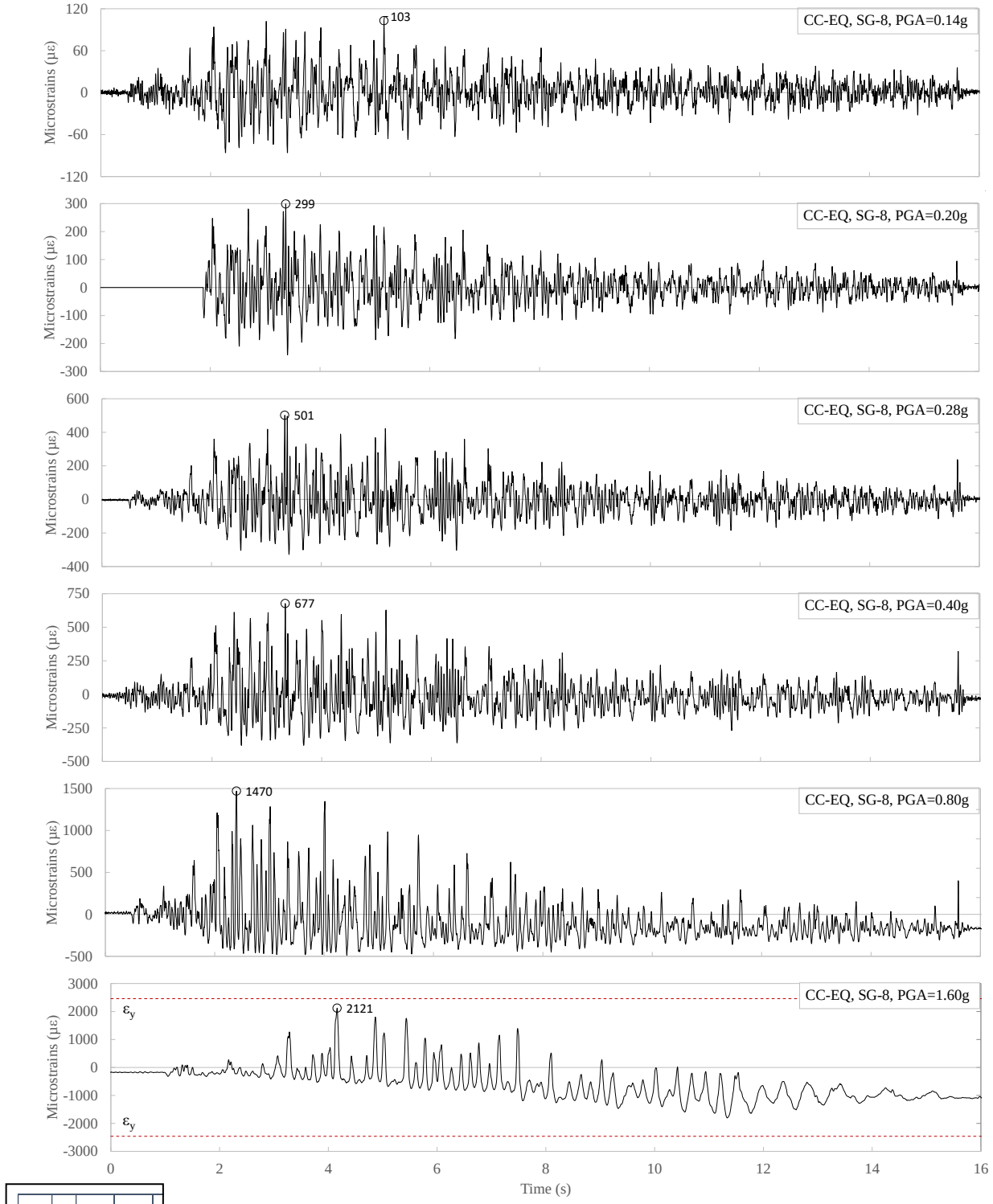

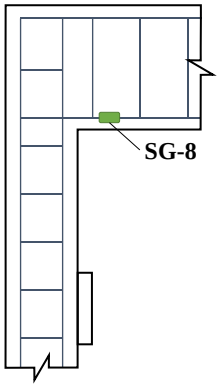

Figure B. 18: Time history strain for CC-EQ beam longitudinal reinforcement (SG-8)

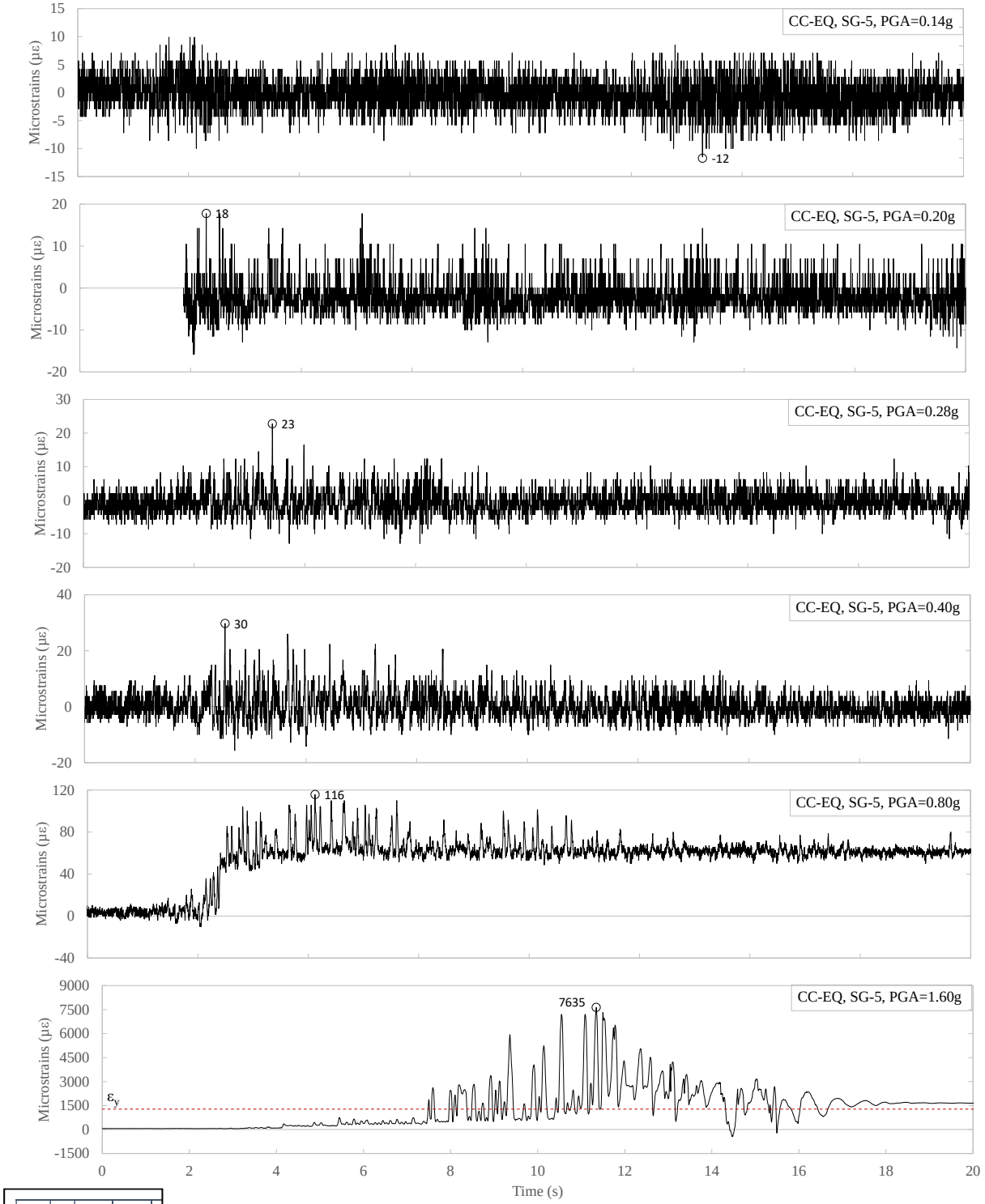

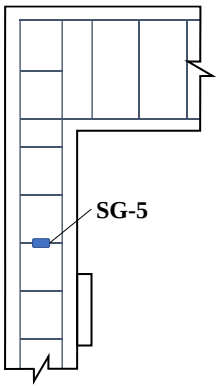

Figure B. 19: Time history strain for CC-EQ column shear reinforcement (SG-5)

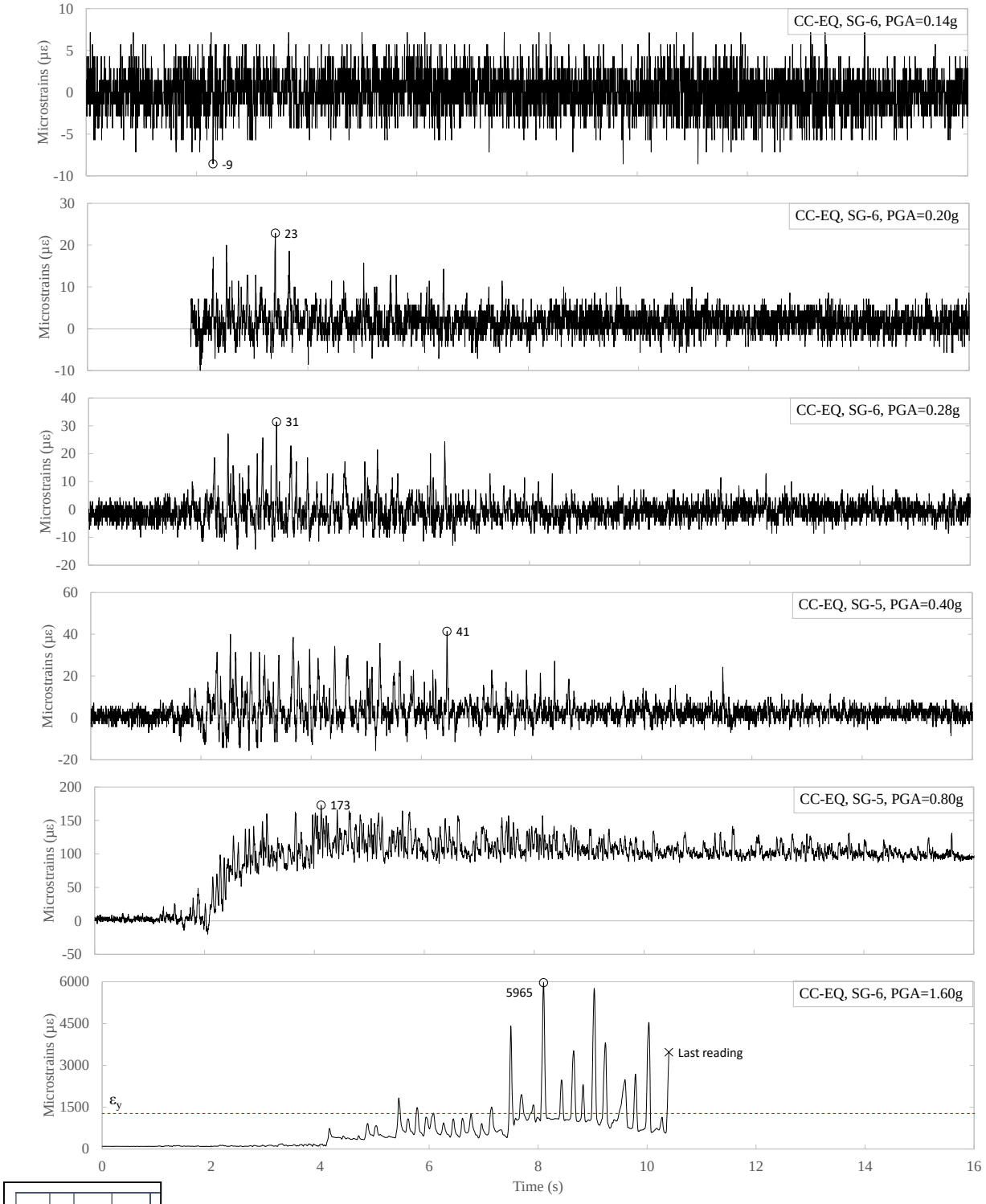

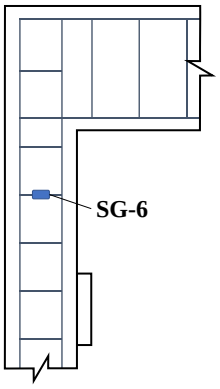

Figure B. 20: Time history strain for CC-EQ column shear reinforcement (SG-6)

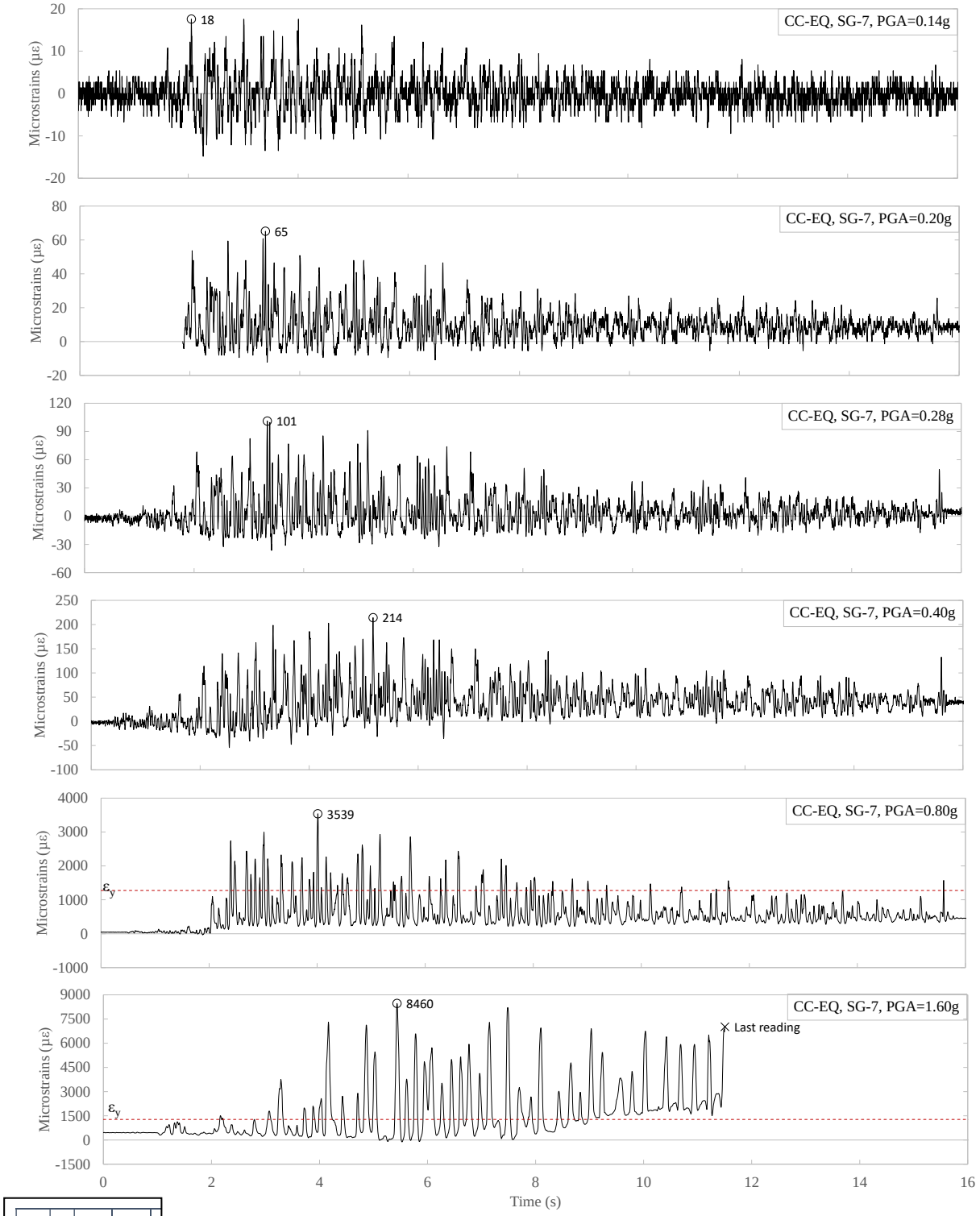

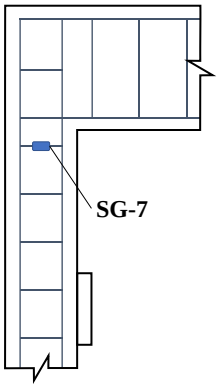

Figure B. 21: Time history strain for CC-EQ column shear reinforcement (SG-7)

Results of the CRuC-EQ shake-table tests

Roof displacement

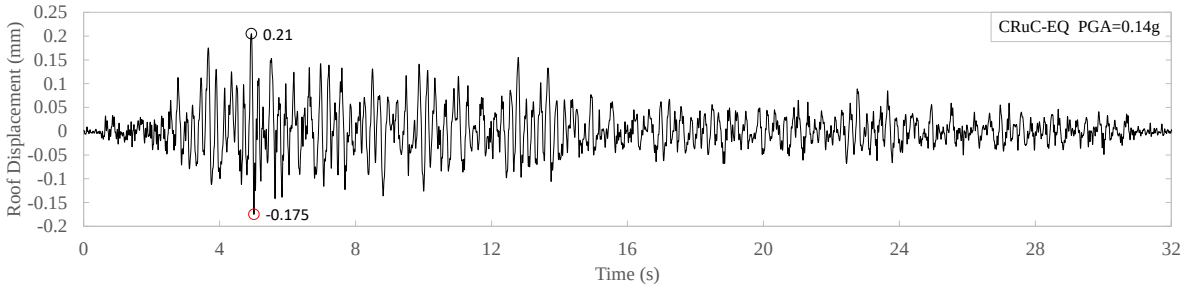

Figure B. 22: Roof displacement time history of the CRuC-EQ building (PGA=0.14g)

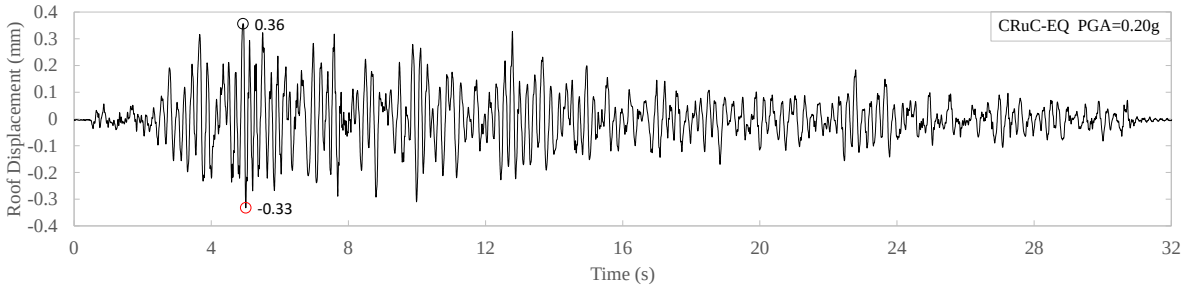

Figure B. 23: Roof displacement time history of the CRuC-EQ building (PGA=0.20g)

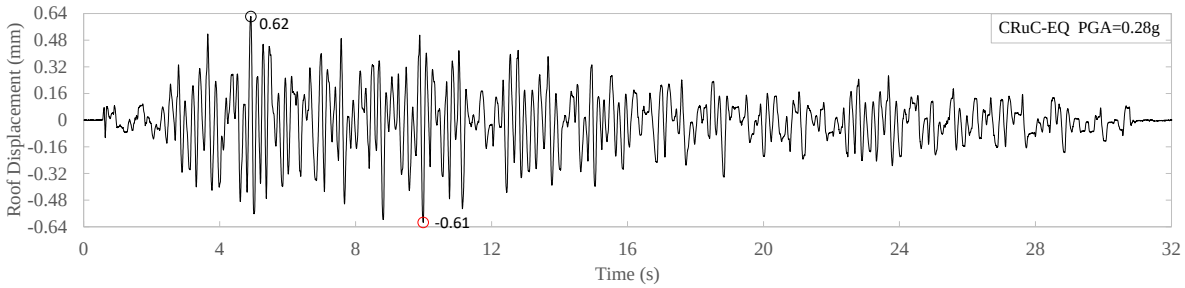

Figure B. 24: Roof displacement time history of the CRuC-EQ building (PGA=0.28g)

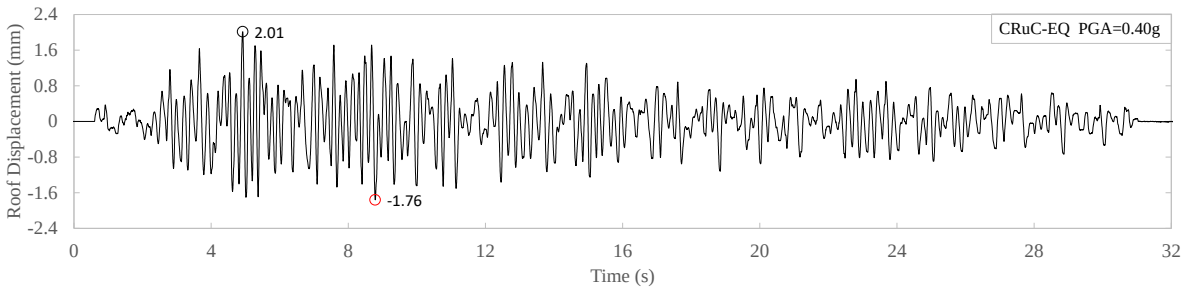

Figure B. 25: Roof displacement time history of the CRuC-EQ building (PGA=0.40g)

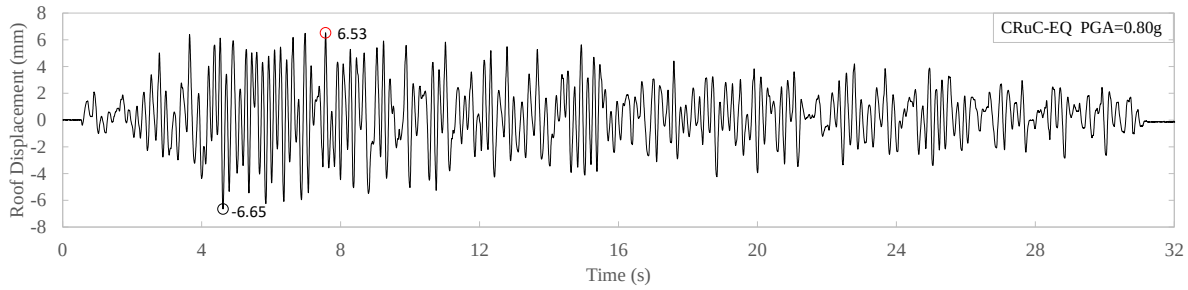

Figure B. 26: Roof displacement time history of the CRuC-EQ building (PGA=0.80g)

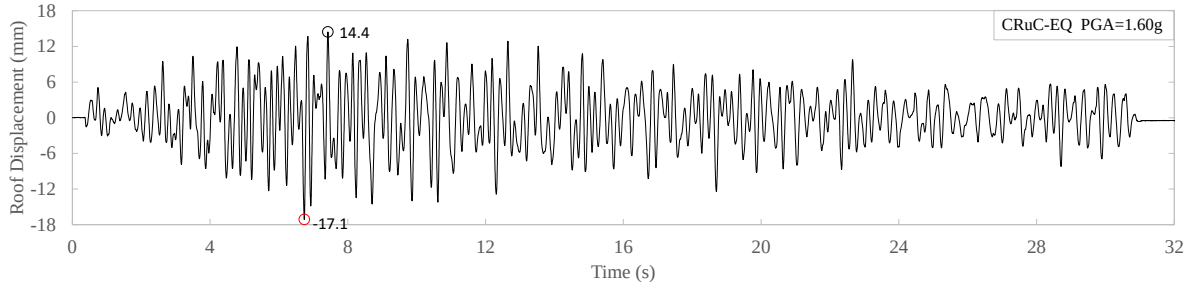

Figure B. 27: Roof displacement time history of the CRuC-EQ building (PGA=1.60g)

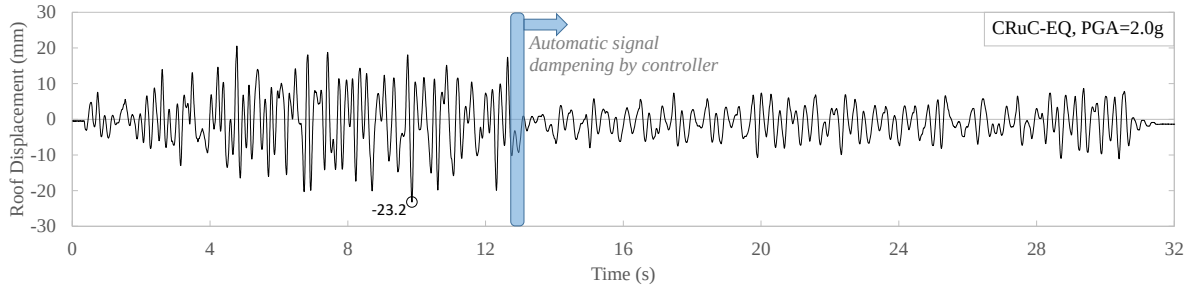

Figure B. 28: Roof displacement time history of the CRuC-EQ building (PGA=2.0g)

Accelerations

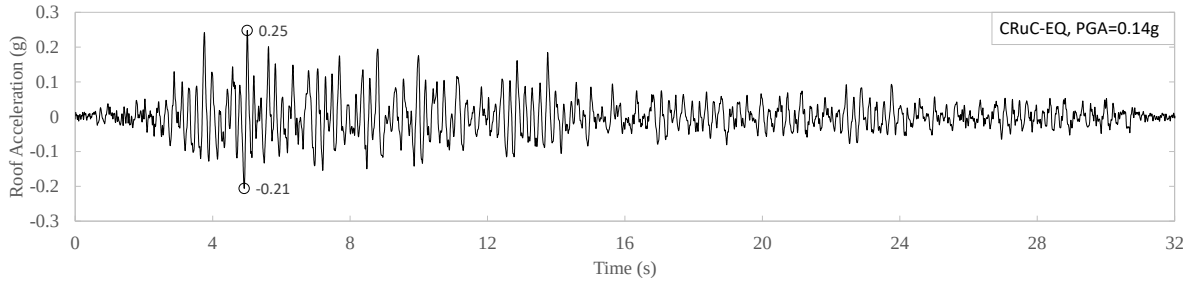

Figure B. 29: Roof acceleration time history of the CRuC-EQ building (PGA=0.14g)

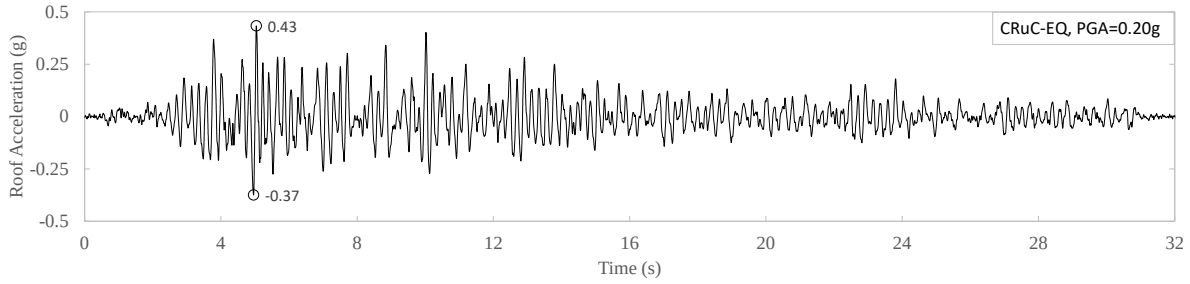

Figure B. 30: Roof acceleration time history of the CRuC-EQ building (PGA=0.20g)

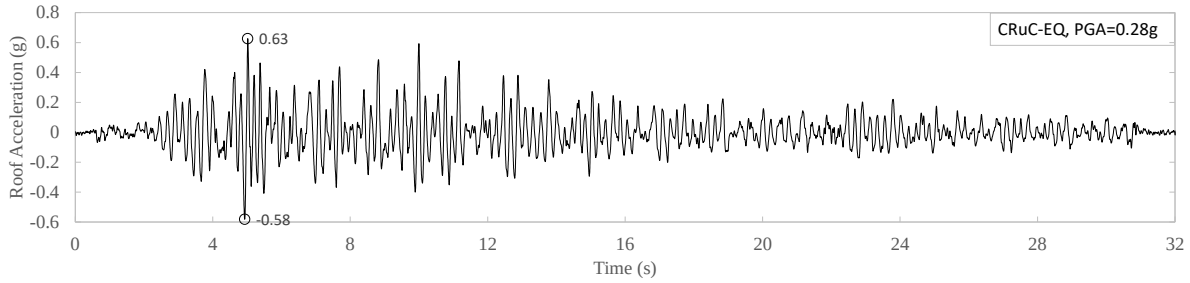

Figure B. 31: Roof acceleration time history of the CRuC-EQ building (PGA=0.28g)

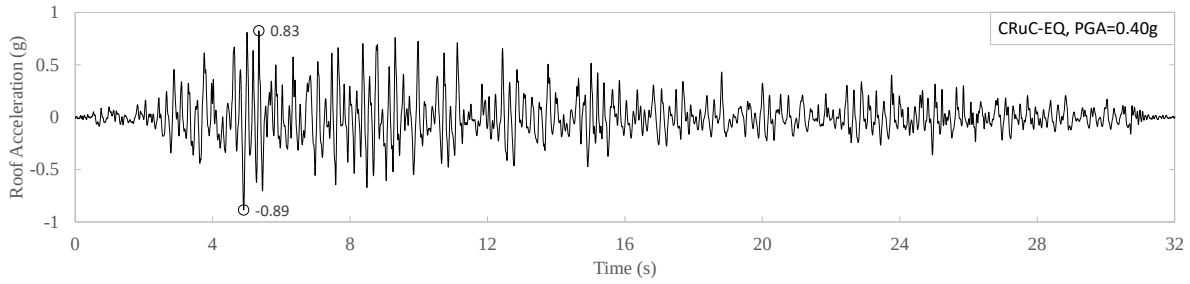

Figure B. 32: Roof acceleration time history of the CRuC-EQ building (PGA=0.40g)

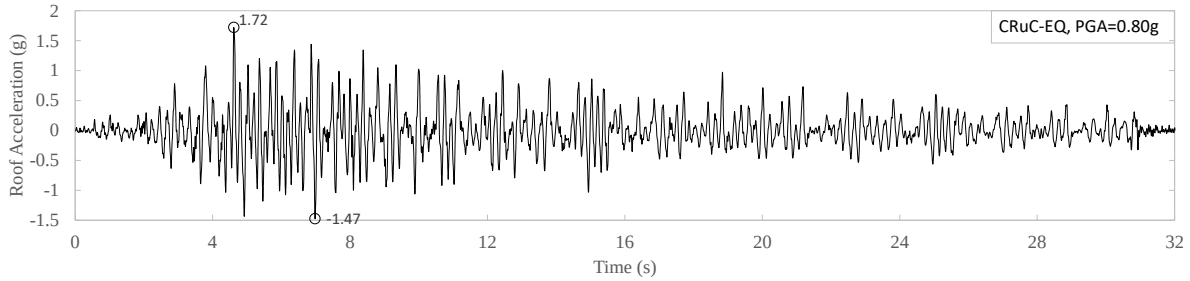

Figure B. 33: Roof acceleration time history of the CRuC-EQ building (PGA=0.80g)

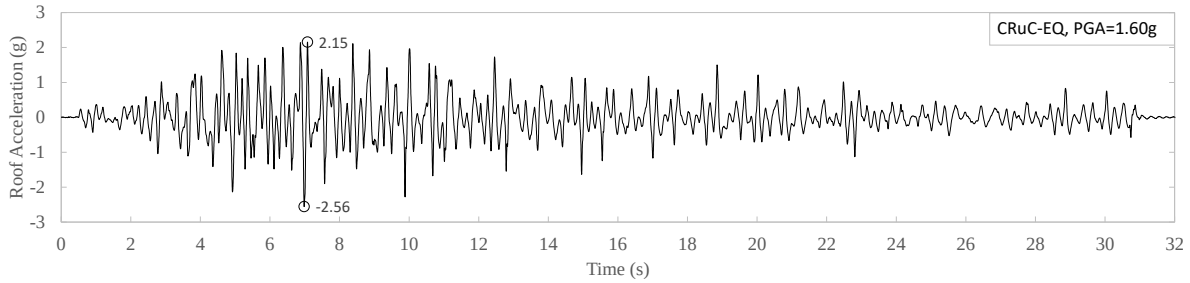

Figure B. 34: Roof acceleration time history of the CRuC-EQ building (PGA=1.60g)

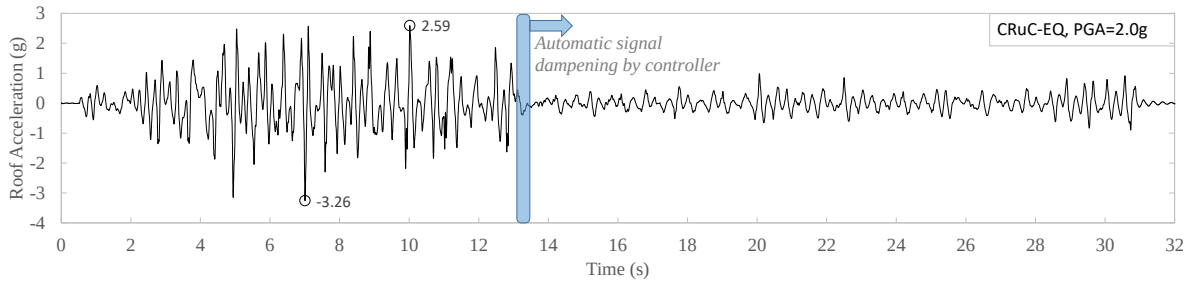

Figure B. 35: Roof acceleration time history of the CRuC-EQ building (PGA=2.0g)

Strains (steel reinforcement)

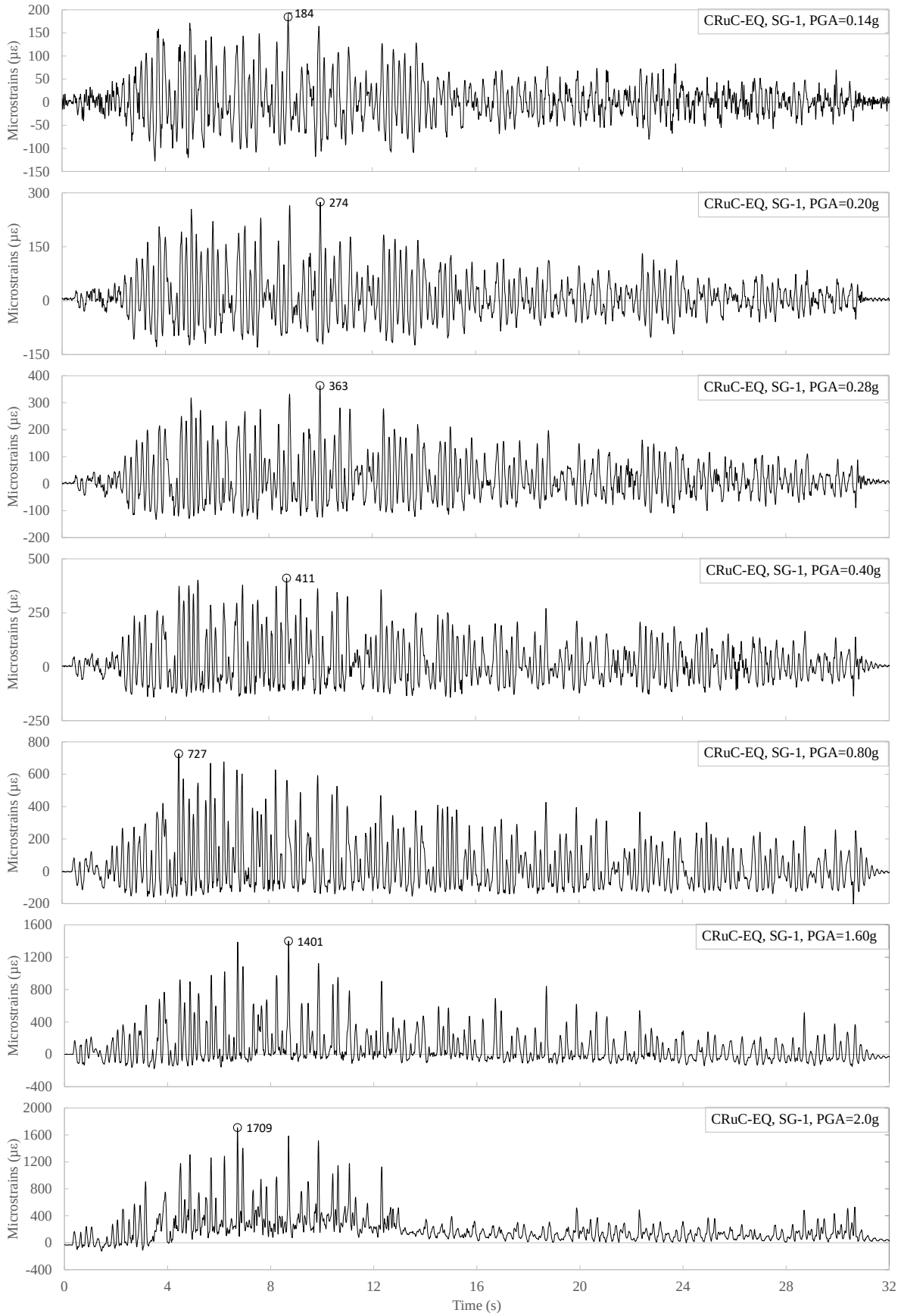

Figure B. 36: Time history strain for CRuC-EQ column longitudinal reinforcement (SG-1)

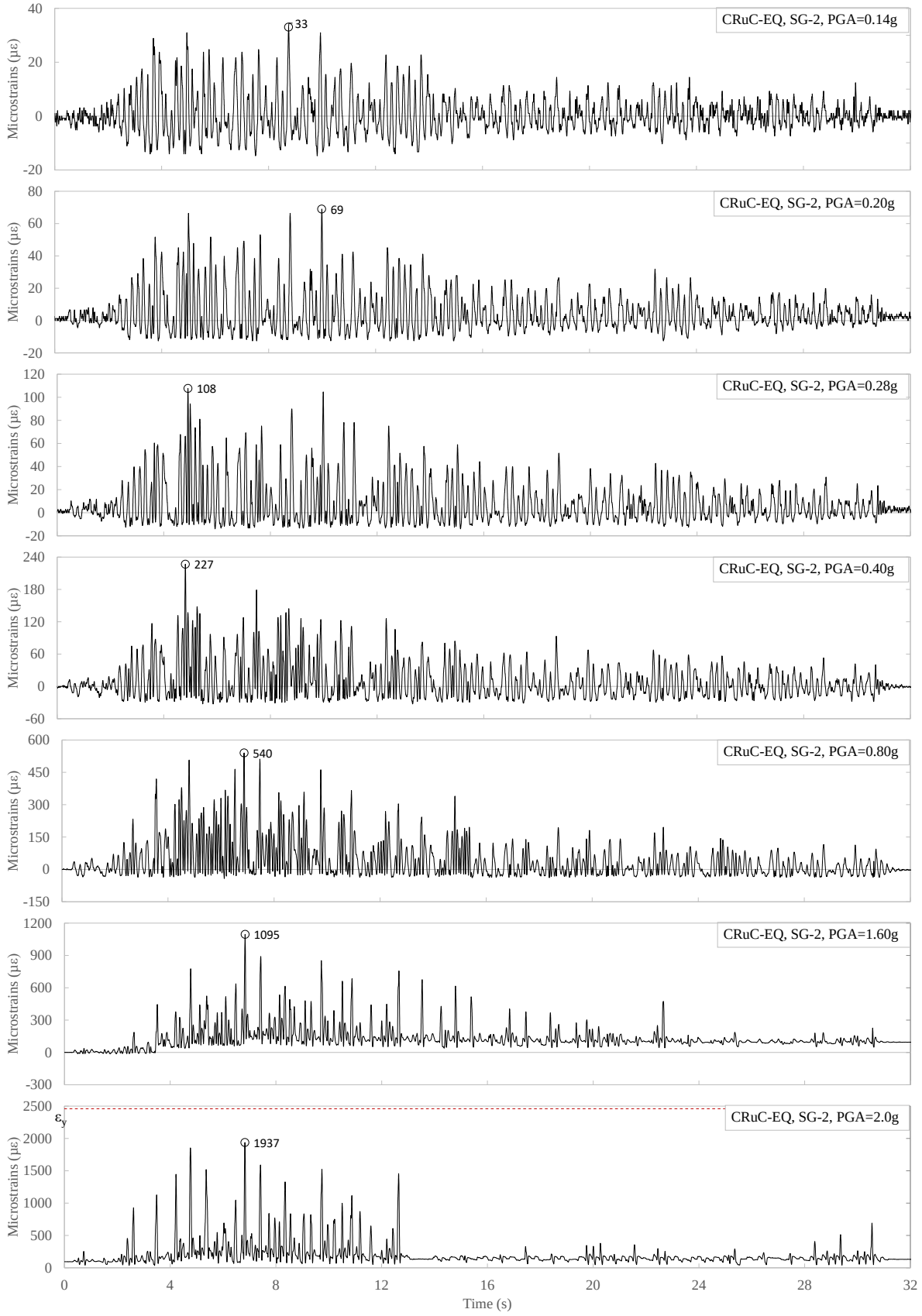

Figure B. 37: Time history strain for CRuC-EQ column longitudinal reinforcement (SG-2)

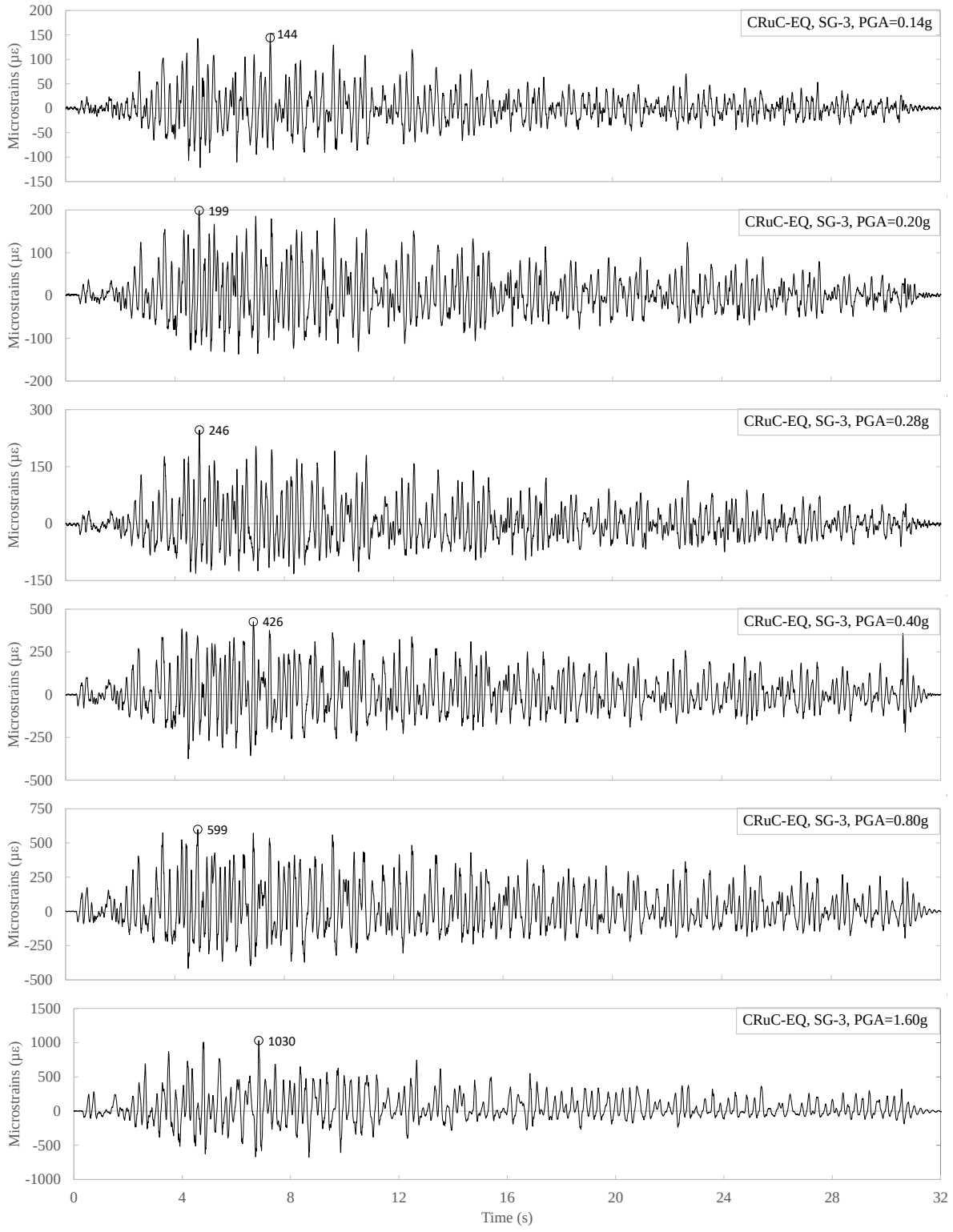

Figure B. 38: Time history strain for CRuC-EQ column longitudinal reinforcement (SG-3)

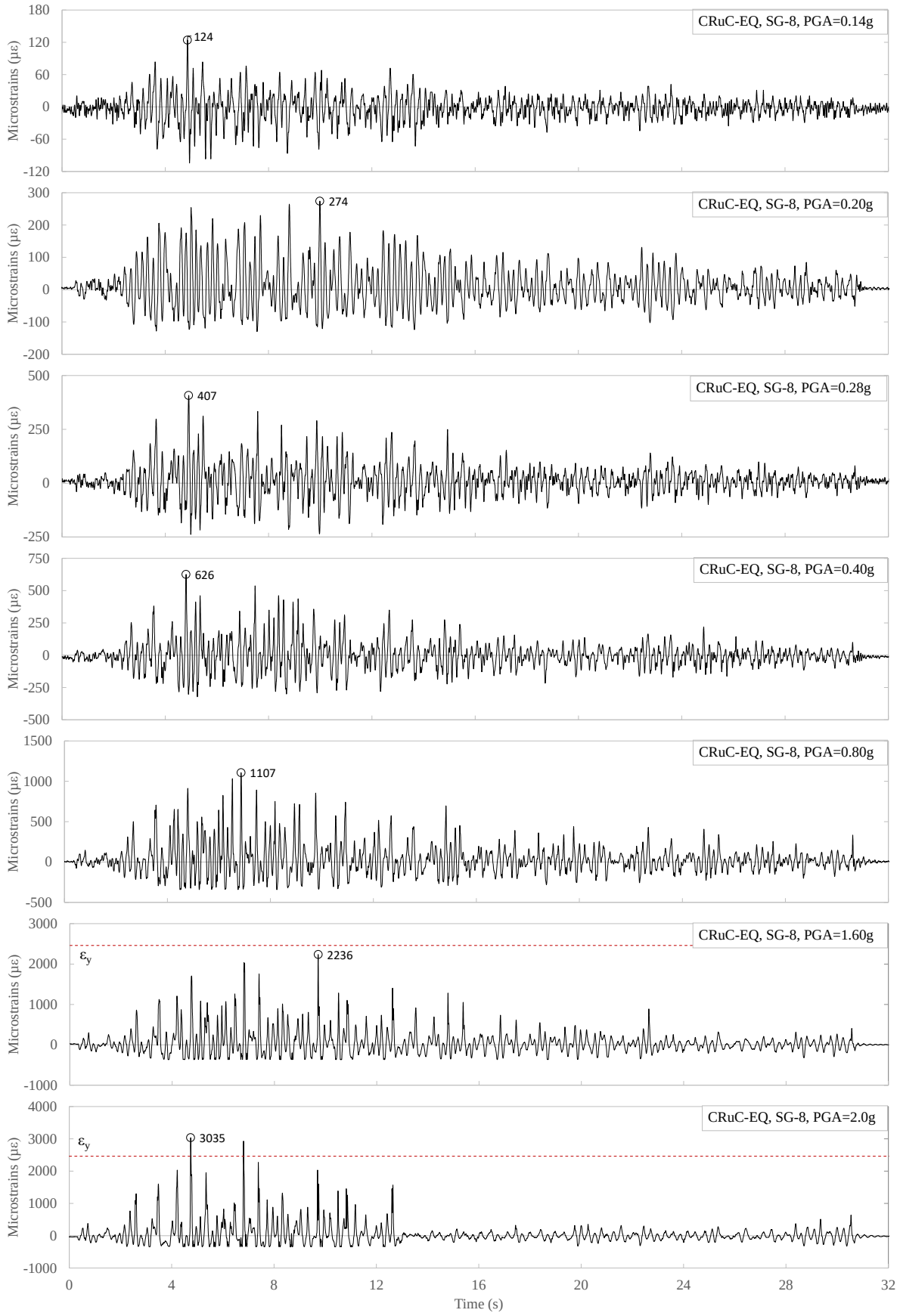

Figure B. 39: Time history strain for CRuC-EQ beam longitudinal reinforcement (SG-8)

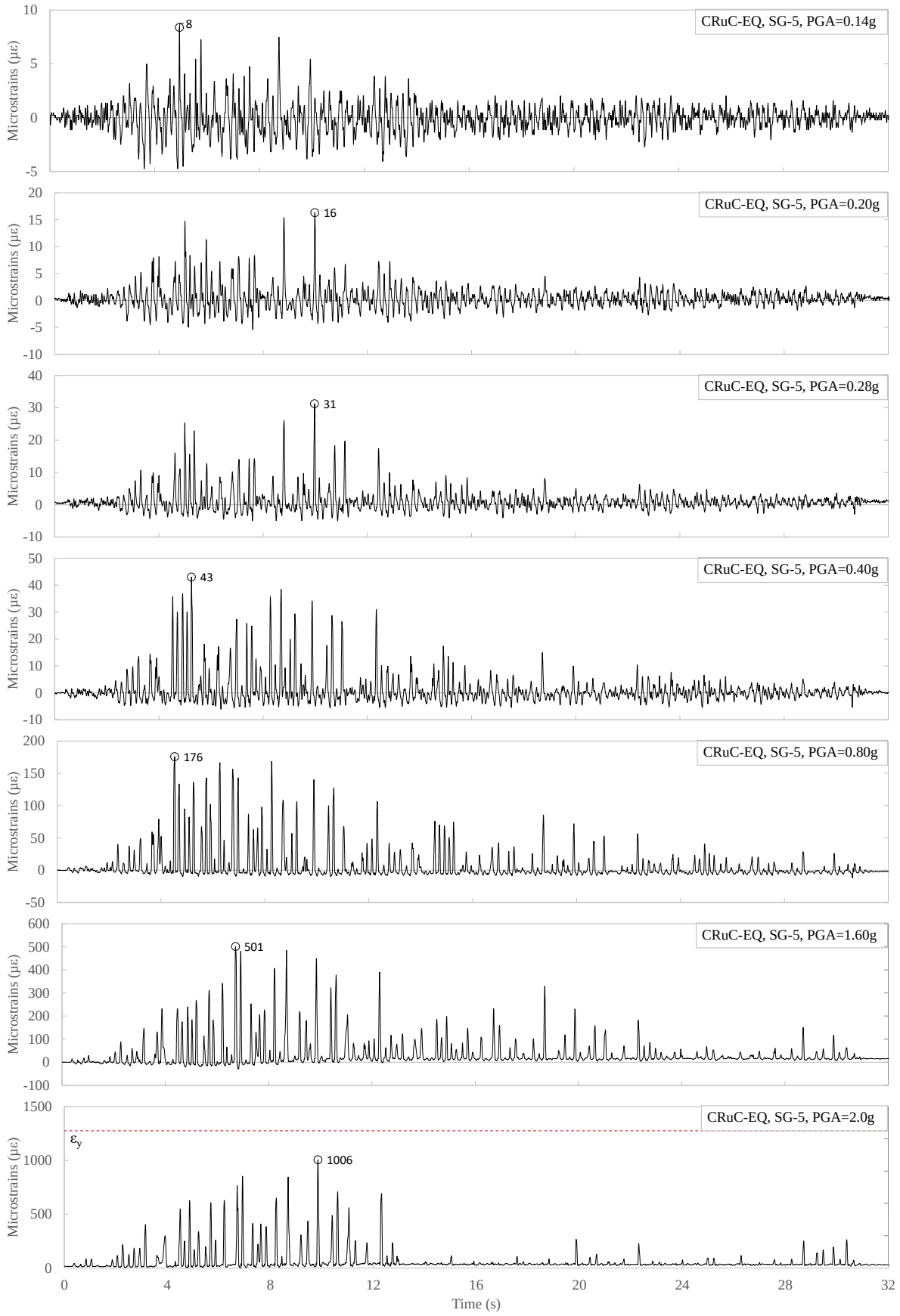

Figure B. 40: Time history strain for CRuC-EQ column shear reinforcement (SG-5)

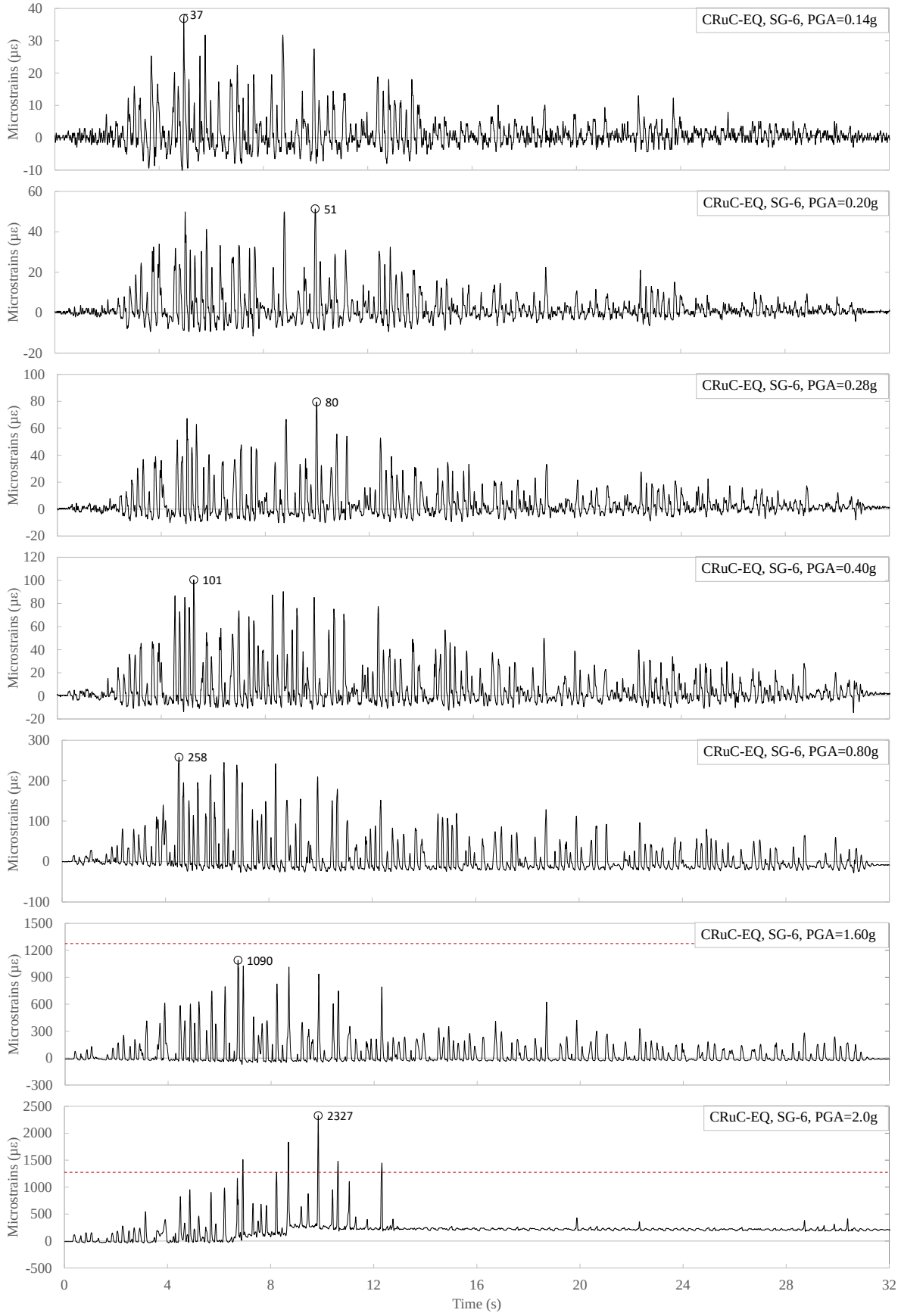

Figure B. 41: Time history strain for CRuC-EQ column shear reinforcement (SG-6)

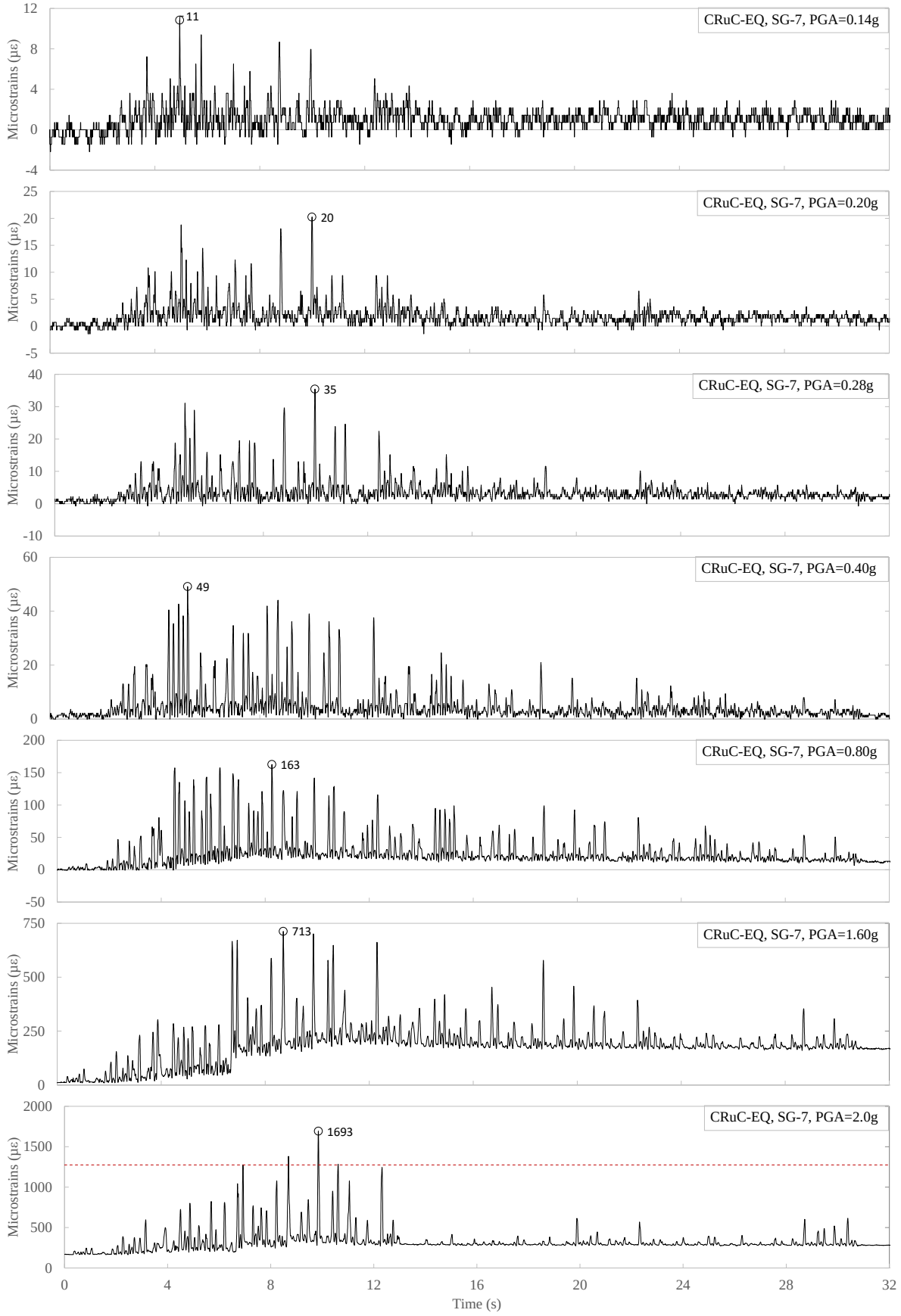

Figure B. 42: Time history strain for CRuC-EQ column shear reinforcement (SG-7)

Strains (AFRP)

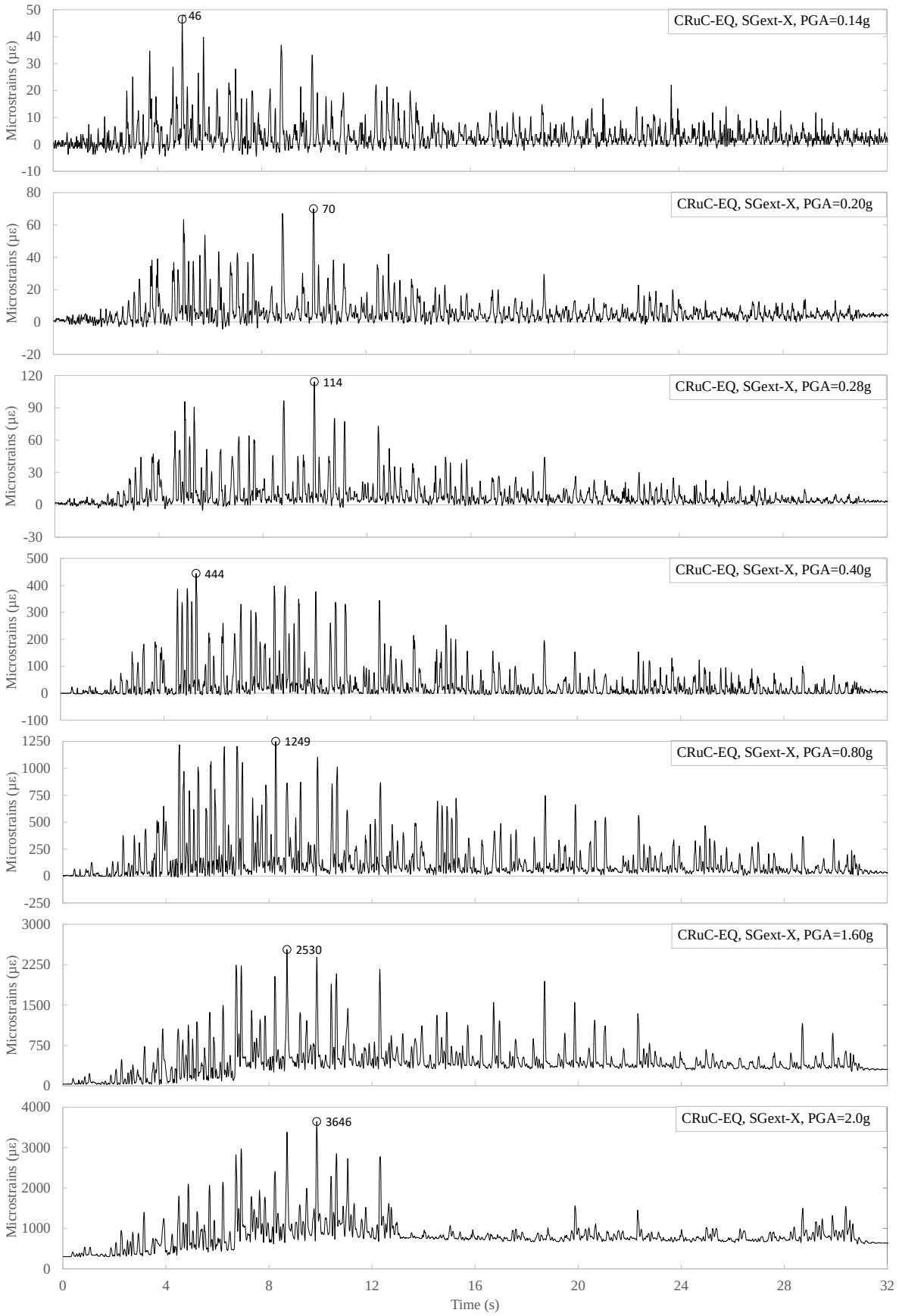

Figure B. 43: Time history strain for CRuC-EQ AFRP confinement in X-direction (SGext-X)

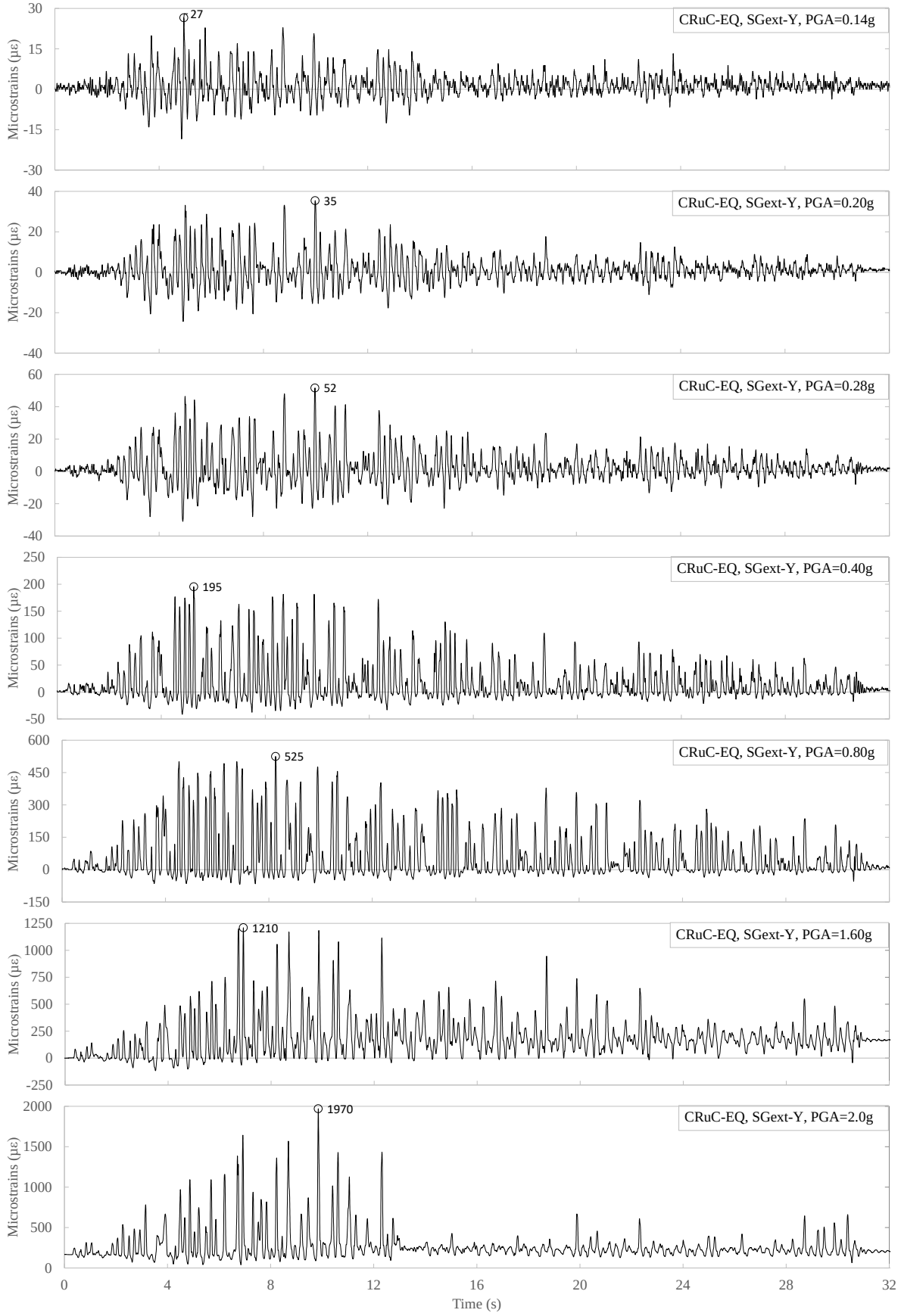

Figure B. 44: Time history strain for CRuC-EQ AFRP confinement in Y-direction (SGext-Y)

Appendix C

Material related to Chapter 5

C1: TIME HISTORY RESULTS OF THE CRUC-ISO SHAKE-TABLE TEST

The following are the time history results of the shake-table tests performed on the CRuC-ISO building.

Base-isolator drift

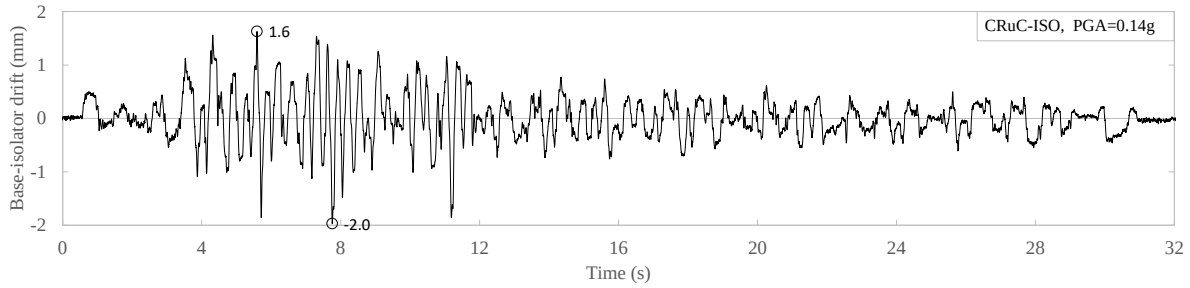

Figure C. 1: Base-isolator drift time history for the CRuC-ISO building (PGA=0.14g)

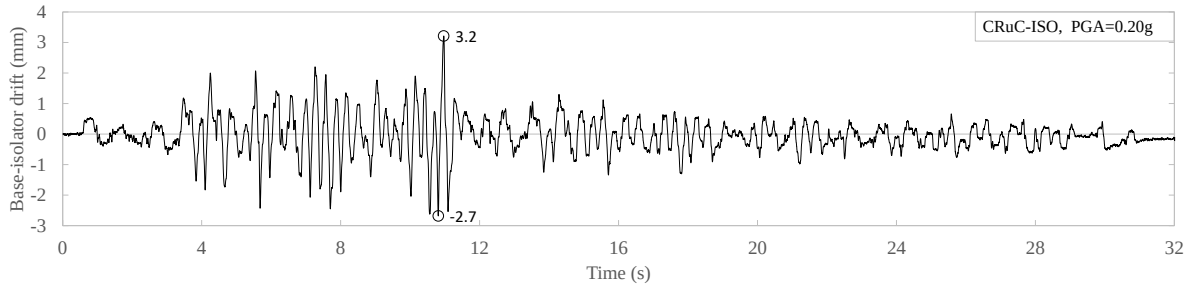

Figure C. 2: Base-isolator drift time history for the CRuC-ISO building (PGA=0.20g)

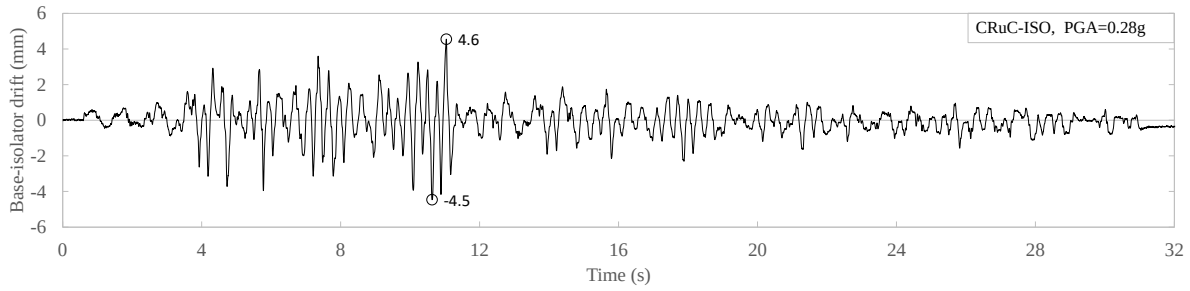

Figure C. 3: Base-isolator drift time history for the CRuC-ISO building (PGA=0.28g)

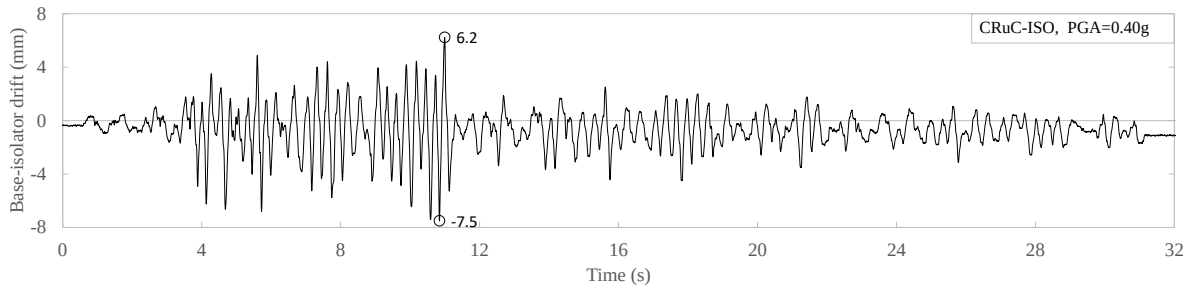

Figure C. 4: Base-isolator drift time history for the CRuC-ISO building (PGA=0.40g)

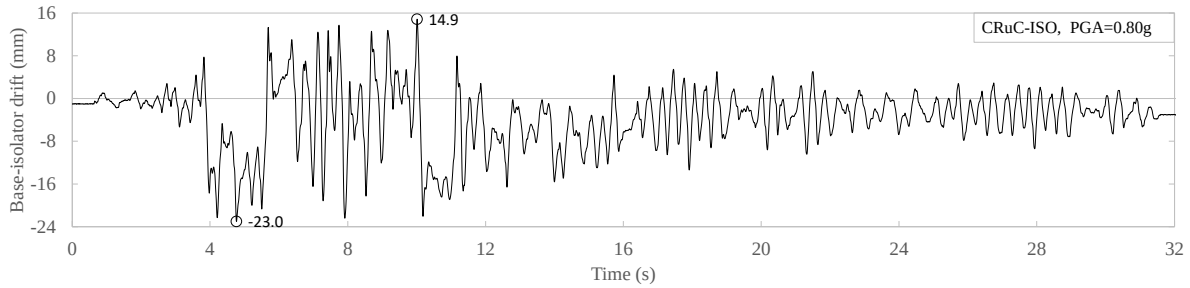

Figure C. 5: Base-isolator drift time history for the CRuC-ISO building (PGA=0.80g)

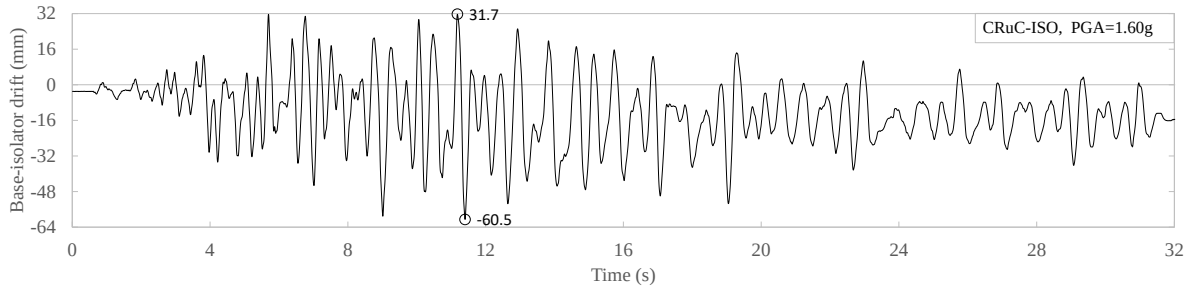

Figure C. 6: Base-isolator drift time history for the CRuC-ISO building (PGA=1.60g)

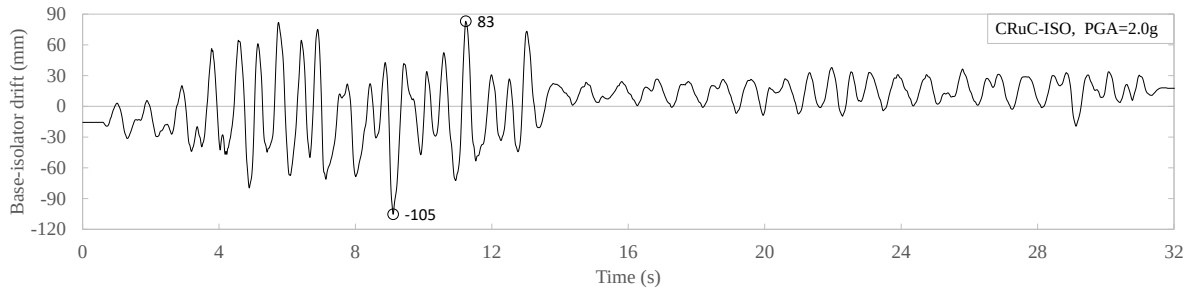

Figure C. 7: Base-isolator drift time history for the CRuC-ISO building (PGA=2.0g)

Short column drift (top of superstructure)

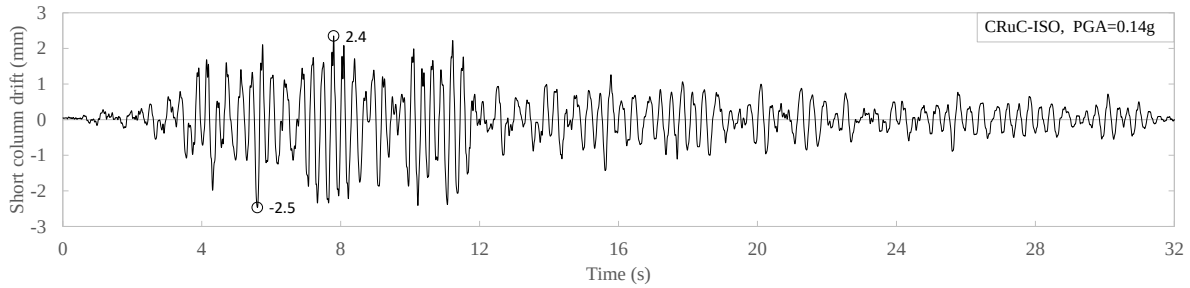

Figure C. 8: Short column drift time history for the CRuC-ISO building (PGA=0.14g)

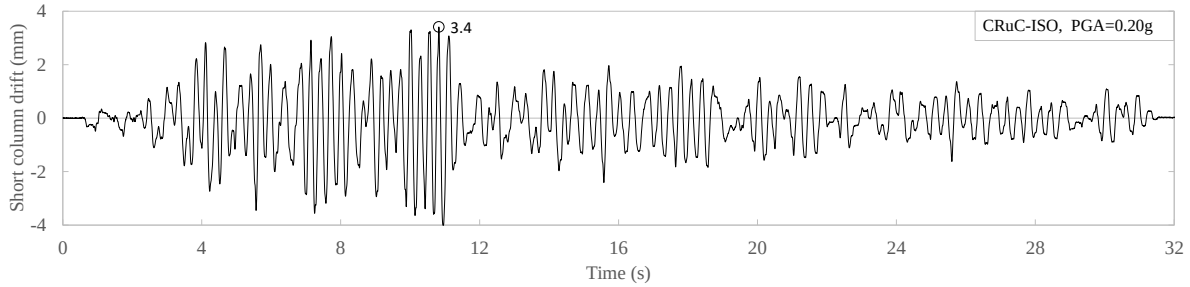

Figure C. 9: Short column drift time history for the CRuC-ISO building (PGA=0.20g)

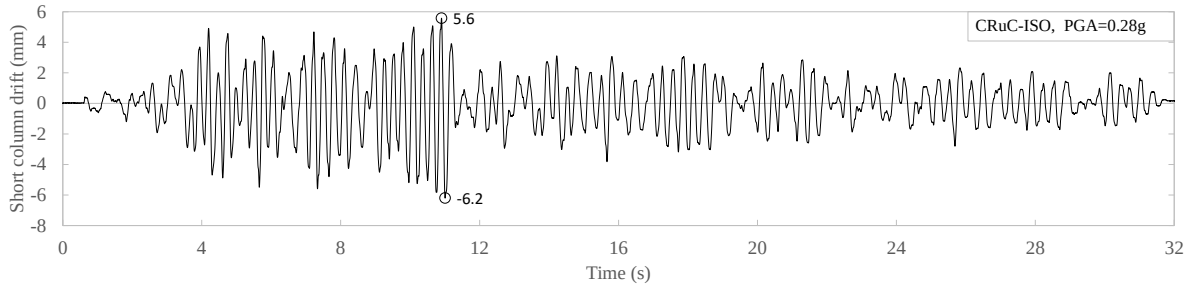

Figure C. 10: Short column drift time history for the CRuC-ISO building (PGA=0.28g)

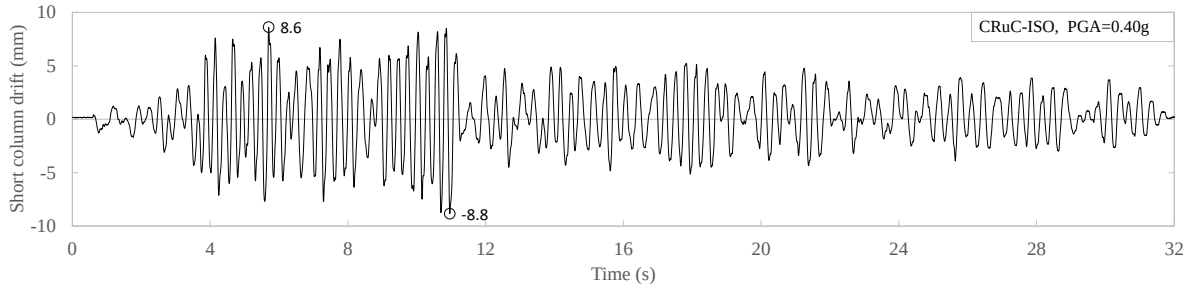

Figure C. 11: Short column drift time history for the CRuC-ISO building (PGA=0.40g)

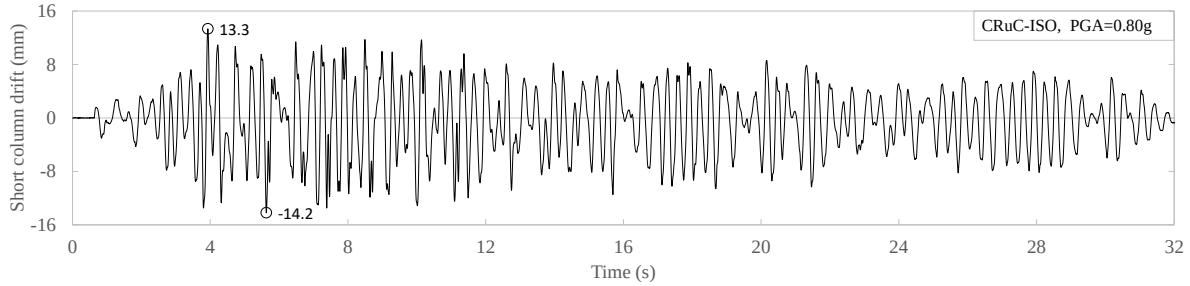

Figure C. 12: Short column drift time history for the CRuC-ISO building (PGA=0.80g)

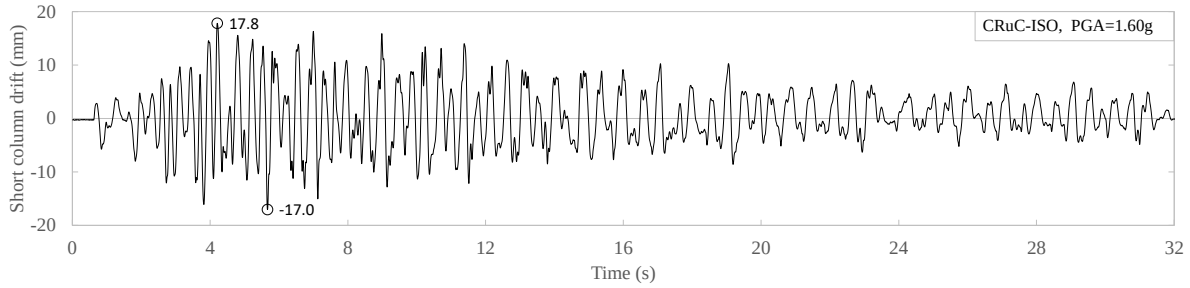

Figure C. 13: Short column drift time history for the CRuC-ISO building (PGA=1.60g)

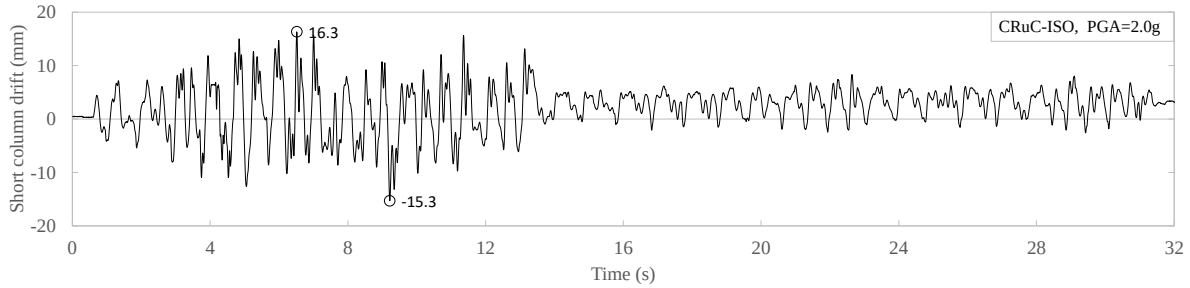

Figure C. 14: Short column drift time history for the CRuC-ISO building (PGA=2.0g)

Accelerations at the top of the base-isolators

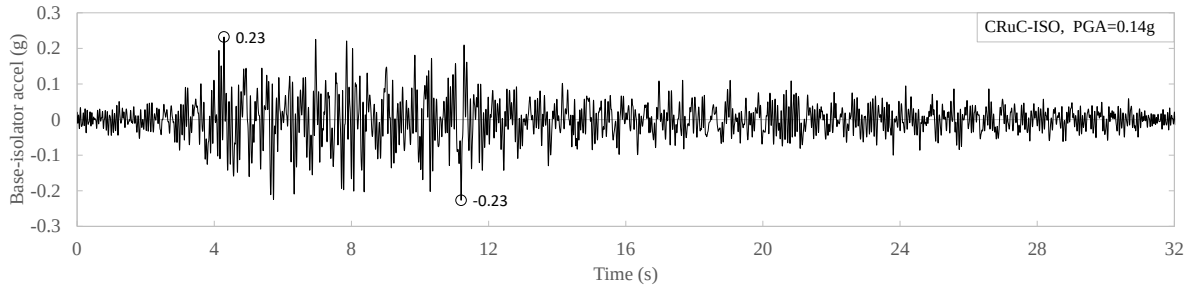

Figure C. 15: Base-isolator acceleration time history of the CRuC-ISO building (PGA=0.14g)

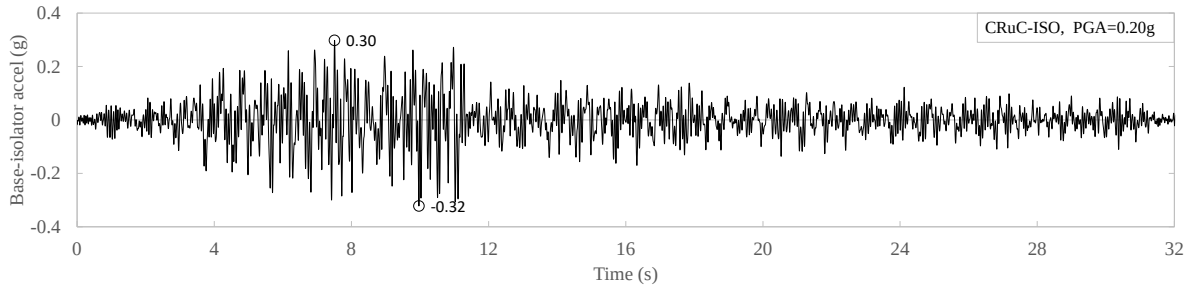

Figure C. 16: Base-isolator acceleration time history of the CRuC-ISO building (PGA=0.20g)

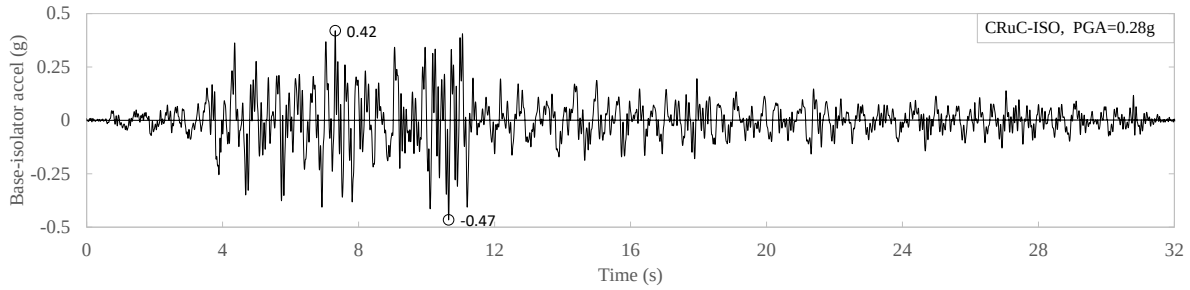

Figure C. 17: Base-isolator acceleration time history of the CRuC-ISO building (PGA=0.28g)

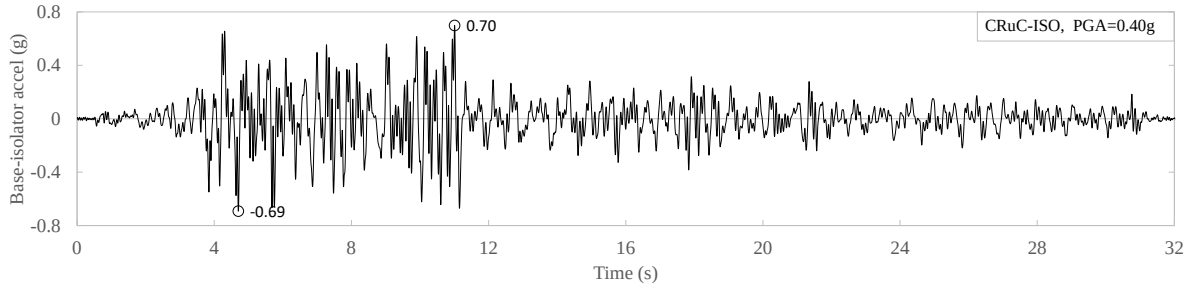

Figure C. 18: Base-isolator acceleration time history of the CRuC-ISO building (PGA=0.40g)

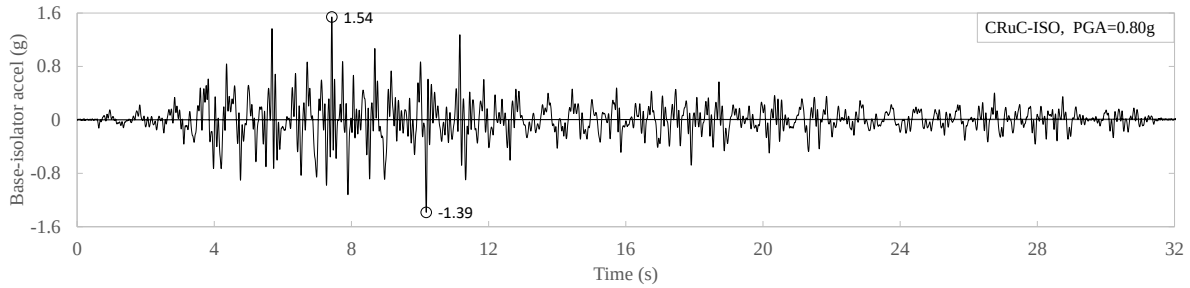

Figure C. 19: Base-isolator acceleration time history of the CRuC-ISO building (PGA=0.80g)

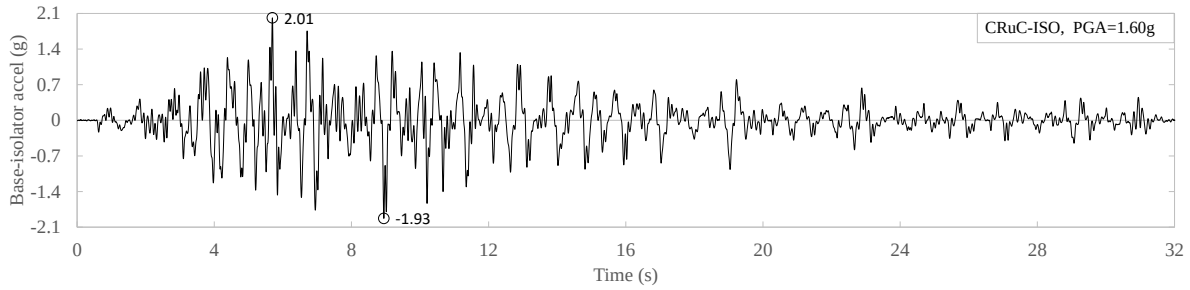

Figure C. 20: Base-isolator acceleration time history of the CRuC-ISO building (PGA=1.60g)

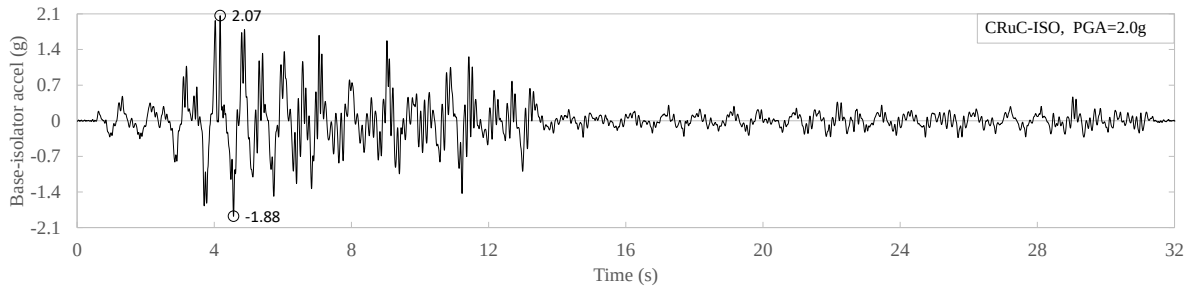

Figure C. 21: Base-isolator acceleration time history of the CRuC-ISO building (PGA=2.0g)

Accelerations at the top of the building (roof accelerations)

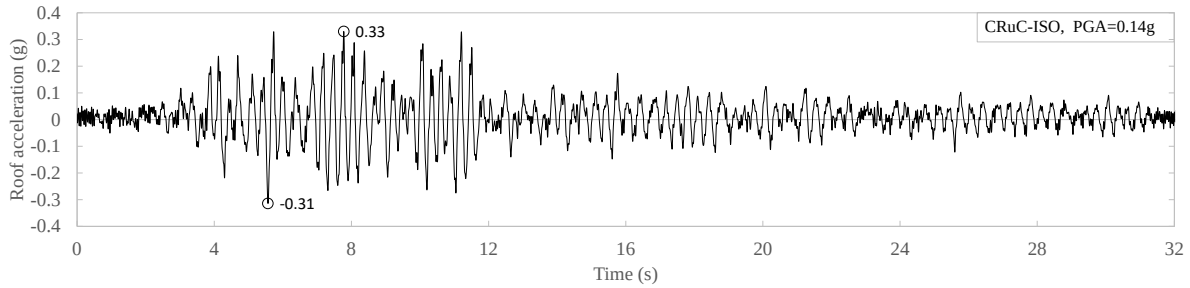

Figure C. 22: Roof acceleration time history of the CRuC-ISO building (PGA=0.14g)

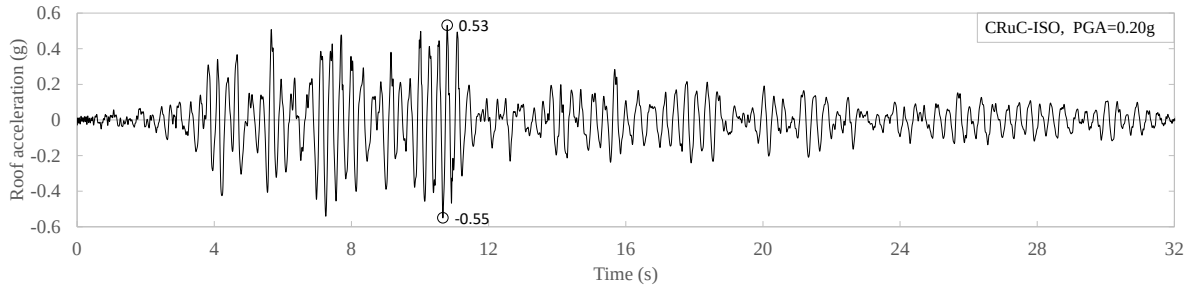

Figure C. 23: Roof acceleration time history of the CRuC-ISO building (PGA=0.20g)

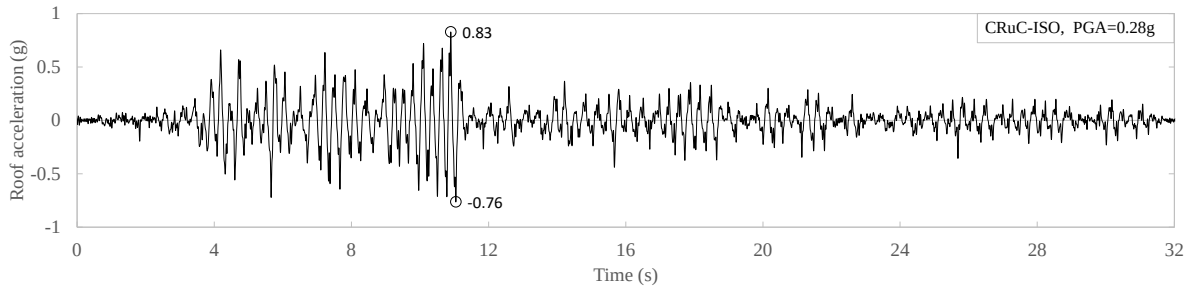

Figure C. 24: Roof acceleration time history of the CRuC-ISO building (PGA=0.28g)

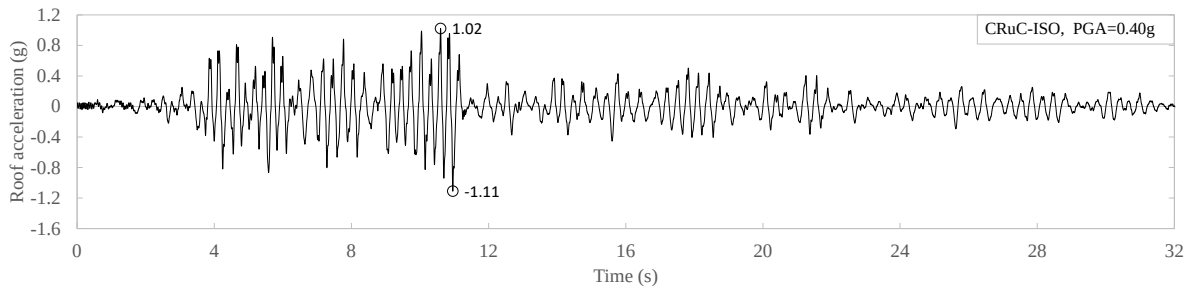

Figure C. 25: Roof acceleration time history of the CRuC-ISO building (PGA=0.40g)

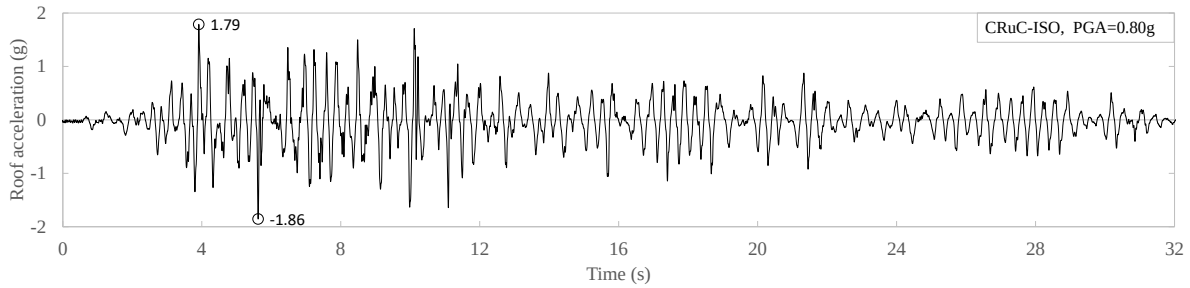

Figure C. 26: Roof acceleration time history of the CRuC-ISO building (PGA=0.80g)

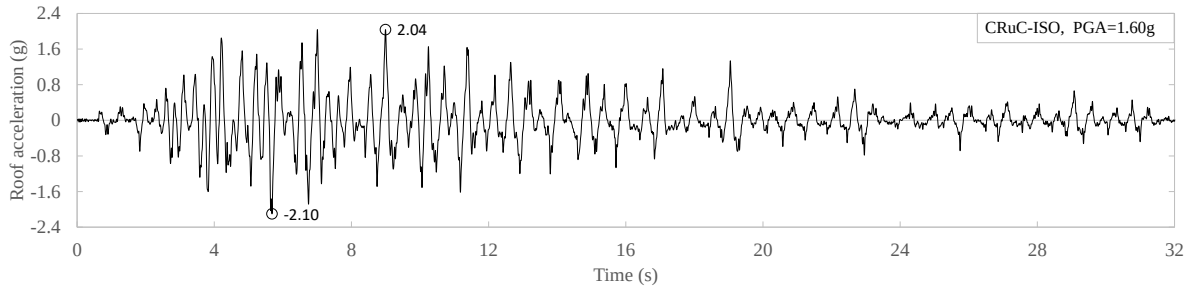

Figure C. 27: Roof acceleration time history of the CRuC-ISO building (PGA=1.60g)

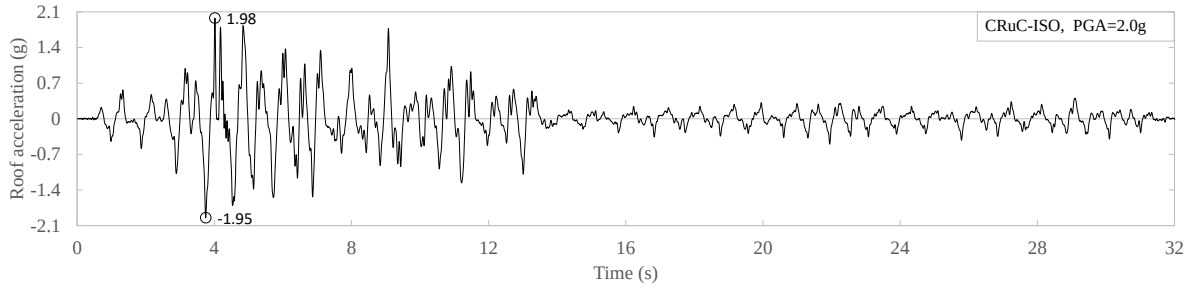

Figure C. 28: Roof acceleration time history of the CRuC-ISO building (PGA=2.0g)

Strain gauge recordings

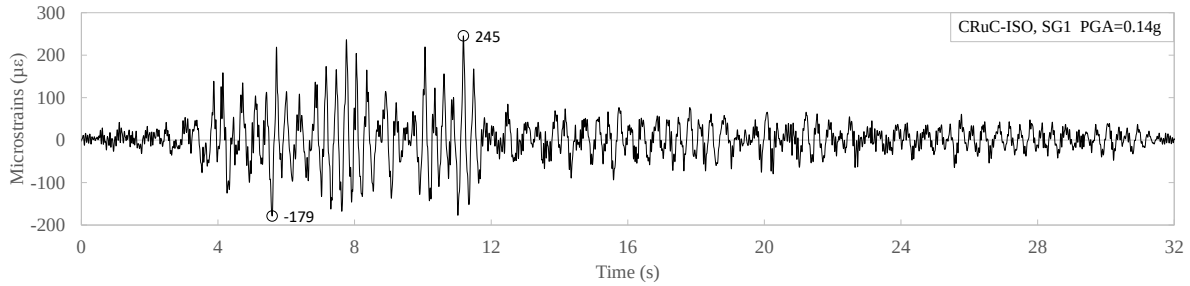

Figure C. 29: Strain time history of the base-isolator flexural reinforcement (PGA=0.14g)

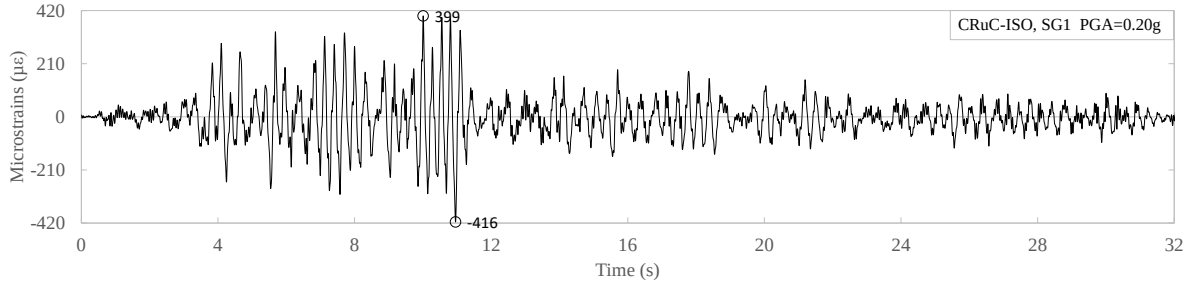

Figure C. 30: Strain time history of the base-isolator flexural reinforcement (PGA=0.20g)

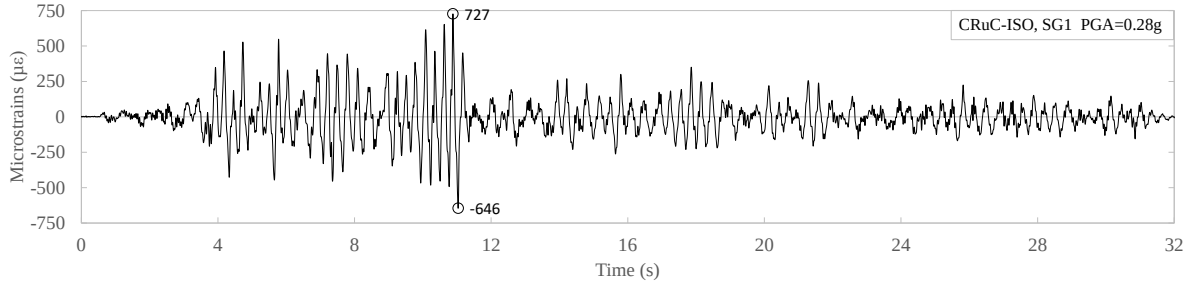

Figure C. 31: Strain time history of the base-isolator flexural reinforcement (PGA=0.28g)

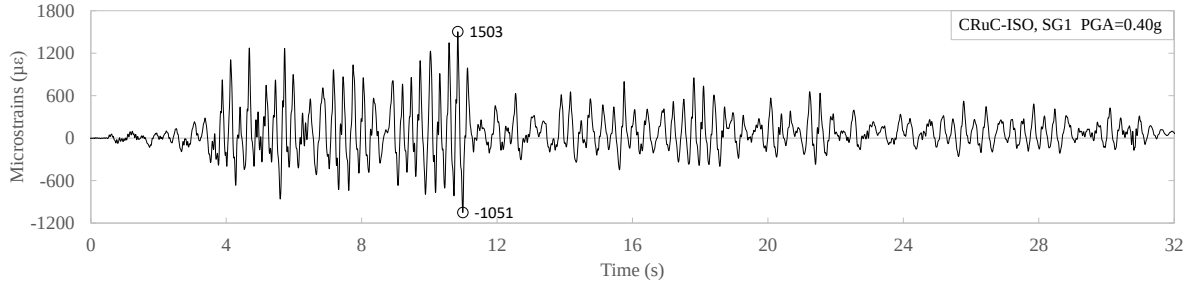

Figure C. 32: Strain time history of the base-isolator flexural reinforcement (PGA=0.40g)

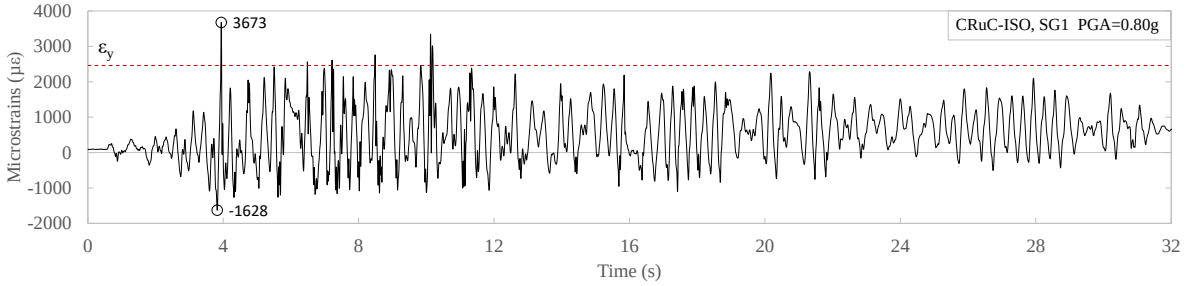

Figure C. 33: Strain time history of the base-isolator flexural reinforcement (PGA=0.80g)

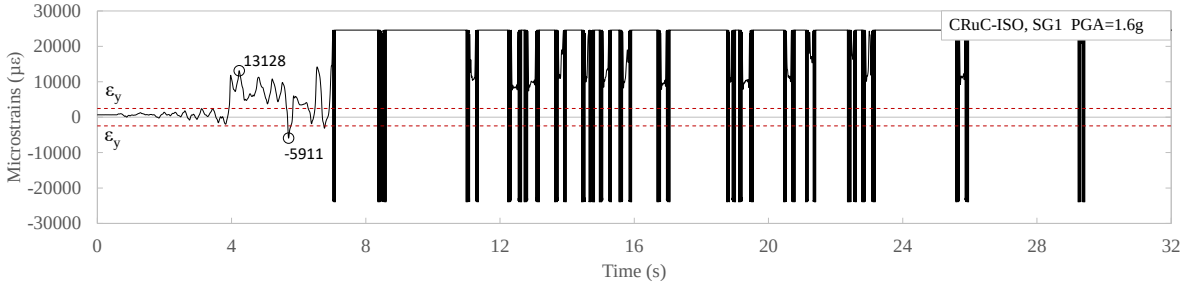

Figure C. 34: Strain time history of the base-isolator flexural reinforcement (PGA=1.60g)

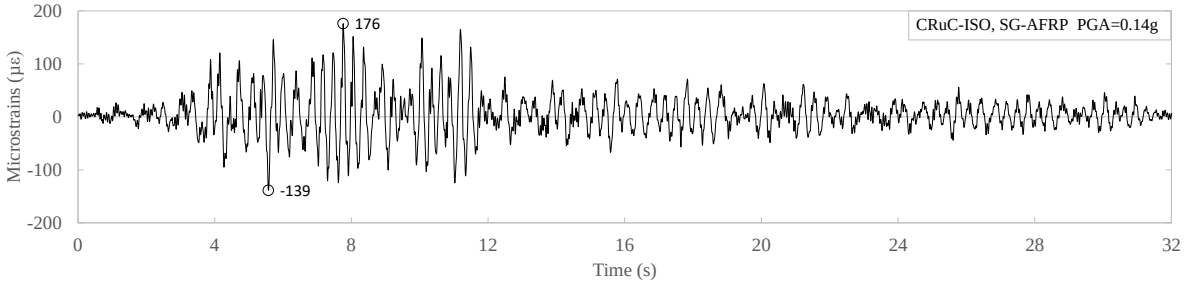

Figure C. 35: Strain time history of the base-isolator AFRP jacket (PGA=0.14g)

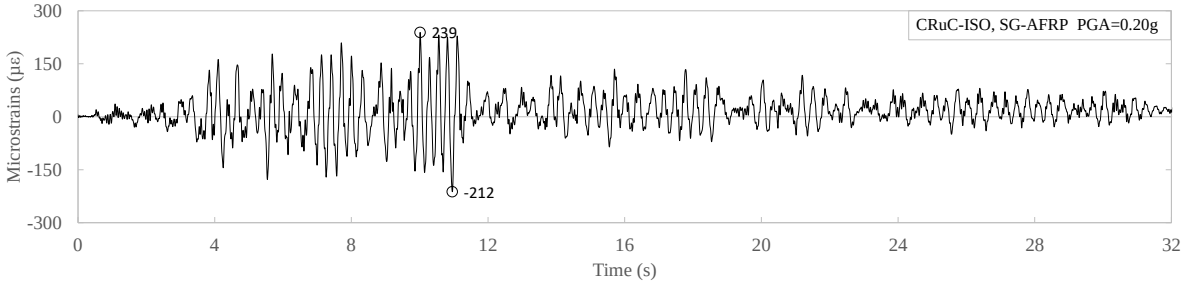

Figure C. 36: Strain time history of the base-isolator AFRP jacket (PGA=0.20g)

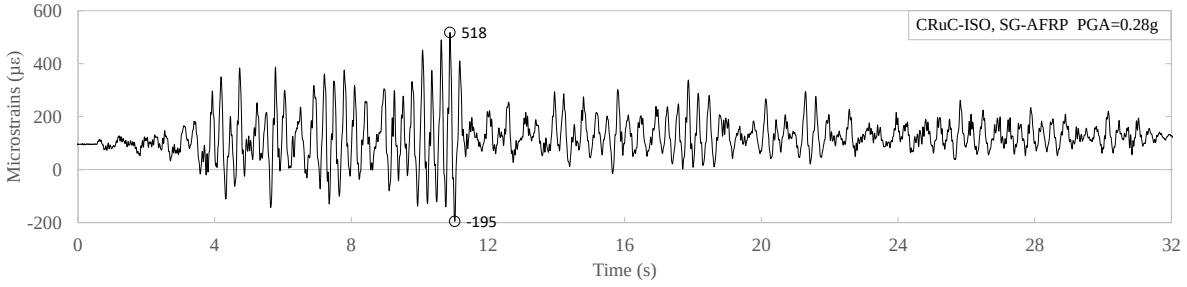

Figure C. 37: Strain time history of the base-isolator AFRP jacket (PGA=0.28g)

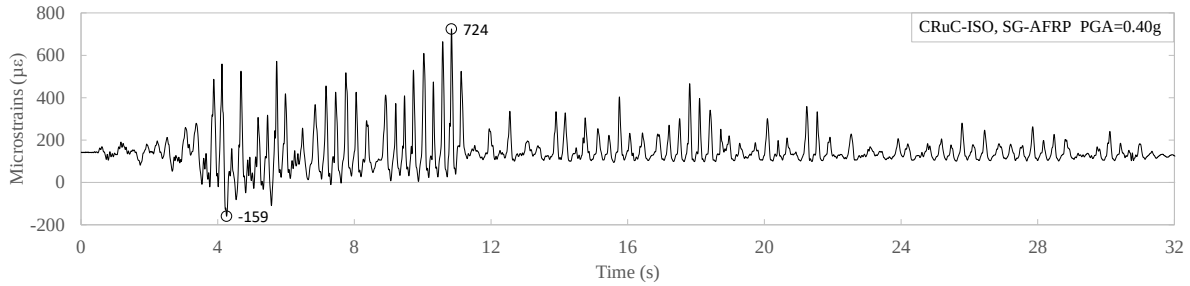

Figure C. 38: Strain time history of the base-isolator AFRP jacket (PGA=0.40g)

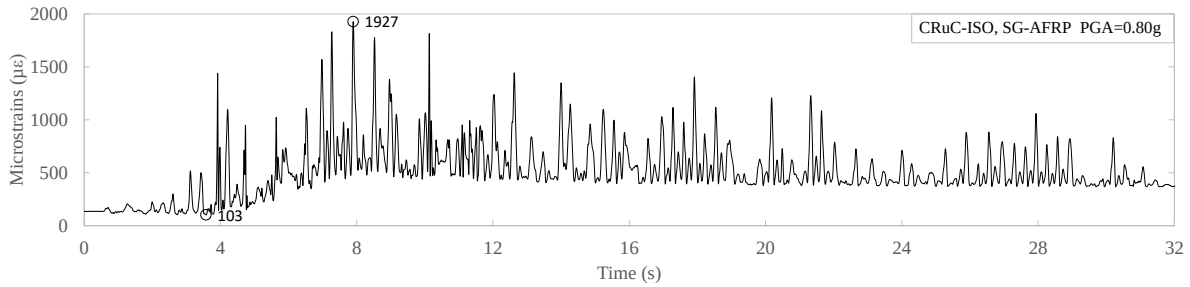

Figure C. 39: Strain time history of the base-isolator AFRP jacket (PGA=0.80g)

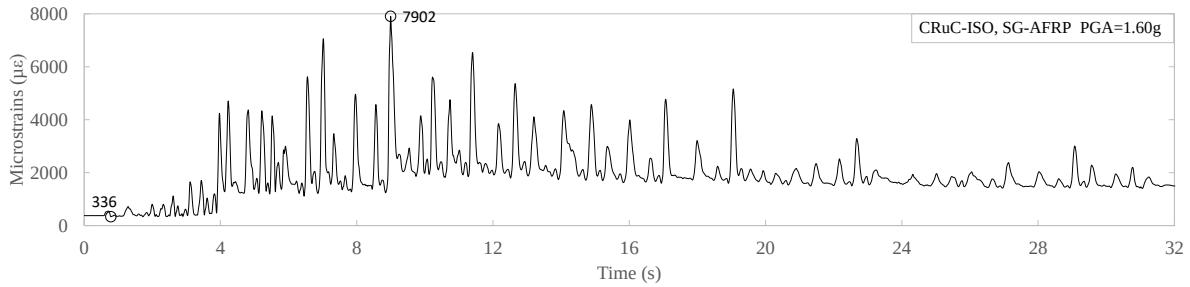

Figure C. 40: Strain time history of the base-isolator AFRP jacket (PGA=1.60g)

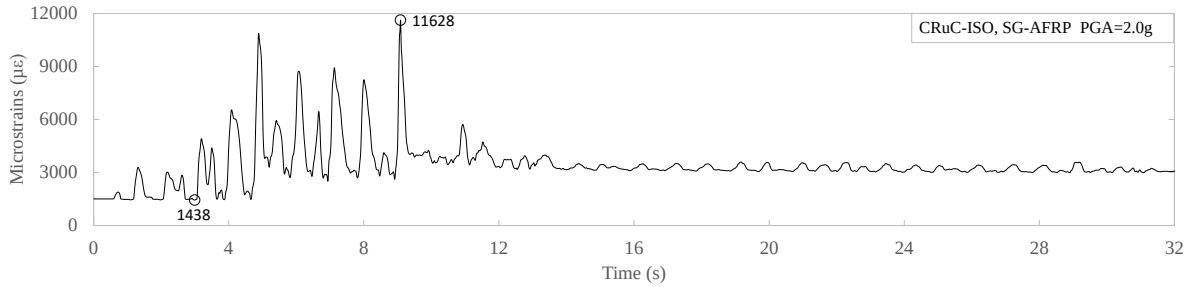

Figure C. 41: Strain time history of the base-isolator AFRP jacket (PGA=2.0g)

C2: BUILDING DESIGN IN SAP2000

The following are snapshot figures that show the axial load, shear, and moment force acting on the beams and columns from the dead, live, and elastic response spectrum analysis performed in SAP2000.

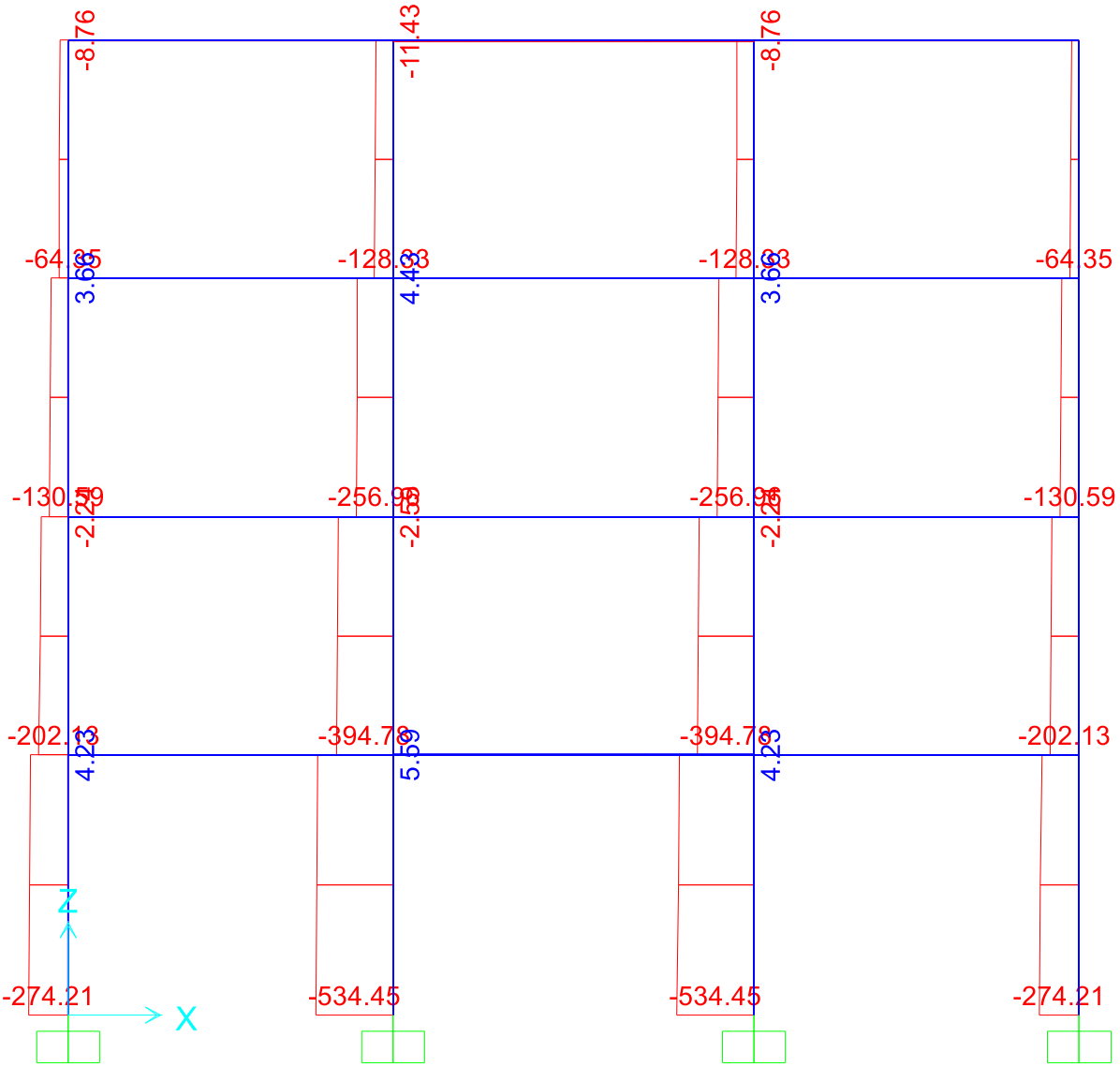

Figure C. 42: Axial force from the dead loads

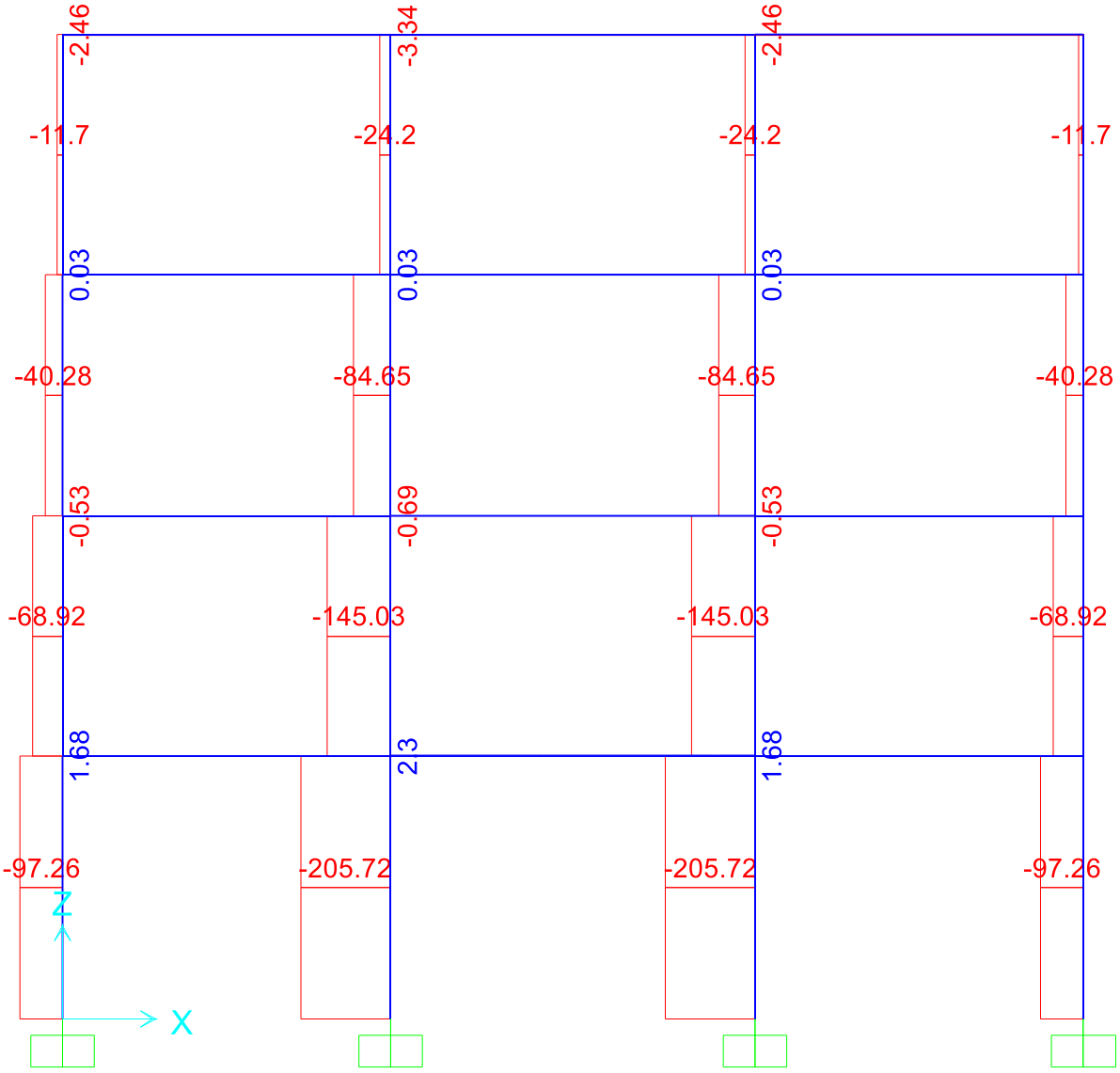

Figure C. 43: Axial force from the live loads

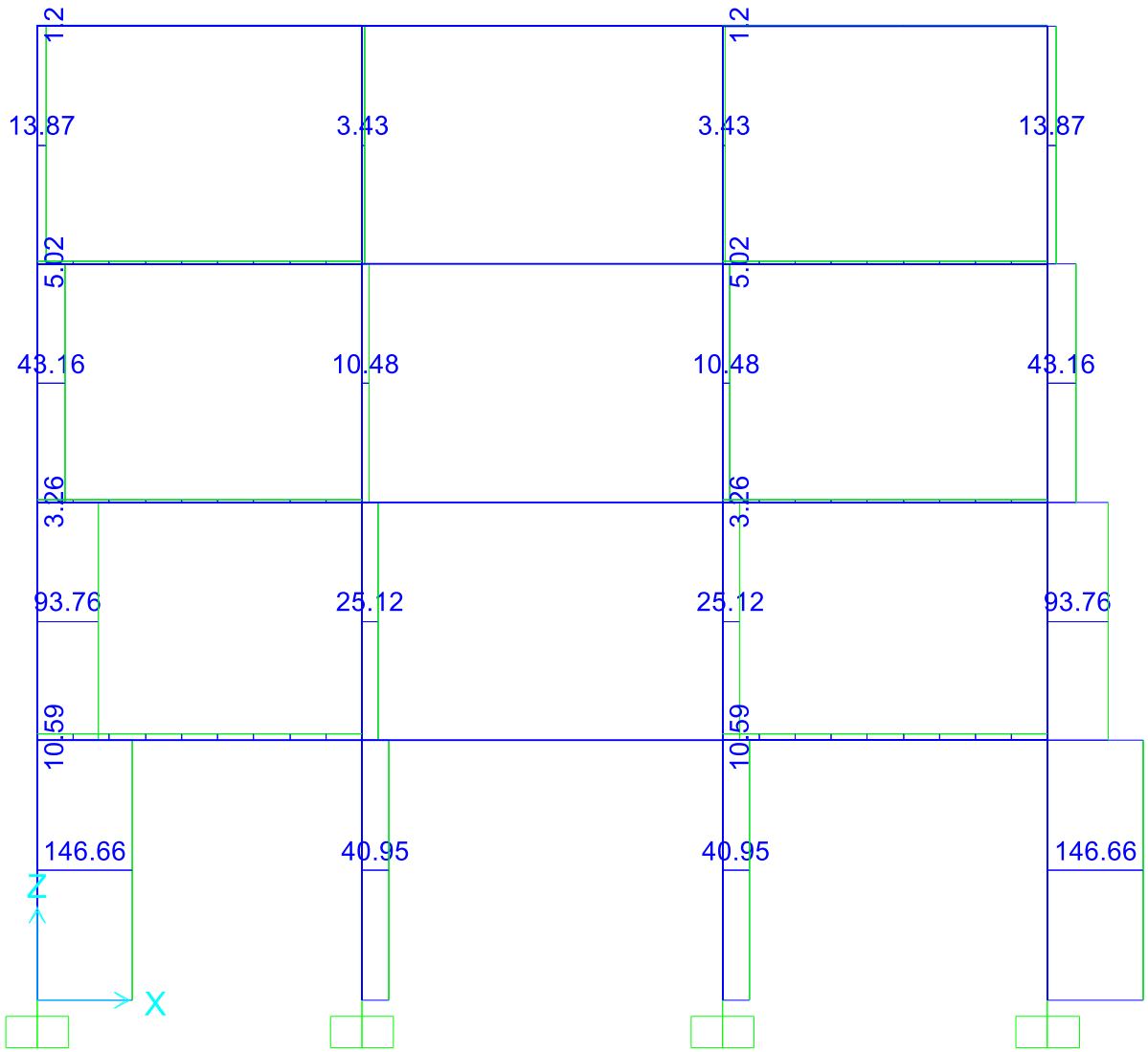

Figure C. 44: Axial force from the elastic response spectrum analysis

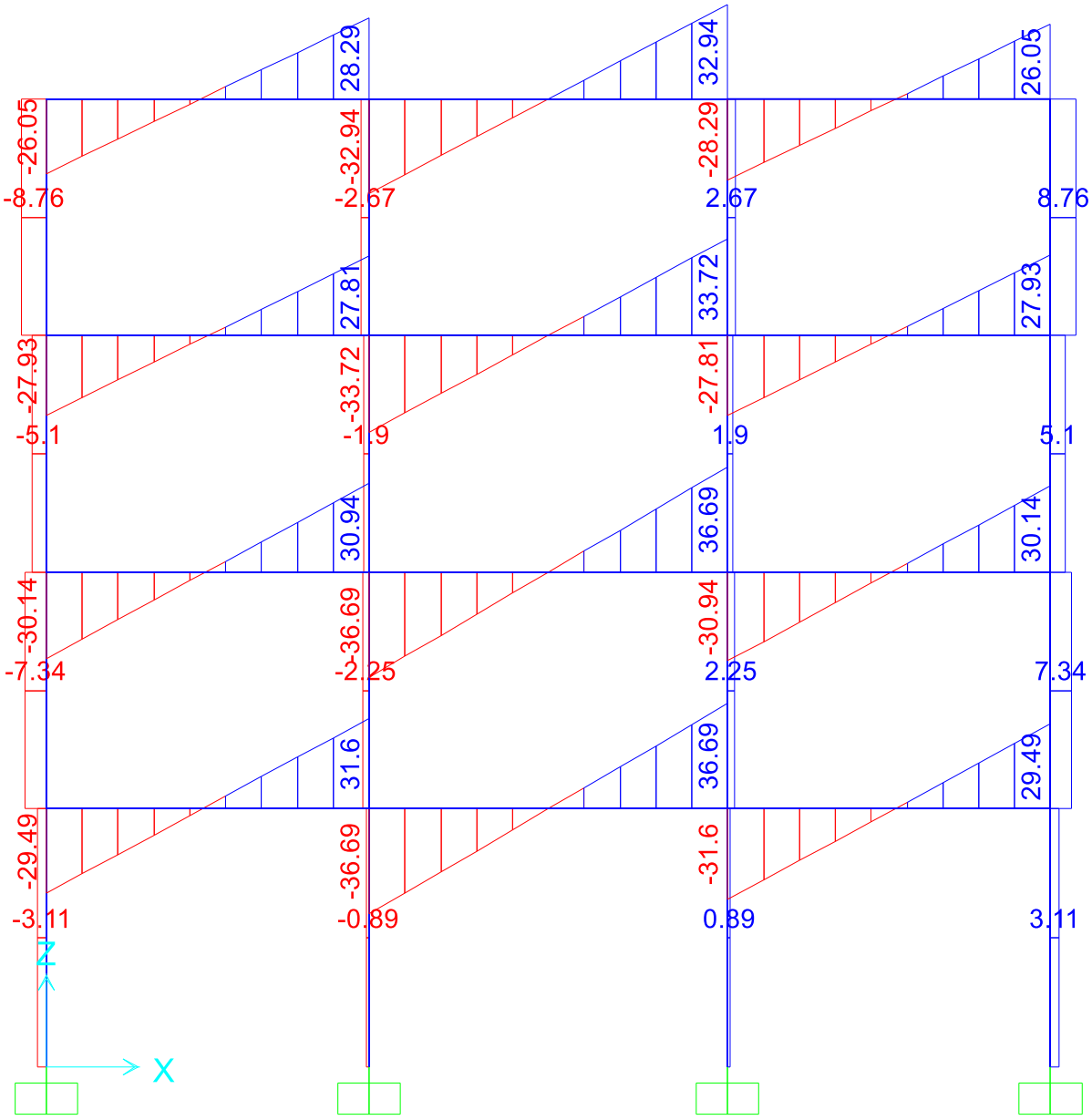

Figure C. 45: Shear force from the dead loads

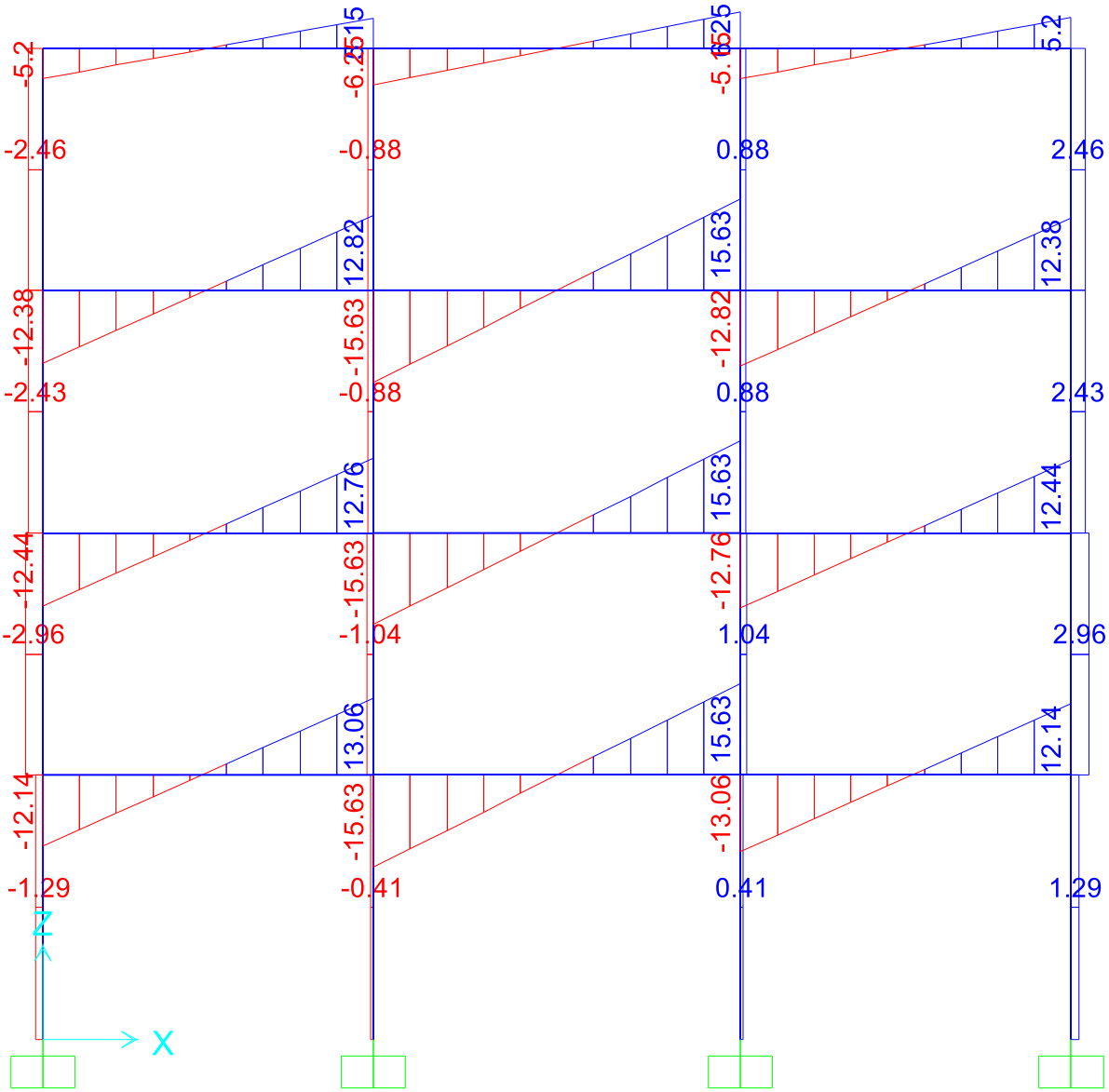

Figure C. 46: Shear force from the live loads

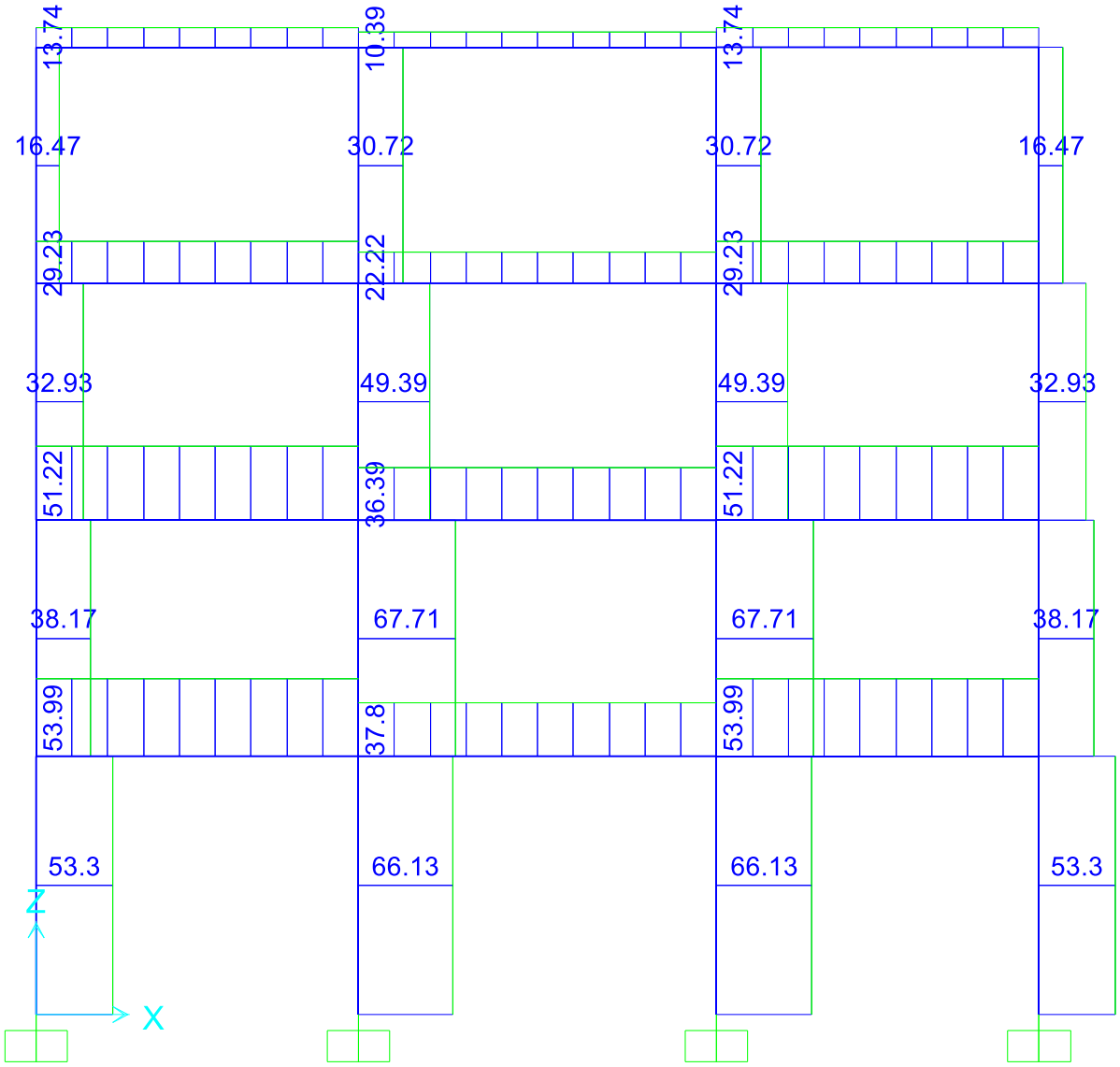

Figure C. 47: Shear force from the elastic response spectrum analysis

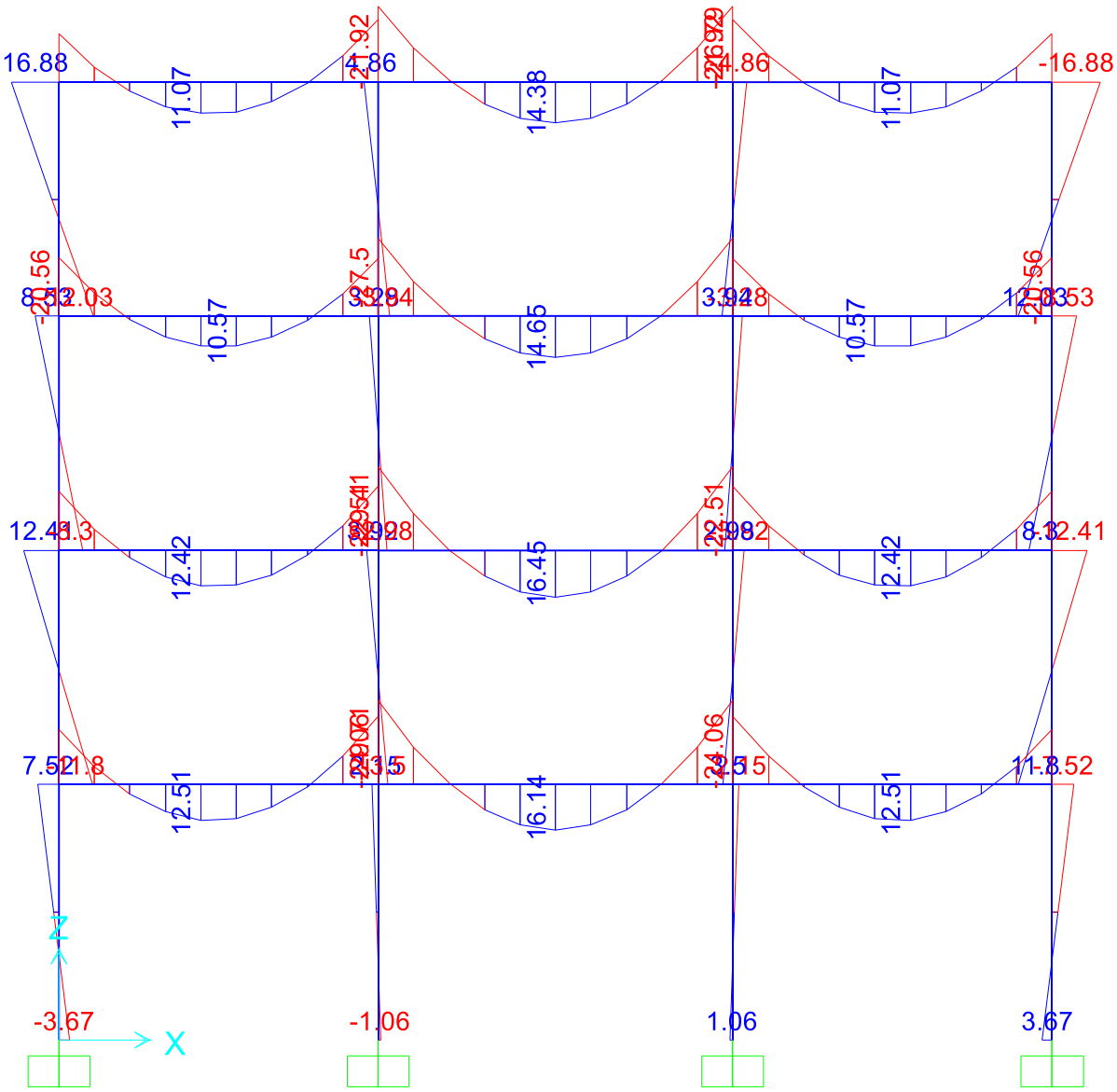

Figure C. 48: Moment from the dead loads

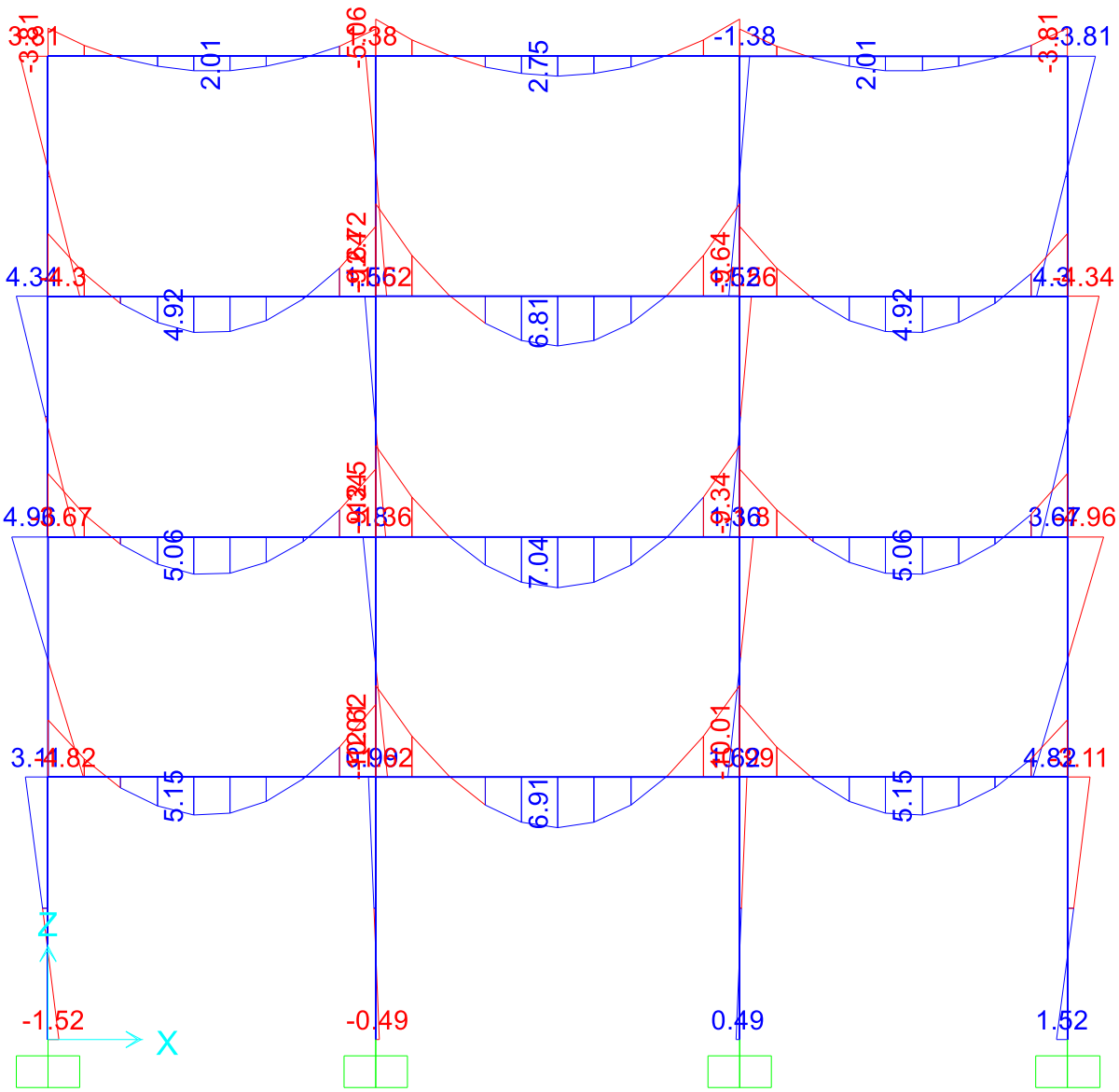

Figure C. 49: Moment from the live loads

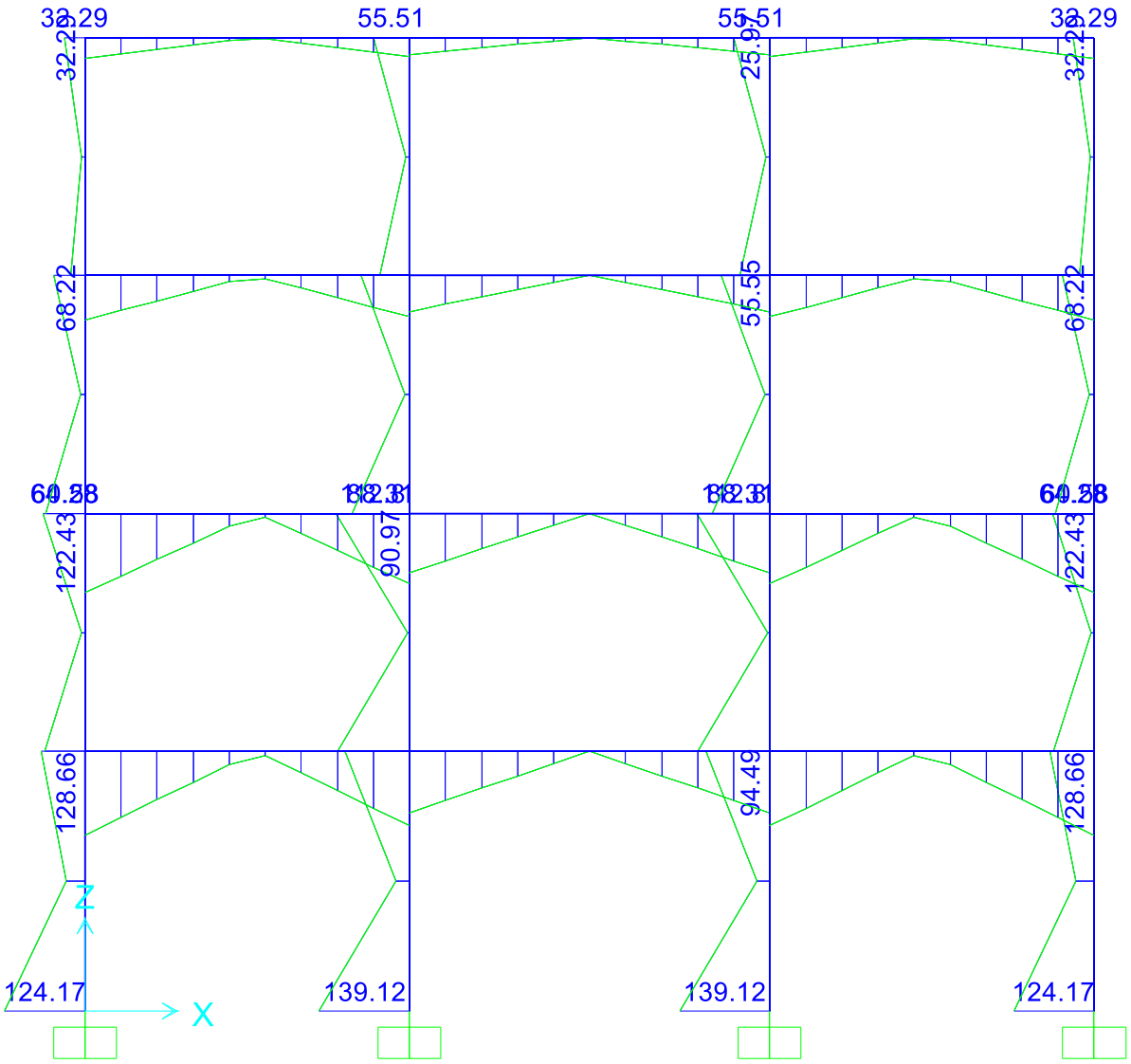

Figure C. 50: Moment from the elastic response spectrum analysis

C3: SEISMIC RESULTS OF THE FIRST CRUC BASE-ISOLATION DESIGN

The following are the seismic results of the first CRuC base-isolation design, with 20 base-isolating columns with a height of 1.5 metre. For reference, Figure C.51 of the building under consideration from Chapter 5 is shown below.

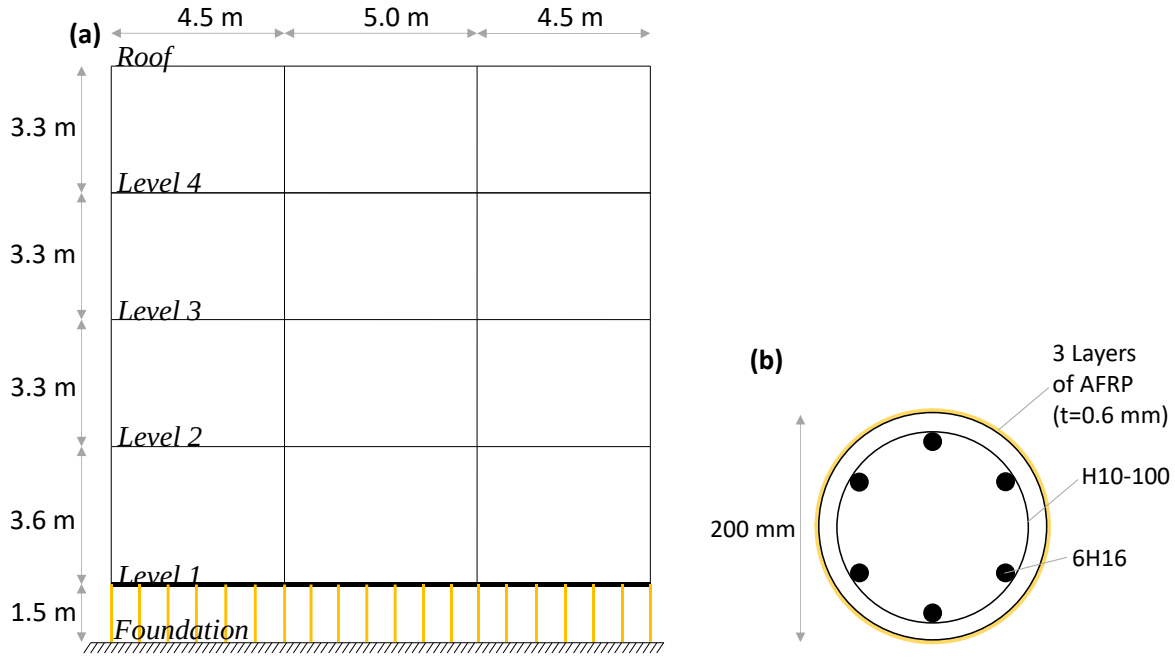

Figure C. 51: a) Elevation view of the base-isolated building, and b) Cross-section description of the CRuC base-isolator

Natural period and global damage index

The global damage index (GDI) provides a quantitative method to assess the global damage taken by a building after an earthquake by comparing the natural period of the structure before and after the earthquake. This study uses the global damage index proposed by DiPasquale et al. (Dipasquale et al., 1990).

$$GDI = 1 - \left(\frac{T_i}{T_f}\right)^2 \tag{5.1}$$

where T_i and T_f are the natural structural period before and after the earthquake, respectively.

A GDI value ranges between zero and one, with zero indicating no change in the natural period and accordingly no damage to the structure, whereas a GDI value of one indicates theoretical collapse of the building. Table 5.4 below shows the undamaged natural period of the two buildings, the period after the application of the excitation record, and the corresponding GDI.

Table C. 1: Natural period evolution of the fixed-base and base-isolated building, and corresponding damage index

PGA	Fixed-base			Base-isolated		
	T_i (s)	T_f (s)	GDI	T_i (s)	T_f (s)	GDI
0.15g	0.643	0.873	0.458	0.778	0.858	0.178
0.30g	0.643	1.115	0.667	0.778	0.950	0.329
0.45g	0.643	1.152	0.688	0.778	1.023	0.422

The base-isolated building had an undamaged natural period of 0.778 s, which is 21% longer than that of the fixed-base. This is generally more for other base-isolation systems, such as lead-rubber bearings (LRB), due to the lower stiffness of the LRB base-isolators. Nonetheless, this shift in the natural period reduces the response acceleration on the building. The GDI was significantly higher for the fixed-base building for all the PGA excitations, which means that the damage taken by the fixed-base building is higher than that of the base-isolated building for the same level of excitation. The better performance of the base-isolated building can be mainly attributed to the reduction in the response acceleration of the building due to the period shift, and the damping properties of CRuC, as well as the localization of damage in the base-isolators themselves, while reducing the damage taken by the superstructure.

Inter-storey drift ratio

Table 5.5 shows the maximum inter-storey drift ratio (IDR) at the various levels of the superstructure for both fixed-base and base-isolated structure for all PGA excitations.

Table C. 2: Maximum inter-storey drift ratio for the fixed-base and base-isolated building

PGA	Fixed-base				Base-isolated*			
	Level 1	Level 2	Level 3	Roof	Level 1	Level 2	Level 3	Roof
0.15g	0.39	0.45	0.55	0.48	0.31 (21%)	0.38 (15%)	0.46 (16%)	0.40 (17%)
0.30g	0.89	1.06	1.40	1.24	0.72 (19%)	0.88 (17%)	1.13 (20%)	0.94 (24%)
0.45g	1.32	1.71	2.22	1.79	0.99 (25%)	1.33 (22%)	1.84 (17%)	1.32 (26%)

Drift ratio is in percent.

* The percent reduction in drift for the base-isolated building is shown in parenthesis.

The base-isolated building had between 15% to 25% less drift ratio compared to the fixed-base building, for various floors and PGA excitations. There is no strong correlation between the PGA level of the earthquake and the percent of reduction, however, more reduction in the drift ratio is observed for the stronger earthquakes. The latter could be due to the softening of the base-isolators at high deformations, which would mean more damping as well as smaller response acceleration.

Eurocode 8 prevents excessive damage by limiting the permissible inter-storey drift ratio (IDR) as shown in Equation 5.3:

$$d_r v \leq \alpha_i h \tag{5.2}$$

where d_r is the storey drift calculated from the difference of the top and bottom storey displacement at that storey, v is the reduction factor and is equal to 0.5 for buildings with importance class I and II, α_i is equal to 0.01 for buildings without non-structural elements, and h is the storey height. Table 5.6 shows the values of $(d_r \cdot v)/\alpha$ values and the corresponding check against the corresponding storey height.

Table C. 3: Eurocode 8 inter-storey drift limitation check; values in table are (dr·ν)/α

PGA	Fixed-base				Base-isolated			
	Level 1 (3.6 m)	Level 2 (3.3 m)	Level 3 (3.3 m)	Roof (3.3 m)	Level 1 (3.6 m)	Level 2 (3.3 m)	Level 3 (3.3 m)	Roof (3.3 m)
0.15g	0.70 ✓	0.74 ✓	0.91 ✓	0.79 ✓	0.56 ✓	0.63 ✓	0.76 ✓	0.66 ✓
0.30g	1.60 ✓	1.75 ✓	2.31 ✓	2.04 ✓	1.29 ✓	1.45 ✓	1.86 ✓	1.55 ✓
0.45g	2.38 ✓	2.82 ✓	3.66 ✗	2.95 ✓	1.78 ✓	2.19 ✓	3.04 ✓	2.18 ✓

(dr·ν)/α values shown are in meters, and compared to 3.6 or 3.3 m depending on storey height.

The limitation of inter-storey drift of the fixed-base building is safe except for the level 3 storey during the 0.45g PGA earthquake (150% of the designed for PGA). The base-isolated building passes the inter-storey drift check for all levels and all PGA excitations applied.

Figure C.52 shows the time-history IDR of the third storey (Level 3), for the three PGA excitations, along with drift limits as given by VISION 2000 (SEAOC, 1995). VISION 2000 specifies an IDR of 0.2% as fully operational (FO), 0.5% imposes minor damage to the building but still operational (O), 1.5% is heavy damage with possible risk to life safety (LS), and an IDR of 2.5% indicates the building is in a near collapse (NC) state due to severe damage.

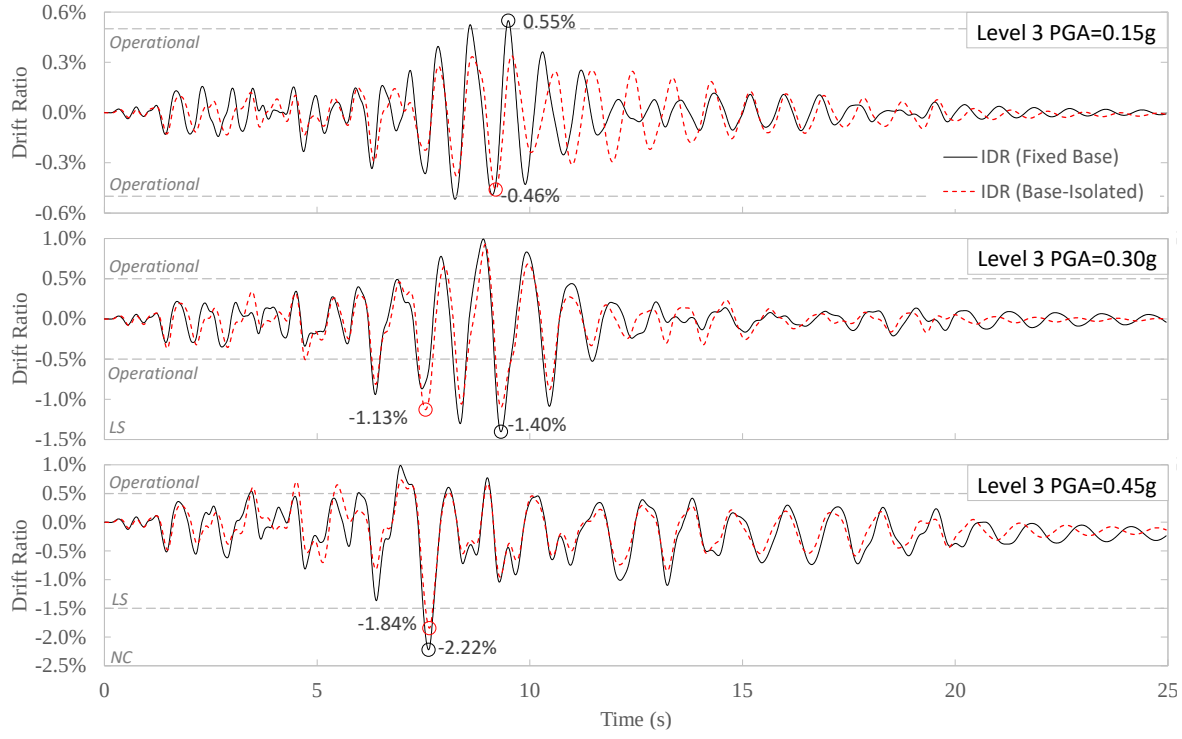

Figure C. 52: Time-history inter-storey drift of the third floor

In general, the time-history response of the base-isolated building had less inter-storey drift. However, few peaks were out-of-phase due to the different structural period and this led to higher IDR for the base-isolated building at some instances. That being said, the maximum drift recorded for all PGA excitations was always higher for the fixed-base building. Although none of the buildings reached a near collapse condition, an IDR of 2.22% was reached at Level 3 of the fixed-base building, during the 0.45g PGA earthquake, which indicates heavy to severe damage of the structure.

Maximum roof displacement and acceleration

Table 5.7 shows the maximum roof displacement relative to the ground level, and the maximum roof acceleration for the fixed-base and base-isolated building.

Table C. 4: Maximum roof displacement relative to ground, and maximum roof acceleration

PGA	Maximum roof displacement (cm)			Maximum roof acceleration		
	Fixed-base	Base-Isolated	Ratio*	Fixed-base	Base-Isolated	Ratio
0.15g	5.35	4.55	0.85	0.39g	0.31g	0.79
0.30g	13.1	10.5	0.80	0.65g	0.51g	0.78
0.45g	20.8	17.1	0.82	0.84g	0.72g	0.85

*Ratio of the base-isolated building's performance parameter to that of the fixed-base building.

The base-isolated building experienced, on average, between 15-20% less roof displacement compared to the fixed-base building, as well as 15-22% less roof acceleration. The reduction is more evident throughout the middle of the excitation time-history, which could be owed to the CRuC base-isolators getting more activated at high accelerations.

Figure C.53 and C.54 show the time-history maximum roof displacement and maximum roof acceleration, respectively.

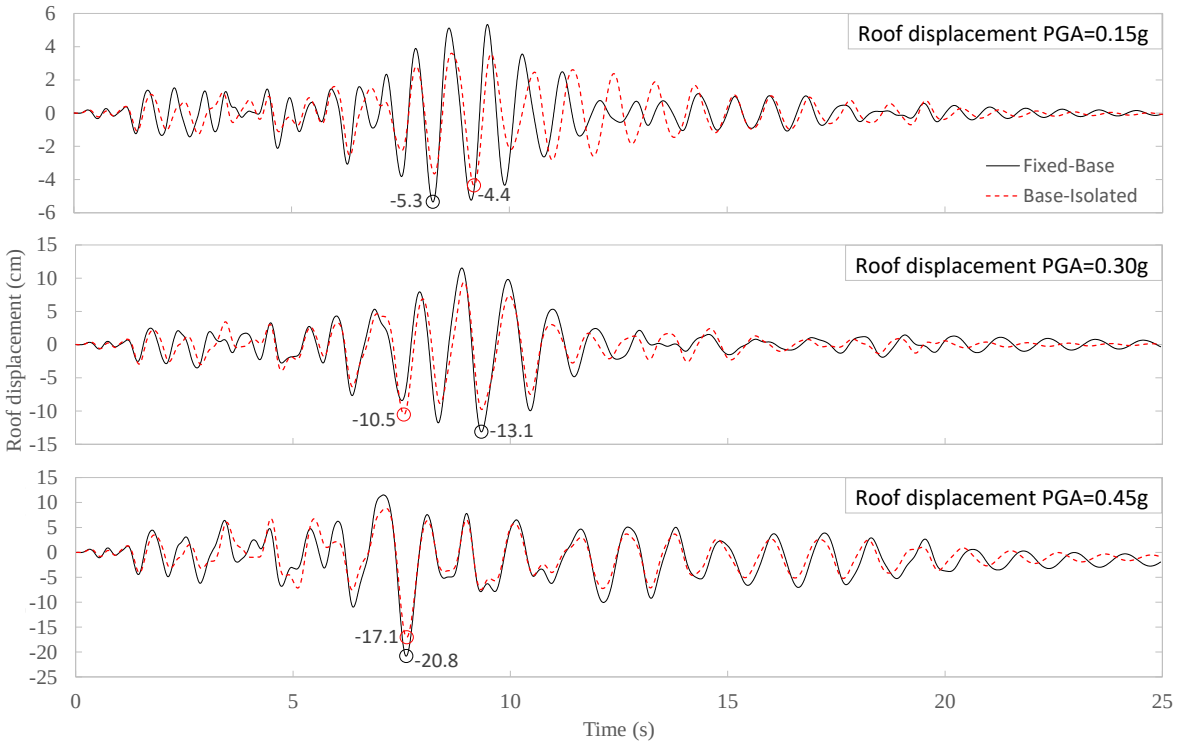

Figure C. 53: Time-history roof displacement relative to ground

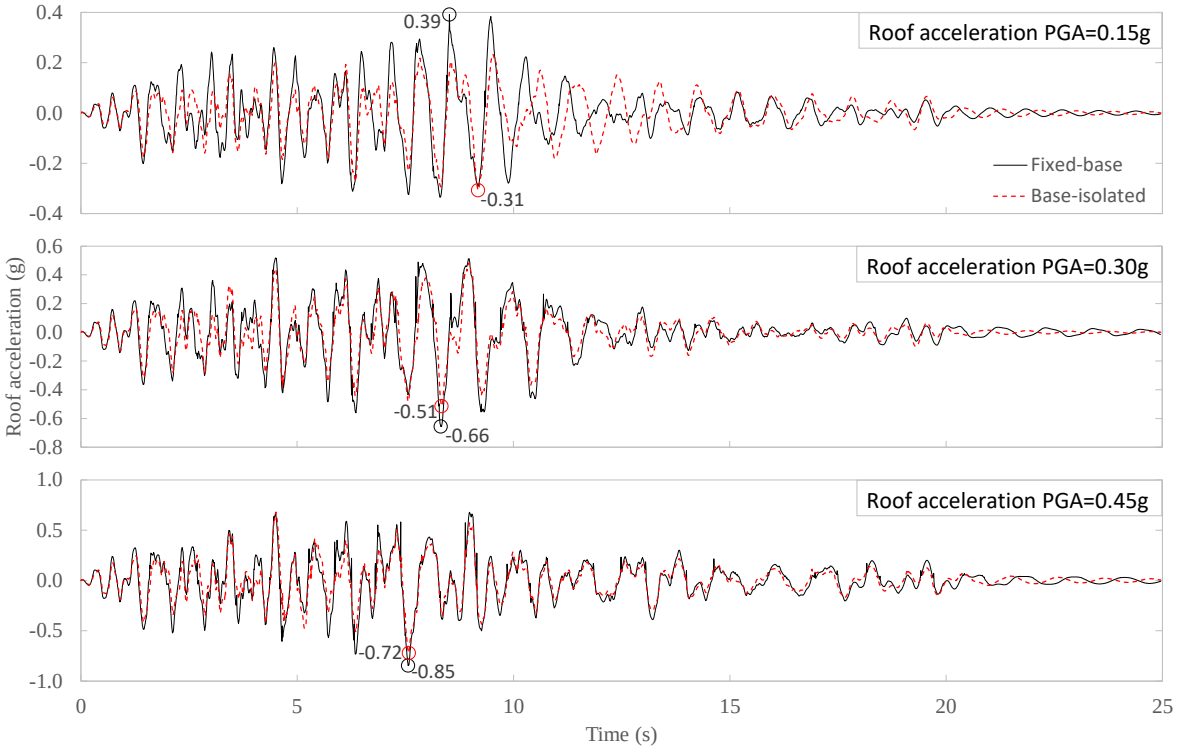

Figure C. 54: Time-history roof acceleration

Maximum base shear and moment

Table 5.8 shows the maximum base-shear and base-moment recorded for the fixed-base and base-isolated buildings.

Table C. 5: Maximum base-shear and base-moment for the fixed-base and base-isolated building

PGA	Maximum base-shear (kN)			Maximum base moment (kNm)		
	Fixed-base	Base-Isolated	Ratio*	Fixed-base	Base-Isolated	Ratio
0.15g	338	263	0.78	728	213	0.29
0.30g	493	372	0.75	1003	301	0.30
0.45g	566	465	0.82	1005	376	0.37

*Ratio of the base-isolated building's performance parameter to that of the fixed-base building.

The base-isolated building experienced, on average, between 18-22% less base-shear compared to the fixed-base building. This is due to the reduced response acceleration of the base-isolated frame, which reduced the inertial forces on the building.

The base-moment of the base-isolated building was significantly less than that of the fixed-base, with a percent reduction ranging between 63-71%. This is attributed to the lesser acceleration response of the base-isolated building, in addition to the fact that the system comprising the CRuC columns and the ground beam behaves differently than the four main columns at the ground floor. As such, the multiple columns sustained significantly less moment. The initial design of the CRuC base-isolators was based on the equivalent moment capacity of the superstructure ground columns, which was based on the linear elastic design using the combined force demands of dead, live, and response spectrum load. Considering the results of the base-moment obtained from the nonlinear time-history analysis, the base-isolating system could be redesigned with less CRuC columns, as both the shear and moment demand was reduced. Smaller number of base-isolator columns would mean an even softer base-isolating system, which would cause a longer shift in the natural period, and hence, reduce the response of the structure.

Figure C.55 and C.56 show the time-history base-shear and base-moment, respectively.

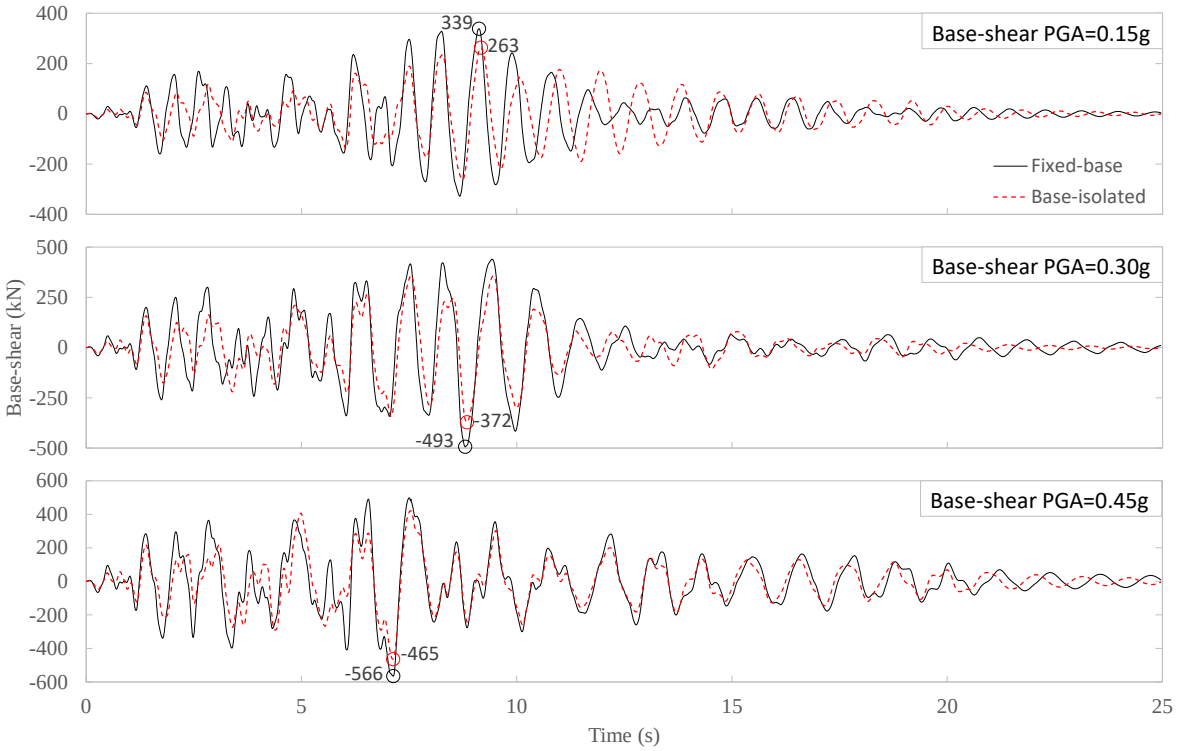

Figure C. 55: Time-history base-shear response in kN

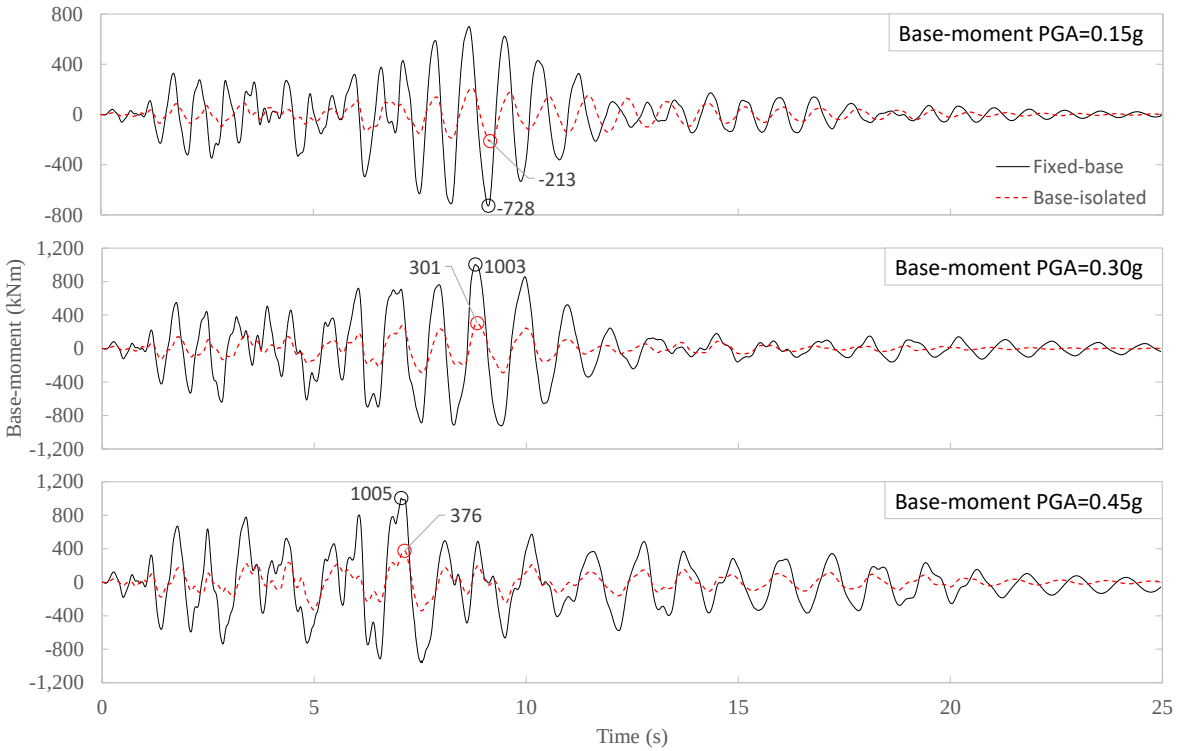

Figure C. 56: Time-history base-moment response in kNm